Diss ETH No. 14586

Extreme Ultraviolet and X-Ray Studies of Flare Heating and Elemental Composition of Stellar Coronae

Marc Audard

Cuvillier Verlag Göttingen

Diss. ETH No. 14586

Extreme Ultraviolet and X-Ray Studies of Flare Heating and Elemental Composition of Stellar Coronae

Diss. ETH No. 14586

Extreme Ultraviolet and X-Ray Studies of Flare Heating and Elemental Composition of Stellar Coronae

A dissertation submitted to the
SWISS FEDERAL INSTITUTE OF TECHNOLOGY
ZÜRICH

for the degree of
Doctor of Natural Sciences

presented by

MARC AUDARD
Dipl. Phys. (Université de Lausanne)

born May 1, 1974
citizen of Lausanne (VD)

accepted on the recommendation of
Prof. Dr. Arnold Otto Benz, examiner
PD Dr. Manuel Güdel and
Prof. Dr. Jan Olof Stenflo, co-examiners

2002

Die Deutsche Bibliothek - CIP-Einheitsaufnahme

Audard, Marc:
Extreme Ultraviolet and X-Ray Studies of Flare Heating and Elemental Composition of Stellar Coronae / presented by Marc Audard. -
1. Aufl. - Göttingen : Cuvillier, 2002
Zugl.: Zürich, ETH, Diss., 2002
ISBN 3-89873-396-3

Nonnenstieg 8, 37075 Göttingen
Telefon: 0551-54724-0
Telefax: 0551-54724-21
www.cuvillier.de

1. Auflage, 2002
Gedruckt auf säurefreiem Papier

ISBN 3-89873-396-3

Acknowledgments

Almost four years have passed since I began my doctoral thesis at the Paul Scherrer Institute and the Institute of Astronomy of the Swiss Federal Institute of Technology Zürich. I have very much enjoyed the days (and nights!) spent at work, and I feel happy to have started to contribute to the exciting world of scientific research in astrophysics. I have realized an old dream of mine since I was thirteen: to become a professional astronomer!

This goal could never have been reached without my supervisor, Manuel Güdel. Thanks to his approach of supervising, I have felt the excitement of being a real scientist. We had countless professional and personal discussions together, also on (infamous) political issues. I feel honored that colleagues have shown interest in our work. Furthermore I appreciate our excellent collaboration and good friendship. Our colleagues are still surprised by our weekly language switch (one week in French, the following in German)! Thanks to Manuel, I feel that I have become a trained scientist ready to continue in astrophysics. I have been constantly supported during my thesis. I sincerely wish that our friendship and collaboration will continue further into the future. I wish every graduate student to have such a supervisor. In brief, *Danke Manuel!*

Since I had two workplaces (PSI/ETHZ), I had the chance to know many people. First of all, I thank Arnold Benz for being my "Doktorvater", and for the many insightful scientific discussions we had. RAPP "coffee breakers", namely Michael Arnold, Kaspar Arzner, Paolo Grigis, Peter Messmer, Urmila Mitra Kraev, Christian Monstein, Gunnar Paesold, Anuschka Pauluhn, Pascal Saint-Hilaire, and Kester Smith are also gratefully acknowledged. We had the pleasure to discuss on many occasions during coffee breaks, in the stairs, or at journal clubs. I am also thankful to my present and former PSI colleagues, Kaspar Arzner (again!), Fritz Burri, Laurent Desorgher, Martin Fivian, Miha Furlan, Lukas Grenacher, Wojtek Hajdas, Reinhold Henneck, Iwan Jerjen, Eugenie Kirk, Philippe Lerch, Alex Mchedlishvili, John Olsen, Knud Thomsen, Damian Twerenbold, and, last but not least, the boss, Alex Zehnder, for creating a good atmosphere during my days in the Laboratory for Astrophysics. I also thank all the former and current members of the Institute of Astronomy at ETHZ, especially Jan Stenflo who provided me with a working place with a most beautiful view over Zürich and who joined as a co-referee for this thesis, Barbara Codoni for her insightful administrative skills, and Peter Steiner for being so patient with my computer needs.

I would like to mention my colleagues from the Reflection Grating Spectrometer Consortium, Ehud Behar, Graziella Branduardi-Raymont, Albert Brinkman, Anton den Boggende, Jean Cottam, Christian Erd, Jan Willem den Herder, Jelle Kaastra, Steven Kahn, Maurice Leuteneg-

ger, Rolf Mewe, Frederick Paerels, John Peterson, Anton Raassen, Andrew Rasmussen, Doug Reynolds, Irini Sakelliou, Masao Sako, Takayuki Tamura, Cor de Vries, with whom I shared the excitement of discovering and exploiting the early *XMM-Newton* data. I had also many discussions with some members of the *XMM-Newton* SAS team, foremost with Jean Ballet, Michael Freyberg, Frank Haberl, Uwe Lammers, Giuseppe Vacanti, and Peter Videler.

During this thesis, I had the honor to meet several colleagues in the field of stellar coronae, with whom I shared many discussions and collaborations, foremost Thomas Ayres, Nancy Brickhouse, Jeremy Drake, Stephen Drake, Elena Franciosini, Vinay Kashyap, Jeffrey Linsky, Hilary Magee, Thierry Montmerle, Jan-Uwe Ness, Rachel Osten, Roberto Pallavicini, Jorge Sanz, Steve Skinner, Randall Smith, Beate Stelzer, and Stephen White. Let me thank them here for accepting me in this field. I especially thank Jan-Uwe and Beate for carefully reading the introductory chapters and for insightful comments.

On a more personal touch, I would like to thank Rolf Mewe for the friendly contacts we had at several occasions. Although about half a century separates our scientific careers, he always made me feel comfortable in our discussions. I have found a friend and an experienced scientist in him to discuss with.

During this thesis, I have always been supported by my family. I deeply regret that my work in Zürich prevented me from seeing them more often. I thank them for their belief in me and for cheering me up with many phone calls. Last but not least, I wish to thank Marjorie for being so patient with my strange working hours, and for providing me with a lot of happy moments.

I acknowledge financial support from the Swiss National Science Foundation (grants 2100-049343 and 2000-058827). Several young-researcher grants from the Swiss Commission for Space Research, from the Swiss Commission of Astronomy, and from the Swiss Society for Astrophysics and Astronomy are also gratefully acknowledged. I also thank Bernard Hauck for providing access to a Jenny Fonds grant from the Swiss Academy of Sciences. Some figures presented in this thesis were extracted from the Extreme Ultraviolet Explorer Guest Observer Program Handbook that was obtained from the Multimission Archive at the Space Telescope Science Institute (MAST). STScI is operated by the Association of Universities for Research in Astronomy, Inc., under NASA contract NAS5-26555. Support for MAST for non-HST data is provided by the NASA Office of Space Science via grant NAG5-7584 and by other grants and contracts. Some figures were also extracted from the XMM-Newton Users' Handbook. XMM-Newton is an ESA science mission with instruments and contributions directly funded by ESA Member States and the USA (NASA). I also thank Albert Brinkman, Adrian Daw, Uri Feldman, Manuel Güdel, Jan Willem den Herder, Fred Jansen, Jeffrey Linsky, and David McKenzie for granting me permission to use some of their published figures in this thesis. I am grateful to the American Astronomical Society, the editor of Astronomy and Astrophysics (Claude Bertout), and Kluwer Academic Publishers for granting me permission to use published material.

Contents

Abstract

Stellar coronae are the most numerous X-ray sources in our Galaxy. They i) display a rich spectrum of X-ray atomic lines from cosmic elements in collisional ionization equilibrium, ii) exhibit a wide range of temperatures ($\approx$ 1–100 MK) and densities (10^9–10^{12} cm^{-3}); and iii) coronal magnetic fields frequently interact through magnetohydrodynamic processes. Stellar coronae are therefore ideal astrophysical plasma laboratories. Their study also pertains to the origin of cosmic rays, to the impact of the young Sun on planetary atmospheres and life, and to fundamental plasma or atomic physical processes.

This doctoral thesis is aimed at studying physical processes taking place in stellar coronae. Chapter 1 gives a short overview of the principal findings in the field of solar and stellar coronae that are relevant for the subsequent chapters in this thesis. In Chapter 2, short technical overviews of the *Extreme Ultraviolet Explorer* and *XMM-Newton* satellites are given, since their data were of principal importance.

The remaining portion of the thesis is divided essentially into two parts. In the first part (*Flare Statistics in Active Stars*), the contribution of flares as a *statistical ensemble* to coronal heating in young active stars is investigated. In a pilot study with two young solar analogs (Chapter 3), the flare occurrence rate distribution in energy is found to be a power law with an index $\alpha \approx 2.2 \pm 0.2$. For power-law indices $\alpha > 2$, flares with small energies contribute most to the total emitted flare energy; this ensemble of flares may suffice to explain all of the observed flaring and "quiescent" X-ray emissions. A considerable fraction, if not all, of the energy required to heat the coronae could thus be provided by flares. From a comprehensive study of the flare activity in main-sequence cool stars (spectral types F to M) with the *Extreme Ultraviolet Explorer* (Chapter 4), power laws are found to describe approximately the flare occurrence rate distributions in energy. The power-law indices range $\alpha = 1.5 - 2.6$, with a suggested trend toward flatter distributions for later-type stars. Although detected flares contributed ≈ 10 % of the observed radiated power loss, a continuation of the power laws to minimum radiated energies of $E_{\rm min} \approx 10^{29} - 10^{31}$ ergs could be sufficient to balance all radiative losses. A clear correlation between the occurrence rate of flares with energies above a critical energy (10^{32} ergs) and the X-ray luminosity implies that energetic flares occur more often in X-ray bright stars than in X-ray faint stars. Saturation of the X-ray emission and of the occurrence rate of flares is however also observed. Taking advantage of a very long exposure on the flare star AD Leonis, its flare rate distribution in radiated energy has been investigated (Chapter 5). The observed light curve has been compared with light curves synthesized from model flares

that are distributed in energy according to a power law with selectable index α. Acceptable solutions range $\alpha = 2.1 - 2.5$. The results again suggest that flares can play an important role and contribute a significant amount of energy to coronal heating in active stars.

In the second part of this thesis (*High-Resolution X-Ray Spectroscopy*), high-resolution X-ray spectra from the *XMM-Newton* satellite have been analyzed. A time-dependent analysis of a large flare in the RS CVn binary HR 1099 has been performed (Chapter 6). The flare emission measure distribution shows two distinct components: a very hot plasma (up to 100 MK) that evolves rapidly, and a stable quiescent plasma. The abundances of low-First Ionization Potential (FIP) elements increase significantly during the flare, while the abundance of the high-FIP element Ne stays constant at the quiescent value. The high signal-to-noise ratio of the RGS X-ray spectrum of Capella shows bright emission lines from Fe L-shell lines (Chapter 7). Its emission measure distribution displays a sharp peak around 7 MK. The best-fit model, however, does not reproduce numerous lines, owing to their absence in the current atomic databases. The spectral variability of the coronal plasma in a very active star, AB Doradus, has been studied (Chapter 8). The high-resolution spectrum shows flux changes in lines of highly ionized Fe during the flares, and an increase of the continuum. Elemental abundances increase in the early flare phases by a factor of three, however an inverse FIP effect (high-FIP elements overabundant relative to low-FIP elements) is observed in the quiescent corona of AB Dor. The average density of the cool plasma is $\approx 3 \times 10^{10}$ cm^{-3}; this value does not change during the flares. For the first time, both Castor A and B of the multiple stellar system Castor AB and YY Geminorum have been spatially separated and identified as frequent flaring sources (Chapter 9). The light curve of the eclipsing binary YY Gem show three deep eclipses. A 3-D inversion of the light curve shows that the coronae of both components are similarly active and relatively compact. In an investigation of the elemental abundances in stellar coronae that cover a wide range of activity (Chapter 10), elements with a low First Ionization Potential are underabundant relative to high-FIP elements in the most active stars, signifying an inverse FIP effect, while less active stars show low-FIP abundance enhancements by factors of about $5 - 7$ (normal FIP effect). This suggests a transition from the inverse to the normal FIP effect as a consequence of decreasing coronal activity.

Finally, an outlook to future investigations of magnetically active stars is given in Chapter 11.

Résumé

Les couronnes des étoiles sont les sources les plus nombreuses de rayons X dans notre Galaxie. Elles émettent un riche spectre de raies atomiques provenant d'éléments cosmiques en équilibre collisionnel d'ionisation; elles ont un large éventail de températures ($\approx 1 - 100$ MK) et de densités ($10^9 - 10^{12}$ cm^{-3}); et les champs magnétiques coronaux interagissent fréquemment par des processus magnétohydrodynamiques. Les couronnes stellaires sont par conséquent des laboratoires idéaux d'étude des plasmas astrophysiques. Leur étude se rapporte aussi à l'origine des rayons cosmiques, à l'impact du jeune Soleil sur les atmosphères des planètes et sur la vie, ainsi qu'aux processus fondamentaux de la physique atomique et des plasmas.

Cette thèse de doctorat a pour but d'étudier les processus physiques dans les couronnes stellaires. Le Chapitre 1 donne une vue générale des découvertes principales (pertinentes pour les chapitres suivants) dans le domaine des couronnes solaire et stellaires. Au Chapitre 2, les données techniques des satellites *Extreme Ultraviolet Explorer (EUVE)* et *XMM-Newton* sont résumées en raison de l'importance de leurs données pour cette thèse.

Le reste de la thèse est divisée en deux parties. Dans la première partie (*Statistiques des flares*[1] *dans les étoiles actives*), la contribution des "flares" comme *ensemble statistique* au chauffage coronal des jeunes étoiles actives est examinée. Dans une étude pilote de deux jeunes analogues solaires (Chapitre 3), il est montré que la distribution en énergie des taux d'événements de flares suit une loi de puissance d'indice $\alpha \approx 2.2 \pm 0.2$. Pour des indices α supérieurs à 2, les flares de petites énergies contribuent principalement à l'énergie totale émise par les flares, énergie qui peut suffire à expliquer l'émission X, qu'elle soit "quiescente" ou non. Une fraction considérable, si ce n'est la totalité, de l'énergie requise pour chauffer les couronnes pourrait ainsi être fournie par les flares. Dans une étude de l'activité des flares chez les étoiles froides de séquence principale (types spectraux F à M) avec *EUVE* (Chapter 4), des valeurs $\alpha = 1.5 - 2.6$ des indices sont trouvées, avec une possible tendance d'indice plus petit chez les étoiles de type spectral plus tardif. Même si les flares détectés contribuent pour ≈ 10 % à la perte radiative de puissance, une continuation des lois de puissances jusqu'à des énergies minimum de rayonnement $E_{\rm min} \approx 10^{29-31}$ ergs pourrait suffire à égaler toutes les pertes radiatives. Une corrélation entre le taux d'événements des flares d'énergies supérieures à un certain seuil (10^{32} ergs) et la luminosité X implique une plus grande fréquence de flares énergétiques chez les étoiles brillantes dans le domaine X que chez les étoiles faibles. Toutefois une saturation de l'émission X et du taux d'événements des flares est aussi observée. La distribution en énergie

[1] Les flares sont définis comme des libérations explosives d'énergie et sont reliés à l'activité magnétique.

des taux d'évenements des flares de l'étoile à flares AD Leonis est examinée, en prenant avantage d'une très longue observation (Chapitre 5). Après comparaison de la courbe de lumière avec des courbes de lumière synthétisées au moyen de flares modélisés et distribués en énergie selon une loi de puissance d'indice déterminable α, les solutions acceptables trouvées sont $\alpha = 2.1 - 2.5$. Ceci suggère à nouveau que les flares peuvent jouer un rôle important et contribuer sensiblement au chauffage des couronnes d'étoiles actives.

Dans la second partie (*Spectroscopie X à haute résolution*), les spectres à haute résolution obtenus par *XMM-Newton* sont analysés. Pendant un large flare dans la binaire de type RS CVn, HR 1099, la distribution de mesures d'émission montre deux composantes distinctes: un plasma très chaud (jusqu'à 100 MK) évoluant rapidement, et un plasma quiescent stable (Chapitre 6). Les abondances des élements à bas premier potientiel d'ionisation (PPI) augmentent sensiblement lors du flare, tandis que l'abondance du Ne (élément à haut PPI) reste constante à la valeur quiescente. Le spectre X de Capella montre des raies brillantes d'émission provenant de raies de la couche L du fer (Chapitre 7) et indique une distribution de mesures d'émission très concentrée autour de 7 MK. Le meilleur modèle ne peut toutefois pas reproduire de nombreuses raies, en raison de leur absence dans les bases de données atomiques actuelles. La variabilité spectrale du plasma coronal de l'étoile très active, AB Doradus, est étudiée (Chapitre 8). Le spectre à haute résolution met en évidence pendant les flares des changements de flux dans les raies de fer hautement ionisé, ainsi qu'une intensification du continu. Les abondances des éléments augmentent pendant les premières phases des flares d'un facteur de trois, toutefois un effet inverse PPI (éléments à haut PPI surabondants relativement aux éléments à bas PPI) est observé dans la couronne quiescente d'AB Dor. La densité moyenne du plasma froid est $\approx 3 \times 10^{10}$ cm^{-3} et ne varie pas lors des flares. Pour la première fois, les deux composantes Castor A et B du système stellaire multiple Castor AB et YY Geminorum sont séparées et identifiées comme des sources fréquentes de flares (Chapitre 9). Une inversion tridimensionnelle de la courbe de lumière de la binaire à eclipses YY Gem montre que les couronnes des deux composantes sont similairement actives et relativement compactes. Lors d'une étude des abondances des éléments dans les couronnes stellaires couvrant un large éventail d'activité (Chapitre 10), les éléments à bas PPI se révèlent être sous-abondants relativement aux éléments à haut PPI dans les étoiles les plus actives, impliquant un effet PPI inverse, alors que les abondances des éléments à bas PPI dans les étoiles moins actives sont surabondantes d'un facteur 5 à 7 (effet PPI normal). Ceci suggère une transition d'un effet PPI inverse à normal comme conséquence de la décroissance de l'activité coronale.

Enfin, quelques perspectives futures de recherche sont proposées au Chapitre 11.

Chapter 1

Introduction

This chapter gives a short overview of the principal findings in the study of solar and stellar coronae that are relevant for the subsequent chapters of this thesis. Parts of this chapter are inspired from the literature, and from various reviews and books (Hénoux 1995; Haisch & Schmitt 1996; Golub & Pasaschoff 1997; Hénoux 1998; Schrijver & Zwaan 2000; Güdel 2002).

1.1 General Overview

Although extremely faint in visible light, the outermost region of the solar atmosphere, the corona, can be observed during total eclipses. However, the links between features observed during eclipses (prominences, corona) and the Sun were not established until the second half of the 19th century. They were rather attributed to artifacts introduced by the observational technique, or by the Earth's atmosphere.

The advent of photography (daguerreotypes) and spectroscopy around 1860 drastically changed the scientific approach to the observations of the solar corona. Comparisons of photographs of the 1860 eclipse taken by De la Rue and Secchi at different locations gave proof that prominences were of solar origin, which added weight to the hypothesis that all of the corona was also solar. The use of spectroscopes during eclipses proved highly noteworthy when bright emission lines were discovered. However, it was not until 1939 that Grotrian showed that the coronal lines are emitted by elements such as iron and calcium in very high stages of ionization, implying that the coronal gas is extremely hot (≈ 1 MK).

Although emission lines were first discovered in the visible part of the electromagnetic spectrum, the hot solar corona primarily emits in the extreme ultraviolet and soft X-ray range ($0.1 - 10$ keV), since most of the electronic transitions of highly ionized species decay radiatively in this range. It is therefore the wavelength range of choice to obtain information about the coronal physical processes. However, note that other regions of the solar spectrum, like the radio/microwave or the hard X-ray emission provide complementary information on the high-energy coronal processes as well. Ultraviolet data provide information about the transition region and chromosphere, and thus make a link between the lower part of the atmosphere

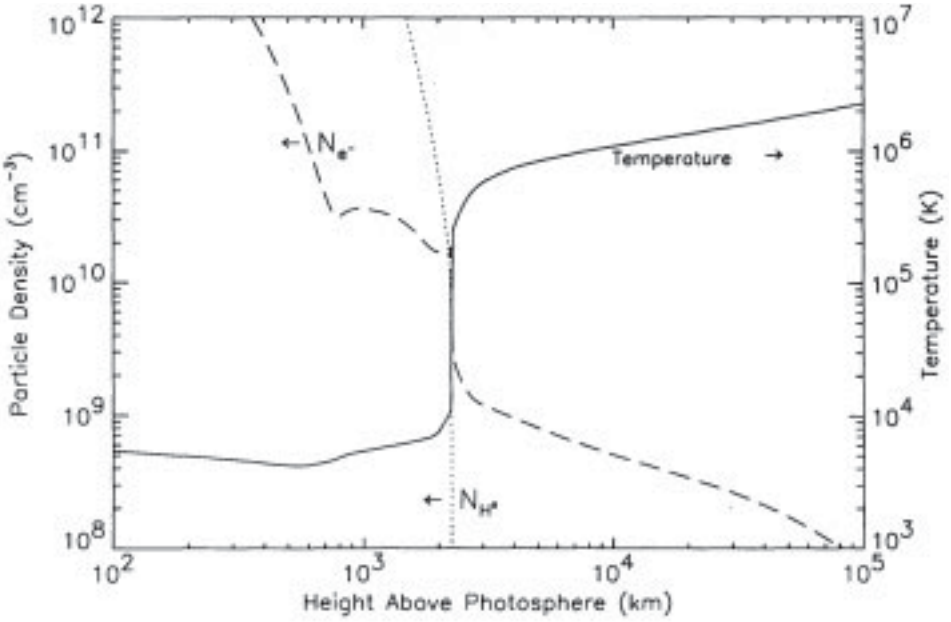

Figure 1.1: *A plane-parallel model of the solar atmosphere showing the temperature (solid) and the electron density (dashed) as a function of height. From Daw, DeLuca, & Golub (1995).*

and the corona. Due to the absorption and scattering of X-ray photons in the Earth's atmosphere, the first detection of X-rays from the solar corona (and from any astrophysical object) had to wait for rocket flight technology (Burnight 1949). The discovery of X-rays from a coronal source other than the Sun, Capella, came a quarter of a century later (Catura, Acton, & Johnson 1975). Numerous satellites (e.g., Skylab, SMM, SOHO, Yohkoh, TRACE) have been dedicated to the observation of the solar corona and have produced excellent high-resolution images and spectra in the soft and hard X-ray ranges. The study of the physical processes in the solar corona is of ongoing interest, for example with the recent launch of the HESSI mission and new missions planned for the near future. In parallel, stellar coronal astrophysics has expanded within the last twenty-five years thanks to detailed investigations of coronal sources with extreme ultraviolet and X-ray satellites (e.g., Einstein, ROSAT, *EUVE*). The launches of the new X-ray observatories, *XMM-Newton* and *Chandra*, at the end of the last century have given a strong impetus to the field of coronal physics.

1.2 The Solar Corona

While the solar surface, i.e., the photosphere, shows an effective temperature of ≈ 5800 K, the solar corona displays an extremely high temperature of a few million degrees. This is unexpected, since in the absence of additional heating, the temperature of the atmosphere above the photosphere should drop with height. However, a steep rise in temperature occurs at an altitude of $2000 - 3000$ km above the solar surface. This narrow region is loosely defined as the transition region (TR). Below the TR lies the chromosphere with temperatures of $6000 -$

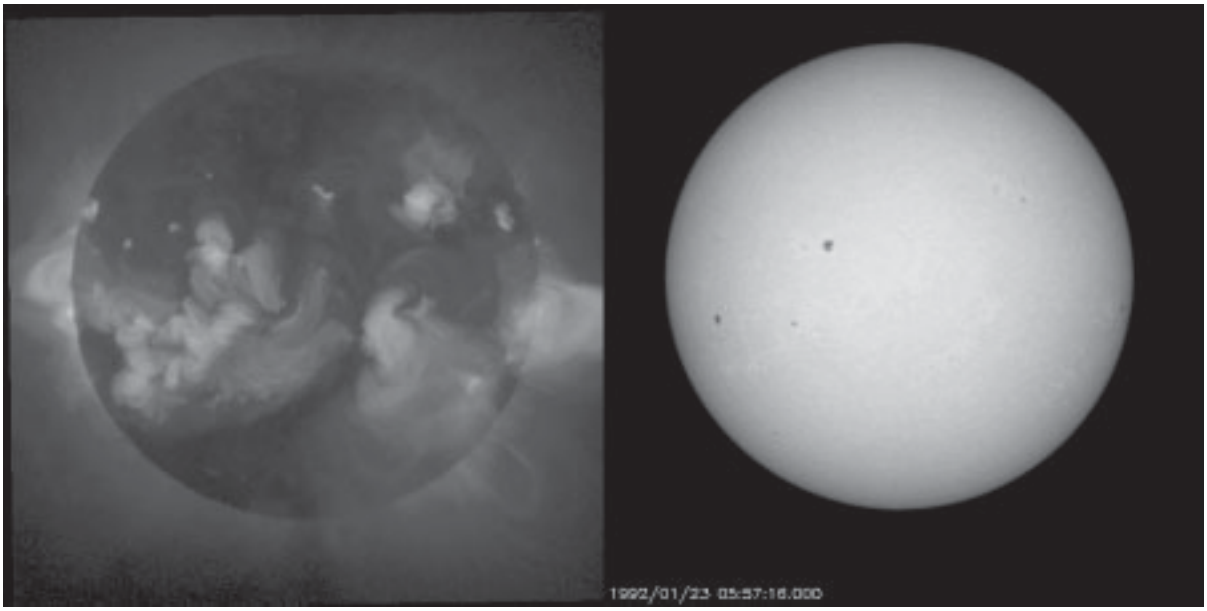

Figure 1.2: *Comparison of the soft X-ray image of the Sun with its simultaneous white light counterpart obtained by Yohkoh, a mission of ISAS, Japan, with NASA cooperation. Coronal holes, X-ray bright points and active regions can be seen in the X-rays. Note the spatial association between sunspots in the visible and coronal active regions in X-rays.*

$10,000$ K (see Fig. 1.1). The mechanisms of coronal heating have been lively debated in solar (and stellar) physics; we address related issues in a subsequent section (§1.4).

1.2.1 A Highly Structured Medium

The solar corona is a highly inhomogeneous medium. X-ray images of the solar corona (Fig. 1.2) reveal the extreme complexity of the coronal structures: bright active regions (associated with underlying photospheric sunspots), quiet regions, and X-ray dark coronal holes (often at the poles). Among others, the Ulysses mission has shown that a steady fast solar wind (750 km s^{-1}) flowing from the solar surface into the interplanetary medium is associated with coronal holes. A slow wind (400 km s^{-1}) is however detected at heliographic latitudes below 20°, with no gradual transition. While certain features persist on long time scales (e.g., coronal holes), the structure of the solar corona changes continuously on time scales of minutes to hours.

A closer look, for example with the high-resolution imaging TRACE satellite, shows the complexity of the coronal structures (Fig. 1.3). The structure of the coronal plasma basically follows the topology of the solar magnetic field: in general, there are closed magnetic fields and field lines that are, from the point of view of coronal physics, open (i.e., they close at very large distances). Coronal holes are generally associated with the latter, while coronal "loops" are with the former. Figure 1.3 shows that the magnetic configuration can be very complex. A loop can be highly stressed, its footpoints can be located in two different active regions, and its

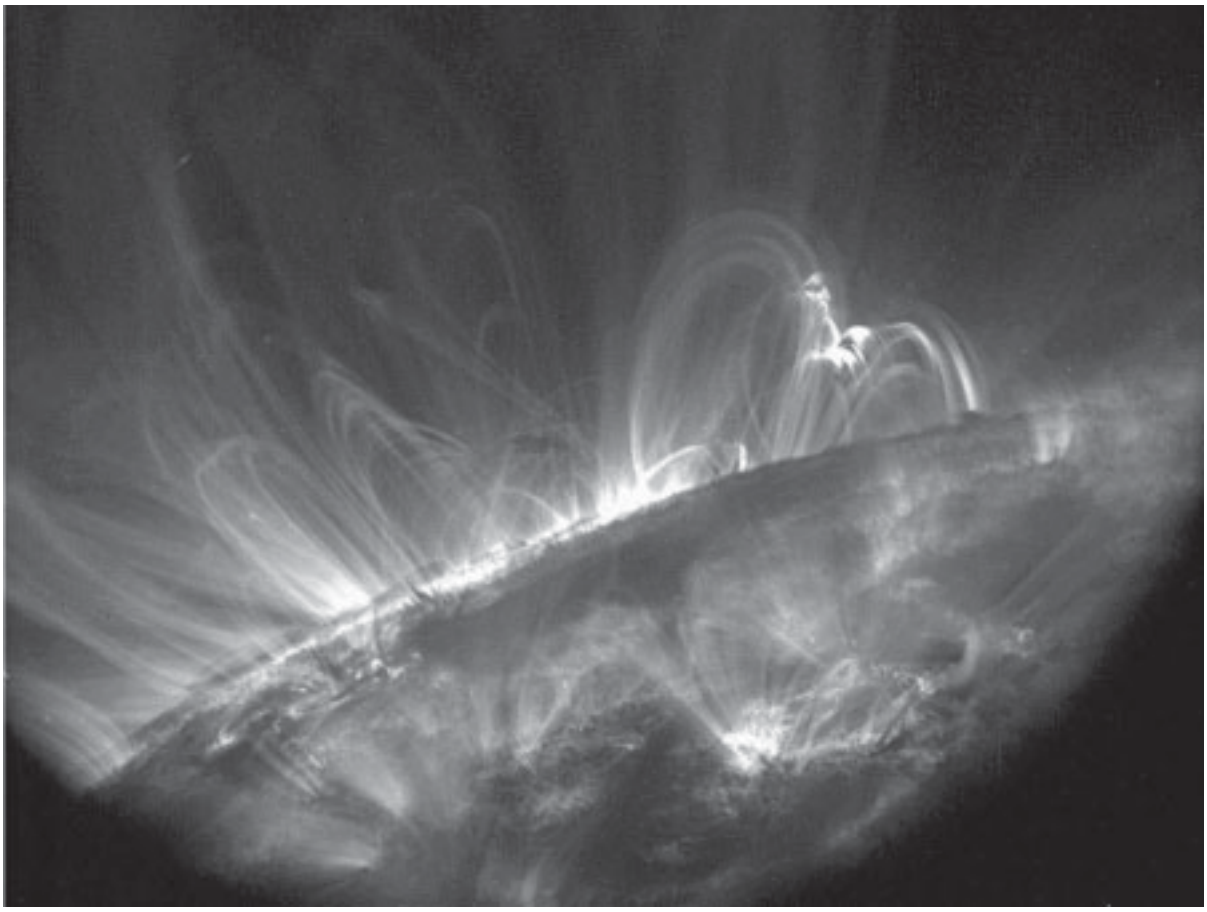

Figure 1.3: *The solar corona and transition region as seen by TRACE on 5 April 2001, around 6:22 UT, in the* Fe IX *line at 171.075 Å ($T_{\max} = 1$ MK). The diversity of magnetic structures is evident. Courtesy of the TRACE team.*

configuration can change to a more stable one by reconnection. Recent results from TRACE also showed that coronal loops can oscillate (Schrijver, Aschwanden, & Title 2002).

1.2.2 The Generation of Magnetic Fields – the Solar Dynamo

The presence of a solar magnetic field and of a 22-year cycle of activity (involving a periodic reversal of the magnetic field; the period of the surface activity cycle is however half shorter, i.e., 11 years) are basic properties of the Sun that need to be explained. The solar dynamo theory attempts to explain these properties. Parker (1955) suggested that the coupling of rising material in the convection zone and Coriolis forces should produce non-axisymmetric motion, producing a steady-state amplification of the magnetic field. Either a weak magnetic field is already present, or the motions will generate it. The amplification process needs a natural limit. "Magnetic buoyancy" lifts the magnetic field from the region of its generation up into the atmosphere, and this process is believed to be the limiting process at work in the Sun.

Buoyancy is thus directly responsible for the presence of activity at the surface of the Sun.

Although decades of theoretical work have been dedicated to solar dynamo theory, no model exists that fully and self-consistently describes the magnetic properties of the Sun. The $\alpha - \omega$ model is believed to be the closest approach. In brief, the α-effect characterizes the generation of a poloidal field from a toroidal field. The vertically moving convective plasma shows helicity, i.e., a preferred sense of rotation (clockwise in the northern solar hemisphere and counterclockwise in the southern hemisphere). As a result, the new poloidal field is eventually directed opposite to the field which started the cycle, thus providing a new cycle of surface activity (11-year cycle). The ω-effect characterizes the differential rotation of the Sun, i.e., its non-rigid rotation, and hence the production of a toroidal magnetic field from the shearing of poloidal magnetic fields. The α-term is much smaller than the ω-term in this model. Such a dynamo has a periodic behavior that accounts for the observed activity cycle. Other dynamo models are sometimes employed. For example, the α^2 dynamo (ω term much smaller than the α term, so that in the generation of both poloidal and toroidal magnetic fields, only the α terms remain) displays no periodic magnetic flip and is thought to better represent the dynamo of fully convective stars or of the Earth.

Since dynamo models need convective motions, magnetic field generation and amplification is believed to exist only in stars with convective envelopes, that is, in late-type stars (spectral types late-A to M). Helioseismological measurements have shown that the differential rotation observed at the solar surface remains constant with depth over the bulk of the convection zone. Consequently, the ω-effect cannot operate in the convection zone itself. Parker (1993) has thus proposed that the dynamo operates at the boundary between the convection zone and the thin overshoot layer just below it (at a depth of $\approx 0.287\ R_\odot$; Christensen-Dalsgaard, Gough, & Thompson 1991).

1.3 Stellar Activity

By chance, Catura et al. (1975) made the first X-ray detection of a coronal source apart from the Sun, Capella. Shortly after, the Dutch satellite ANS confirmed the detection (Mewe et al. 1975). The *IUE* satellite made a large contribution to the study of the chromospheric and transition region of stars (e.g., Linsky et al. 1978), while in the X-rays, the all-sky survey of the *HEAO-1* observatory established the RS CVn systems as a class of bright stellar X-ray sources (Walter et al. 1980). The major breakthrough in the field of stellar coronae however came with the *HEAO-2* (or *Einstein*) observatory: more than one thousand coronal X-ray sources were discovered (Vaiana et al. 1981). By the early eighties, most of the Hertzsprung-Russell (HR) diagram was populated with stars presenting evidence of solar-like coronae (Fig. 1.4; Linsky 1985). F to M dwarfs, and late-F through early-K giants show the presence of coronal emission, while late-K giants and supergiants appear to lack magnetic coronae thus defining a dividing line in the HR diagram of coronal emission (Ayres et al. 1981). Although early-type OB stars are X-ray sources, their X-ray emission is believed to originate from shock instability in their massive winds rather than from a corona. In the 1990's the *ROSAT* All-Sky Survey (RASS)

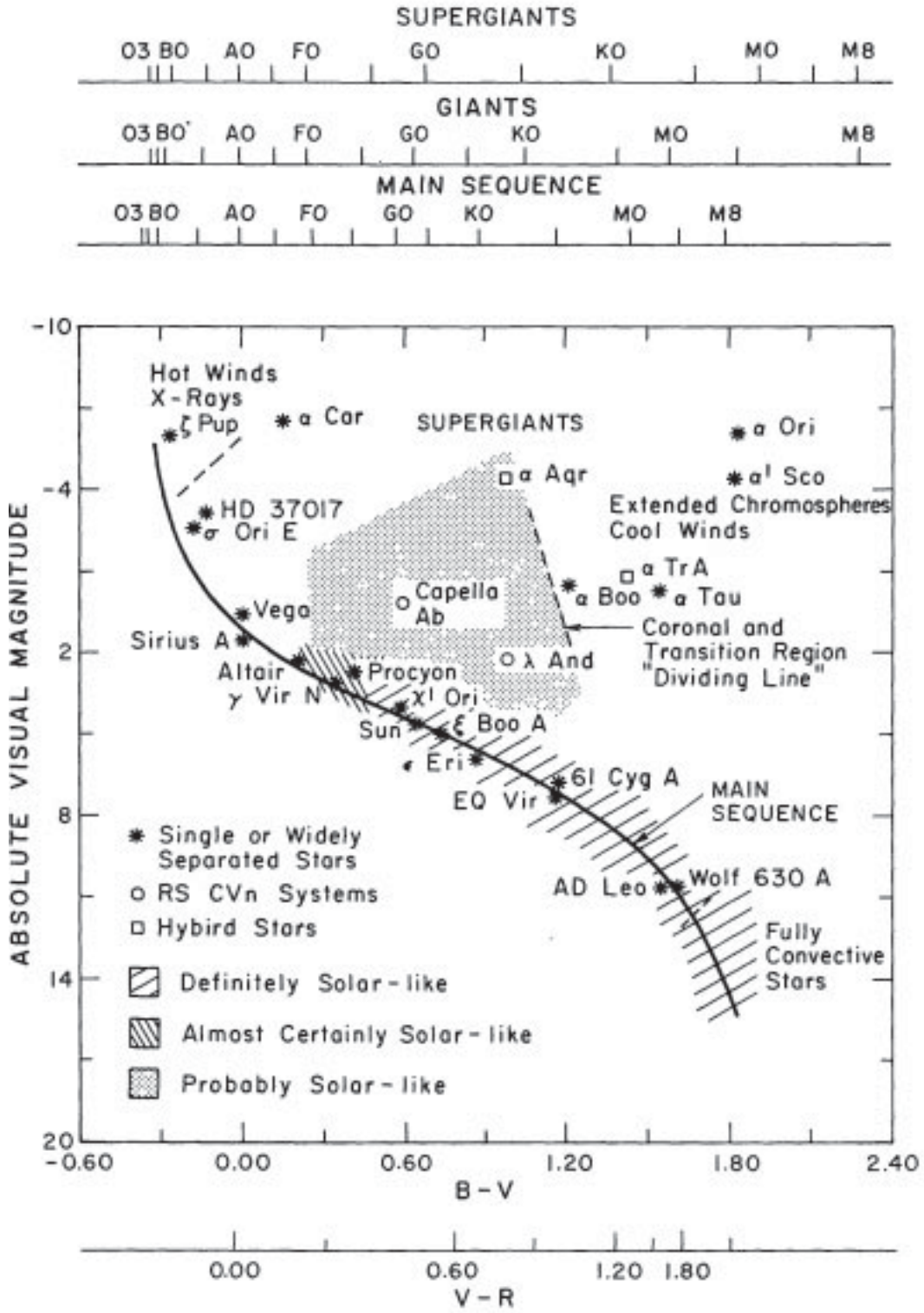

Figure 1.4: *A Hertzsprung-Russell diagram schematically showing the location of solar-like stars, i.e., stars displaying direct or indirect signs of magnetic activity. From Linsky (1985), with kind permission of Kluwer Academic Publishers.*

has increased the number of coronal X-ray sources to tens of thousands (Hünsch, Schmitt, & Voges 1998, 1999; Voges et al. 2000).

While the X-ray luminosity of the Sun amounts to about 10^{-6} of its total power, the X-ray luminosity of stellar coronae can reach 10^{-3} of their respective bolometric luminosity ($L_{\rm X}/L_{\rm bol}= 10^{-3}$). Walter et al. (1980) suggested that the large X-ray output in RS CVn binaries might be due to scaled-up activity. Such an interpretation is at the origin of the *solar-stellar connection* paradigm. Solar properties are extrapolated to explain stellar phenomenology. Similarly, since solar parameters (e.g., rotation period, temperature, spectral type) are given, stars play an important role in providing us with physical conditions completely different from those in the Sun. However, appealing as it is, there is a continuing debate on whether it is valid.

1.3.1 Relation of Activity to Rotation and Age

Late-type stars are characterized by convection zones. Similarly to the solar dynamo (§1.2.2), a dynamo mechanism is believed to be at the origin of magnetic activity in stars. Rotation therefore should play an important role, and correlations between rotation parameters (e.g., rotation period, rotational velocity, Rossby number) and activity parameters (e.g., X-ray luminosity, its ratio to the bolometric luminosity) can be expected (Kraft 1967).

Pallavicini et al. (1981) has shown that the X-ray luminosity of stellar coronae is related to the projected rotational velocity, $L_{\rm X} = 10^{27}(v \sin i)^2$, or to the equatorial rotational velocity (after statistical deprojection), $L_{\rm X} = 2 \times 10^{27} v_{\rm rot}^2$. However, Walter (1982) proposed that this relation was too simplistic, and that saturation occurs at $L_{\rm X}/L_{\rm bol} \approx 10^{-3}$ (Vilhu 1984; Vilhu & Walter 1987). Noyes et al. (1984) proposed that the Rossby number (defined as the ratio between the rotation period and the convective turnover time) determines the activity level, which was later observed (Stępień 1993). Note, however, that the stellar activity-rotation relation needs to be taken with a grain of salt. Indeed, solar data show a wide range of variability in its X-ray output ($\log L_{\rm X} \approx 26 - 28$ erg s^{-1} from solar minimum to maximum, respectively) without any change in the rotation rate. Hence a certain statistical dispersion must be expected in the stellar context, under the assumption that stars show activity cycles as well.

Low-mass stars rotate slowly during the early stages of pre-main-sequence evolution and spin up as they contract to the main sequence (e.g., Stauffer & Hartmann 1986). This spin-up culminates in a brief period of very rapid rotation at an age of order 50 million years. Then the rotation rate declines with age: the Sun rotates at a speed of 2 km s^{-1} at the equator. Such a slow-down is attributed to magnetic braking: the large-scale magnetized stellar wind carries away angular momentum (e.g., Weber & Davis 1967), and thus brakes the stellar rotation. Consequently it weakens the dynamo and the magnetic surface activity. Skumanich (1972) showed that rotation and chromospheric emission both decay as $\tau^{-1/2}$, where τ is the main-sequence age. However, Simon, Boesgaard, & Herbig (1985) proposed that an exponential decay would be more suitable; they also found shorter e-folding times for TR lines compared to those for chromospheric lines.

Güdel, Guinan, & Skinner (1997b) have studied the long-term evolution of coronae of solar-

type stars with ages ranging from 70 Myr to 9 Gyr. They found a relation between the hot coronal temperature and the X-ray luminosity, $L_{\rm X} \propto T_{\rm hot}^{4-5}$, while the latter was correlated to age $T_{\rm hot} \propto \tau^{-0.3}$. Similarly, they confirmed the relation between $L_{\rm X}$ and rotation, $L_{\rm X} \propto P_{\rm rot}^{-2.64}$ (although they pointed out that saturation should occur around $P_{\rm rot} < 2$ d). The structure of the emission measure distributions (EMD) was found to gradually evolve, the hotter component rapidly decreasing with age and becoming unimportant at ages beyond ≈ 500 Myr. Güdel et al. (1997b) proposed that the high-temperature component of the EMD results from a statistical superposition of flaring events. Flares could thus play an important role in the coronal heating mechanism.

1.4 Coronal Heating of Magnetically Active Stars

The heating mechanism responsible for high temperatures ($\approx$ 1–100 MK) in solar and stellar coronae is one of the major mysteries of solar physics. A number of heating mechanisms have been proposed (e.g., Ionson 1985; Narain & Ulmschneider 1990; Zirker 1993; Haisch & Schmitt 1996; Narain & Ulmschneider 1996, for reviews), such as

- Acoustic wave heating
- Heating by fast and slow magnetoacoustic body waves
- Heating by Alfvén body waves
- Heating by slow and fast magnetoacoustic surface waves
- Heating by current (or magnetic field) dissipation
- Heating by microflares/transients
- Heating by mass/particle flows and flux emergence

In particular, flares – explosive events that provide direct evidence of magnetic activity in a stellar atmosphere – are attractive heating agents in the Sun. Parker (1988) proposed that the X-ray corona of the Sun could be due to a superposition of a very large number of small flares with an energy of the order of 10^{24} ergs each. For stars, a correlation between the apparently non-flaring ("quiescent") coronal X-ray luminosity and the time-averaged chromospheric flare luminosity (Doyle & Butler 1985) suggests that flares can release a sufficient amount of energy to produce the subsequently observed quiescent coronal emission. Broadened transition region emission-line profiles (Linsky & Wood 1994; Wood et al. 1996) have been interpreted in terms of a large number of explosive events. Further evidence for flare heating comes from their energy distribution. Solar flares are distributed in energy according to a power law (e.g, Crosby, Aschwanden, & Dennis 1993), with the flare rate (or number of flares) dN within the energy interval $[E, E + dE]$,

$$\frac{dN}{dE} = k_1 E^{-\alpha}. \tag{1.1}$$

Table 1.1: *Previous Measurements of Flare Energy Distributions (Selection)*

Measurement	Photon energy range	Flare energy	α	Reference
Solar:				
Thermal energy	EUV Fe IX, X, XII	$10^{25} - 3 \times 10^{26}$ erg	2.3–2.6	Krucker & Benz 1998
Thermal energy	EUV Fe IX, X, XII	$3 \times 10^{23} - 10^{26}$ erg	2.0–2.6	Parnell & Jupp 2000
Thermal energy	EUV Fe IX, X, XII	$10^{24} - 2 \times 10^{26}$ erg	1.79 ± 0.08	Aschwanden et al. 2000
Thermal and radiated energy	SXR	$10^{27} - 10^{29}$ erg	1.5–1.6	Shimizu 1995
Peak flux	SXR	$10^{25} - 10^{29}$ erg	1.4–1.8	Shimizu 1995
Peak flux	1–6 keV	normal flares	1.75	Drake 1971
Radiated energy	1–6 keV	normal flares	1.44	Drake 1971
Peak flux	1.5–12 keV	GOES A2−C8 flares	1.88±0.21	Feldman et al. 1997
Peak flux	3.5–5.5 keV & UV	microflares	2.18–2.23	Porter et al. 1995
Peak flux	10–300 keV	normal flares	1.8	Datlowe et al. 1974
Peak flux	13–600 keV	HXR microflares	~ 2.0	Lin et al. 1984
Peak count rate	25–500 keV	normal flares	1.8	Dennis 1985
Peak count rate	>25 keV	normal flares	1.73±0.01	Crosby et al. 1993
Peak flux	>25 keV	normal flares	1.59±0.01	Crosby et al. 1993
Peak count rate	>25 keV	normal flares	1.7–1.9	Bai 1993
Peak flux	>30 keV	normal flares	1.8–2.2	Bromund et al. 1995
Stellar:				
Radiated energy, M dwarfs	0.05–2 keV	$10^{30.6} - 10^{33.2}$ erg	1.52±0.08	Collura et al. 1988
Radiated energy, M dwarfs	0.05–2 keV	$10^{30.5} - 10^{34.0}$ erg	1.7±0.1	Pallavicini et al. 1990a
Radiated energy, RS CVn	EUV	$10^{32.9} - 10^{34.6}$ erg	1.6	Osten & Brown 1999
Radiated energy, two G dwarfs	EUV	$10^{33.5} - 10^{34.8}$ erg	2.0–2.2	Audard et al. 1999, Chap. 3
Radiated energy, F-M dwarfs	EUV	$10^{30.6} - 10^{35.0}$ erg	1.8–2.3	Audard et al. 2000, Chap. 4
Radiated energy, AD Leo	EUV & 0.1–10 keV	$10^{31.1} - 10^{33.7}$ erg	2.1–2.5	Güdel et al. 2002a, Chap. 5

The cumulative distribution for $\alpha > 1$ is thus defined by

$$N(>E) = \int_E^\infty \frac{dN}{dE'} dE' = k_2 E^{-\alpha+1}, \tag{1.2}$$

where the normalization factors k_1 and $k_2 = k_1/(\alpha - 1)$ are constants. For $\alpha > 2$, an extrapolation to energies below the detection limit could be sufficient to explain the quiescent X-ray luminosity because the integral diverges if the minimum energy $E_{\rm min}$ of flares moves toward 0:

$$L_{\rm X} = \int_{E_{\rm min}}^{E_{\rm max}} \frac{dN}{dE} E \, dE = k_2 \frac{\alpha - 1}{\alpha - 2} \left(E_{\rm min}^{2-\alpha} - E_{\rm max}^{2-\alpha} \right). \tag{1.3}$$

Here $E_{\rm max}$ is the energy of the most energetic relevant flare. Solar observations suggest several values of the power-law index. For "normal" flares, $\alpha \approx 1.5 - 1.8$ (Crosby et al. 1993), while the index steepens in the quiet Sun for flares with very small energies, $\alpha \approx 2.3 - 2.6$ (e.g., Krucker & Benz 1998). Stellar studies are rare, due to the paucity of stellar flare statistics. Shallow distributions have been reported ($\alpha \approx 1.6$, Collura et al. 1988; Osten & Brown 1999). A summary of a few relevant observations of solar and stellar flare energy distributions is given in Table 1.1. Audard, Güdel, & Guinan (1999, see Chap. 3), Audard et al. (2000, see Chap. 4), and Güdel et al. (2002a, see Chap. 5) have investigated the flare occurrence rate distribution in energy in active stars and found suggestions that flares could contribute a significant amount of energy to coronal heating when treated as a statistical ensemble.

1.4.1 High-Energy Processes – Flares

Highly energetic processes in coronae do not occur solely in the X-ray regime. For example, the presence of non-thermal mildly relativistic electrons in stellar coronae is inferred from radio/microwave observations (e.g., Drake et al. 1989, 1992; Güdel et al. 1995). A correlation between the microwave emission and the X-ray luminosity has been found in RS CVn binaries (Drake et al. 1989) and applies to main-sequence active stars (Güdel & Benz 1993) and solar flares as well (Benz & Güdel 1994). In the latter, gyrosynchrotron emission is produced together with flare plasma of high temperatures ($20 - 30$ MK), while such microwave emission is not found in "quiescent" regions of the Sun. Large stellar flares can display very high temperatures; Franciosini, Pallavicini, & Tagliaferri (2001) detected hard X-rays up to 50 keV during a large flare of the RS CVn binary UX Ari observed with *BeppoSAX*. Tsuboi et al. (1998) reported temperatures of at least 100 MK in a flare on the weak-lined T Tau star V773 Tau. Similarly Güdel et al. (1999) showed that the EM distribution of another flare of UX Ari evolved to temperatures of 50 to 100 MK

Multi-wavelength observations have been important for our understanding of the physical processes occurring in stars. For example, signatures of chromospheric evaporation from flares are expected in the radio and X-rays: a beam of accelerated electrons travels along the magnetic fields from the flare reconnection site down to the lower atmospheric layers. While electrons

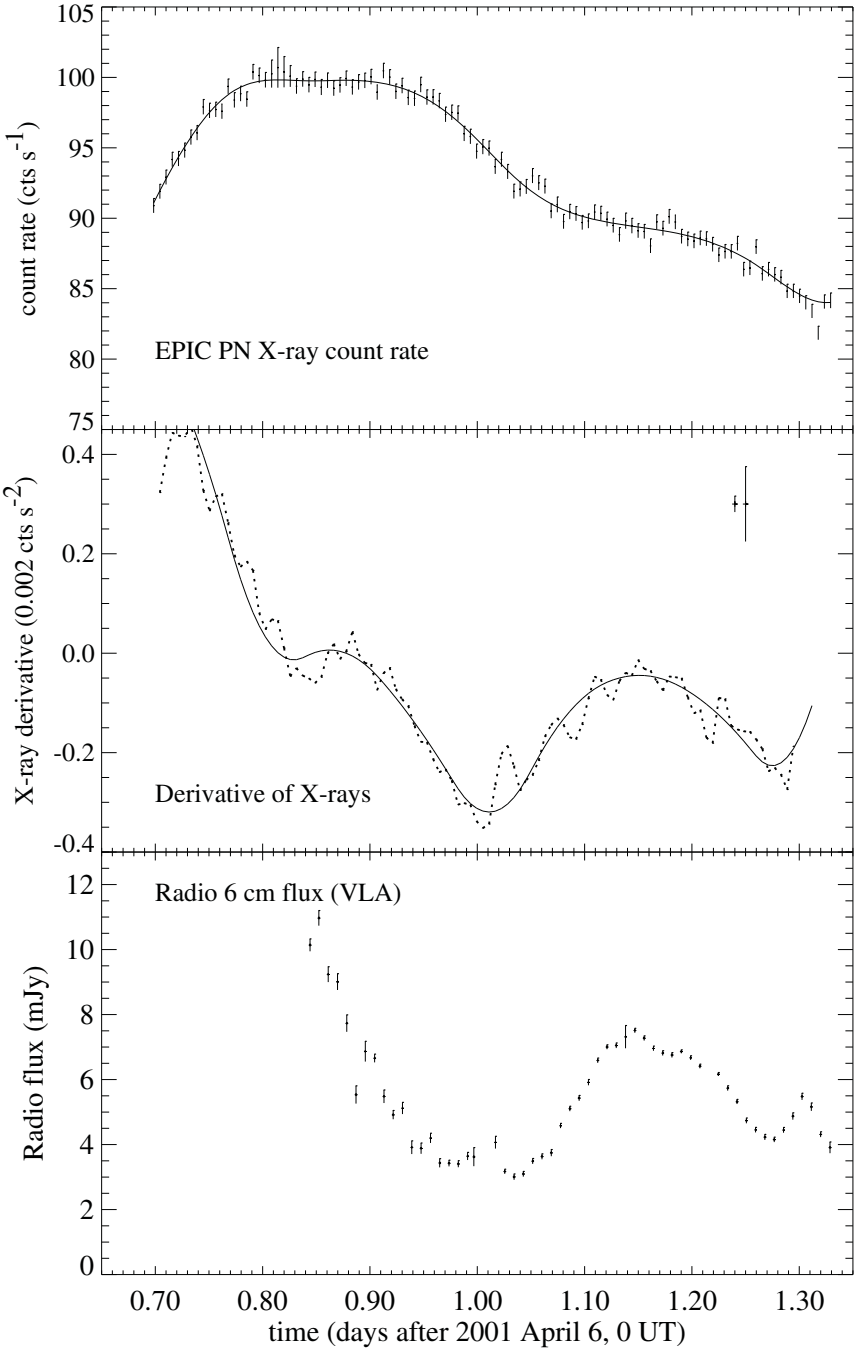

Figure 1.5: *Evidence for the Neupert effect in σ Gem. Top: XMM-Newton light curve with its boxcar smoothed curve (solid). Middle: The time derivative of the smoothed X-ray light curve. Bottom: The radio VLA 6 cm light curve. From Güdel et al. (2002c).*

with large velocity components perpendicular to the magnetic fields (large pitch angle) radiate gyrosynchrotron emission detected at radio wavelengths, electrons with small pitch angles impact the dense chromosphere and emit hard X-rays (> 20 keV) through Coulomb collisions (e.g., Dennis 1985). The upper layer of the chromosphere is heated and lifted into the corona by the pressure gradient, filling the coronal loops and cooling through soft X-ray radiation and conduction (e.g., Antonucci et al. 1984). Therefore the radio (and hard X-ray) light curve reflects the "power" injected into the chromosphere, while the soft X-ray light curve is a tracer of the accumulated energy after evaporation. Note that optical/UV data can play the role of tracers of the non-thermal processes as well. A characteristic time dependence thus relates the light curves: the derivative of the soft X-ray light curve resembles the shape of the radio (and hard X-ray) light curve ("Neupert effect"; Neupert 1968), as observed in solar impulsive flares. Observations of the Neupert effect have been reported in active dwarf-star coronae using extreme ultraviolet and optical data (Hawley et al. 1995), and using X-ray and radio data (Güdel et al. 1996). Recent results with *XMM-Newton* and the VLA show an outstanding example of the Neupert effect in an RS CVn binary system (Güdel et al. 2002c, see Fig. 1.5). Ongoing investigation of our nearest star apart from the Sun, Proxima Centauri, with the X-ray and U-band data of *XMM-Newton* shows evidence for several Neupert-like effects, even for the smallest flares. Furthermore the light curves show continuous flickering, suggesting that the X-ray light curve virtually shows no "quiescent" emission at all.

1.5 Coronal Abundances in the Sun and Stars

The composition of elements in coronae may be an important tracer for the heating mechanism since ultimately the latter is responsible for transporting material from the surface to the corona. The critical mass transport phenomena are thus expected to take place in the interface between the photosphere and the corona, i.e., the chromosphere and transition region, for example by evaporation processes (Antonucci et al. 1984). Coronal elemental abundances indeed probe this region. The elemental composition of the solar corona, of the solar wind, and of solar energetic particles (and even of galactic cosmic rays) shows a systematic pattern relative to solar photospheric abundances: elements with a low First Ionization Potential (FIP; $<$10 eV) are overabundant by factors of $4 - 6$ relative to their respective photospheric abundances, while high-FIP elements are of photospheric composition (Feldman 1992; see also Meyer 1985; Fig. 1.6). Note that abundances have also been found to differ in different environments. In the fast solar wind emanating from high solar latitudes and coronal holes the FIP bias appears to be weak and close to photospheric, while the slow wind shows a coronal composition (e.g., von Steiger et al. 1995; Feldman et al. 1998). However, Laming, Drake, & Widing (1995) showed that the usual FIP effect is recovered in solar full-disk observations.

The solar FIP effect implies the presence of a fractionation mechanism in the chromosphere which has the adequate temperature ($5,000 - 10,000$ K) to ionize low-FIP elements and leave high-FIP elements mostly in a neutral stage (e.g., Geiss 1982). Enrichment models have been proposed to explain the solar FIP effect (see §1.5.1; also Hénoux 1995 for a review). However, a quantitative prediction of the resulting coronal abundances is still challenging. The presence

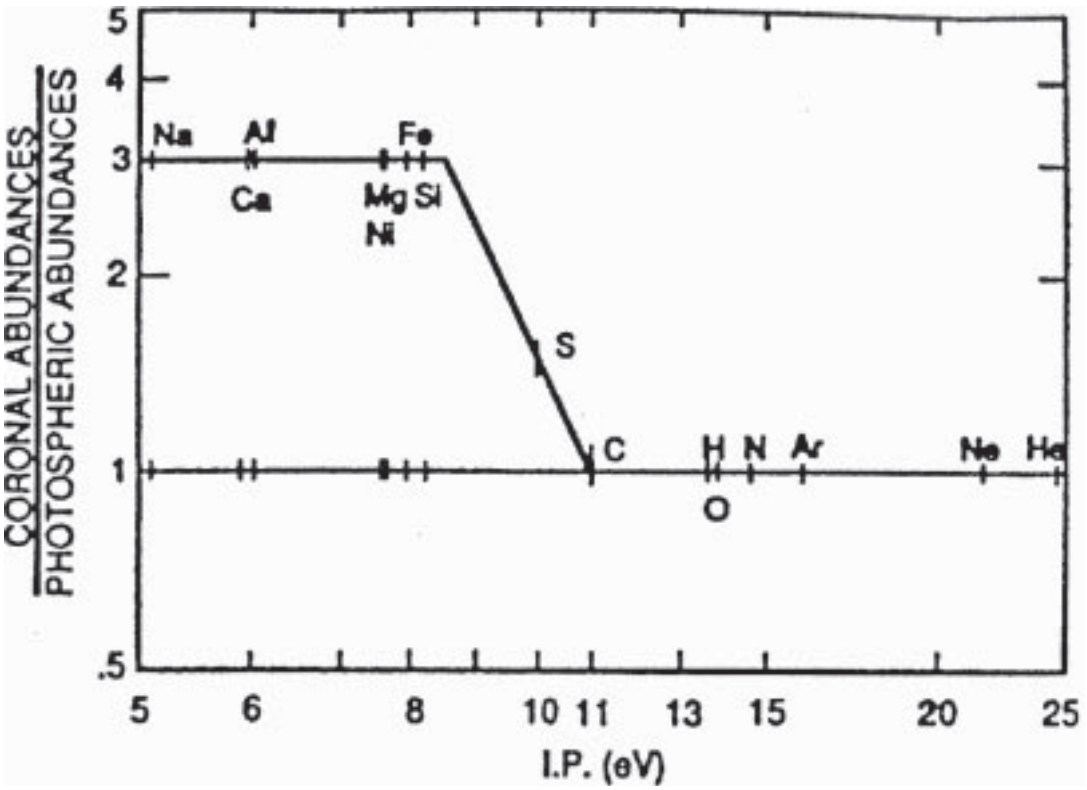

Figure 1.6: *Schematic representation of the coronal abundance FIP bias in the Sun. A two-plateau structure is shown, with low-FIP elements being overabundant by a factor* ≈ 3 *in the solar corona relative to the photospheric value, while high-FIP elements show photospheric composition. A transition occurs around 10 eV. From Feldman (1992).*

of a FIP bias in stars is expected to provide important information on dynamical processes in their outer atmospheres and an insight into the solar FIP effect itself.

The situation in stellar coronae has been somehow confusing before the advent of the new X-ray observatories with high-resolution spectral capability and high effective areas. A solar-like FIP effect has been reported for some rather inactive stars (Laming, Drake, & Widing 1995; Drake, Laming, & Widing 1997; Laming & Drake 1999), although the inactive F5 subgiant Procyon has shown no signs of abundance anomalies (Drake, Laming, & Widing 1995). In contrast, coronae of magnetically active stars have been found to display a marked depletion of iron (low-FIP) by factors of 5 to 10 relative to solar photospheric abundances (e.g., Schmitt et al. 1996; Singh et al. 1996; Mewe et al. 1997). These results have led to a lively debate on the reality of the metal abundance deficiency. The determination of coronal abundances could be biased by either the low spectral resolution of CCD spectrometers or by the small effective area of higher-resolution instruments. Additionally, any measured FIP bias may also simply reflect the stellar photospheric composition which is unfortunately largely unknown or very uncertain in active stars.

A major breakthrough in this field came with the launches of *XMM-Newton* and *Chandra* in 1999. From a deep *XMM-Newton* RGS exposure of the RS CVn binary HR 1099, coronal abundances of several elements were obtained (Ne, N, O, C, S, Fe, Mg, and Ni). A peculiar abundance pattern as a function of the First Ionization Potential was observed: evidence for an inverse FIP effect was found, i.e., the abundances (relative to oxygen) increase with increasing FIP (Brinkman et al. 2001). A number of highly active stars apparently show a similar pattern for coronal abundances (Audard et al. 2001a; Güdel et al. 2001a,b, see Chap. 6, 8, and 9, respectively). This FIP bias could be interpreted as an overabundance of high-FIP elements (Drake et al. 2001), or as an underabundance of low-FIP elements.

Audard et al. (2001b, see Chap. 7), Audard & Güdel (2002) and Güdel et al. (2002b) (see Chap. 10 for a combined version of the two papers) have shown that the inverse FIP effect is not ubiquitous in active stars. The intermediately active Capella shows an absence of any FIP bias (Audard et al. 2001b), as previously suggested from medium-resolution CCD spectra (Brickhouse et al. 2000). To circumvent the problem of the uncertainty of stellar photospheric abundances, we have studied solar analogs of known photospheric composition (Güdel et al. 2002b). A transition from an inverse to a normal FIP effect with decreasing activity or increasing age was found. Low-FIP elemental abundances significantly vary with activity, while the high-FIP composition stays constant (see Fig. 10.6). The marked inverse FIP bias in the coronae of highly active RS CVn binaries and the absence of FIP bias in Capella fit well into this scheme (Audard et al. 2001b; Audard & Güdel 2002).

While the above results apply to apparently quiescent times, the situation can drastically change during flares. In the Sun, chromospheric evaporation brings "fresh" material from the lower chromosphere up into the corona, suppressing the FIP effect (Feldman & Widing 1990). More complex situations can also occur: Schmelz (1993) analyzed two solar flares with the SMM mission Flat Crystal Spectrometer and reported enrichments of the high-FIP elements Ne and S in the impulsive flare, while the gradual flare showed coronal abundances. In contrast, Sylwester, Lemen, & Mewe (1984) reported enrichment of Ca, a low-FIP element. Stellar flares also often display abundance variations (e.g., Ottmann & Schmitt 1996; Favata et al. 2000). The spectral resolution of *ASCA* CCD spectrometers allowed Güdel et al. (1999) to find that low-FIP elements increased more significantly than the high-FIP elements during a large flare in UX Ari. Audard et al. (2001a, Chap. 6) have identified a similar behavior in a flare in HR 1099 with the high-resolution X-ray spectrometers on board *XMM-Newton*. It suggests a replenishment of the corona by the underlying material.

1.5.1 Models for the First Ionization Potential Effect

Thanks to the comprehensive observational evidence of abundance anomalies in the solar atmosphere, several models of ion-neutral fractionation leading to an enhancement of the low-FIP to high-FIP abundance ratio have been proposed. Such models either consider a steady-state situation or follow the time evolution of the fractionation, which is assumed to take place in the chromospheric temperature plateau (see Fig. 1.1). While all models use the same basic equations, namely the continuity and momentum balance equations, they mostly differ in their

interpretation of the role of the magnetic field.

The first category of models suggest that the magnetic field plays no role (except for guiding the ions). In such models, ion-neutral fractionation is the resulting process of the *diffusion* of minor species (basically all elements except hydrogen) along the magnetic field lines, through collisions with neutral hydrogen atoms and protons propagating upward. Marsch, von Steiger, & Bochsler (1995) and Peter (1996, 1998) have proposed steady-state models of fractionation by diffusion. In their models, minor species are slowed down by collisions. However, Peter (1996, 1998) assumes that at the "base" of the chromospheric level the minor species move up faster than the main hydrogen gas, while for Marsch et al. (1995), the main hydrogen gas moves downward. Their models treat the diffusion process in one dimension, assuming that at the "base" minor species are fully neutral, while at the "top" the plasma is fully ionized and all ions have the same velocity. Note that they differ by their boundary conditions. In the limit of a small main hydrogen gas velocity they both obtain that the fractionation degree,

$$f_{j,k} = \frac{(n_j^{\rm top}/n_k^{\rm top})}{(n_j^{\rm bottom}/n_k^{\rm bottom})} \qquad (n_j = n_{j^0} + n_{j^+}, n_k = n_{k^0} + n_{k^+}), \tag{1.4}$$

is equal, at the "top", to the ratio of the ionization-diffusion speeds of element j and k at the "bottom", $f_{j,k}^{\rm top} = w_j^{\rm bottom}/w_k^{\rm bottom}$. Here, $w_j = v_j/\sqrt{\tau_j \nu_{j\rm H}}$, and $v_j = \sqrt{k_{\rm B} T_j/m_j}$ is the thermal velocity, τ_j the ionization time of species j, and $\nu_{j\rm H}$ the collision frequency between a neutral element j and a neutral hydrogen atom. Note that the Marsch et al. model treats the diffusion of minor species all the way from the bottom to the top of the chromospheric plateau, hence they derive a more general form, $f_{j,k} = w_j/w_k$, at every location from "bottom" to "top".

A third model of this category has been proposed by Wang (1996). It differs from the Marsch et al. and Peter models in that it is based on the diffusion of ionized minor species in an upward flow of protons. Indeed, Wang (1996) noted that the collisional frequency ν_{j^+p} between protons and ionized minor species is larger than the collisional frequency ν_{j^0p} between protons and neutral minor elements. This model properly reproduces the solar FIP effect at the "top", although its requirement for an energy input from "above" and deposited at the base of the chromosphere is problematic. This energy must not fully ionize the atmosphere above, or all ionized species would rise with the protons and no fractionation could then take place.

Fontenla & Avrett (1992) have proposed a diffusion model in a strong vertical temperature gradient. In this model the magnetic field plays no role at all. The presence of a strong temperature gradient leads to diffusion, upward for neutral hydrogen and downward for ionized hydrogen. Collisions between downward propagating protons and neutral species provoke a decrease of the abundances of the latter at higher temperatures. Ionized species however suffer collisions with both neutral hydrogen and protons, and are also affected by a downward electric field resulting from electron thermal diffusion. Unfortunately, since the diffusion velocities are small (≤ 0.2 km s^{-1}), the time scales involved to create an abundance pattern are too large and therefore this mechanism probably does not play a significant role.

The second category of models suggests that the magnetic field does play a role. Fractionation here results from the difference between the drift velocities of ionized and neutral minor species moving across the magnetic field lines. Hence the ion-neutral collision frequency is smaller than the ion gyro-frequency, which is achieved either if the plasma density is low enough or if the magnetic field is sufficiently high. Under these conditions, ionized species are frozen in the magnetic field, while neutral species can move across it. In this model category, the magnetic field can either be horizontal (Vauclair & Meyer 1985; Vauclair 1996) or vertical (von Steiger & Geiss 1989; Antiochos 1994; Hénoux & Somov 1997).

Separation between neutral and ionized minor species in a horizontal magnetic field under the effect of gravity (gravitational settling) in the upper part of the chromosphere has been proposed by Vauclair & Meyer (1985). However, this process turned out to be too slow compared to the time evolution of observed structure. More recently, the "skimmer" model (Vauclair 1996) proposed a new approach of fractionation in horizontal magnetic fields. Ions (mostly low-FIP elements) would be lifted up by horizontal magnetic fields moving upward through the chromospheric plateau. However field lines are in general not horizontal when they cross the chromospheric plateau, and ions should thus fall back to the photosphere along the field lines.

Antiochos (1994) proposed that ion-neutral separation in a vertical magnetic field could occur during chromospheric evaporation. Downward moving non-thermal electrons create a current that is balanced by a thermoelectric electric field parallel to the magnetic field. Since, in a static magnetic field, $\nabla \times \mathbf{E} = \mathbf{0}$, a perpendicular component must exist. In the upper chromosphere, the perpendicular field is directed into the flux tube (and outside in the TR). Hence it will tend to drag positive ions (mostly low-FIP elements) into the evaporating flux tube. It is however unclear what the effect of the outward electric field in the TR is. von Steiger & Geiss (1989) treat the time-dependent ion-neutral separation perpendicular to a uniform magnetic field by gravity and/or a pressure gradient. An initial mixture of neutral gas in a vertical slab parallel to the magnetic field is photoionized by UV radiation. Under the effect of gravity or/and of a small density gradient, the neutrals diffuse with time across the magnetic field lines, while the ionized species are frozen in the field. The ionization time scale is the dominant effect: species with a small ionization time (compared to both the rise time and the diffusion time) will all be ionized and be trapped, and will reach the corona. Those with a large ionization time will escape without reaching the corona. Such a model is time-dependent and quantitatively reproduces the solar FIP effect. However, the density in the model of 10^9 cm^{-3} (required to efficiently ionize the neutral gas) is too low compared to the chromospheric density of 10^{13} cm^{-3}. Hénoux & Somov (1997) proposed that the electric currents flowing along vertical magnetic flux tubes (Hénoux & Somov 1991) together with a strong pressure gradient perpendicular to the magnetic field could produce ion-neutral fractionation.

Previous data for stellar coronae have not shown evidence for a special FIP bias other than a solar-like FIP effect nor its absence (e.g., Drake et al. 1995, 1997). The new results by *XMM-Newton* and *Chandra* have broken new ground by showing evidence for a transition from a solar-like FIP effect in inactive stars to an "inverse" FIP effect in the most active stars (e.g., Audard & Güdel 2002; Güdel et al. 2002b). Güdel et al. (2002b) have put forward first

ideas to explain the inverse FIP effect seen in active stars: downward propagating electrons detected by their gyrosynchrotron emission in active stars could prevent chromospheric ions (mostly low-FIP elements) from escaping into the corona by building up a downward-pointing electric field. As the density of high-energy electrons decreases with decreasing activity, the inverse FIP effect is quenched. During large flares, however, the high-energy electrons heat a significant portion of the chromosphere to bring up a near-photospheric mixture of elements into the corona. Although appealing, this approach needs a more detailed analysis.

1.6 Overview of the Thesis

This doctoral thesis is aimed at investigating physical processes taking place in stellar coronae. Coronal heating by flares has been studied by means of flare statistics (Chapters 3, 4, 5) and by means of X-ray spectroscopic data (Chapter 6). Emission measure distributions and electron densities in active stars have been derived, together with their elemental composition (Chapters 7, 8, 9). From line ratios of the O VII He-like triplet in AB Dor, the density during flares was found not to differ from that in quiescence (Chapter 8). A realization of the spatial structure of the coronal plasma in the eclipsing binary system YY Gem has been reconstructed (Chapter 9). The elemental composition of magnetically active stellar coronae has been systematically investigated. Studies of young solar analogs with known photospheric abundances allowed us to derive a transition in the coronal FIP bias from a solar-like FIP effect in inactive stars to its reverse (inverse FIP effect) in the most active stars (Chapter 10). In Chapter 11, a short outlook to future investigations of magnetically active stars is given.

Chapter 2

Instrumental Aspects

This chapter presents short technical overviews of the *Extreme Ultraviolet Explorer* and *XMM-Newton* satellites, since their data were of principal importance for all subsequent chapters of this thesis. Most of this chapter is based on information taken from users' handbooks (Miller 1997; Ehle et al. 2001), from dedicated web sites, from instrument papers (e.g., den Herder et al. 2001), and, in the case of *XMM-Newton*, from personal knowledge gained from participation in its calibration, performance verification, and guaranteed time phases after its launch.

2.1 The Extreme Ultraviolet Explorer

The *Extreme Ultraviolet Explorer* (*EUVE*; Fig. 2.1) was an Explorer-class NASA project proposed by the University of California in Berkeley. The *EUVE* satellite was launched on June 7, 1992, on a Delta II rocket from Cape Canaveral into a near-Earth orbit, at an altitude of 550 km. Its science mission effectively began on July 24, 1992, and its three scientific objectives were the following:

1. To carry out an all-sky survey in the extreme ultraviolet range ($50 - 740$ Å) using three scanning telescopes.

2. To survey simultaneously a $2^\circ \times 180^\circ$ swath of sky along the ecliptic in two passbands ($65 - 360$ Å), reaching much deeper sensitivity levels (factor of 20) than the scanning telescopes.

3. To follow up on the survey with medium-resolution spectroscopy ($1 - 2$ Å) of individual detected sources in the $70 - 760$ Å range.

While the first two objectives constituted the science program of the mission's principal investigator (UC Berkeley), the last objective was open to Guest Observers selected by NASA on the basis of the evaluation by review committees. Although the mission proved successful since its launch, NASA decided in 2000 to cease its mission operations. *EUVE* science operations

Figure 2.1: *An artist view of the Extreme Ultraviolet Explorer satellite.*

ended on January 26, 2001[1]. It was placed into safehold at 23:59 UTC on January 31, 2001. Finally, *EUVE* re-entered the Earth's atmosphere on January 30, 2002 at 23:15 EST.

2.1.1 Scientific Payload

The science payload used grazing-incidence Wolter-Schwarzschild type II telescopes (Fig. 2.2). The mirrors were made of aluminium cut to a precise figure by a diamond-turning lathe; they were nickel-plated, polished and finally gold-coated for maximum reflectivity. Graze angles of $5 - 10^{\circ}$ were used, which are still very reflective in the EUV but are large enough to eliminate unwanted X-ray reflections. Five separate instruments were incorporated in the science payload: four photometric imaging systems and a three-channel EUV spectrometer.

2.1.1.1 The Sky Survey Instruments

Three of the telescopes were co-aligned and together point at right angles to the satellite spin axis. A two-dimensional imaging microchannel plate detector was placed at the focal plane of each telescope. These three imaging systems were used as all-sky scanners and recorded photons in four wavelength passbands ($50 - 180$, $160 - 240$, $345 - 605$, and $500 - 740$ Å).

2.1.1.2 The Deep Survey Instrument

The last imaging system was the Deep Survey (DS) instrument. Actually, this instrument was half of a telescope: the fourth *EUVE* telescope had its mirrors divided into six equal segments. Three of the six segments were used for spectroscopy (see §2.1.1.3) and the remaining three segments formed a single image onto a field of view that was divided into two halves by different filters (Lexan/Boron and Aluminium/carbon). Usually, targets of Guest Observer programs were placed in the Lexan/Boron ($65 - 190$ Å) half of the detector. This telescope was aligned

[1] Author's note: my awarded Type II observation of UX Ari could therefore not be carried out.

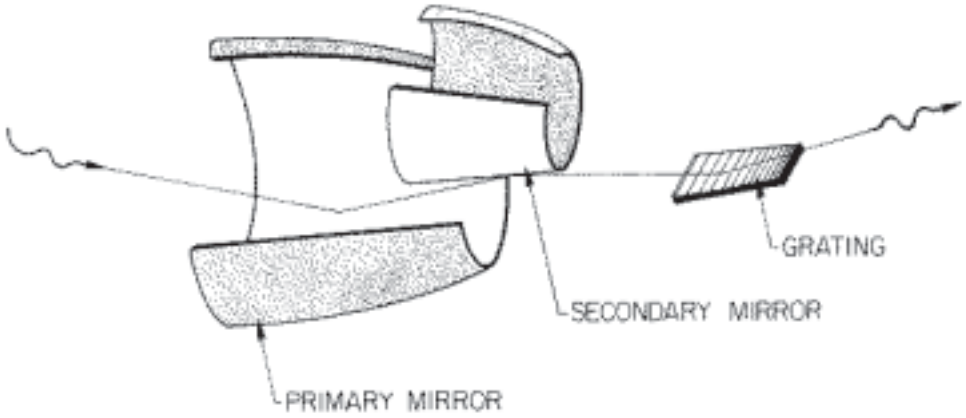

Figure 2.2: *Schematic representation of the grazing-incidence technique of the Wolter-Schwarzschild telescopes. The grating stack was only used for the spectrometers (figure from EUVE Users' Handbook).*

along the spin axis and during the all-sky survey always pointed in the anti-sun direction. It thus obtained a much deeper exposure than the scanners. During pointed observations it was simultaneously used with the spectrometers as an EUV photometer. The DS instrument has been the centerpiece of our investigation of flare statistics with *EUVE*. Figure 2.3a shows the DS effective areas for the two filters.

2.1.1.3 The Spectrometer

The spectrometer (composed of three detectors) shared the mirror assembly with the Deep Survey instrument. The regions of the mirror devoted to the spectrometer and Deep Survey were defined at the front aperture, which was an annulus divided into six segments. Each of the spectrometer channels received a beam of light from one of three alternating segments. After the mirror, each converging beam then stroke one of three gratings which focused the spectra onto three detectors (see Fig. 2.2), arranged in a circle around the central Deep Survey detector. Each detector of the spectrometer had filters that were sensitive to different, overlapping

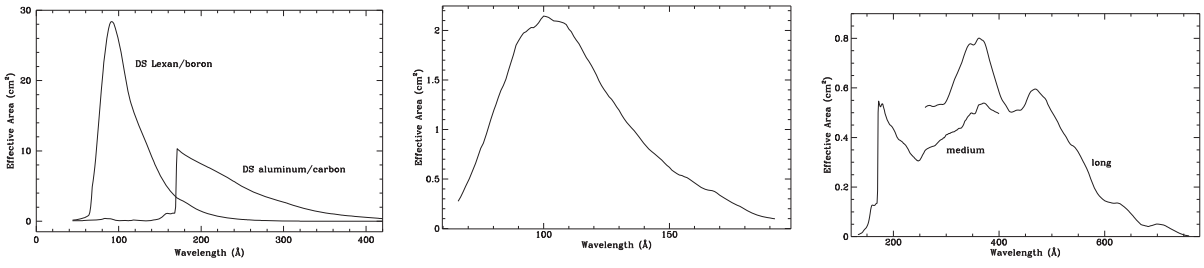

Figure 2.3: *Effective areas of the Deep Survey (left) instrument, the Short Wavelength (middle), and the Medium and Long Wavelength (right) spectrometers (figures from EUVE Users' Handbook).*

wavelength bandpasses: the Short Wavelength detector ($70 - 190$ Å, Lexan/Boron filter), the Medium Wavelength detector ($140 - 380$ Å, Aluminium/Carbon filter), and the Long Wavelength detector ($280 - 760$ Å, Aluminium filter). While their geometric areas were identical ($72.44\,\mathrm{cm}^2$), their effective areas were drastically smaller ($\approx 0.5 - 2\,\mathrm{cm}^2$; Fig. 2.3bc). Since the resolution element was ≈ 0.5 Å, ≈ 1.0 Å, ≈ 2.0 Å, for the SW, MW, and LW, respectively, the *EUVE* spectrometers had a medium-resolution spectroscopic capability ($\Delta\lambda/\lambda \approx 200$) with small effective areas.

2.2 The XMM-Newton Observatory

The X-ray Multimirror Mission (XMM) satellite is one of the cornerstone missions of the European Space Agency (ESA). It was launched with an Ariane 5 rocket from Kourou in French Guyana on December 10, 1999 and was renamed to *XMM-Newton* in honour of Isaac Newton. *XMM-Newton* carries two different types of telescopes: three Wolter type I X-ray telescopes with different X-ray detectors in their foci and an optical/ultraviolet telescope of 30 cm diameter with a microchannel plate pre-amplified CCD detector in its focal plane.

XMM-Newton can thus provide simultaneous coverage of the X-ray and optical/UV ranges.

There are three types of scientific instruments on board *XMM-Newton*. A sketch of the *XMM-Newton* payload is displayed in Fig. 2.4:

1. EUROPEAN PHOTON IMAGING CAMERAS (EPIC). Three CCD cameras for X-ray imaging with moderate spectroscopic resolution and X-ray photometry. *XMM-Newton* carries two MOS cameras and one pn camera.
2. REFLECTION GRATING SPECTROMETERS (RGS). Two identical spectrometers consisting of CCD cameras and Reflection Grating Arrays. They combine high-resolution X-ray spectroscopy with timing information.
3. OPTICAL MONITOR (OM). An optical/UV telescope with a microchannel plate to perform imaging, photometry, and grism spectroscopy.

Each mirror module is composed of 58 thin nested mirror shells (Fig. 2.5). The point-spread function (PSF) reaches a full width at half maximum (FWHM) of the order of $6''$ and a half-energy width (HEW; 50 % of the total energy encircled) of $15''$.

2.2.1 The European Photon Imaging Cameras

Two front-illuminated EPIC cameras using the MOS (Metal Oxide Semiconductor) technology are placed at the focus of two X-ray telescopes with Reflection Grating Arrays for the Reflection Grating Spectrometers (see §2.2.2; also Fig. 2.6), while the back-illuminated EPIC camera

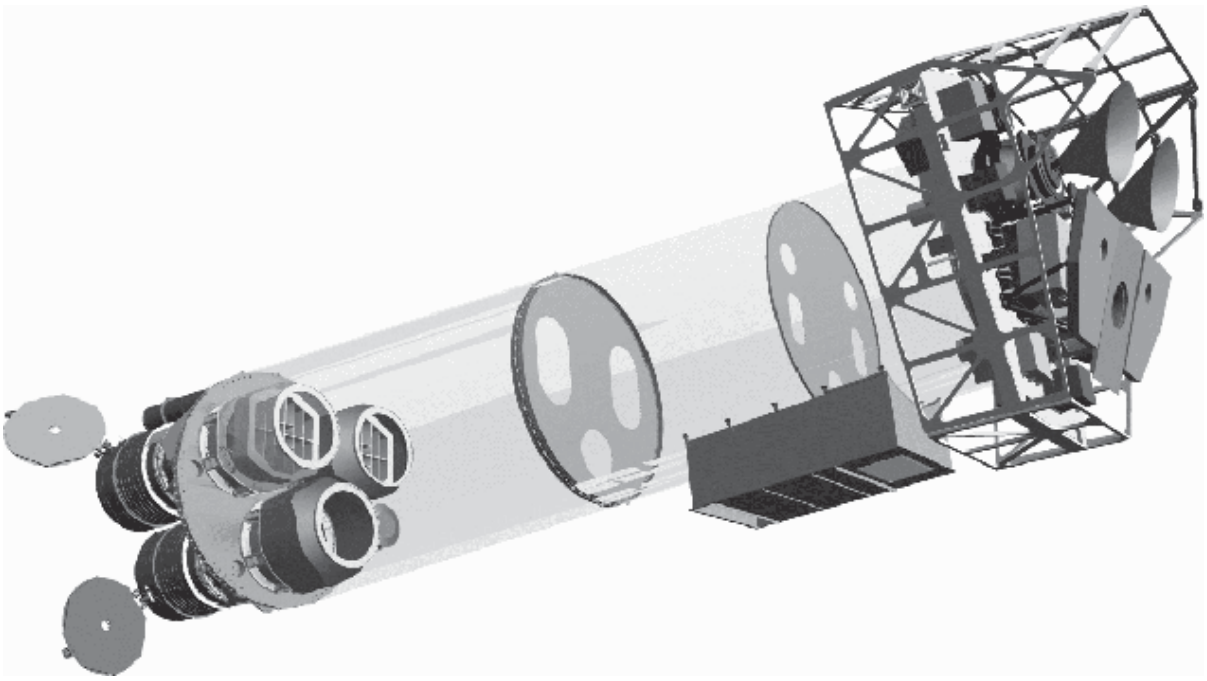

Figure 2.4: *Sketch of the XMM-Newton payload. The three mirror modules, two of which are equipped with Reflection Grating Arrays, are visible at the lower left. At the right end of the array, the focal X-ray instruments are shown: The EPIC MOS cameras with their "conical" ("horns") radiators, the radiator of the EPIC pn camera (below, with a large central hole), and those of the RGS detectors (symmetrically placed next to that of the EPIC pn). The OM telescope is seen at the right of the lower mirror module. Courtesy of Dornier Satellitensysteme GmbH.*

of pn technology lies at the focus of the third X-ray telescope. The cameras are composed of arrays of 7 and 12 CCDs for MOS and pn, respectively. A rough sketch of their array configuration over the field of view is shown in Fig. 2.7. They offer sensitive imaging capabilities over a field of view of $30'$ with moderate spectral ($E/\Delta E \approx 20 - 50$ over $0.15 - 15$ keV) and angular resolution ($6''$ FWHM; $15''$ HEW).

The EPIC cameras allow for several modes of data acquisition, independently for each camera. In brief, in the "full frame" and "extended full frame" (pn only), all pixels of all CCDs are read out (every 2.6 s for MOS, and every 73.4 ms and 200 ms for pn, in normal and extended modes, respectively) and thus the full field of view is covered. There are also various "partial window" modes; for MOS, these modes essentially reduce the area of pixels read out from the central chip (while the outer 6 chips still are fully read out; 0.9 s and 0.3 s frame time for large and small window modes, respectively). For the pn camera, either half of the area in all 12 CCDs is read out (48 ms), or only a part of CCD number 4 is used to collect data (6 ms). In the "timing" mode, imaging is made only in one dimension along the column axis. Along the row direction, data from a predefined area on one CCD chip are collapsed into a one-dimensional row to be read out at high speed (1.5 ms for MOS and 30 μs for pn). Since the orientations of the 2 MOS

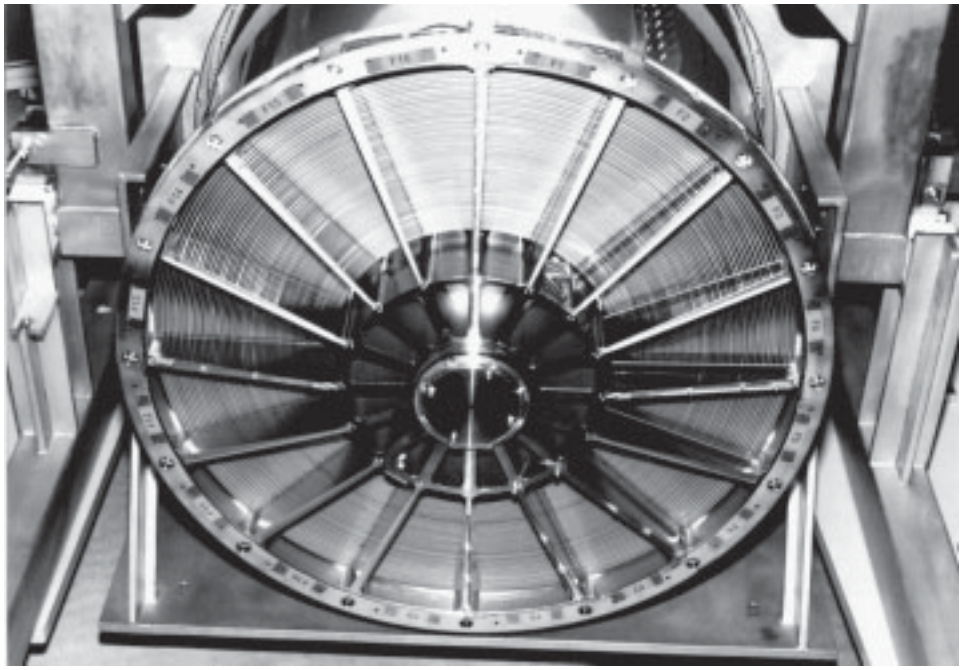

Figure 2.5: *A mirror module with its 58 thin nested mirror shells. Courtesy of D. de Chambure, XMM Project (ESTEC).*

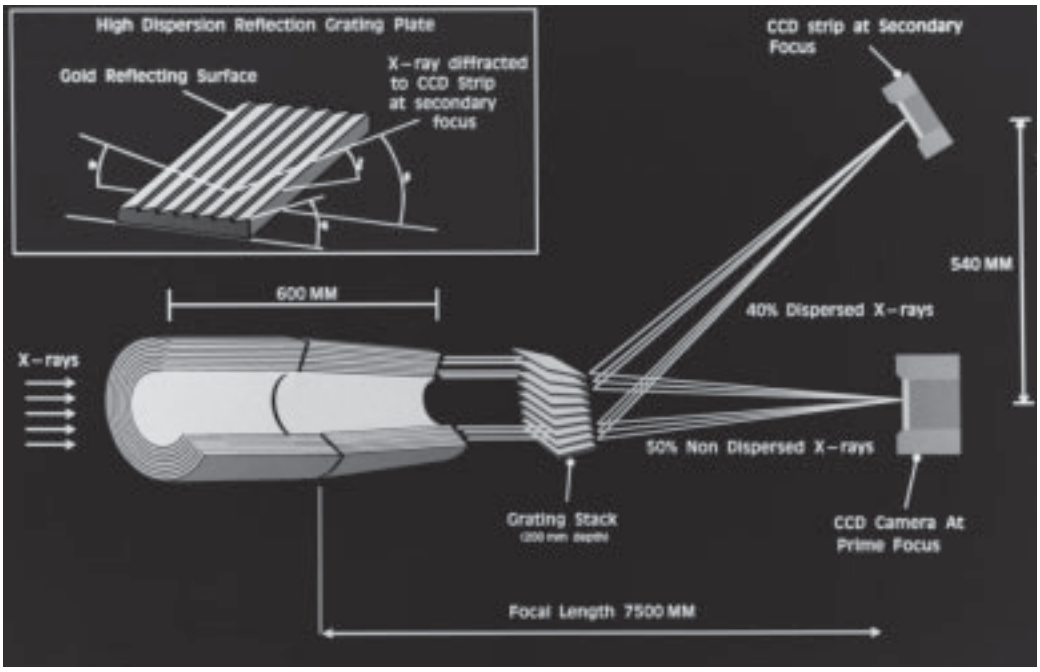

Figure 2.6: *The light path in the two XMM-Newton telescopes with grating arrays (not to scale). Note that the actual fraction of the non-intercepted light that passes to the primary MOS focus is 44%, while 40% of the incident light is intercepted by grating plates of the Reflection Grating Array (figure from XMM-Newton Users' Handbook).*

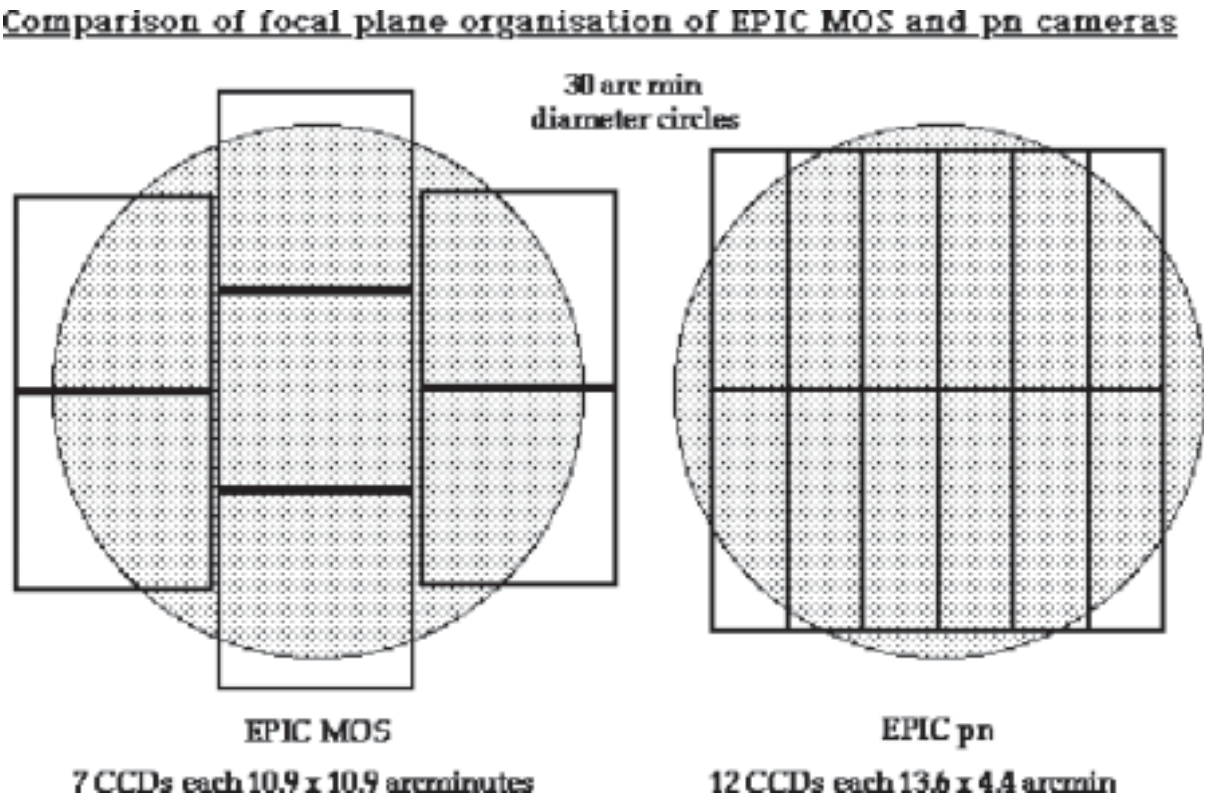

Figure 2.7: *A rough sketch of the field of view of the two types of EPIC cameras; MOS (left) and pn (right). The shaded circle depicts a 30′ diameter area. Note that the two EPIC MOS cameras are rotated by 90° with respect to each other, and that the EPIC pn array is slightly offset with respect to the optical axis so that the nominal on-axis observation does not fall on the central chip boundary (figure from XMM-Newton Users' Handbook).*

cameras differ by 90°, the "imaging" directions in the 2 MOS are perpendicular to each other. Again, the 6 outer MOS chips are operated in the normal imaging mode. For the EPIC pn, the "timing" mode uses only the whole CCD 4. Note that there is (for pn only) a special flavour of the timing mode, the "burst" mode, which offers very high time resolution (7 μs).

Since the EPIC cameras are not only sensitive to X-ray photons, but also to infrared, visible, and ultraviolet light, it is necessary to use an optical blocking filter if a target has a high optical-to-X-ray flux ratio. Each EPIC camera is therefore equipped with a set of 3 separate filters, named thick, medium, and thin, that reduce the soft X-ray response of the cameras. Figure 2.8 shows the EPIC effective areas for each of the optical blocking filters and without a filter. For our stellar coronal targets, it was generally necessary to use the medium filter in combination with a partial window mode. However, there were cases of very bright targets in the X-ray and optical where the thick filter with a timing mode was needed.

Because of the finite frame time of a CCD chip, photon pile-up (i.e., the arrival of more than one X-ray photon in one camera pixel or in adjacent pixels before it is read out) can affect both

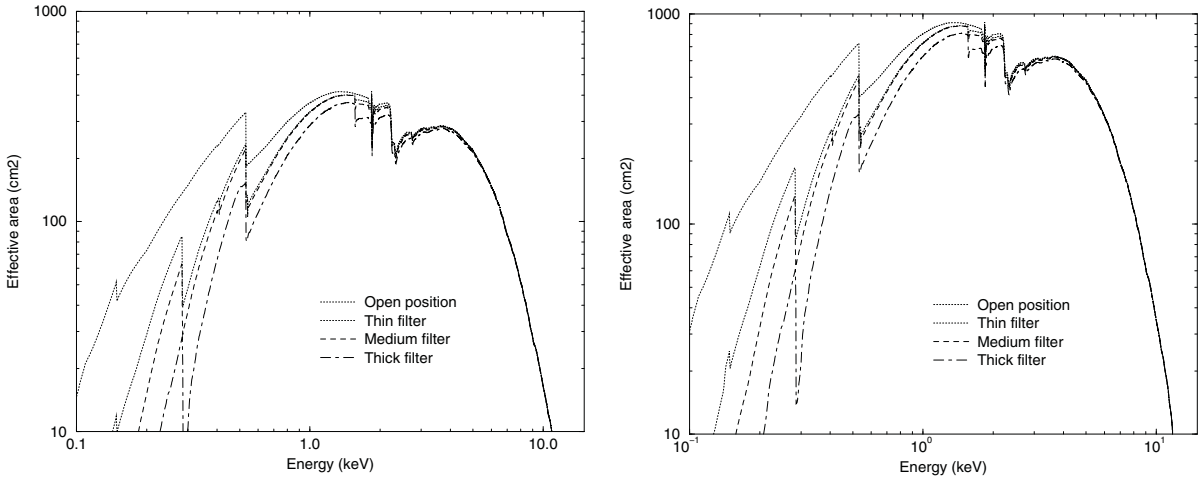

Figure 2.8: *The EPIC MOS (left) and pn (right) effective areas for each of the optical blocking filters and without a filter (figures from XMM-Newton Users' Handbook).*

the PSF and the spectral resolution of the EPIC cameras. Pile-up creates artificial multi-pixel photon patterns that are then rejected. In the most extreme cases, an artificial "hole" in the centre of the PSF can appear. The standard spectral response is incorrect as well, since the charge deposited by more than one photon is added up before being read out, thus creating artificial "hard" photons where there have actually been two or more soft photons. Pile-up effects on the spectral shape are largely reduced by selecting single events (mono-pixel). A reduction of the absolute flux is inherent. In the case of very strong pile-up (e.g., in the case of HR 1099, see chapter 6), it is still possible to obtain accurate spectra by excising the heavily piled-up core from the analysis.

2.2.2 The Reflection Grating Spectrometers

There are two identical RGSs behind two of the three mirror modules. The RGS design is illustrated in Fig. 2.9. Each incorporates an array of reflection gratings placed in the converging beam of the *XMM-Newton* telescope. The grating stack consists of 182 aligned reflection gratings and intercepts about half of the light emanating from the telescope. The undeflected light passes through and is intercepted by EPIC in the telescope focal plane. The gratings are actually located on a toroidal Rowland surface, formed by rotating the Rowland circle about an axis passing through the telescope and spectroscopic foci, as illustrated in the left panel of Fig. 2.9. The gratings are slightly trapezoidal, since their edges lie along rays converging on the telescope focus. The field of view in the cross dispersion direction is determined by the width of the CCDs ($\pm 2.2'$). In the dispersion direction the situation is more complex: the source extent affects the wavelength resolution.

Nine[2] back-illuminated CCDs (per RGS) are located on the Rowland circle to detect the dis-

[2]One CCD per RGS has been lost since launch, due to failing drive electronics on CCD4 (RGS2) and CCD7 (RGS1). Since they do not cover the same wavelength range, there is no loss of wavelength coverage.

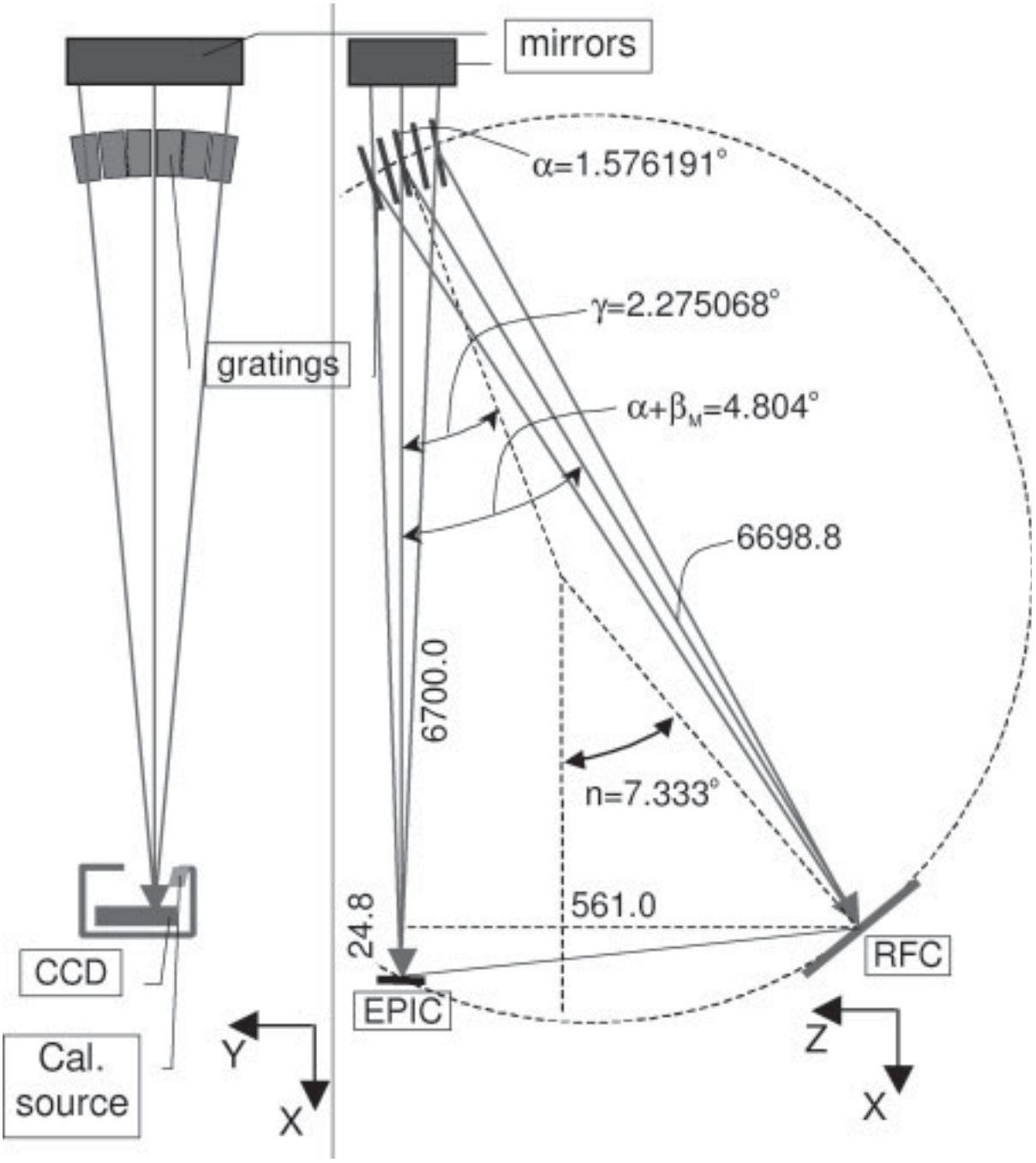

Figure 2.9: *Optical design of the RGS (not to scale). X-rays enter from the top. Numerical values for a few key dimensions and angles are indicated (linear dimensions in mm, angles in degrees). From den Herder et al. (2001).*

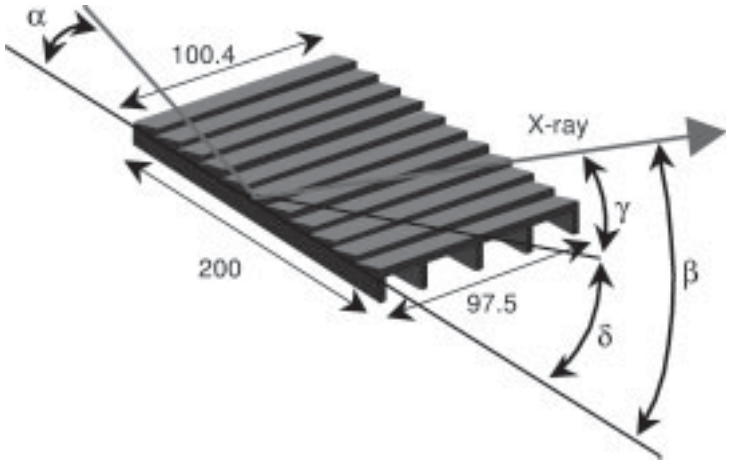

Figure 2.10: *Schematic drawing of a grating, including some of the key dimensions and angles ($\alpha = 1.5762°$, $\gamma = 2.2751°$, $\delta = 0.6989°$, β is the dispersion angle). From den Herder et al. (2001).*

persed spectra in single photon counting mode. For an ideal grating stack and ideal detector, the position of an X-ray photon on the detector gives the wavelength through the dispersion equation:

$$m\lambda = d \times (\cos\beta - \cos\alpha), \tag{2.1}$$

where m is the spectral order (-1, -2, ...), d is the groove spacing ($1/d = 645.6$ lines/mm) and α ($1.5762°$) and β are the angles of the incident and dispersed rays, respectively, both measured from the grating plane. First, second, and higher order spectra are overlapping on the detectors, however, they are easily separated using the intrinsic energy resolution of the CCDs.

The RGS achieve high spectral resolution ($E/\Delta E \approx 100 - 500$, FWHM, or $100 - 800$ HEW) in the energy range $0.33 - 2.5$ keV ($5 - 38$ Å). The wavelength accuracy currently reaches $\Delta\lambda \approx 8$ mÅ. The total effective area reaches 140 cm^2 in the first order (Fig. 2.11). The energy range covered by the RGS has a particularly high density of X-ray emission lines, thus offering a large number of diagnostic tools to investigate the physical conditions in the emitting material and its composition, e.g., the L-shell transitions of heavy elements like Fe and Ni, and K-shell transitions of lighter elements, such as C, N, O, Ne, Mg, and Si.

2.2.3 The Optical Monitor

Besides its three X-ray telescopes, *XMM-Newton* also carries a co-aligned 30 cm optical/UV telescope (OM) that provides for the first time the possibility to observe simultaneously in the X-ray and optical/UV regime from a single space observatory. While the use of the OM was often not possible for our stellar sources (most of the targets are too bright and the OM had to be closed), it can prove an excellent complement to the X-ray instruments. In particular, its UV (or U band) filters can provide access to the response of the chromosphere/transition region to stellar flares.

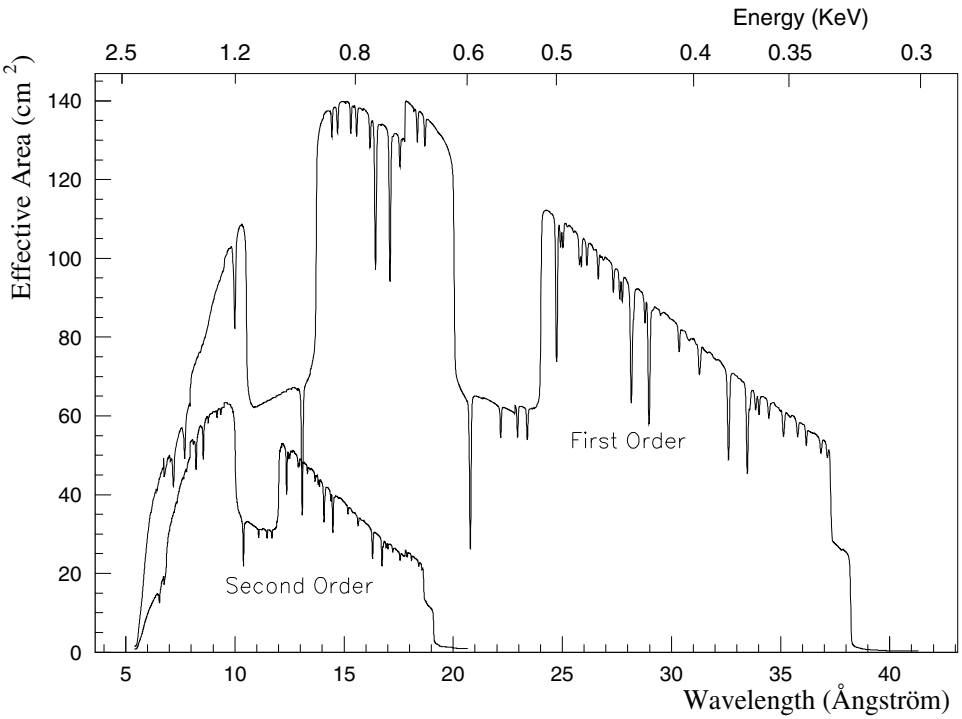

Figure 2.11: *The effective area of both RGS units combined as a function of energy and wavelength (top and bottom horizontal scale, respectively). Note the following features: i) the effective area has broad gaps at the locations corresponding to the inoperational CCDs; ii) the chip boundaries appear, since the RGS are aligned such that the inter-chip gaps do not coincide in wavelength; iii) bad pixels and columns cause weak sharp decreases of the effective area (figure from XMM-Newton Users' Handbook).*

The OM telescope consists of an f/12.7 modified Ritchey Chrétien optics. The OM is operated as a photon-counting instrument in two modes allowing either imaging or fast photometry (time resolution of 0.5 s) or both simultaneously. The field of view is $17' \times 17'$. The OM detectors consist of a microchannel plate (MCP) intensified CCD. The total bandwidth ranges from $160 - 600$ nm, with a sensitivity limit of 23.5 mag (6-σ detection of an A0 star in 1 ksec). The OM is equipped with a filter wheel holding several optical elements that can be moved into the light path. These elements comprise not only lenticular filters, but also two grisms for spectroscopy in the optical and the UV. Usual Johnson photometry filters are available (U, B, V), together with three UV filters ($UVW1$, $UVM2$, $UVW2$). Finally, a white light filter is also available. Figure 2.12 shows the OM effective area folded through the various photometric filters.

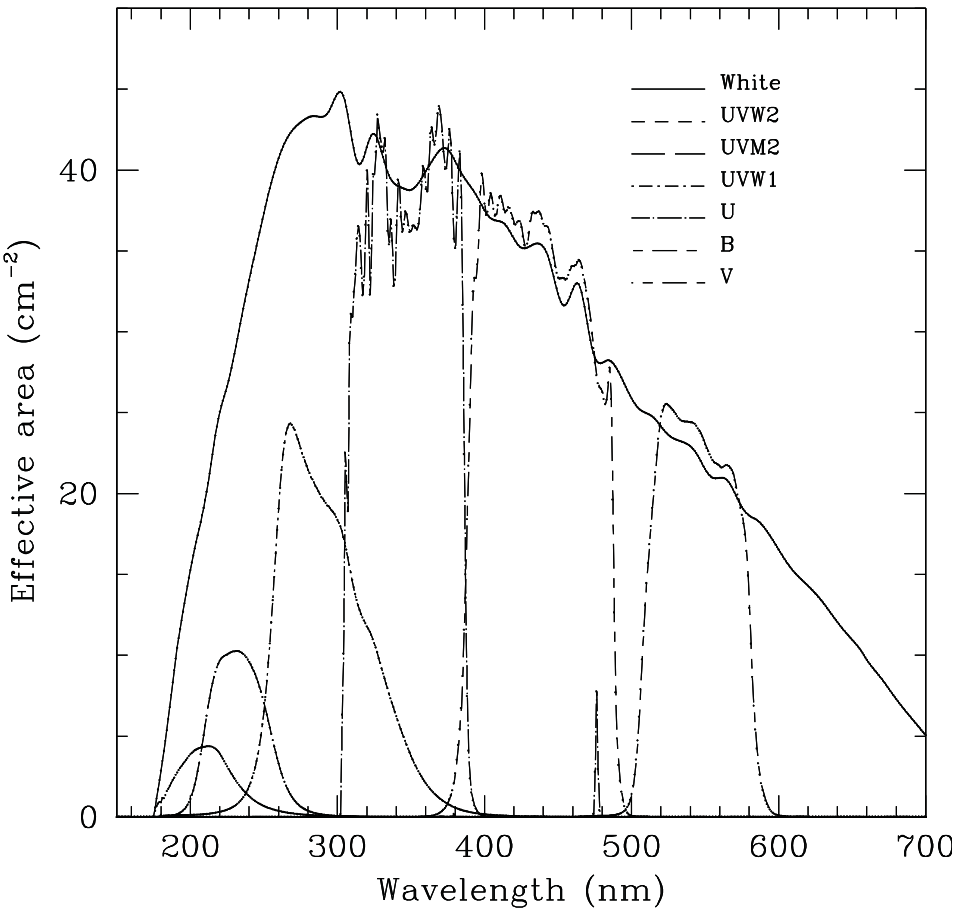

Figure 2.12: *The OM effective area folded through the various photometric filters. Note that the label of the y-axis is incorrect in this figure taken from the XMM-Newton Users' Handbook. It should read "Effective area (cm^2)". The center of the filter spectral ranges increases in wavelength from $UVW2$, $UVM2$, $UVW1$, U, B, and V. The white light filter encompasses the whole wavelength range.*

Part I

Flare Statistics in Active Stars

One of the principal questions in the field of solar and stellar coronae is the cause for their hot ($1 - 20$ MK) temperature and the origin of coronal heating. While a number of potential heating mechanisms have been identified (see, e.g., Zirker 1993), flares (explosive events through magnetic energy release) are particularly appealing and could be relevant heating agents in solar-type stars (e.g., Parker 1988; Güdel 1997).

This part of the thesis concentrates on the investigation of the role of flares in young active stars by means of light curves. In Chapter 3, a pilot study of two young solar analogs is presented. A comprehensive follow-up investigation of flare activity in active stars with the *Extreme Ultraviolet Explorer* is presented in Chapter 4. Finally, Chapter 5 discusses tentative results from an ongoing investigation of flare statistics in the active dwarf AD Leo.

Chapter 3

Investigation of Flare Statistics in Two Young Solar Analogs: A Pilot Study

Summary

Extreme Ultraviolet Explorer (*EUVE*) data of two active solar analogs, 47 Cas and EK Dra, were used to investigate flare statistics and the distribution of the flare occurrence rate in energy. The *EUVE* satellite observed each star for almost 7 days. Simultaneous spectral data from its spectrometers were used to derive temperature and abundance characteristics of their coronae. The emission models were derived from differential emission measure distributions by fitting optically thin thermal models to the spectra. The Deep Survey instrument photon lists were analyzed by applying different time binnings. A total of 28 flares were identified for further analysis. The timing study provided estimates for the total radiative energy loss of each flare. The differential distribution of flares in total X-ray energy is found to be a power law ($dN/dE \propto E^{-\alpha}$), with $\alpha \approx 2.2 \pm 0.2$, valid in the energy range between $3 \times 10^{33} - 6 \times 10^{34}$ ergs. The power-law index is larger than for typical solar flares but similar to indices found recently for small-scale solar events. If the power law continues to energies of moderate solar flares, then the total energy emitted by the ensemble of all flares may suffice to explain all of the observed flaring and "quiescent" X-ray emissions of the two stars. A considerable portion, if not all, of the energy required to heat their coronae could thus be provided by flares.

3.1 Introduction

A lively debate on heating mechanisms of solar and stellar coronae to temperatures exceeding 10^6 K has identified numerous possible processes (e.g., Zirker 1993, see §1.4). Recent observations and theoretical work have given momentum to one particular class of coronal heating mechanisms, those that involve flares that heat the outer atmospheric layers of the stars.

The work presented in this chapter has been published in Audard, Güdel, & Guinan (1999). Some figures are taken from Audard, Güdel, & Guinan (1998).

There is ample support for the hypothesis that flares can heat coronae although no evidence is unequivocal. Doyle & Butler (1985) and Skumanich (1985) noted that the "quiescent" coronal X-ray luminosity of active stars, $L_{\rm X}$, is correlated with their time-averaged U-band flare luminosity, suggesting that flares could release sufficient energy that is ultimately observed as "quiescent" coronal emission. $L_{\rm X}$ is itself correlated (at least for active stars) with the "quiescent" radio luminosity (Güdel & Benz 1993). The latter is due to synchrotron radiation from relativistic electrons. On the Sun (and on flaring stars), these electrons are accelerated during flare episodes. Benz & Güdel (1994) found that the stellar correlation is approximately followed by solar flares, thus providing a strong link between "quiescent" emission and flares.

Active stellar coronae show "quiescent" temperatures of $10 - 30$ MK (e.g., Haisch & Schmitt 1996), values that the solar corona attains exclusively during flares (Watanabe et al. 1995). Characteristic emission measure distributions of active solar analogs were successfully reproduced by simple statistical hydrodynamic simulations of a rapid sequence of flares (Güdel 1997). Robinson et al. (1995) found evidence for numerous transition region (TR) flares in late-type active stars. Also, broadened TR emission line profiles have been interpreted (Linsky & Wood 1994; Wood et al. 1996) in terms of a large number of explosive events similar to flare events previously identified in the solar TR (Dere, Bartoe, & Brueckner 1989).

Solar flares have been found to be distributed in energy according to a power law with index α (eqs. 1.1 and 1.2, §1.4). The typical power-law index ranges $\alpha \approx 1.5 - 1.8$ (Crosby et al. 1993, see also Tab. 1.1). A similar power-law index was found for soft X-ray flares on M dwarfs (Collura et al. 1988). If $\alpha > 2$, then an extrapolation to flare energies below the detection limit could be sufficient to produce the luminosity of the "quiescent" corona, because the integrated power can be arbitrarily large for small values of $E_{\rm min}$ (see eq. 1.3). It is crucial to investigate whether the solar flare energy distribution steepens at lower energies (Hudson 1991), perhaps allowing for "quiescent" coronal heating by "microflares" (see, e.g., Lin et al. 1984; Parker 1988). Recent solar observations are now supporting this flare-heating hypothesis. Although Shimizu (1995) reported $\alpha \approx 1.6$ for small active-region transient brightenings ($\geq 10^{27}$ ergs), Porter et al. (1995) found $\alpha \approx 2.3$ for still smaller events, and Krucker & Benz (1998) measured $\alpha = 2.3 - 2.6$ for microflares in the quiet solar corona.

We investigated the question of coronal flare heating for two young stars whose coronae could be scaled-up versions of the solar corona. We took advantage of long, uninterrupted (except for occultations by the Earth) observations in the $40 - 190$ Å range, using the *Extreme Ultraviolet Explorer* (*EUVE*; $P_{\rm orb} = 96$ min, Malina & Bowyer 1991). This range contains a number of emission features that are formed in typical coronal flare plasmas but that are also present in the "quiescent" coronal emission seen on active stars.

3.2 Observations and Data Reduction

Our first target, 47 Cas (HD 12230; F0V), is a nearby star ($\mathrm{distance} \approx 33.6$ pc). Judged from its space motions, it is a probable member of the Pleiades Moving Group with an age of ≈ 100 Myr. Güdel et al. (1998) found it to be an astrometric binary with the secondary

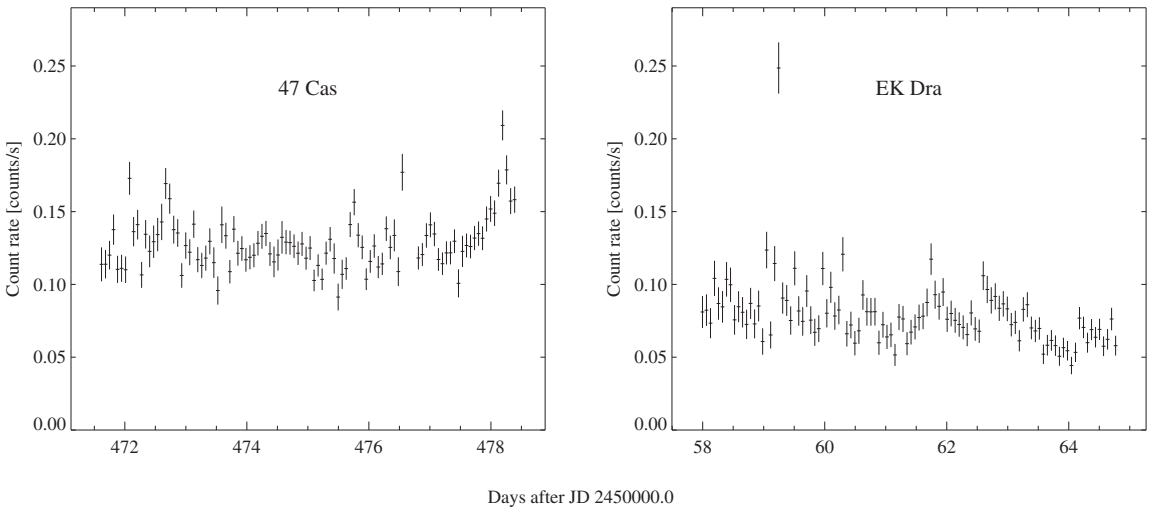

Figure 3.1: *The EUVE Deep Survey light curves of 47 Cas and EK Dra. The bin size corresponds to one EUVE orbit (96 minutes).*

star most likely being an active G dwarf that is responsible for most of the observed coronal X-ray emissions. We observed 47 Cas in the Guest Observer Program of *EUVE* during almost 7 contiguous days. A short ($5^{\rm h}40^{\rm m}$) cut in the last part of the observation was due to a target of opportunity event (TOO). We also reanalyzed the *EUVE* data of EK Dra (HD 129333; G0V). EK Dra is also a probable member of the Pleiades Moving Group and reveals rapid rotation ($P_{\rm rot} = 2.7$ d), indicating youth. The *EUVE* spectral analysis with a description of the observation and the star is given by Güdel et al. (1997a).

For the spectral analysis of 47 Cas, we used the Short and Medium Wavelength spectrometer (SW, MW) data only, since no obvious emission lines were visible in the Long Wavelength spectrometer data. Standard reduction in IRAF was performed. We extracted each spectrum along the dispersion direction using rectangular boxes for the sources and two parallel boxes for the backgrounds. We extracted the light curves from the Deep Survey (DS) data, using circles around the sources and concentric annuli to define the backgrounds. The influence of the detector "dead spot" on the light curve variability of both stars was also investigated and no significant effect was found. Figure 3.1 shows the light curves with one Good Time Interval (GTI; bin size of 1 orbit, about 2000 s on source) in each bin.

3.3 Analysis Methods and Results

The *EUVE* spectrum of the complete observation of 47 Cas was analyzed with the Utrecht software SPEX (Kaastra et al. 1996a) in the same way as was previously analyzed the spectrum of EK Dra (Güdel et al. 1997a). We present in Figure 3.2 the *EUVE* SW/MW spectra of 47 Cas (from Audard et al. 1998). This spectrum represents the average state of the corona, including flares. The observations are not sensitive enough to derive the run of the temperature across the

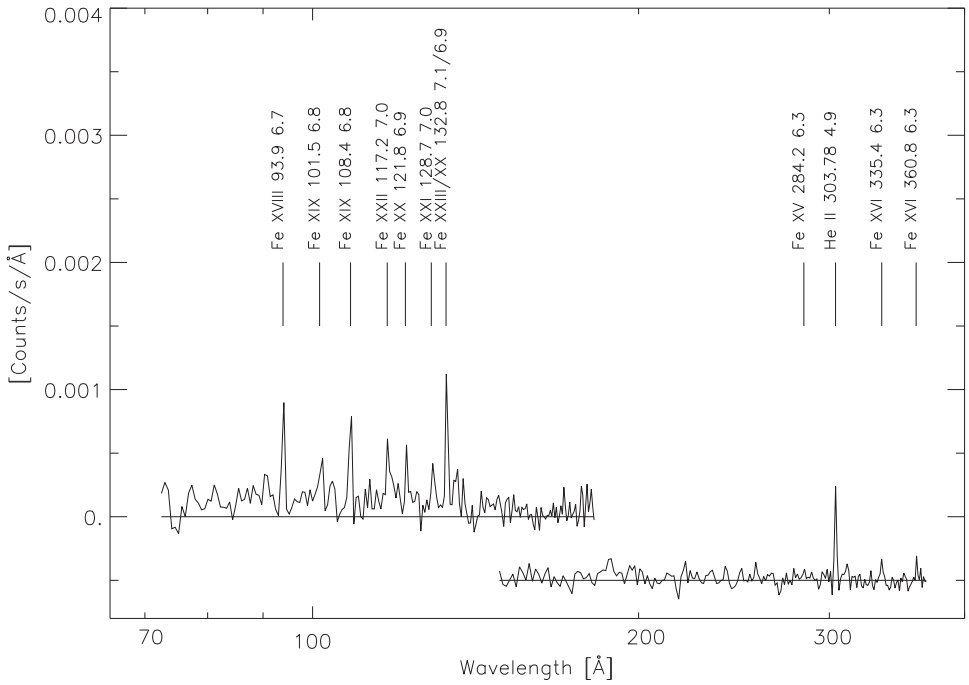

Figure 3.2: *EUVE SW and MW spectra of the 47 Cas, rebinned to widths of 0.52 and 0.104 Å, respectively (from Audard et al. 1998). The MW spectrum is shifted along the y-axis by* -5×10^{-4} *ct* $s^{-1}Å^{-1}$ *for illustration. Significant lines are labeled by the element, its ionization stage, the wavelength and the logarithm of the maximum formation temperature.*

flares. The coronal temperatures measured by *ASCA* during a purely "quiescent" state of EK Dra were, however, very similar to the present results (Güdel et al. 1997a). We rebinned the observed spectrum to resolutions commensurate with those of the *EUVE* spectrometers (0.5 and 1 Å for the SW and MW, respectively), leading to 385 useful data channels (excluding the He II $\lambda 303.78$ line). Several iron lines with ionization stages from Fe XV to Fe XXIII were detected, implying line formation temperatures ranging from $10^{6.3}$ to $10^{7.0}$ K. The Collisional Ionization Equilibrium (CIE) model in SPEX was used with a hydrogen absorption component to determine the iron abundance and the interstellar hydrogen column density $N_{\rm H}$. From a three-temperature CIE model, we found an Fe abundance of about 0.3 times the solar photospheric value, and $N_{\rm H} \approx 10^{18}$ cm^{-2}. We then carried out a differential emission measure distribution (DEM) fit to the spectrum using various methods, such as Chebychev polynomials, a CLEAN algorithm, and a regularization method (Fig. 3.3; also Audard et al. 1998). Details on the methods to derive an emission measure distribution can be found in Kaastra et al. (1996b).

For the flare statistics, we adapted a procedure from Robinson et al. (1995). In short, this method characterizes the statistical distribution of the number of counts per bin for any given regular time binning of the "quiescent" time intervals. Sufficiently long stretches of quiescent emission were available from the 47 Cas light curve. For EK Dra, we simulated a stochastic photon list with an average count rate identical to the relatively short quiescent intervals toward

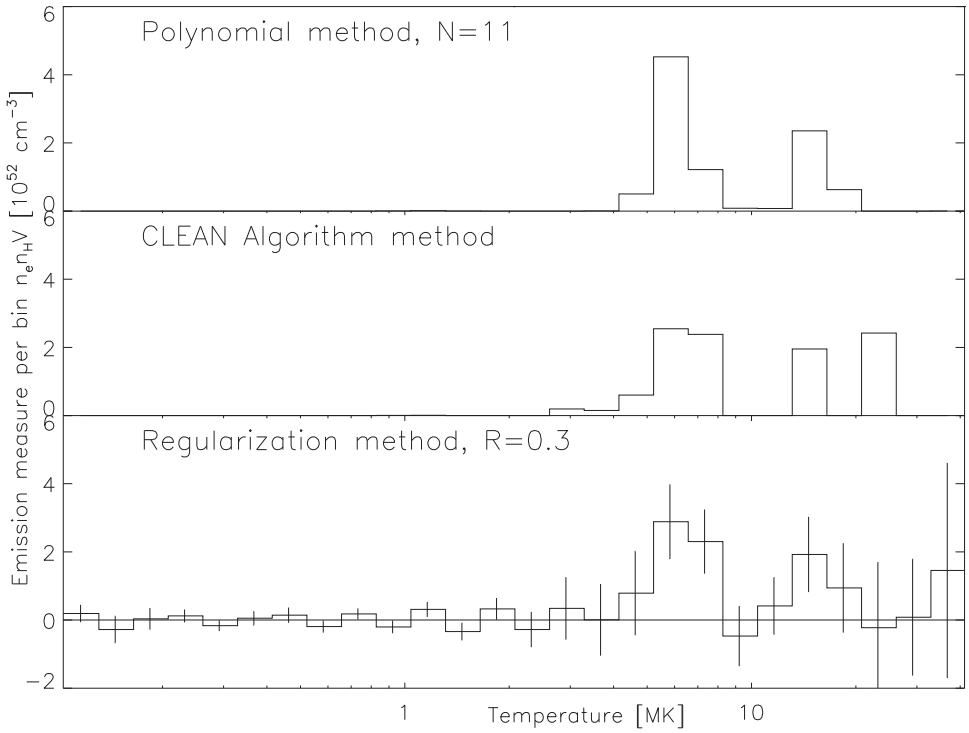

Figure 3.3: *Realizations of the emission measure distribution of 47 Cas (from Audard et al. 1998) using various methods. The EUVE SW and MW spectra (see Fig. 3.2) have been simultaneously fitted.*

the end of the observation. We started the procedure with small bins ($1/50$ of 96 min) which were first randomized in time and then rebinned with binning factors between 10 and 100 (resulting in bin sizes of $1/5$ to 2 times 96 min). The rebinning was applied for 100 different relative time shifts (phases) by a fraction of a bin, but for each bin we retained only the highest number of counts that it could thus comprise. The complete procedure was repeated for many different realizations of the initial randomization to obtain a robust quiescent count distribution (for each rebinning factor, e.g., Fig. 3.4; see Robinson et al. 1995 for further details). These distributions define the probability for a bin to be in a quiescent state, given its number of counts. We next binned the full data set (including the flares) with any binning factor and phase shift and could therefore, by comparing with the quiescent distribution, find the probability for each bin to be quiescent.

We plot the probability for the presence of quiescent bins as a function of time (x-axis) and bin size (y-axis; see Figure 3.4 for 47 Cas). The flare significance increases from light grey (probability for quiescence to occur by chance between 10^{-3} and 10^{-4}) to black (probability smaller than 10^{-6}). A flare on 47 Cas just before the TOO interruption was excluded because its end time could not be determined. Finally, 12 flares were extracted for 47 Cas and 17 for EK Dra. Next, we defined a lower envelope to each star's light curve with smoothed splines, above which we fitted Gaussians to the identified flares. The duration of a flare was defined as

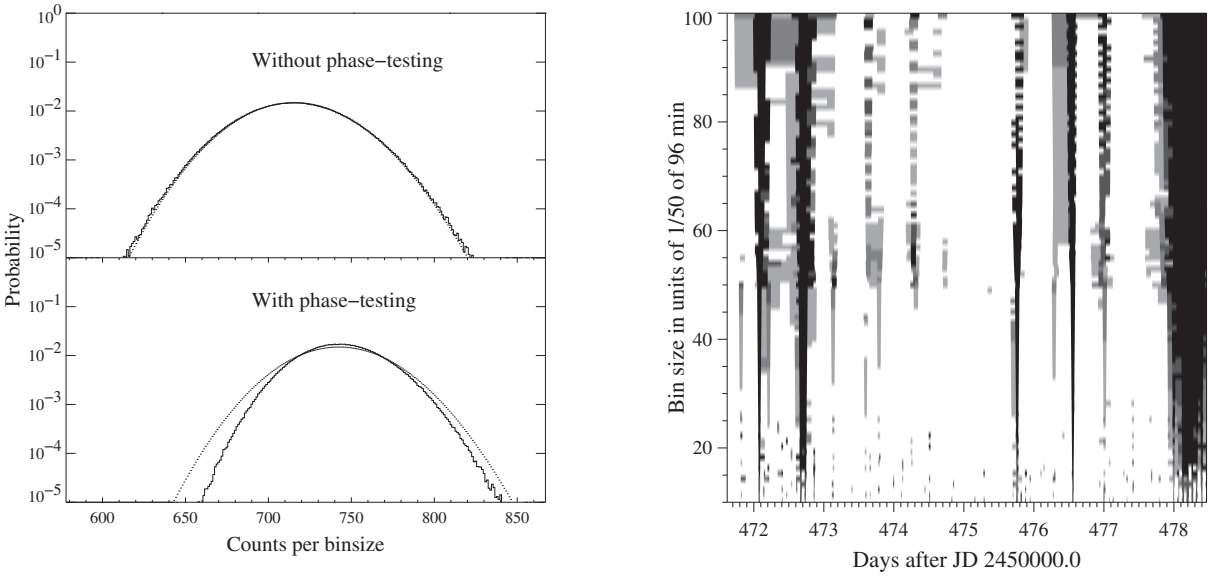

Figure 3.4: *Left: Count distributions for a bin size of 96 min. The count distribution during quiescence (for a chosen phase start) is given with the corresponding Poisson distribution (dotted line; top panel). A new count distribution is obtained after having performed tests with different integration phases and having chosen the largest number of counts in each bin (bottom panel). The former Poisson distribution is then shifted by the square root of the mean number of counts. See Robinson et al. (1995) for a complete description of the method. Right: Probability of flaring emission as a function of time and bin size for 47 Cas. The flare significance increases from light grey to black. We excluded the detection at day 476.6 that is affected by the short interruption during the TOO.*

the Full Width at Half Maximum (FWHM), its beginning and end as the times separated from the maximum by 2σ. The parameters of the last flare of 47 Cas had to be estimated because of its peculiar shape. The total EUV+X-radiated energy of each flare and the cumulative flare rate distributions were determined as follows. We derived the total number of counts between the beginning and the end of each flare ("quiescent"+flare contribution). The mean background level was estimated just before and after the flare to derive the "flare-only" counts. The DEM fits were used to compute the conversion factor (C) that relates the DS count rate (μ) to the total radiative energy loss from the corona. From the computed average EUV+X-ray luminosity L_X between 0.01 and 10 keV, we obtained $C \approx 1.97 \times 10^{31}$ ergs per count for 47 Cas ($L_{\rm X} = 2.5 \times 10^{30}$ erg s^{-1}, $\mu = 0.127$ cts s^{-1}), and $C \approx 2.1 \times 10^{31}$ ergs per count for EK Dra ($L_{\rm X} = 1.54 \times 10^{30}$ erg s^{-1}, $\mu = 0.074$ cts s^{-1}).

Approximately 60 % of the duration of the EUV light curve of each star is occupied by identified flares. Overlapping flares are therefore likely. Because our flare identification procedure naturally detects the stronger flare in any overlapping pair, the flare rates had to be corrected iteratively. The flare rate at the energy of the second-largest flare was corrected by a factor $T_{\rm total}/(T_{\rm total} - T_{\rm largest})$, where $T_{\rm total}$ is the total observing time span (≈ 7 days for each obser-

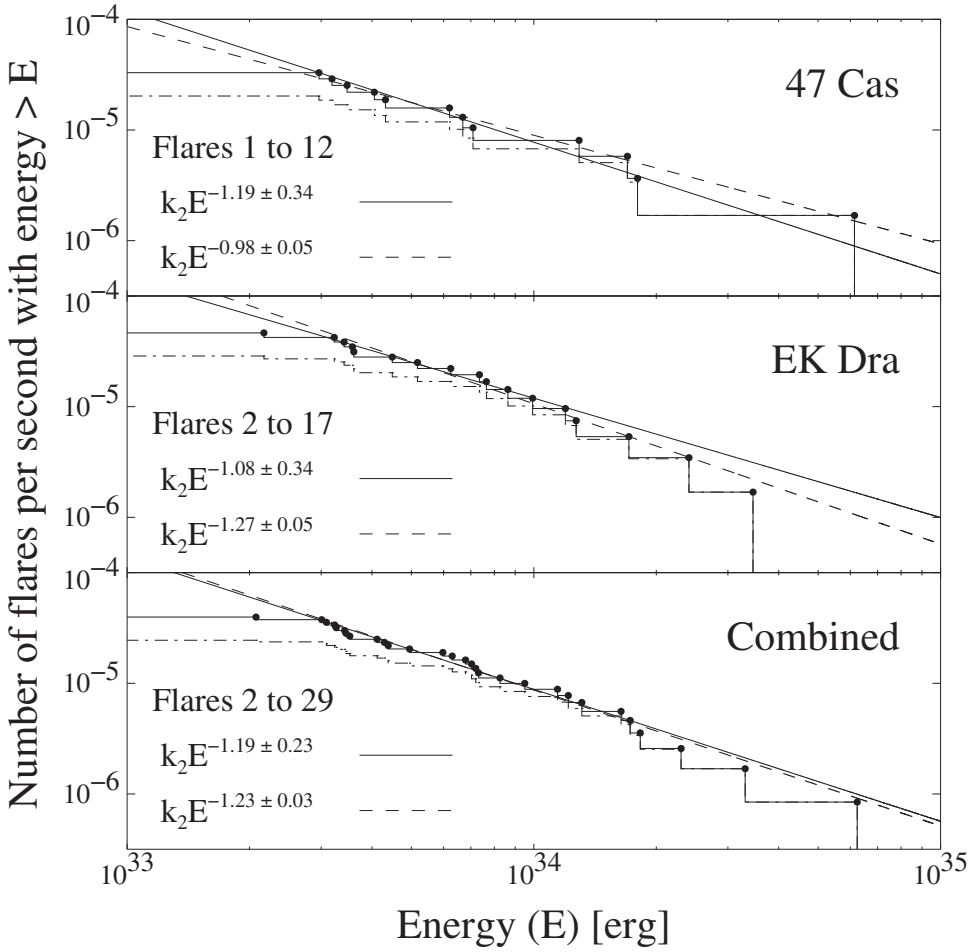

Figure 3.5: *Cumulative flare rate distributions in energy for 47 Cas, EK Dra, and the combined distribution. Corrected distributions are plotted solid, while uncorrected distributions are dash-dotted. Also shown are power-law fits to the corrected distributions using the method of Crawford et al. (solid) and, for comparison, a least-squares fit (dashed). Note that the power-law indices of these cumulative distributions are* $\alpha - 1$ *(see after eqs. 1.1 and 1.2).*

vation), and $T_{\rm largest}$ is the interval of time between the beginning and the end of the largest flare. Analogously, the correction for the third-largest flare took into account the time intervals of the largest and second-largest flares, and so on. Finally, the combined distribution was constructed for a total time span equal to the sum of both observation time spans. A conversion factor equal to the mean of the conversion factors, weighted with the inverse square of the DS count rates, was applied.

Figure 3.5 shows the resulting corrected (*solid*) and uncorrected (*dash-dotted*) cumulative energy distributions for 47 Cas (*top*), EK Dra (*middle*), and both combined (*bottom*). For all panels, we fitted the *corrected* distributions. The solid line shows the best fit using the method of Crawford, Jauncey, & Murdoch (1970) adapted to our distributions. For comparison, a least-

squares fit is shown dashed. The lowest-energy flare of EK Dra was too close to the detection threshold and was not considered. The indices derived from the method of Crawford et al. ($\alpha = 2.19 \pm 0.34$, 2.08 ± 0.34, 2.19 ± 0.23 for 47 Cas, EK Dra and the combined distribution, respectively) are very similar and larger than 2. Fits to the *uncorrected* distributions yield $\alpha \approx 1.8$ but these distributions obviously deviate largely from power laws. We estimated the minimum energy $E_{\rm min}$ in equation (1.3) using the best-fit power law (with $\alpha = 2.19 \pm 0.23$) and an upper limit $E_{\rm max} \approx 6.2 \times 10^{34}$ ergs (corresponding to the largest flare of the combined distribution). We obtained $\log E_{\rm min} = 30.2^{+1.4}_{-14.6}$ and $31.2^{+0.8}_{-4.8}$ using the average luminosities of 47 Cas and EK Dra, respectively. These energies are far below the detection threshold but include, within the confidence limits, flare energies typical for the Sun, possibly even microflares.

EUVE has a low ($\approx$ 30 %) duty cycle, meaning that GTIs are no longer than ≈ 2000 s, and some 3000 s per orbit are lost in "bad time intervals". Many flares with durations $\lesssim 3000$ s could therefore remain undetected. From a linear regression on the log-log plane, we found that the relation between the FWHM durations (D) and the total X-radiated energies of the flares followed approximately a power law $D \propto E^{0.4}$, similar to solar results (Crosby et al. 1993). For $D \approx 3000$ s, the flare energy should be about 10^{32} ergs, an order of magnitude below the lowest-energy flare detected. This effect should therefore be irrelevant. If it were not, the distribution would steepen. Smaller flares are especially prone to poor coverage; the peak region of the flare curve may be missed. The possible underestimation of the energies of the smallest flares could lead to a further slight steepening of the distribution. Another steepening effect is possible if the energy of larger flares were reduced by simultaneous, undetected smaller-scale flares. We neglect these effects but note that they could increase the value of α.

3.4 Discussion and Conclusions

We have analyzed two week-long *EUVE* observations of two active, young solar analogs, 47 Cas B and EK Dra. These are considered to represent our Sun at younger stages of its evolution. They show enhanced levels of activity, with frequent flares superimposed on a "quiescent" emission level $2-3$ orders of magnitude larger than the Sun's. The temperatures of the average coronal plasmas are high, with peaks of the emission measure up to 20–30 MK.

We consider the observed flares to originate from various active regions, since flaring occurs during various phases of the stellar rotation, and both stars are extremely active. Therefore, the flare rate distribution required a correction for effects due to superposition. For 47 Cas and EK Dra, respectively, 12 and 16 flares, in the range $3 \times 10^{33} - 6 \times 10^{34}$ ergs were used in the analysis. Despite the somewhat small statistics, the flare rate distribution in energy over the complete 1.5 orders of magnitude is a power law, with a best-fit index $\alpha \approx 2.2 \pm 0.2$ derived from the method of Crawford et al. (1970). Our value of α is larger than that derived by Collura et al. (1988) for M dwarfs, and also larger than for solar flares (Crosby et al. 1993). However, our index α agrees with new statistics for small-scale solar flares (Krucker & Benz 1998; Porter et al. 1995, but see Shimizu 1995). We note that the available *EUVE* data do not allow for the determination of coronal plasma temperatures. While such information would improve the

estimates of the energy losses, we expect that corrections due to variable temperatures during each flare would only slightly shift the energy scale by a constant factor. Our determination of α slightly exceeds the critical limit of 2, suggesting for both observations that flares could heat a considerable part, if not all, of the observable X-ray/EUV corona. Inclusion of flares down to radiative-energy ranges of $\log E_{\rm min} \approx 30.2^{+1.4}_{-14.6}$ and $31.2^{+0.8}_{-4.8}$, respectively, would provide sufficient heating for the whole corona of each star. Such energies comprise radiative energies of solar flares and microflares. Our observations support the flare-heating hypothesis for these two young solar-like stars during the given observing times *if* the power law continues down to energies of moderate flares. A considerable portion, if not all, of the energy required to heat their coronae could thus be provided by flares.

Chapter 4

Extreme-Ultraviolet Flare Activity in Late-Type Stars

Summary

Extreme Ultraviolet Explorer Deep Survey observations of cool stars (spectral type F to M) have been used to investigate the distribution of coronal flare rates in energy and its relation to activity indicators and rotation parameters. Cumulative and differential flare rate distributions were constructed and fitted with different methods. Power laws are found to approximately describe the distributions. A trend toward flatter distributions for later-type stars is suggested in our sample. Assuming that the power laws continue below the detection limit, we have estimated that the superposition of flares with radiated energies of about $10^{29} - 10^{31}$ ergs could explain the observed radiative power loss of these coronae, while the detected flares are contributing only ≈ 10 %. While the power-law index is not correlated with rotation parameters (rotation period, projected rotational velocity, Rossby number) and only marginally with the X-ray luminosity, the flare occurrence rate is correlated with all of them. The occurrence rate of flares with energies larger than 10^{32} ergs is found to be proportional to the average total stellar X-ray luminosity. Thus, energetic flares occur more often in X-ray bright stars than in X-ray faint stars. The normalized occurrence rate of flares with energies larger than 10^{32} ergs increases with increasing $L_{\rm X}/L_{\rm bol}$ and stays constant for saturated stars. A similar saturation is found below a critical Rossby number. The findings are discussed in terms of simple statistical flare models in an attempt to explain the previously observed trend for higher average coronal temperatures in more active stars. It is concluded that flares can contribute a significant amount of energy to coronal heating in active stars.

The work presented in this chapter has been published in Audard et al. (2000).

4.1 Introduction

Stellar activity of "normal" stars has been explored extensively in the X-ray regime for more than two decades (e.g., Vaiana et al. 1981; Linsky 1985). The chromospheres and coronae of some late-F to M main-sequence stars have been found to show enhanced magnetic activity. The latter is underlined by enhanced activity indicators such as the X-ray luminosity $L_{\rm X}$, its ratio to the bolometric luminosity $L_{\rm X}/L_{\rm bol}$, the presence of flares in the optical U band (and in other wavelength regions), flux variations in chromospheric lines, spots on the stellar surface, etc. A dynamo mechanism is thought to be the primary cause for stellar and solar activity as suggested by the empirical relation between rotation and activity (for a recent review, see Simon 2001). Rotation parameters (such as the rotation period, the Rossby number, or the angular velocity) are therefore prime parameters that determine the stellar activity level.

Stellar rotation was proposed to determine the level of activity of solar-type stars by Kraft (1967). Quantitative relationships between activity indicators and rotation parameters (e.g., Skumanich 1972; Pallavicini et al. 1981; Walter 1982; Noyes et al. 1984; Randich et al. 1996) provide information on the physical origin of stellar activity. In a study of X-ray emission from stars, Pallavicini et al. (1981) found that X-ray luminosities of late-type stars are dependent on the projected rotational velocity but are independent of bolometric luminosity. Walter & Bowyer (1981) and Walter (1981) presented observational evidence that RS CVn systems and G-type stars show a quiescent $L_{\rm X}/L_{\rm bol}$ ratio proportional to their angular velocity. However, in the same series of papers, Walter (1982) proposed that the simplistic view of a power-law dependence should be replaced by either a broken power law or by an exponential dependence of $L_{\rm X}/L_{\rm bol}$ on the angular velocity. This led to the concept of saturation of stellar activity (Vilhu 1984; Vilhu & Walter 1987) at high rotation rate. Noyes et al. (1984) suggested that the Rossby number R_0 (defined as the ratio $P/\tau_{\rm c}$ of the rotation period P and the convective turnover time $\tau_{\rm c}$) mainly determines the surface magnetic activity in lower main-sequence stars. Stępień (1993) showed that, for main-sequence late-type stars, R_0 correlates with activity indicators better than P does.

Flares are direct evidence of magnetic activity in stellar atmospheres. They are also in the center of the debate on the origin of coronal heating. Although several possible heating mechanisms have been identified (e.g., Ionson 1985; Narain & Ulmschneider 1990; Zirker 1993; Haisch & Schmitt 1996), there is increasing evidence that flares act as heating agents of the outer atmospheric layers of stars. A correlation between the apparently non-flaring ("quiescent") coronal X-ray luminosity $L_{\rm X}$ and the stellar time-averaged U-band flare luminosity (Doyle & Butler 1985; Skumanich 1985) suggests that flares can release a sufficient amount of energy to produce the subsequently observed quiescent coronal emission. Robinson et al. (1995, 1999) found evidence for numerous transition region (TR) flares in CN Leo and YZ CMi. Further evidence for dynamic heating has been found in broadened TR emission line profiles (Linsky & Wood 1994; Wood et al. 1996) that were interpreted in terms of a large number of explosive events.

Stellar X-ray and EUV flares have been found to be distributed in energy according to a power

law (see Collura, Pasquini, & Schmitt 1988; Audard, Güdel, & Guinan 1999; Osten & Brown 1999), similar to power laws found for solar flares (e.g, Crosby, Aschwanden, & Dennis 1993). While the differential distribution of flares in energy (see eq. 1.1) is a power law of index α and normalization k_1, the cumulative distribution (for $\alpha > 1$) is a power law of index $\alpha - 1$ and normalization $k_2 = k_1/(\alpha - 1)$ (see eq. 1.2). For $\alpha > 2$, an extrapolation to flare energies below the instrumental detection limit could be sufficient to produce a radiated power equivalent to the X-ray luminosity $L_{\rm X}$ of the quiescent corona (see eq. 1.3). Thus the low-energy part of the flare rate distributions in energy in the Sun and in stars can provide important information (e.g., Hudson 1991). Parker (1988) suggested that the heating of the quiescent solar corona could be explained by "microflares". In the solar context, several estimates of the power-law index have recently been given. For "normal" flares, $\alpha \approx 1.5 - 1.8$ (Crosby et al. 1993); it takes different values for smaller flare energies, from $\alpha \approx 1.6$ for small active-region transient brightenings (Shimizu 1995) to $\alpha = 2.3 - 2.6$ for small events in the quiet solar corona (Krucker & Benz 1998), and other "intermediate" values (e.g., Porter, Fontenla, & Simnett 1995; Aschwanden et al. 2000; Parnell & Jupp 2000). Stellar studies on flare occurrence distributions in X-rays are rare, probably due to the paucity of stellar flare statistics. Using *EXOSAT* data, Collura et al. (1988) found a power-law index α of 1.52 for soft X-ray flares on M dwarfs. Osten & Brown (1999) reported $\alpha = 1.6$ for flares in RS CVn systems observed with *EUVE*. On the other hand, Audard et al. (1999, Chapter 3) found a power-law index $\alpha \approx 2.2 \pm 0.2$ for two young active solar analogs.

In this chapter, we present a flare survey of *EUVE* observations of active late-type main-sequence stars. Together with an investigation of coronal heating by flares, a more general picture of the relation between flares and stellar activity in general is developed. Section 4.2 presents the method for the data selection and reduction, section 4.3 explains the construction of cumulative and differential flare rate distributions in energy. Section 4.4 provides the methodology for fitting the distributions, while section 4.5 explores quantitatively the correlations between various physical parameters. Finally, section 4.6 gives a discussion of the results, together with conclusions.

4.2 Data Selection and Reduction

We use data from the *Extreme Ultraviolet Explorer* (*EUVE*, e.g., Malina & Bowyer 1991) to study the contribution of flares to the observable EUV and X-ray emission from stellar coronae. In order to identify a sufficient number of flares in the *EUVE* Deep Survey (DS) light curves, data sets with more than 5 days of monitoring, or with a significant number of flares (more than ten flares identified by eye) were selected. Active coronal sources were our prime choice, as these stars often show several distinct stochastic events. We have focused our analysis on young, active stars that do not display rotationally modulated light curves and that can be considered as single X-ray sources. Some stars in the sample are detected or known binary systems, in which only one of the components is believed to contribute significantly to the EUV and X-ray emitted radiation. If a star was observed several times (more than a few days apart), we considered the different data sets as originating from different coronal sources, as

Table 4.1: *Target Selection List.*

Source Name (1)	Spectral Type (2)	d (pc) (3)	P (day) (4)	$\mathrm{Ref_1}$ (5)	$v \sin i$ (km $\mathrm{s^{-1}}$) (6)	$\mathrm{Ref_2}$ (7)	$B-V$ (mag) (8)	V (mag) (9)	μ (count $\mathrm{s^{-1}}$) (10)	$\log L_{\mathrm{X}}$ (erg $\mathrm{s^{-1}}$) (11)	*EUVE* Observing Window (12)
HD 2726 ...	F2 V	45.07	...	...	13.2	1	0.367	5.67	0.11	30.47	1995 Aug 9–16
47 Cas.....	G0–5 V	33.56	1.0	1	62.1[a]	...	0.620[a]	... [a]	0.14	30.31	1997 Jan 23–29
EK Dra	G1.5 V	33.94	2.605	2	17.3	2	0.626	7.60	0.08	30.09	1995 Dec 6–13
κ Cet.....	G5 V	9.16	9.4	3	3.9	3	0.681	4.84	0.08	28.98	1994 Oct 13–18
	...	...	...	...	...	...	...	...	0.11	29.10	1995 Oct 6–13
AB Dor	K1 V	14.94	0.515	4	93.0	4	0.830	6.88	0.28	30.05	1994 Nov 12–17
ϵ Eri.....	K2 V	3.22	11.3	5	2.0	3	0.881	3.72	0.30	28.62	1995 Sep 5–13
GJ 411	M2 V	2.55	...	...	< 2.9	5	1.502	7.49	0.02	27.29	1995 Mar 22–Apr 4
AD Leo	M3 V	4.90	2.7	6	6.2	5	1.540	9.43	0.28	28.95	1996 May 3–6
EV Lac.....	M4.5 V	5.05	4.376	7	6.9	5	1.540	10.29	0.16	28.74	1993 Sep 9–13
CN Leo.....	M6 V	2.39	...	...	< 2.9	5	2.000	13.54	0.03	27.38	1994 Dec 16–19
	...	...	...	...	...	...	...	...	0.02	27.27	1995 Jan 24–30

[a] $v \sin i$: estimated equatorial velocity; $B-V$: value set to account for the X-ray star's spectral type; V: no data for X-ray emitter; (see text)
REFERENCES— Rotation period ($\mathrm{Ref_1}$). (1) Güdel, Schmitt, & Benz 1995, (2) Strassmeier, Bartus, & Rodonò 1997, (3) Noyes et al. 1984, (4) Innis et al. 1988, (5) Baliunas et al. 1983, (6) Spiesman & Hawley 1986, (7) Pettersen, Olah, & Sandmann 1992. Projected rotational velocity ($\mathrm{Ref_2}$). (1) Groot, Piters, & van Paradijs 1996, (2) Strassmeier & Rice 1998a, (3) Fekel 1997, (4) Kürster, Schmitt, & Cutispoto 1994, (5) Delfosse et al. 1998.

the activity level of these stars is usually not identical at two different epochs. We carefully checked the DS data and rejected data that presented evident problems, such as "ghost" images in the DS remapped event files, or incursions into the DS "dead spot". The final list contains 12 stellar sources (1 F-type, 4 G-type, 2 K-type, and 5 M-type coronal sources). We do not claim our sample to be complete in any sense. However, this sample is representative of the content of the magnetically active cool main-sequence stellar population in the *EUVE* archive. Table 4.1 gives the name of the stellar source (Col. 1), its spectral type (Col. 2), its distance d in parsecs from Hipparcos (Perryman et al. 1997; except for AD Leo and CN Leo which are from Gliese & Jahreiss 1991; Col. 3), the rotation period P in days together with its reference (Cols. 4 & 5), the projected rotational velocity[1] and its reference (Cols. 6 & 7), the color index[2] $B-V$ and the visual magnitude V from Hipparcos (Perryman et al. 1997; except for AD Leo and CN Leo for which data were retrieved from Simbad; Cols. 8 & 9), the mean DS count rate (Col. 10), the derived (see below) EUV+X-ray (hereafter "coronal") luminosity in the 0.01–10 keV energy range (Col. 11), and the *EUVE* observing window (Col. 12).

We have made extensive use of the data from the *EUVE* archive located at the Multimission Archive at the Space Telescope Science Institute (STScI)[3]. DS Remapped Archive QPOE files were rebuilt using the EUV1.8 package within IRAF[4]. Light curves (Fig. 4.1) were created using a DS background region ten times larger than the source region area. Event lists were extracted from the source region for further analysis. Thanks to the sufficiently large count rates of our sources, the contribution of the DS background was very low, and could be neglected (after a check for its constancy). Also, with our analysis method, flare-only count rates (count rates above the "quiescent" level) were required; therefore the small contribution of the background was eliminated in any case. Event and Good Time Interval (GTI) files were then read and processed with a flare identification code. Audard et al. (1999, Chapter 3) explain in detail the procedure applied to identify flares in the DS event files. In brief, the method, adapted from Robinson et al. (1995), performs a statistical identification of flares. It assigns occurrence probabilities to light-curve bins. Note that several time bin lengths and time origins for the binning are used so that the identification of flares is not dependent on the choice of these parameters. Note also that, due to gaps between GTIs, the effective exposure of a bin had to be taken into account. We refer to Robinson et al. (1995) and Audard et al. (1999, Chapter 3) for more details.

Figures 4.1(a), 4.1(b), and 4.1(c) (upper panels) show background-subtracted *EUVE* DS light curves[5] for our data sets. Only for plotting purposes, the data have been binned to one bin per orbit ($P_{\rm orb} = 96$ min). Note that for our data analysis, we have not restricted ourselves to the

[1] For 47 Cas, the X-ray emitter is the probable, optically hidden G0–5 V companion (Güdel et al. 1998), therefore we have set $B-V = 0.62$. We have estimated the equatorial velocity from the rotation period of the X-ray bright source, from the bolometric luminosity and an effective temperature of $T_{\rm eff} \approx 5900$ K.

[2] See footnote 1 above.

[3] IRAF is distributed by the National Optical Astronomy Observatories (NOAO). STScI and NOAO are operated by the Association of Universities for Research in Astronomy, Inc.

[4] See footnote 3 above.

[5] With task QPBIN of EUV1.8, the last bin of a light-curve plot is generally omitted (D. J. Christian 1999, priv. comm.)

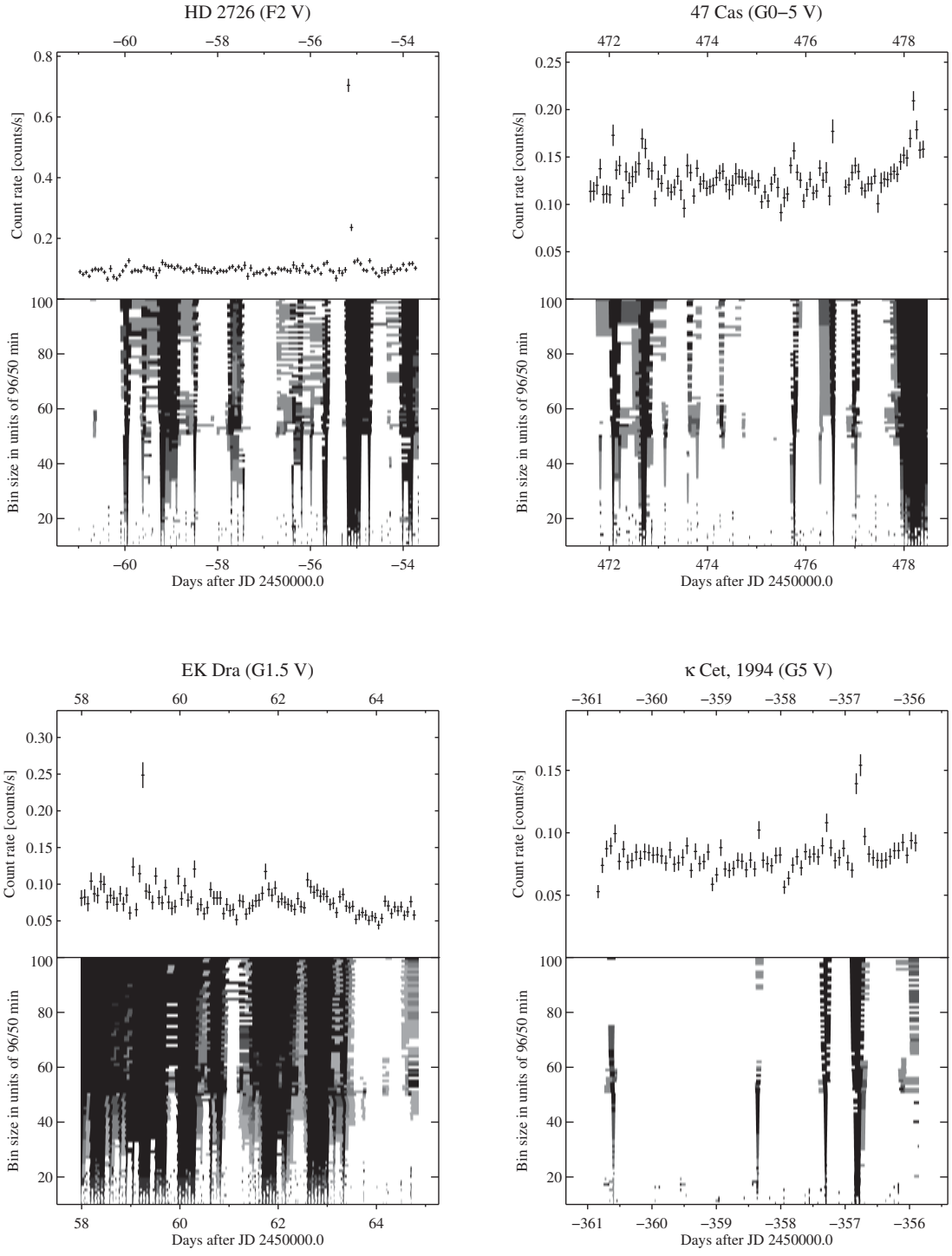

(a)

Figure 4.1: *EUVE DS light curves of the targets and their respective significance plots.*

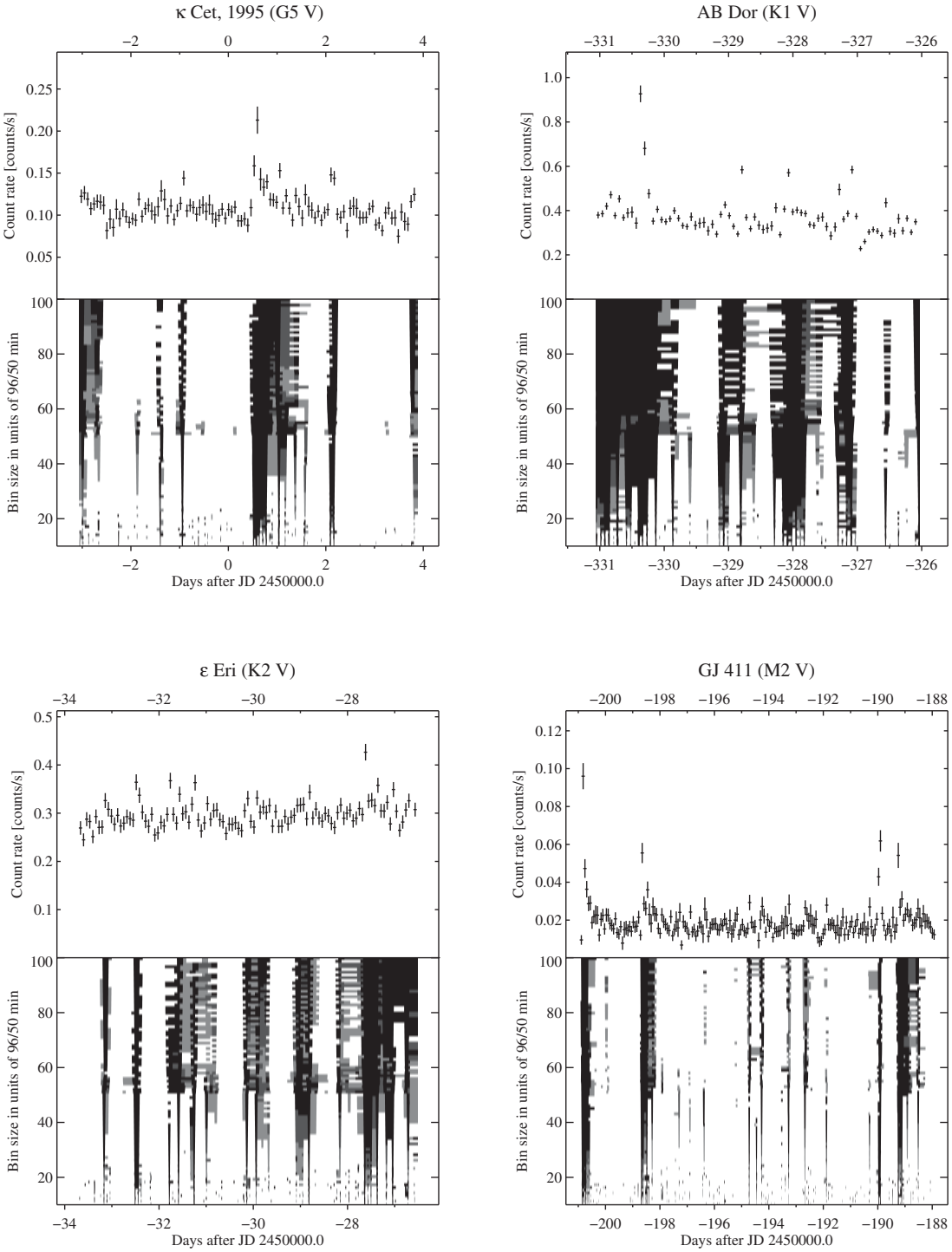

(b)

Figure 4.1: *EUVE DS light curves and their respective significance plots (continued).*

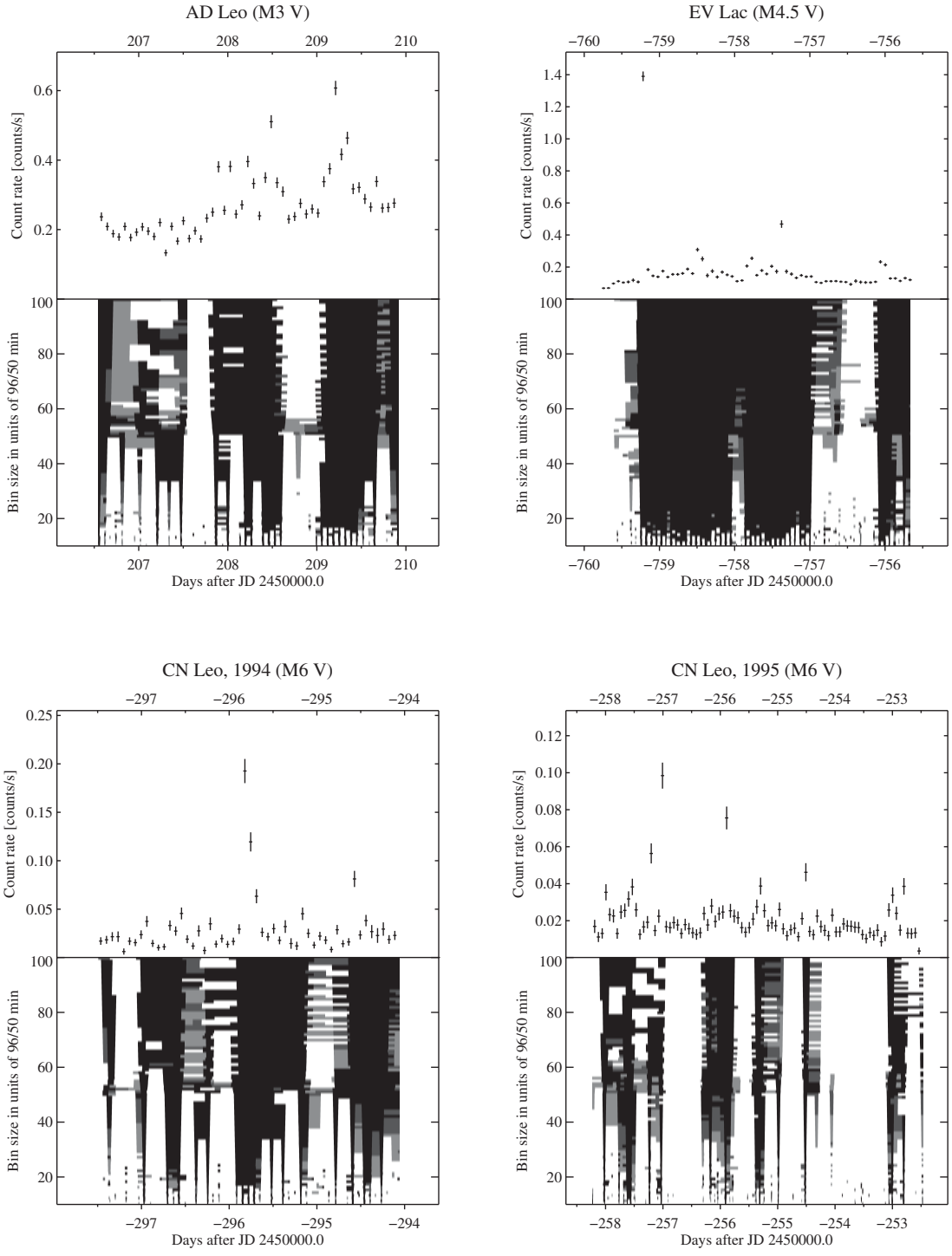

(c)

Figure 4.1: *EUVE DS light curves and their respective significance plots (end).*

above bin size: bin durations from 1/5 to twice the orbital period have been used (see Fig. 4.1). The lower panels show the corresponding "significance plots", which give the probability for the presence of quiescent bins as a function of time (x-axis) and bin size (y-axis). The flare significance increases from light gray to black. Physical parameters (start time, end time and total duration) were determined from smoothed high-resolution light curves, using a Gaussian fit to the flares above a smooth lower envelope characterizing the quiescent contribution. Thus the start and end times of a flare were defined as the times separated from the maximum by $2\,\sigma$, where σ is the standard deviation of the Gaussian function. Within this interval, we calculated a mean flare count rate above the quiescent emission by subtracting the mean background levels just before and after the flare, and multiplied it by the flare total duration to derive the total number of flare counts C. We then used a constant count-to-energy conversion factor ($f = 1.06 \times 10^{27}$ ergs counts^{-1} pc^{-2}) together with the source distance d to derive the total energy E radiated in the EUV and X-rays,

$$E = C \times f \times \left(4\pi d^2\right). \tag{4.1}$$

We derived the conversion factor f from mean DS count rates of archival *EUVE* cool-star data sets and published X-ray luminosities (Pallavicini et al. 1988; van den Oord, Mewe, & Brinkman 1988; Pallavicini, Tagliaferri, & Stella 1990a; Dempsey et al. 1993a,b; Schmitt, Fleming, & Giampapa 1995; Monsignori Fossi et al. 1996; Dempsey et al. 1997; Tagliaferri et al. 1997; Audard et al. 1999; Hünsch et al. 1999; Sciortino et al. 1999). We corrected the published X-ray luminosities to the new, Hipparcos-derived distances (Perryman et al. 1997). Then, using a typical model for young active stars (2-temperature collisional ionization equilibrium MEKAL model [$T_1 = 0.6$ keV, $T_2 = 2.0$ keV] with the iron abundance $\mathrm{Fe} = 0.3$ times the solar photospheric value), we estimated factors to apply to the published luminosities in order to convert them to 0.01–10 keV luminosities. We finally defined the conversion factor f as the mean ratio between the observed fluxes $L_\mathrm{X}/(4\pi d^2)$ and the mean DS count rates μ. Note that for our targets, the corona radiates mostly in the X-ray band ($\approx 0.1 - 5$ keV) rather than in the EUV band.

4.3 Flare Occurrence Rate Distributions

Cumulative flare rate distributions in energy were constructed for each source (Fig. 4.2). Similarly to Audard et al. (1999), we applied a correction to the effective rate of identified flares. For each cumulative distribution, the flare rate at the energy of the second-largest flare was corrected by a factor $D_\mathrm{total}/(D_\mathrm{total} - D_\mathrm{largest})$, where D_total is the total observing time span, and D_largest is the total duration of the largest flare. Analogously, the correction for the third-largest flare took into account the total durations of the largest and second-largest flares, and so on. This correction was necessary since usually more than 50 % of the DS light curves were occupied by identified flares, i.e., it is common for flares to overlap in time.

For each cumulative distribution, we have two series of parameters, namely the flare energy (E_i) and the flare rate at this energy (s_i), with the indices running from 0 (largest-energy flare,

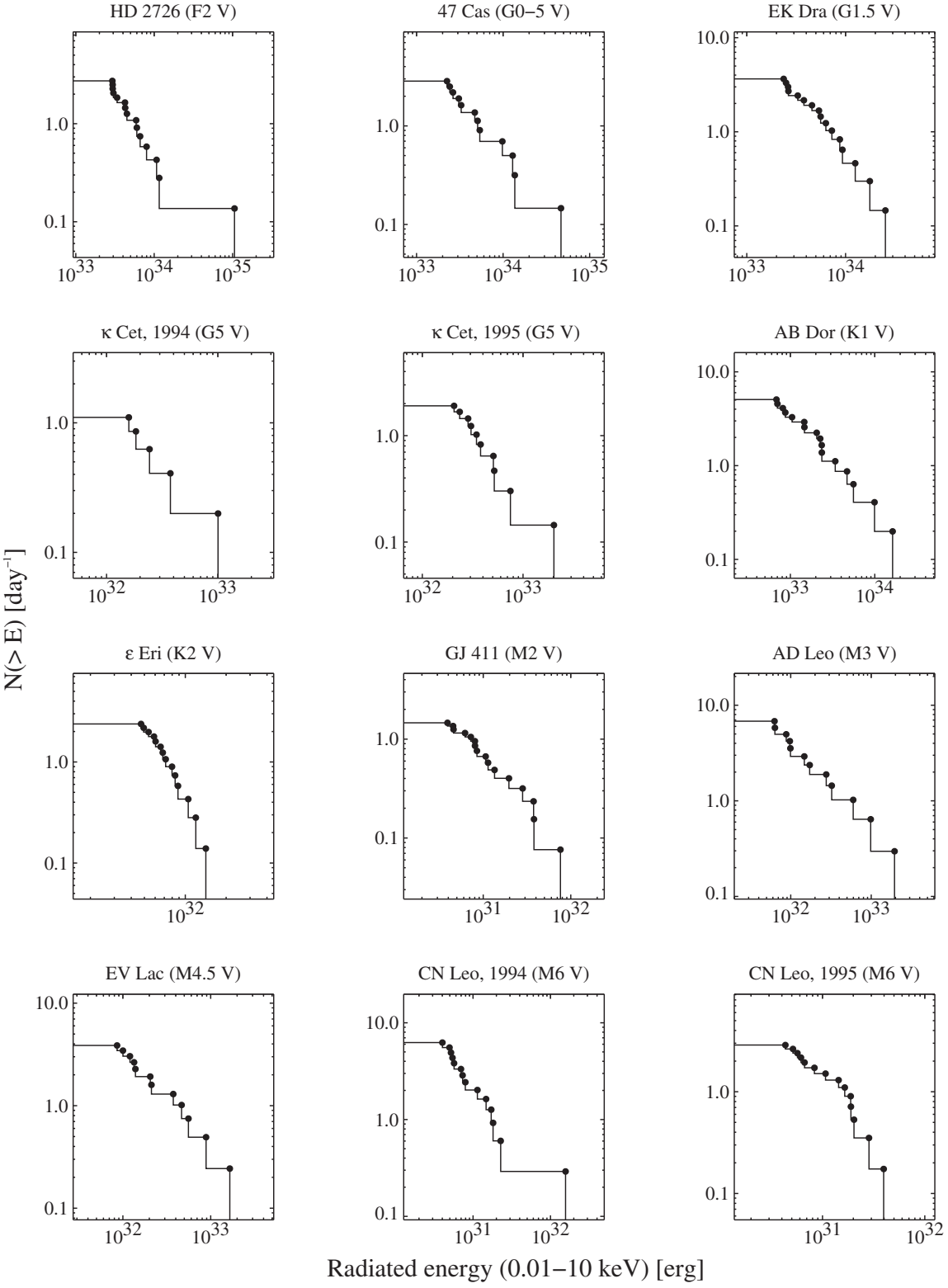

Figure 4.2: *Cumulative flare occurrence rate constructed for all twelve data sets.*

$s_0 = 1/D_{\rm total}$ by definition) to M (lowest-energy flare). The cumulative occurrence rates $N(> E_i)$, i.e., the rate of flares per day with energies exceeding E_i, were defined as

$$N(> E_0) = \frac{1}{D_{\rm total}} = s_0, \tag{4.2a}$$

$$N(> E_i) = N(> E_{i-1}) + s_i, \quad i = 1, \ldots, M. \tag{4.2b}$$

We then constructed differential distributions. For the energy interval $[E_i, E_{i+1}]$, we defined differential flare occurrence rates (n_i) as

$$n_i = \frac{s_i}{E_i - E_{i+1}}, \quad i = 0, \ldots, M-1. \tag{4.3}$$

We calculated uncertainties for the flare occurrence rates per unit energy; we assumed that each number of flares ($s'_i = s_i \times D_{\rm total}$) with energy E_i has an uncertainty $\Delta s'_i$ estimated from a Poisson distribution. This approximation accounts for the larger relative uncertainty ($\Delta s'_i / s'_i$) of the number of detected flares at higher flare energies than at lower flare energies. However, instead of setting $\Delta s'_i = \sqrt{s'_i}$, we have used the approximations proposed by Gehrels (1986), who showed that for small k following a Poisson distribution, the 1 σ upper error bar can be approximated with $1 + (k + 3/4)^{1/2}$, while the the 1 σ lower error bar is still approximated by the usual definition $\sqrt{k}$. Therefore, we have defined $\Delta s'_i$ as the geometrical mean of the upper and lower error bars:

$$\Delta s'_i = \left\{ \sqrt{s'_i} \times \left(1 + \sqrt{s'_i + \tfrac{3}{4}} \right) \right\}^{1/2}. \tag{4.4}$$

It follows that each differential occurrence rate n_i has an uncertainty Δn_i equal to

$$\Delta n_i = \frac{\Delta s'_i / D_{\rm total}}{E_i - E_{i+1}}. \tag{4.5}$$

4.4 Fits to the Distributions

4.4.1 Cumulative Distributions

The power-law fitting procedure to the cumulative flare occurrence rate distributions is adapted from Crawford, Jauncey, & Murdoch (1970). This method is based on a maximum-likelihood (ML) derivation of the best-fit power-law index α. The best-fit normalization factors k_2 (see eq. [1.2]) were then computed; using equation (1.3), the minimum flare energy $E_{\rm min}$ required for the power law to explain the mean observed radiative energy loss ($L_{\rm X}$) was calculated, assuming that the cumulative flare occurrence rate distribution in radiated energy follow the same power law below the flare energy detection limit:

$$E_{\rm min} = \left\{ \frac{L_{\rm X}}{k_2} \left(\frac{\alpha - 2}{\alpha - 1} \right) + E_{\rm max}^{2-\alpha} \right\}^{1/(2-\alpha)}, \tag{4.6}$$

Table 4.2: *Fits To The Flare Rate Distributions in Energy.*

	Cumulative			Differential		Simultaneous	
Name	α[a]	$\log(E_{\rm min})$[d] [ergs]	α[b]	α[c]	Type	α[c]	
HD 2726	2.61 ± 0.38	31.7 (29.7, 32.3)	1.89[e]	2.43 (1.80, 3.93)	F+G	2.28	(2.03, 2.57)
47 Cas	2.19 ± 0.34	29.7 ($\cdots$, 31.6)	1.98	2.62 (1.72, 5.41)	$\cdots$	$\cdots$	
EK Dra.....	2.08 ± 0.34	30.2 ($\cdots$, 32.0)	2.27	1.78 (1.26, 2.49)	$\cdots$	$\cdots$	
κ Cet 1994.....	2.18 ± 0.89	27.2 ($\cdots$, 31.0)	1.90	2.55 (0.31, $\cdots$)	$\cdots$	$\cdots$	
κ Cet 1995.....	2.29 ± 0.51	29.5 ($\cdots$, 31.1)	2.21	2.45 (1.65, 3.80)	$\cdots$	$\cdots$	
AB Dor	1.88 ± 0.26	$\cdots$ ($\cdots$, 28.8)	1.97	1.76 (1.24, 2.72)	K	1.87	(1.50, 2.39)
ϵ Eri	2.40 ± 0.81	29.1 ($\cdots$, 30.7)	2.50	2.38 (1.06, 4.05)	$\cdots$	$\cdots$	
GJ 411	1.63 ± 0.29	$\cdots$ ($\cdots$, $\cdots$)	1.96	1.57 (1.08, 2.22)	M	1.84	(1.63, 2.06)
AD Leo	2.02 ± 0.28	26.2 ($\cdots$, 29.8)	1.85	1.65 (1.18, 2.35)	$\cdots$	$\cdots$	
EV Lac.....	1.76 ± 0.33	$\cdots$ ($\cdots$, 29.1)	1.90	1.75 (0.98, 3.33)	$\cdots$	$\cdots$	
CN Leo 1994 ...	2.21 ± 0.30	29.3 (27.0, 29.8)	1.91	2.24 (1.78, 3.04)	$\cdots$	$\cdots$	
CN Leo 1995 ...	1.46 ± 0.39[f]	$\cdots$ ($\cdots$, $\cdots$)	2.14	1.59 (0.84, 2.56)	$\cdots$	$\cdots$	

[a] From an adapted version of Crawford et al. (1970)
[b] χ^2 linear fit in the $\log - \log$ plane
[c] χ^2 fit within XSPEC with 68 % confidence ranges for a single parameter
[d] Minimum energy $E_{\rm min}$ required for the power law to explain the total observed radiative energy loss; limits are given in parentheses
[e] Influenced by the largest flare energy; $\alpha = 2.43$ if removed
[f] Influenced by the flat low-energy end of the distribution

where the coronal luminosity $L_{\rm X}$ was estimated from μ, the mean DS count rate,

$$L_{\rm X} = \mu \times f \times \left(4\pi d^2\right). \tag{4.7}$$

Columns 2 and 3 of Table 4.2 give the power-law indices α of the cumulative distributions, and the corresponding minimum flare energies $E_{\rm min}$. The best-fit power-law indices α derived from simple linear fits (χ^2 method) in the $\log N(>E) - \log E$ plane have been added for comparison in Column 4.

We find a possible trend for decreasing power-law indices with increasing color indices; sources of spectral type F or G tend to show indices above the critical value of 2, although $\alpha < 2$ is acceptable within the 1 σ confidence range (except for the F star HD 2726). On the other hand, K and M stars show various power-law indices, with $\alpha > 2$ being usually marginally acceptable, although some individual sources show best-fit values above 2. The minimum flare energies $E_{\rm min}$ can be associated with relatively small *stellar* flare energies. In the solar context, however, they correspond to medium-to-large flares ($E \approx 10^{29} - 10^{31}$ ergs).

4.4.2 Differential Distributions

Our cumulative distributions do not account for uncertainties in the flare occurrence rates. Differential distributions allow us to avoid this problem, and they include uncertainties in a natural way (see section 4.3). Therefore, we propose to use this different approach in order to compare the results. The differential distributions were transformed into FITS files and were read into the XSPEC 10.00 software (Arnaud 1996). Due to the characteristics of XSPEC, energy bins were created in which each bin δE_i is defined as the interval between two consecutive flare energies (namely $\delta E_i = [E_{i+1}, E_i]$, $i = 0, \ldots, M-1$). Finally, a power-law fit (implemented in the software, using the χ^2 minimization method) was performed for each distribution. To estimate the uncertainties derived for the index α, confidence ranges for a single parameter were calculated by varying the index α and fitting the distribution until the deviation of χ^2 from its best-fit value reached $\delta\chi^2 = 1.00$. The power-law indices and their corresponding confidence ranges can be found in Col. 5 (Table 4.2). Note that the small "signal-to-noise" of the distributions did not allow us to better determine the confidence ranges. Relative uncertainties of the n_i values were usually larger than 50 %, reaching about 150 % at most. We also note that the values of α derived from fits to the cumulative distributions are similar to those derived from fits to differential distributions; confidence ranges for the second method are, however, larger and originate from the inclusion of uncertainties in the flare rates, together with the small number of detected flares. A strong support for this statement comes from the confidence range derived for κ Cet 1994. Only four energy bins were used, leading to large confidence ranges and an unconstrained upper limit for α.

4.4.2.1 Combined Data Sets

A possible dependence of α with the stellar spectral type has been mentioned above. To test this trend further and also to obtain tighter results for our power-law fits, we have performed *simultaneous* fits to the differential distributions within XSPEC. In brief, all data sets belonging

Table 4.3: *Correlation tests for the power-law index α.*

α versus:	$L_{\rm X}$	$L_{\rm X}/L_{\rm bol}$	P	$v \sin i$	R_0
			Spearman Test[a]		
DG1 ...	0.50 (0.10)	−0.28 (0.38)	0.50 (0.25)	−0.36 (0.38)	0.54 (0.22)
DG2 ...	0.63 (0.03)	−0.34 (0.28)	0.07 (0.88)	0.05 (0.91)	0.18 (0.70)
			Kendall's τ Test[a]		
DG1 ...	0.42 (0.05)	−0.24 (0.27)	0.33 (0.29)	−0.29 (0.32)	0.43 (0.17)
DG2 ...	0.45 (0.04)	−0.33 (0.13)	0.05 (0.88)	0.07 (0.80)	0.14 (0.65)

[a] Spearman's rank-correlation coefficients $r_{\rm S}$ and Kendall's coefficients τ. In parentheses, the two-sided significances of their deviation from zero ($\equiv$no correlation)

to a spectral type (we combined the only F star with the G-type sources) were fitted simultaneously with power laws of identical index α and one normalization factor for each data set. Note that, with this procedure, the confidence range for α is better determined than in the case of individual distribution fits. The implicit hypothesis of this procedure assumes that the coronae of stellar sources within a given spectral class behave similarly, without any influence by age, rotation period, projected stellar velocity, etc. Columns 6 & 7 of Table 4.2 show the result of the simultaneous fits, together with 68.3 % confidence ranges for a single parameter. Again, we find a trend for lower indices at later spectral types, although the significance is marginal at best.

4.5 Correlations with Physical Parameters

We have explored correlations of the best-fit power-law indices α and occurrence rates of flares showing energies larger than a typical energy observed in our data ($E_{\rm c} = 10^{32}$ ergs) with rotation parameters (rotation period P, projected rotational velocity $v \sin i$, Rossby number R_0) and activity indicators (coronal luminosity $L_{\rm X}$, and its ratio $L_{\rm X}/L_{\rm bol}$ to the bolometric luminosity). Two nonparametric rank-correlation tests (Spearman's $r_{\rm S}$ and Kendall's τ; Press et al. 1992) were used. These robust tests allow us to calculate correlation coefficients and to obtain a two-sided (correlation or anticorrelation) significance for the *absence* of correlation. Thus, a low correlation coefficient ($r_{\rm S}$ or τ) can be associated with a high probability that the sample is not correlated. Note that Kendall's τ is more nonparametric than Spearman's $r_{\rm S}$ because it uses only the relative ordering of ranks instead of the numerical difference between ranks (Press et al. 1992). No uncertainty was included in the tests. In Table 4.3, we give the rank-correlation coefficients together with their two-sided significances in parentheses. We

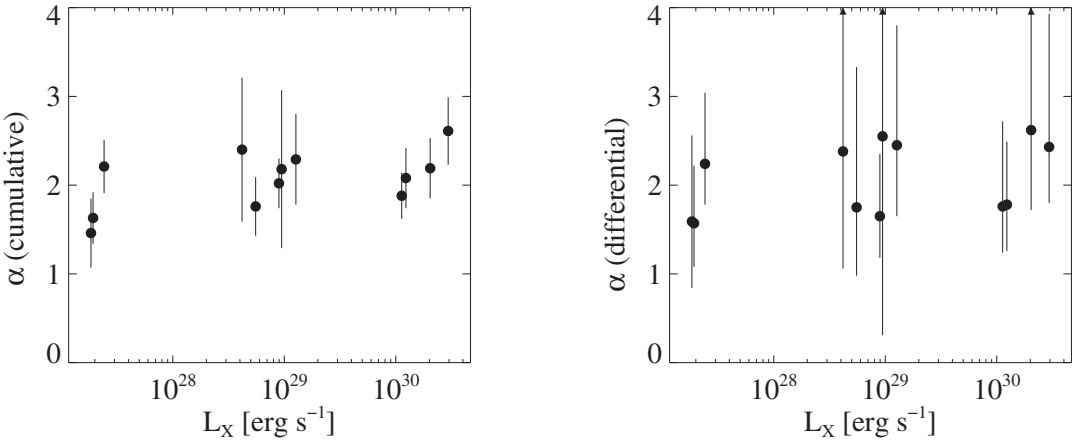

Figure 4.3: *Power-law index α versus coronal luminosity $L_{\rm X}$.*

have defined two data groups for the tests. Power-law indices or flare rates have been derived from ML fits to the cumulative distributions and from fits to the differential distributions, for the first group (DG1) and the second group (DG2), respectively.

4.5.1 Correlations of the Power-Law Index α

4.5.1.1 Coronal Luminosity $L_{\rm X}$

Coronal luminosities (see eq. [4.7]) were used to test their correlation with α (Fig. 4.3). For each data group, the significance levels (Table 4.3) are usually smaller than 5 %, the highest level reaching 10 %. Therefore, placing a limit of 5 % to the two-sided significance level, the correlation between α and $L_{\rm X}$ is marginally significant at best. Such a correlation can be explained as follows. For saturated stars ($L_{\rm X} \approx 10^{-3} L_{\rm bol}$), the X-ray luminosity should decline for stars with spectral type from F to M (hence increasing color index $B-V$) because of the decrease of their bolometric luminosity. In section 4.4.2.1, we have found a suggestion that the power-law index α is weakly correlated with the stellar spectral type. Therefore, a weak correlation of $L_{\rm X}$ with α can be expected. Note that due to the scatter in the $L_{\rm X}/L_{\rm bol}$ ratio in our sample, this can lead to a scatter in the dependence of $L_{\rm X}$ on the spectral type, hence in the dependence of $L_{\rm X}$ on the index α.

4.5.1.2 Ratio $L_{\rm X}/L_{\rm bol}$

We have tested the correlation between $L_{\rm X}/L_{\rm bol}$ and the power-law index. The bolometric luminosities were calculated[6] from parameters in Table 4.1 and corresponding bolometric corrections. Two-sided significance levels (Table 4.3) show that the correlation between $L_{\rm X}/L_{\rm bol}$ and α is not significant.

[6] $\log L_{\rm bol} = \log L_{\rm bol,\odot} + 0.4(M_{\rm bol,\odot} - M_{\rm bol})$, where $M_{\rm bol} = V - (5 \log d - 5) + BC$. Here, $M_{\rm bol,\odot} = 4.64$ mag, $L_{\rm bol,\odot} = 3.85 \times 10^{33}$ erg s^{-1} and BC is taken from Schmidt-Kaler (1982).

4.5.1.3 Rotation Period P

For stars with known rotation periods (Table 4.1), we have tested the correlation between the power-law index α and P. Note that for κ Cet, for which there are two data sets, we have used weighted means[7] of the indices α. Our final sample then comprised 7 data points. From the two-sided significance levels, we can state that no correlation between the power-law index α and the rotation period P is present in our sample (Table 4.3).

4.5.1.4 Projected Rotational Velocity $v \sin i$

Projected rotational velocities from Table 4.1 were used. We used the same procedure as above to calculate the weighted mean of α for κ Cet; for the tests, the upper limits (GJ 411, CN Leo) have been omitted. Our sample then contained 8 data points for each data group. The two-sided significances for the present correlation tests (Table 4.3) imply the absence of a significant correlation between the power-law index α and the projected rotational velocity $v \sin i$ in our data sample.

4.5.1.5 Rossby Number R_0

We have used the available periods in Table 4.1 and have calculated the convective turnover times $\tau_{\rm c}^{(2)}$ (the number 2 refers to the ratio of the mixing length to the scale height) from the $B-V$ color index and equation (4) of Noyes et al. (1984) in order to derive R_0. The nonparametric tests again suggest an insignificant correlation between the index α and the Rossby number.

4.5.2 Correlations of the Flare Occurrence Rate

4.5.2.1 Flare Rate vs. $L_{\rm X}$

Figure 4.4 shows the occurrence rate of flares with energies larger than 10^{32} ergs ($E_{\rm c}$) versus the coronal luminosity $L_{\rm X}$. Quiescent X-ray luminosities (corrected to an energy range between 0.01 and 10 keV) taken from the literature (Collier Cameron et al. 1988; Pallavicini, Tagliaferri, & Stella 1990a; Hünsch, Schmitt, & Voges 1998, 1999) were also used for comparison (crosses), although they were not taken into account in the following tests. The evident correlation between $N(> E_{\rm c})$ and $L_{\rm X}$ is confirmed by Spearman's $r_{\rm S}$ and Kendall's τ tests. The former has rank-correlation coefficients of 0.95 and 0.94, with two-sided significances for deviation from zero of 2×10^{-6} and 4×10^{-6} for DG1 and DG2, respectively. The latter test has coefficients of 0.85 and 0.82, while significances are 1×10^{-4} and 2×10^{-4}. This implies that a correlation between $L_{\rm X}$ and the flare occurrence rate is highly significant for our data sample (Figure 4.4). The linear best-fit in the $\log - \log$ plane for DG1 is $\log N(> E_{\rm c}) = (-26.7 \pm 2.9) + (0.95 \pm 0.10) \log L_{\rm X}$ (number of flares per day), while the best-fit for DG2 was $\log N(> E_{\rm c}) = (-25.5 \pm 2.8) + (0.90 \pm 0.10) \log L_{\rm X}$, hence the relation between the flare rate and the luminosity is compatible with proportionality. Note that, as the

[7] $\alpha = (w_1\alpha_1 + w_2\alpha_2) \,/\, (w_1 + w_2)$, where $w_i = 1/\,(\sigma_{i,{\rm u}}\sigma_{i,{\rm l}})$, and $\sigma_{i,{\rm u}}$ and $\sigma_{i,{\rm l}}$ are upper and lower error bars, respectively. For power-law indices of DG1, we have $\sigma_{i,{\rm u}} = \sigma_{i,{\rm l}} = \sigma_i$.

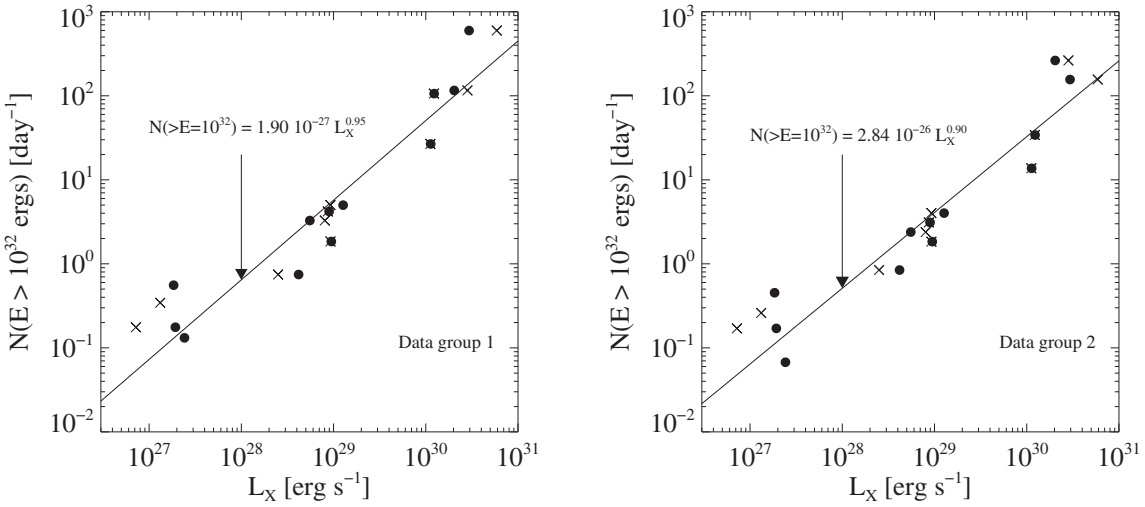

Figure 4.4: *Occurrence rates of flares with energies larger than* 10^{32} *ergs vs. coronal luminosity* $L_{\rm X}$*. Data group 1 corresponds to the rates derived from the fits to cumulative distributions, while data group 2 corresponds to the rates derived from the fits to differential distributions. The* χ^2 *linear best-fits in the* $\log - \log$ *plane are shown as straight lines together with the analytical formulation. Crosses represent* $L_{\rm X}$ *values for these sources taken from the literature (see text).*

correlation between α and $L_{\rm X}$ was marginal at best (section 4.5.1.1), we can safely state that proportionality exists between $L_{\rm X}$ and the normalization factor k_2 (and hence k_1).

4.5.2.2 Normalized Flare Rate vs. $L_{\rm X}/L_{\rm bol}$

The canonical saturation limit for stars with different spectral types has been found to appear at different $v \sin i$ (e.g., Caillault & Helfand 1985; Stauffer et al. 1994; Randich et al. 1996; Stauffer et al. 1997), and therefore, based on the relation of Pallavicini et al. (1981) between $v \sin i$ and $L_{\rm X}$ for unsaturated stars, at different X-ray luminosities. Figure 4.5 shows the coronal luminosity $L_{\rm X}$ against the bolometric luminosity $L_{\rm bol}$. It emphasizes the different loci of our coronal sources with respect to saturation. Note that $L_{\rm X}/L_{\rm bol}$ ratios range from $\approx 10^{-5}$ to $\approx 10^{-3}$. For our correlation tests, we have normalized, for each source, the occurrence rates of flares with energies larger than 10^{32} ergs with the occurrence rate $N(> E_{\rm c})_{\rm sat}$ *at the saturation turn-on for the given spectral type* ($L_{\rm X,sat} = 10^{-3} L_{\rm bol}$) derived from the best-fits to $N(> E_{\rm c})$ vs. $L_{\rm X}$ in the previous section. Thus, we are able to check whether or not the normalized flare occurrence rate stays constant at unity at activity saturation. Figure 4.6 suggests that it does and that the flare rate saturates at activity saturation. In the following sections, we will suggest that this effect is not biased by the absence of stars "beyond" saturation. Note a few discrepant features, such as for 47 Cas (point 2). Its point in DG2 is about 1/2 dex higher than in DG1. Since its index is larger ($\alpha \approx 2.6$) for DG2 than for DG1 ($\alpha \approx 2.2$), and since its minimum observed flare energy is about 10^{33} ergs, it follows that $N(> E_{\rm c})$ is larger for DG2

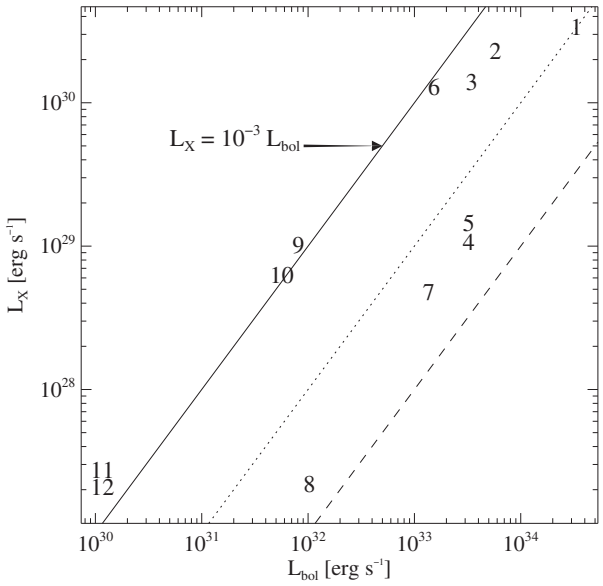

Figure 4.5: *Coronal luminosity $L_{\rm X}$ vs. bolometric luminosity $L_{\rm bol}$. The source identification numbers refer to Table 4.1. The solid line represents the saturation level ($L_{\rm X}/L_{\rm bol} = 10^{-3}$), while the dotted line is for $L_{\rm X}/L_{\rm bol} = 10^{-4}$, and the dashed line for $L_{\rm X}/L_{\rm bol} = 10^{-5}$.*

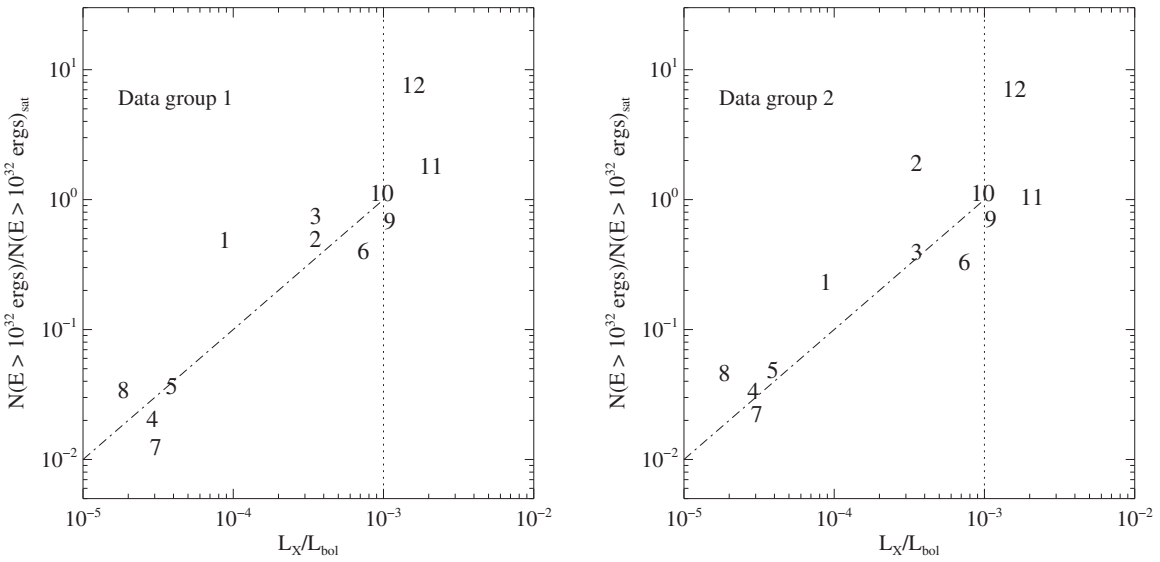

Figure 4.6: *Normalized occurrence rate of flares with energies larger than 10^{32} ergs vs. ratio $L_{\rm X}/L_{\rm bol}$ of the coronal luminosity and the bolometric luminosity. Data groups 1 and 2 are identical to Fig. 4.4. The numbers are as in Fig. 4.5. The dash-dotted lines are lines with slope 1. The dotted lines represent the saturation level ($L_{\rm X} = 10^{-3} L_{\rm bol}$). Note that, for clarity, the $N(> E_{\rm c})$ of points 4 and 9 have been multiplied and divided by a factor of 1.5, respectively.*

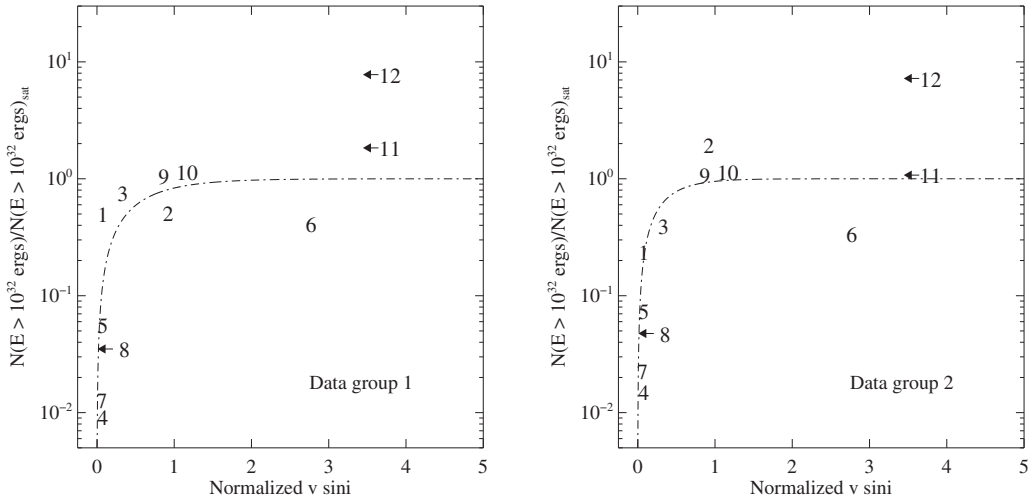

Figure 4.7: *Normalized occurrence rate of flares with energies larger than* 10^{32} *ergs vs. normalized projected rotational velocity* $v \sin i/(v \sin i)_{\rm sat} = x$ *(spectral-type dependent). Data groups 1 and 2 are identical to Fig. 4.4. "Saturation" fits of the form* $1-\exp(-x/\zeta)$ *are plotted dot-dashed. Arrows indicate upper limits. Note that, for clarity, the* $N(> E_{\rm c})$ *of points 4 and 5 have been divided and multiplied by a factor of 1.5, respectively.*

than for DG1. Similarly, CN Leo (points 11 & 12) has two different α indices for the 1994 and 1995 observations ($\alpha \approx 2.2$ and 1.5). This large discrepancy (due to the flat low-energy end of the 1995 distributions) induces different normalized flare occurrence rates.

4.5.2.3 Normalized Flare Rate vs. Normalized $v \sin i$

As before, it was necessary to normalize the flare occurrence rates. In section 4.5.2.2, we have shown that, for our sample, the normalized flare occurrence rate does not show a trend to increase at saturation. However, our sample contains stars "beyond" saturation, i.e., stars that appear saturated ($L_{\rm X}/L_{\rm bol} \approx 10^{-3}$) but that rotate faster than a star at the onset of saturation. Therefore, we have normalized $v \sin i$ with $(v \sin i)_{\rm sat}$, where the latter were obtained from the Pallavicini et al. (1981) relation ($L_{\rm X} = 1.4 \times 10^{27} [v \sin i]^{1.9}$) at the saturation turn-on for each stellar spectral type. Stars at the saturation level thus have normalized velocities around 1, while those beyond that level have values significantly higher than 1 (Fig. 4.7). In our sample, two stars show high values. The first is the bright K1 dwarf AB Dor, and the second is the M6 dwarf CN Leo, although its projected rotational velocity is an upper limit. Hence, AB Dor is the only star that supports the suggestion of constant normalized flare rates at $v \sin i$ saturation. However, in the following section, we will show that the result is also supported by a correlation with the Rossby number R_0, which is less dependent on spectral type. We have performed a fit to the data, assuming a saturation function of the type

$$\frac{N(> E_{\rm c})}{N(> E_{\rm c})_{\rm sat}} = 1 - \exp\left(-\frac{1}{\zeta}\frac{v \sin i}{(v \sin i)_{\rm sat}}\right), \tag{4.8}$$

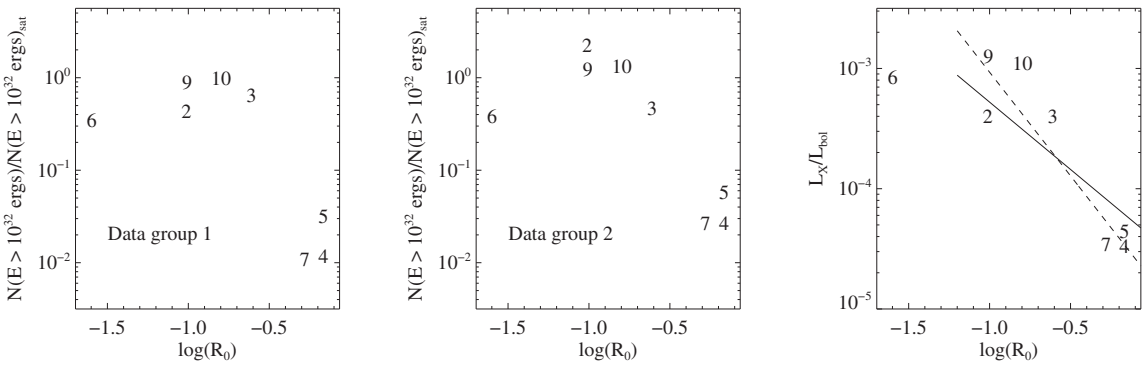

Figure 4.8: *Left and middle panels: Normalized flare rate versus Rossby number. Data groups and identifications are like in Fig. 4.5. Right panel: Ratio $L_{\rm X}/L_{\rm bol}$ versus the Rossby number for our sample. The solid line corresponds to the fit by Randich et al. (1996), while the dashed line refers to our best fit (see text).*

with ζ as the single fit parameter. We derived $\zeta = 0.56$ for DG1, and $\zeta = 0.33$ for DG2. For the fits, we have used the estimated equatorial velocity for 47 Cas, the logarithmically averaged flare rate for κ Cet, and we have not taken into account the upper limits for CN Leo and GJ 411.

4.5.2.4 Normalized Flare Rate vs. R_0

We have further tested the saturation of the flare rate using R_0. Compared to the normalized projected rotational velocity, the Rossby number does not contain the uncertainty due to the projection angle i. Furthermore, it does not need to be normalized as it already corresponds to a normalized rotation period. However, the rotation period is not available for each star of our sample. Figure 4.8 (upper and middle panels) suggests a saturation effect, although again only AB Dor supports it. Also, the $N(> E_{\rm c})/N(> E_{\rm c})_{\rm sat}$ vs. R_0 plots (upper and middle panels) are very similar to the well-known activity saturation relation with the Rossby number (lower panel of Figure 4.8). Similarly to the normalized flare rate saturation, the luminosity saturation appears at $\log R_0 < 1.2$. Both the normalized flare rate and the luminosity decrease above this limit, as previously found for $L_{\rm X}/L_{\rm bol}$ (e.g, Randich et al. 1996; Stauffer et al. 1997). Two lines were overlaid for $\log R_0 \geq 1.2$. The solid line corresponds to the best fit to the data of Randich et al. (1996, $\log L_{\rm X}/L_{\rm bol} = -4.4 - 1.12 \log R_0$), while the dashed line corresponds to our best-fit solution, $\log L_{\rm X}/L_{\rm bol} = (-4.76 \pm 0.30) - (1.72 \pm 0.42) \log R_0$, with the ratios $L_{\rm X}/L_{\rm bol}$ of κ Cet being logarithmically averaged. Our sample follows approximately the Randich et al. relation. Hence, together with the upper and middle panels, the lower panel of Fig. 4.8 reinforces the suggestion that there is a saturation of the flare rate at the activity saturation.

4.5.3 Flare Power vs. $L_{\rm X}$

In Figure 4.9, we have plotted the X-radiated power P_F from the detected flares as a function of the average luminosity $L_{\rm X}$. There is an obvious correlation (Spearman: $r_{\rm S} = 0.93$, $P[r_{\rm S} =$

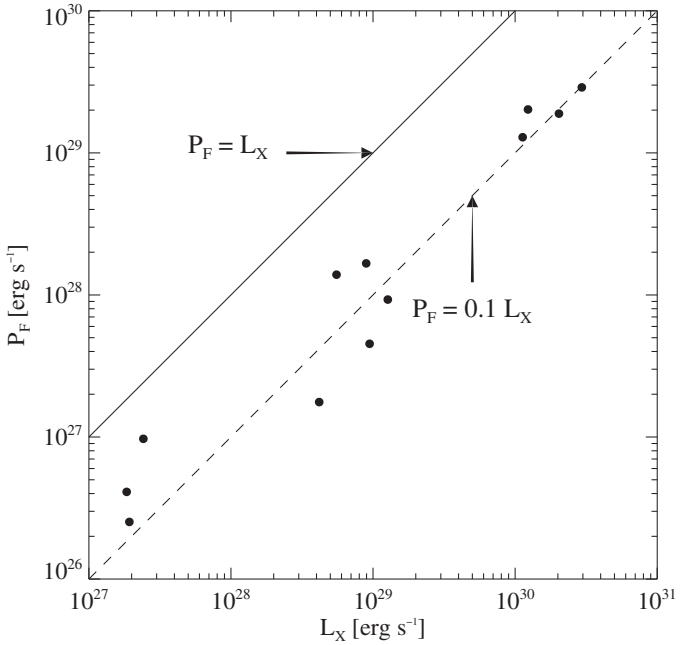

Figure 4.9: *X-radiated power P_F from the detected flares vs. coronal luminosity L_X. The solid line represents proportionality ($P_F = L_X$), while the dashed line is for $P_F = 0.1 L_X$.*

$0] = 1.2 \times 10^{-5}$; Kendall: $\tau = 0.82$, $P[\tau = 0] = 2.1 \times 10^{-4}$) between the parameters. This again demonstrates the importance of the flare contributions to the observed radiation from active coronae. Note that, for our sample and for our flare detection threshold, *about 10 % of the X-ray luminosity originates from detected flares*.

4.6 Discussion and Conclusions

In the present work we have investigated statistical properties of EUV flare events on time scales of days and weeks. Although the sensitivity of the *EUVE* DS instrument is quite limited, it provides long time series that are sufficient to draw rough conclusions on the statistical flare behavior of active stellar coronae.

The first aspect of interest is the distribution of flare energies. In the solar case, X-ray flares are distributed in energy according to a power law with a power-law index around 2 (e.g., Crosby et al. 1993). Many of the active stars studied here are quite different from the present-day Sun, with distinct coronal behavior. For example, high-energy particles are continuously present in their coronae as inferred from their steady gyrosynchrotron emission (e.g., Linsky & Gary 1983; Güdel 1994); quiescent coronal temperatures reach values of 20 MK which are typical on the Sun only in rather strong flares. Individual flare energies accessible and observed by *EUVE* in this study are, in several cases, not observed on the Sun at all. Since a limited amount of magnetic energy is available in the reconnection zones of the coronal magnetic fields, one would even expect some upper threshold to observable flare energies from solar-like stars (and

therefore to the observed flare X-ray radiation).

Our investigation on active main-sequence stars has shown that, for the energy range observed, the flare occurrence rate distributions in energy can be fitted by power laws. We have not found significant evidence for broken power laws that indicate a threshold energy. The largest amount of radiated energy was found to be 10^{35} ergs in our flare sample, exceeding the X-ray output of very large solar flares by two to three orders of magnitude.

Measuring the value of the power-law indices of the distributions is pivotal for assessing the role of flares in coronal heating. The quite limited statistics make conclusions somewhat tentative, although we emphasize the following. The power-law indices definitely cluster around a value of 2; they may be slightly different for different stellar spectral types (Table 4.2). The stellar distributions are thus broadly equivalent to solar distributions, which implies that a) the cause of flare initiation in magnetically very active stars may be similar to the Sun, and b) that the trend continues up to energies at least two orders of magnitude higher than observed on the Sun. We are conversely motivated to extrapolate our distributions to lower energies given the rather large range over which solar flares follow a power law. Caution is in order, however, toward low-energy flares for which the distributions may steepen (Krucker & Benz 1998).

Hudson (1991) argued that, for a power-law index above 2, an extrapolation to small flare energies could explain the radiated power of the solar corona. We derived (eq. [4.6]) the minimum flare energies $E_{\rm min}$ required for the power laws to explain our stellar X-ray luminosities (Table 4.2). For stars with $\alpha > 2$ or just barely below 2, minimum flare energies around $10^{29} - 10^{31}$ ergs were obtained. Such energies correspond to intermediate solar flares. Explicit measurements of flare energies below our detection thresholds will however be required to conclusively estimate their contribution to the overall radiation.

We have found a trend for a flattening of the flare rate distributions in energy toward later spectral types. F and G-type stars tend toward power-law indices > 2, while K and M dwarfs tend toward indices < 2. If supported by further, more sensitive surveys, it suggests that flares play a more dominant role in the heating of F and G-type coronae, while they cannot provide sufficient energy to explain the observed radiation losses in K and M dwarfs. On the other hand, part of this trend could be due to the bias introduced by the identification method and the length of the GTIs. Although not supported by our data, later-type (K and M-type) stars may show flares that are typically shorter than those of G dwarfs, partly because of the smaller distances of the stars that give access to less energetic (and therefore, as on the Sun, typically shorter) flares. But then the flare duration is smaller than the typical GTI gaps (about 3000 s) so that flares that occur between the GTIs remain completely undetected. This effect can considerably flatten the observed flare rate distributions.

Given that our study is restricted to flares with energies typically exceeding $10^{31} - 10^{32}$ ergs, it is little surprising that the observed flare radiation amounts to only a fraction of the total EUV and X-ray losses. We infer an (observed) fraction of approximately 10 % relative to the average (quiescent) coronal luminosity. This lower limit will undoubtedly increase with better instrument sensitivity. Our study therefore clearly indicates that flares provide an important

and significant contribution to the overall heating of active stellar coronae.

We have further explored whether statistical flare properties are correlated with some physical properties of the stars, such as activity indicators and rotation parameters. The power-law index α does not correlate with any of the rotation parameters (P, $v \sin i$, R_0) nor with the ratio $L_{\rm X}/L_{\rm bol}$. The absence of clear correlations suggest that the activity phenomena related to flares are similar on stars of all activity levels. A marginally significant correlation with the coronal luminosity was found. This result is probably related to the trend found for the dependence of α on the stellar spectral type.

On the other hand, the flare occurrence rate above a given lower energy threshold is correlated with each of the activity indicators and rotation parameters. A single power law ($N[> E_{\rm c}] \propto L_{\rm X}$) fits the correlation between flare rate and the coronal luminosity quite well, indicating that energetic flares occur more frequently in X-ray luminous stars than in X-ray weak stars. In order to compare the activity levels between stars of our sample, we have normalized the flare rate to its value that a star adopts at its saturation level. The normalized flare occurrence rate increases with increasing activity but stays constant for saturated stars. Flare rate saturation underlines the close relation between flares and the overall "quiescent" coronal emission. We now ask more specifically whether the apparently quiescent X-ray radiation could be related to the derived flare distributions.

In simple terms, we expect a larger magnetic filling factor on magnetically more active stars, or more numerous (or larger) active regions than on low-activity stars. A higher filling factor naturally implies a proportionally higher quiescent X-ray luminosity and proportionally more numerous flares, so that we expect a linear correlation between $L_{\rm X}$ and the flare rate. But what is the nature of the quiescent emission?

It is known from X-ray observations that the average quiescent coronal temperatures characteristically increase with increasing activity. The concept of an average coronal temperature is, however, somewhat problematic. Schrijver, Mewe, & Walter (1984) used single-T fits to *Einstein*/IPC data that roughly imply that the total stellar volume emission measure in X-rays $\mathrm{EM}_\star$ is proportional to T^3 (as discussed in Jordan & Montesinos 1991). Since the radiative cooling function $\Lambda(T)$ in the range of interest ($3 - 30$ MK) scales approximately like $T^{-\phi}$ with $\phi \approx 0.3$ (Kaastra, Mewe, & Nieuwenhuijzen 1996a), we have for $L_{\rm X}$

$$L_{\rm X} \approx \mathrm{EM}_\star \, \Lambda(T) \propto \mathrm{EM}_\star \, T^{-\phi} \tag{4.9}$$

and hence $L_{\rm X} \propto T^{2.7}$. Considering that the typical coronal emission measure is distributed in temperature, multi-T fits appear to better represent average coronal temperatures. Also, to disentangle functional dependencies from other stellar parameters (e.g., the stellar radius), a uniform sample of stars should be used. Güdel, Guinan, & Skinner (1997b) derived two-temperature models from *ROSAT* data for a sample of stars that differ only in their activity levels but are otherwise analogs to the Sun. For the hotter component, they found $L_{\rm X} \propto T_{\rm hot}^{4.16-5.09}$, the range of the exponent illustrating two different spectral models applied. If, however, we compute the mean of the two temperatures weighted with the corresponding emission measures from their Table 3, we find $L_{\rm X} \propto T^{4.8}$ independent of the spectral model. The two more active

stars for which *ASCA* 3-T fits were available in Güdel et al. (1997b) agree well with this trend (for cooler coronae, *ASCA* is not sufficiently sensitive to derive a coronal emission measure distribution). Note that the 3-T fits in turn represent the derived emission measure distributions in Güdel et al. (1997b) quite well. We therefore conclude that the emission-measure weighted average coronal temperature roughly scales as $L_{\rm X} \propto T^{4.8}$, although with a considerable uncertainty in the exponent.

Hearn (1975) and Jordan et al. (1987) discuss "minimum flux" coronae that follow a relation $\mathrm{EM}_\star \propto T^3 g_\star$ where $g_\star$ is the stellar surface gravity. In a similar way, Rosner, Tucker, & Vaiana (1978) find scaling laws for closed static magnetic loops that relate external heating, loop pressure, loop-top temperature, and loop length. The two scaling laws combine to

$$\dot{E}_{\rm H} \propto \frac{T^{21/6}}{L^2} \tag{4.10}$$

where $\dot{E}_{\rm H}$ is the heating rate, T is the (dominating) loop-top temperature, and L is the loop length. Schrijver et al. (1984), based on these scaling laws, conclude that different families of loops must be present on active stars. In either case, explaining the locus of the measured (T, $\mathrm{EM}_\star$) on the empirical relation requires an explanation for a specific amount of heating energy input to the system. Our investigation suggests that flare events contribute significantly to the observed overall emission. If the concept of a truly quiescent radiation is abandoned completely for magnetically active stars, then we may ask whether flares themselves can explain the observed relation between $\mathrm{EM}_\star$ and T while at the same time accounting for the proportionality between flare rate and $L_{\rm X}$. We briefly discuss two extreme cases:

i) *Filling factor-related activity.* We first assume that flares are statistically independent and occur at many different, unrelated flare sites. The quiescent emission in this case is the superposition of all flare light curves. The proportionality between flare rate and $L_{\rm X}$ is simply due to more numerous flare loops on stars with higher magnetic filling factors (and hence higher activity), in which the explosive energy releases build up the observed loop emission measure. We ask whether the statistical flare distribution determines the average coronal temperature as well.

From our flare samples, we have found that the flare duration does not obviously depend on the flare energy (as typically found for impulsive flares on the Sun; Crosby et al. 1993). We therefore first assume one fixed time constant for all flares. For example, radiatively decaying flares with a similar evolution of coronal densities, abundances and temperatures show similar decay time scales. In this case, the *single flare peak* luminosity $\mathcal{L}_{\rm X}$ is proportional to the total radiated flare energy E. Further, for solar (and stellar) flares, a rough relation between *peak* emission measure EM and *peak* temperature T has been reported by Feldman, Laming, & Doschek (1995). For the interesting range between $5-30$ MK, the relation can be approximated by

$$\mathrm{EM} = aT^b \quad [\mathrm{cm}^{-3}] \tag{4.11}$$

with $a \approx 10^{12}$ cm^{-3}, $b \approx 5 \pm 1$, and T measured in K. We approximate the flare contribution to the radiative losses by the values around flare peak. For the flare radiative losses, we have,

equivalent to equation (4.9),

$$\mathcal{L}_{\rm X} \approx {\rm EM}\ \Lambda(T) \propto {\rm EM}\ T^{-\phi} \tag{4.12}$$

again with $\phi \approx 0.3$ over the temperature range of interest. With equations (4.11) and (4.12), we obtain

$$E \propto \mathcal{L}_{\rm X} \propto T^{b-\phi}. \tag{4.13}$$

To derive a characteristic, emission-measure weighted, time-averaged mean coronal temperature $\overline{T}$, we average over all flare temperatures $[T_{\rm s}, T_0]$ by using their peak EM and their occurrence rates as weights:

$$\overline{T} = \frac{\int_{T_{\rm s}}^{T_0} T\ {\rm EM(T)}\ dN/dE\ dE/dT\ dT}{\int_{T_{\rm s}}^{T_0} {\rm EM(T)}\ dN/dE\ dE/dT\ dT}. \tag{4.14}$$

Here, $T_{\rm s}$ represents the typical temperature of the smallest contributing flares. From equations (4.11)–(4.14), we obtain

$$\overline{T} = \frac{z}{z+1}\ T_0\ \frac{1-(T_{\rm s}/T_0)^{z+1}}{1-(T_{\rm s}/T_0)^{z}} \tag{4.15}$$

where

$$z = (2-\alpha)b - (1-\alpha)\phi. \tag{4.16}$$

Without loss of generality, we assume $T_{\rm s} = 1$ MK. The upper temperature limit T_0 corresponds to the largest flare energy E_0 typically contributing to the apparently quiescent emission. Since the flare rate is given by the power law (eq. [1.1]), the characteristic value for E_0 scales like $k_1^{1/\alpha}$, i.e., with equation (4.13), $T_0 \propto k_1^{1/(\alpha(b-\phi))}$. The normalization factor k_1 is proportional to the overall stellar X-ray luminosity $L_{\rm X}$ for given α. The steepest dependence of $\overline{T}$ on k_1 is obtained in the limit of small α, i.e., $z > 0$, so that $\alpha < (2b-\phi)/(b-\phi)$, implying $\alpha \lesssim 2.1$. Then, for $T_0 \gg T_{\rm s}$, we find $\overline{T} \propto T_0$, i.e., $L_{\rm X} \propto \overline{T}^{\beta}$ with $\beta = \alpha(b-\phi)$. For reasonable values of $\alpha = 1.5 - 2.1$, we find $\beta \approx 5.5 - 12$, i.e., a dependence that is at least somewhat steeper than observed.

We can repeat the derivation under the assumption of some dependence between flare energy E and duration D. Typically, larger flares last longer. The function $D(T) = D(E[T])$ should then be used as an additional weighting factor in equation (4.14). Assuming that $D \propto E^{1/2}$ (e.g., in the case of an energy-independent "flare curve shape"), we find $E \propto \mathcal{L}_{\rm X}^2$. In that case, equation (4.15) remains valid, while $z = (4-2\alpha)b - (3-2\alpha)\phi$ and $L_{\rm X} \propto \overline{T}^{\beta}$ with $\beta = 2\alpha(b-\phi)$ for "small" α, hence a steeper dependence on $\overline{T}$ than for the first case.

ii) *Loop reheating.* In the other extreme case, the flares repeatedly reheat the same coronal plasma in certain "active" loop systems (e.g., Kopp & Poletto 1993). In that case, for most

of the time the coronal loops fulfill a quasi-static approximation equivalent to the loop scaling law given by Rosner et al. (1978) (see Jakimiec et al. 1992). The situation is equivalent to steadily heated loops. The first scaling law of Rosner et al. (1978), $T_{\max} \propto (pL)^{1/3}$, implies EM $\propto T^4$ and hence $L_{\rm X} \propto T^{3.7}$ for a given loop length with T in the range of interest. For loops exceeding the coronal pressure scale height, Schrijver et al. (1984) give an expression EM $\propto T^5$ (with other parameters fixed), and hence $L_{\rm X} \propto T^{4.7}$. In this limit, we attribute the higher temperatures of more active stars to higher reheating rates in a similar number of loops rather than to a larger number of statistically independent heating events in more numerous active regions or loops. The cause of an enhanced reheating rate on more active stars in a similar number of loop systems remains to be explained, however.

Comparing the observed average coronal temperatures with the two extreme results, we see that the observed trend lies in the middle between the extreme values. Flare heating is thus a viable candidate to explain the trends seen in $L_{\rm X}$ and in T, although it is not conclusive whether flares occur independently or whether they act as reheating agents of coronal loops. It appears unlikely that either extreme is appropriate. While a larger magnetic filling factor on more active stars undoubtedly produces more numerous active regions and thus a higher flare rate, the higher coronal filling factor is also likely to lead to more numerous reheating events. This is compatible with the observed trend between $L_{\rm X}$ and $\overline{T}$.

This study has shown that flares can provide a significant amount of energy to heat the coronae of active stars. Although the definite answer to which mechanism is responsible for coronal heating is not yet available, our data sample suggests that flares are promising contributors. Better sensitivity together with uninterrupted observations (such as those provided by the new generation of X-ray satellites *XMM-Newton* and *Chandra*) will be needed to solve part of the mystery. Our method is limited to flares explicitly detectable in the light curves. Alternative methods are available that model light curves based on statistical models. These investigations are the subject of a forthcoming paper (Kashyap et al. 2002).

Chapter 5

Extreme Ultraviolet and X-Ray Flare Statistics for AD Leo

Summary

In this chapter, we present tentative results from an ongoing investigation of the EUV and X-ray flare rate distribution in radiated energy of the late-type active star AD Leo. We have obtained long exposures on AD Leo from the *EUVE* and *BeppoSAX* satellites. Numerous flares have been detected, ranging over almost two orders of magnitude in their radiated energy. We have compared the observed light curves with light curves synthesized from model flares that are distributed in energy according to a power law with selectable index α. Two methods are applied, the first comparing flux distributions of the binned data, and the second using the distributions of photon arrival time differences in the unbinned data (for *EUVE*). Subsets of the light curves are tested individually, and the quiescent flux has optionally been treated as a superposition of flares from the same flare distribution. We find acceptable α values between $2.1 - 2.5$ for the different data sets. Some variation is found depending on whether or not a strong and long-lasting flare occurring in the *EUVE* data is included. Further, the *BeppoSAX* MECS data result in a somewhat harder energy distribution than the simultaneously observed LECS data, which is attributed to the harder range of sensitivity of the MECS detector and the increasing peak temperatures of flares with increasing total (radiative) energy. The results suggest that flares can play an important role in the energy release of this active corona.

5.1 Introduction

The physics of coronal heating remains one of the most fundamental problems in stellar (and solar) astrophysics. The subject has been reviewed extensively from the point of view of theoretical concepts (e.g., Ionson 1985; Zirker 1993), observational solar physics (e.g., Benz & Güdel 1994), and stellar physics (e.g., Haisch & Schmitt 1996). It is somewhat surprising that

The work presented in this chapter has been published in Güdel et al. (2002a).

the nature of the "coronal heating mechanism(s)" still eludes agreement given high-resolution imaging of solar coronal structures or large statistical samples of stellar coronal X-ray observations. For example, there is no unequivocal agreement on whether all, or any, of the X-ray coronal energy detected from certain classes of stars is magnetic in origin.

The flare heating hypothesis has gained momentum in particular from solar, but also from stellar observations during recent years. If the quasi-steady ("quiescent") coronal emission is to be explained by flare contributions, flares must act as statistical heating agents. Parker (1988) proposed that shuffling of magnetic field footpoints in the photosphere by the convective motions leads to tangled magnetic field lines in the corona and thus current sheets. With increasing winding of magnetic fields, the necessary energy may be transported into the coronal magnetic field where it is released by sudden relaxation involving reconnection. Parker estimates that energy dissipation occurs in packets involving $10^{24} - 10^{25}$ ergs ("nanoflares"). The flare-heating hypothesis resolves to the basic question of whether or not the *statistical ensemble* of flares (in time and energy) suffices to heat the apparently non-flaring coronae.

In statistical flare studies, the identification of weak flares close to the apparently quiescent emission level becomes an ill-defined problem (see Chapter 4). Explicit detection methods discriminate against small flares due to overlap with larger flares, confusion between the many approximately simultaneous small flares, or short detection times above the significance level (Hudson et al. 1969; Audard et al. 2000). Limited signal-to-noise ratios add to the problem. These complications can be overcome to some extent by fully modeling the superposition of a statistical ensemble of flares. We do so in the present chapter, applying two different methods.

5.2 Data Selection and Reduction

Our target for the present investigation is the nearby dMe star AD Leo. AD Leo is a well-studied flare star with a high flare rate. Its spectral class is M3 V, and its X-ray luminosity amounts to $\log L_{\rm X} = 28.95$ [erg s^{-1}]. We use a distance of $d = 4.90$ pc (see Chapter 4 for further details on the target, and for references). Its quiescent count rates in the *EUVE* DS, the *BeppoSAX* LECS and MECS used here are, respectively, ≈0.15, 0.125, and 0.025 cts s^{-1}.

The *Extreme Ultraviolet Explorer* data presented here were obtained in several segments between 1999 April 2 and 1999 May 15, see Table 5.1. For our method 1 (see below) in which we used binned data, we applied primbsching and deadtime corrections to all data sets, and excluded time intervals for which the combined correction factors exceeded 30%. To avoid fluctuations that may still occur within one satellite orbit window due to residual inaccuracies in these corrections (e.g., the due to the South Atlantic Anomaly), we decided to generally bin data to one bin per orbit (5663 s), which turns out to be sufficient to recognize all flares, to resolve them in time, and to provide a good signal-to-noise ratio per bin. The light curve is shown in Figure 5.1. The last time interval (see Table 5.1) suffered from high radiation. This segment was *not* used in the subsequent analysis (by any of the methods). The final data set used for method 1 contained 470 bins.

Table 5.1: *Observing Log (1999 April/May)*

Instrument	from UT	to UT MM/DD hh:mm	HJD range MM/DD hh:mm	-2400000.5
I	*EUVE*	04/02 16:09	04/04 04:54	11270.673–11272.204
II	*EUVE*	04/05 00:46	04/14 16:41	11273.032–11282.695
III	*EUVE*	04/17 03:32	04/24 09:27	11285.147–11292.394
IV	*EUVE*	04/25 16:29	05/04 11:41	11293.687–11302.487
V	*EUVE*	05/06 16:41	05/16 05:11	11304.695–11314.216
I	*BeppoSAX*	05/01 06:34	05/03 04:48	11299.274–11301.200
II	*BeppoSAX*	05/08 05:47	05/10 13:10	11306.241–11308.549
III	*BeppoSAX*	05/12 08:39	05/15 15:05	11310.360–11313.628

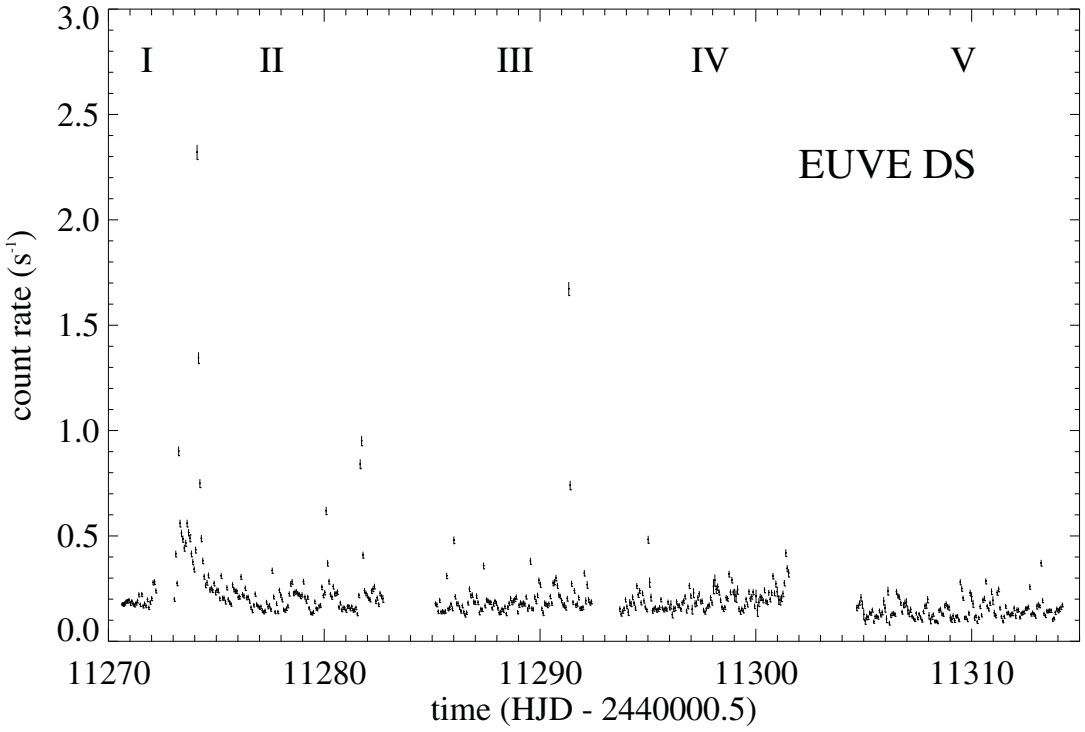

Figure 5.1: *EUVE DS light curve of AD Leo (before primbsching and dead time corrections), obtained between April 2, 1999, and May 16, 1999. Segment V suffers from "dead spot" reduction in effective area and from high radiation. The* 1σ *error bars are typically* ± 0.01 *ct* s^{-1} *and have been plotted.*

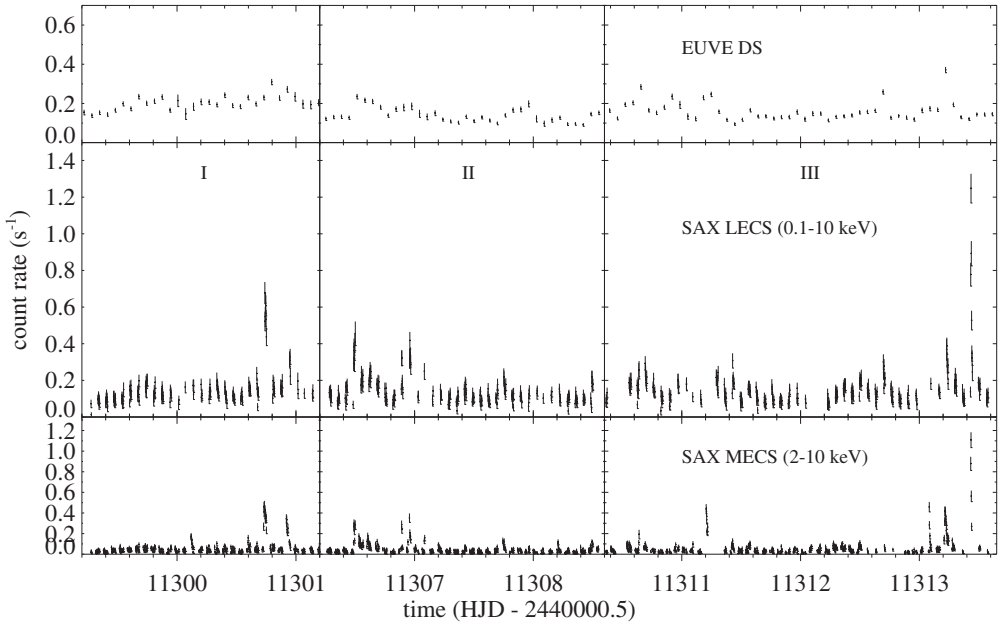

Figure 5.2: *BeppoSAX MECS and LECS light curves, compared with simultaneous EUVE DS data. Roman numerals refer to the BeppoSAX segments (see Table 5.1).*

The *BeppoSAX* satellite (Boella et al. 1997a) pointed its Low and Medium Energy Concentrator Systems (LECS and MECS, respectively; Parmar et al. 1997; Boella et al. 1997b) and its Phoswich Detector System (PDS; Frontera et al. 1997) towards AD Leo three times (Table 5.1), spanning a total time of 15 days for 270 ksec of exposure time. Most of the observations were performed simultaneously with the *EUVE* observations. No significant signal was detected in the HXR instrument PDS, even during flares. The three different pointings were similar, allowing us to merge the individual data sets into single LECS and MECS data sets. The cleaned and linearized event files from LECS and MECS23 (MECS2 and MECS3 combined file) from the SAX Science Data Center pipeline processing were filtered with the good time intervals that exclude the events occurring while there was no attitude solution. The data were binned using a bin size of 200 s. This resulted in a total of 658 bins for the LECS light curve, and 1363 bins for the MECS light curve. The MECS has more bins since it observed somewhat longer during each orbit, and it suffered from fewer bad time intervals during the on-source observations. The light curves of all three segments are shown in Figure 5.2.

Average quiescent spectra were extracted for LECS and MECS, excluding obvious large flares (but still including small flares as, in our working hypothesis, there is no strict difference between flaring and non-flaring emission). The source was extracted inside circular regions of radius $8.17'$ and $4'$ for LECS and MECS, respectively. Blank sky pointings were used to model the instrumental and sky X-ray backgrounds. We checked the *local* background with two semi-annular regions for LECS (see Parmar et al. 1999 for full details) and two regions perpendicular

Table 5.2: *Fit to the Quiescent BeppoSAX data*

kT_1 (keV)	kT_2 (keV)	kT_3 (keV)	$EM_1/10^{50}$ (cm^{-3})	$EM_2/10^{50}$ (cm^{-3})	$EM_3/10^{50}$ (cm^{-3})
0.18 ± 0.01	0.68 ± 0.01	1.80 ± 0.08	5.4 ± 0.4	13.6 ± 0.4	4.5 ± 0.2
	$\log N_{\mathrm{H}}^{\mathrm{a}}$ (cm^{-2})	Fe[b]	f[c]	χ^2/dof	
	$= 18.0$	0.54 ± 0.03	0.69 ± 0.03	315.48/261	

[a] Fixed value
[b] Abundance relative to the solar photospheric value (Anders & Grevesse 1989)
[c] Effective-area cross-calibration factor LECS/MECS23

to the on-board calibration sources for MECS. We found that the blank-sky backgrounds are suitable for our data. We used the LEMAT tool in SAXDAS 2.0.1 to create LECS response matrices, and the provided standard MECS responses (September 1997). Finally, the data were grouped with a minimum of 25 counts per bin. Data from 0.12 to 4 keV were kept for the LECS spectrum, while data from 1.65 to 10.5 keV were kept for the MECS23 spectrum (see Fiore, Guainazzi, & Grandi 1999). We fitted the combined spectra in XSPEC (Arnaud 1996) using several isothermal collisionally ionized equilibrium plasmas with a fixed interstellar hydrogen absorption column density $N_{\mathrm{H}} = 10^{18}$ cm^{-2} (Sciortino et al. 1999). We also introduced a free constant factor to the LECS spectrum to account for cross-calibration discrepancies in the overall effective areas. Finally, we left the Fe abundance free while we kept the other abundances at solar photospheric values. A 3-T model provided a reasonable fit (Table 5.2).

5.3 Analysis

We analyzed the calibrated and cleaned data using two different methods. The first method is applied to *binned* data with sufficient time resolution to recognize flare light curves while keeping the signal-to-noise ratio sufficiently high. The flux distributions are compared with distributions of simulated model light curves using equivalent binning. The second approach analyses the statistical distribution of photon arrival times specifically for the *EUVE* data for which we have performed the corresponding instrumental modeling.

5.3.1 Method 1: Count Rate Distributions

We compare the count rate distributions of the light curves with simulated data sets composed of a statistical flare distribution. We first calculate a statistical power-law distribution of flare energies (equation 1.1) specified by three free parameters: the total number of flares during the simulation time (flare rate C_f), the power-law index α, and a lower cut-off energy E_{min}. The

flares, initially defined as delta functions, are randomly distributed in time within a model light curve of about ten times longer than the binned *EUVE* and *BeppoSAX*/LECS light curves and about 4 times longer than the MECS light curve, i.e., we compare the observation with about ten (resp. four) statistical realizations of a simulation of equal length. This model light curve is then convolved with a flare decay profile $\tau = 3600$ s. Experiments with a profile that was half as wide for the LECS and the MECS data showed that the results are quite insensitive to the precise profile shape.

All bins of the model and observed light curves are then sorted, in order of increasing count rate C to obtain a cumulative flux distribution $\mathcal{N}(> C)$ (number of bins with a count rate exceeding a given C, where we normalize $\mathcal{N}$ by the total number of bins, i.e., $0 \leq \mathcal{N} \leq 1$; see Fig. 5.3). Since the two distributions are not mutually normalized in their count rates, we renormalize the model distribution such that the average flux within a range $[\mathcal{N}_1, \mathcal{N}_2]$ is the same as the average flux in the corresponding $\mathcal{N}$ range of the observed distribution. Since the low-flux end of the flux distribution is too sensitive to statistical fluctuations from the superposition of numerous weak flares, and since the relative errors are largest in that range, we have kept the final normalization interval above zero, namely at $[\mathcal{N}_1, \mathcal{N}_2] = [0.1, 0.5]$, and we do not further consider the portion at $\mathcal{N} < 0.2$ (< 0.1 for LECS/MECS).

We then measure the largest vertical distance between the two cumulative distributions as a function of the power-law index α and the flare rate C_f during the simulation and minimize this distance by varying the two parameters. Tentative best-fit values for α and C_f are then obtained from the 2-D maps. For error ranges, we refer to method 2.

We have used two realizations of our analysis for the *EUVE* data that show a well-developed quiescent emission. First, we applied it to the data from which the (constant) quiescent level was subtracted. In this case, we test whether we can find a model distribution that is compatible with the *observed* flare emission. Second, we applied the method to the complete data including the quiescent emission. Since the latter, in our model, should be the superposition of unresolved small flares, the addition of a quiescent level simply corresponds to the extrapolation of the power law to lower energies, and we expect that the power-law index does not significantly change. This second realization also allows us to derive the lower cut-off energy required to explain the quiescent emission. The comparison between the two realizations could potentially reveal a basic difference between quiescent and flaring emission. If the flare energy distribution does not steadily continue toward more numerous small flares that eventually merge with the quiescent level, then the first realization would be subject to a cut-off energy possibly above the quiescent level (bi-modal flux distribution), and the derived values for α may differ. These two extreme cases will further be discussed below. We verified the results by subtracting approximately 50% of the quiescent level, and the results were indeed found in between the extreme cases. The contrast between flares and the quiescent emission is much larger in the *BeppoSAX* data; we treated only the complete data sets in these cases.

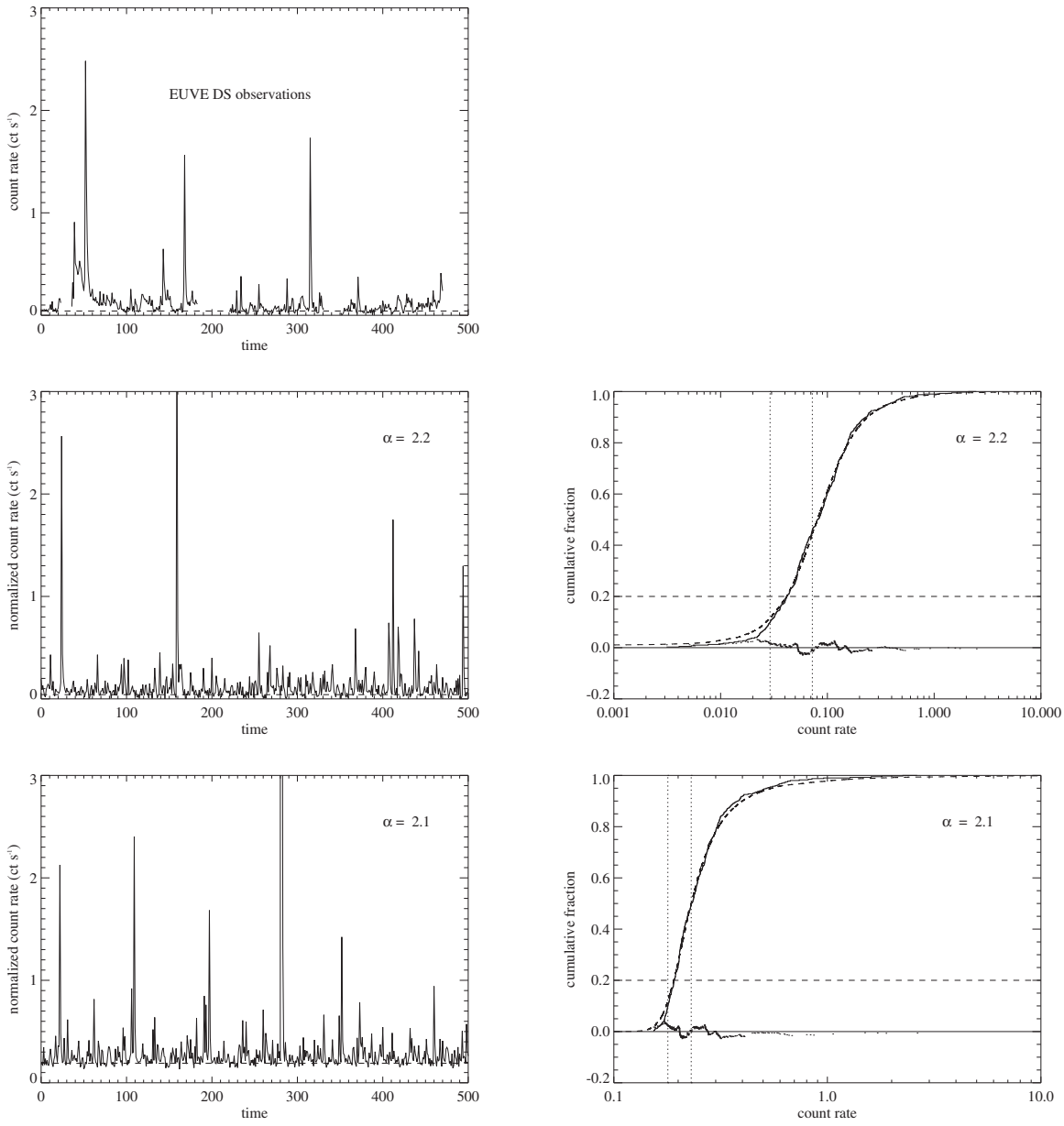

Figure 5.3: *Examples of statistical flare simulations from method 1 for different power-law distributions. Left column gives the observed EUVE DS light curve (top) and simulated light curve (extract, normalized). Right column gives cumulative flux distribution for data (solid) and model (dashed), and the difference (dotted, around the zero line). The maximum difference (vertical bar) is measured; the count rate and power-law index are adapted to minimize this vertical distance. The two vertical dotted lines mark the interval for the model flux normalization. The horizontal dashed line marks the flux level above which the discrepancies between observation and model were considered.* **Middle figures:** *Only the emission that exceeds the quiescent level has been modeled; the optimum case ($\alpha = 2.2$) is shown.* **Bottom figures:** *In this figure, all emission, including the quiescent emission, has been modeled. The optimum case ($\alpha = 2.1$) is shown.*

5.3.2 Method 2: Analysis of Photon Arrival Time Differences

The basis of the method (Kashyap et al. 2002) is that, as count rates rise and fall with flaring activity, the intervals between photon arrival times decrease and increase according to the Poisson distribution appropriate for the count rate at any given moment. These changes in the arrival time differences (δt) cast a signature on the photon event list that changes according to the nature of the underlying source variability. Thus, for a given observation, the observed distribution $f(\delta t)$ summarizes the character of the variability of the source during that observation. A fixed flare distribution (equation 1.1) gives rise to a definite $f(\delta t)$ provided that the observation is of sufficient duration to contain a representative range of intensities, and different flare distributions will give rise to different arrival-time difference distributions. The power-law index, α, that best describes the observed light curve is determined by comparing the observed arrival time difference distribution $f_{\rm obs}(\delta t)$, with simulated distributions $f_{\rm sim}(\delta t)$.

We assume here that the observed light curves can be described by the sum of a flaring component, with a power-law frequency distribution of flare energies as described by equation 1.1, and a constant component. The flaring and constant components are described by the flare rate C_f, and a "quiescent background" rate C_b. As for the first method, the flares are assumed to be impulsive events whose count rates decay exponentially with a time scale of a few thousand seconds. For specified values of C_f and C_b, a synthetic light curve corresponding to the entire interval covered by the observed light curve can then be realized through a Monte Carlo algorithm, assuming a random distribution of flares in time but subject to the power-law frequency distribution of total energies. This light curve is then windowed by the observed photon event "good time intervals" and a synthetic event list is derived through a Poisson realization of the resulting light curve. The synthetic event list is then pruned by discarding photons at a rate corresponding to the observed Primbsch factor. The remaining set is identical in its "instrumental characteristics" to the observed data and the observed and synthetic event lists can be compared directly.

Observed photon arrival time differences are compared to those synthesized across a grid of the parameters α, C_f and C_b using the χ^2 statistic to compare $f_{\rm sim}(\delta t)$ with $f_{\rm obs}(\delta t)$. A number of simulations (typically ≈ 10) are carried out and the median value among the resulting χ^2 are used to compute the likelihood of obtaining the observed data for the given set of parameters $\{\alpha, C_f, C_b\}$. In the case of AD Leo, we have examined each of the three *EUVE* observation segments II, III, and IV independently (Table 5.1), treating them as three different observations, as well as treating the whole sequence at once. This enabled us to examine the degree of consistency of our derivation of α from segment to segment.

5.4 Results

5.4.1 The Power-Law Indices

The following systematics are evident (Table 5.3): (i) In all cases, we find best-fit values for α exclusively above 2, typically $2.1 \leq \alpha \leq 2.6$ for the DS and LECS data and $2.1 \leq \alpha \leq 2.3$

Table 5.3: *α values for AD Leo from method 1; Minimum model flare energies and fluxes*[a]

Data set, segment	bin size (s)	α	Minimum flare counts	Minimum flare energy (erg)	Minimum peak luminosity (erg s^{-1})	Detection limit flare energy (erg)	Detection limit peak luminosity (erg s^{-1})
DS I–IV[b]	5663	$\approx$2.2	62	1.7×10^{31}	5.8×10^{27}	3×10^{31}	1×10^{28}
DS I–IV[c]	5663	2.3–2.6	60	1.7×10^{31}	5.5×10^{27}	3×10^{31}	1×10^{28}
DS I–IV[d]	5663	$\approx$2.1	0.5	1.4×10^{29}	4.8×10^{25}	3×10^{31}	1×10^{28}
DS I–IV[e]	5663	2.2–2.4	3.5	9.6×10^{29}	3.2×10^{26}	3×10^{31}	1×10^{28}
LECS I–III	200	2.3–2.6	0.8	3.8×10^{29}	1.0×10^{27}	1.4×10^{31}	4×10^{28}
MECS I–III	200	2.1–2.3	0.4	1.1×10^{30}	2.9×10^{27}	3.6×10^{31}	1×10^{29}

[a] For given time bin size and for the optimum case; minimum flare counts/energy/peak luminosity refer to smallest flares used in the simulation with optimum KS test result. Detection limit refers to 3σ peak flux for the respective bin size.
[b] Quiescent level subtracted, all data
[c] Quiescent level subtracted, large flare excluded
[d] Quiescent flux included, all data included
[e] Quiescent flux included, large flare excluded

Table 5.4: *α values for AD Leo from method 2(DS)*

Segment DS	Most probable α	95% Confidence Interval
II	2.07	2.00–2.13
III	2.22	2.11–2.31
IV	2.25	2.13–2.30
II–IV	2.19	2.14–2.23

for the MECS data. The width of the acceptable range is ± 0.1. Exclusion of the large flare in the DS light curve softens the distribution by $\Delta\alpha \approx 0.1$, an effect that is to be understood as follows: The presence of a large flare will tend to give a smaller α because comparatively less power will be contained in smaller flare events. Conversely, the selective elimination of the population of the strongest flares softens the distribution although a genuine single power law cannot be retained if too large a fraction of the distribution is eliminated. We therefore put less faith in these distributions, but note that the distribution derived from the LECS observation (which did not cover the large flare) is very similar. The MECS range appears to be systematically harder than the LECS range although this trend is marginally significant ($\Delta\alpha \approx 0.1-0.2$; see next section).

The results from the second method, based on photon arrival statistics, are illustrated in Figures 5.4a−5.4d, where the derived probabilities of power-law indices α matching the observed index are plotted as a function of α. The results are also summarized in Table 5.4. The first three figures illustrate the derived probabilities for three segments treated separately, while the fourth shows the results of the analysis of the whole data set treated as a single observation. The important feature of all these figures is that the most probable value of α is again always greater than 2 but less than 2.3, based on the 95% confidence intervals. The first segment appears to have an optimum index that is slightly lower than that of the last two segments. This is caused by the large flare, which contains a fraction of the total observed counts in that segment which is significant for the variability analysis (see above). The 95% confidence intervals for the last two segments are remarkably similar, indicating $2.1 \leq \alpha \leq 2.3$. The most probable value of α based on all three segments (Figure 5.4d) is $\alpha = 2.2$. The values found here are thus in excellent agreement with results from the first method.

5.4.2 The Minimum Flare Energies and Quiescent Emission

A lower cut-off to the flare energies is required if $\alpha \geq 2$. The cut-off does not imply that lower-energetic flares do not exist. But it implies that their occurrence rate cannot follow the extrapolation of the power law found at higher energies but must be considerably smaller, effectively introducing a cut-off below which flares contribute little. Our simulated model light curves were calculated assuming such an energy cut-off. We determined the cut-off energy

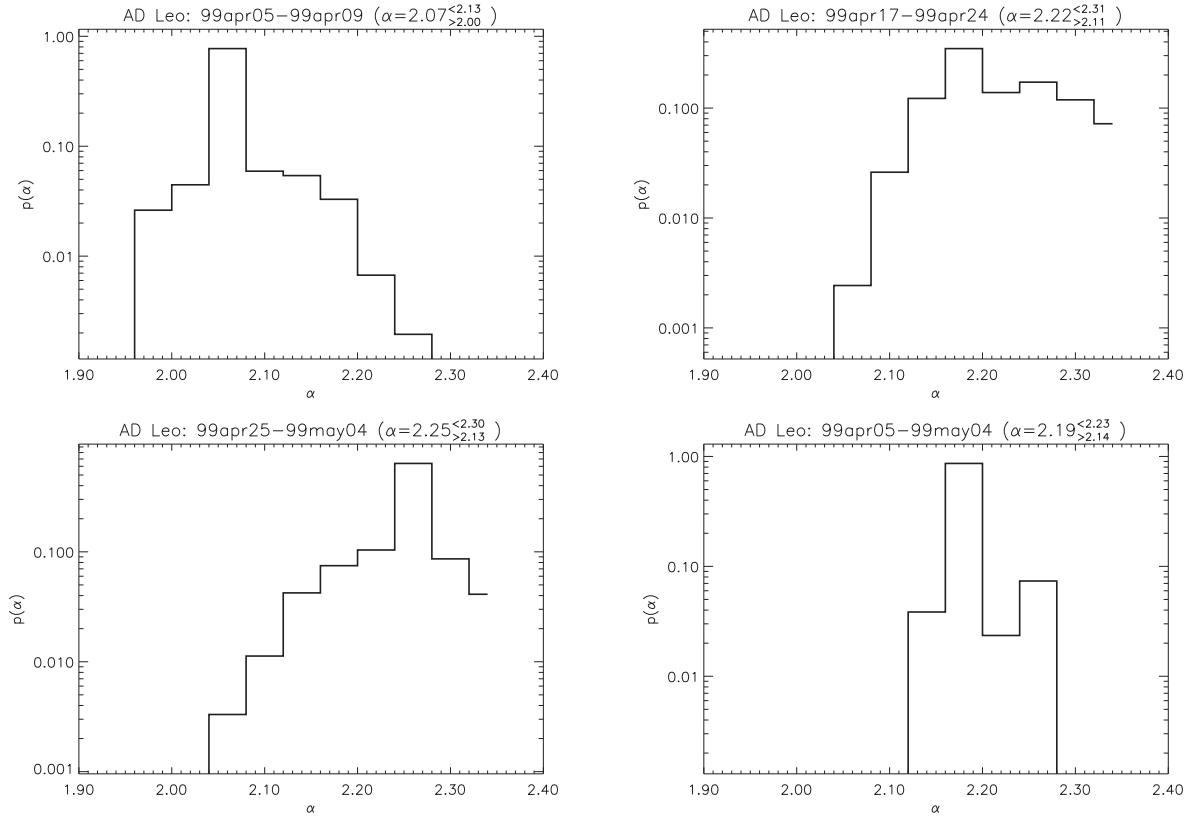

Figure 5.4: *The derived probability of the power-law index α matching that of the EUVE DS observations of AD Leo based on the cumulative distributions of photon arrival time differences (method 2). The most probable value of α corresponds to the peak value of each distribution and is printed together with the corresponding 95% confidence intervals at the top of each figure. From top to bottom: a) Segment II, including the large flare. b) Segment III. c) Segment IV. d) Segments II-IV combined.*

after renormalization and thus found the minimum number of counts of any of the simulated flares. The values are reported in Table 5.3, column 4, and range from $\approx 10^{29} - 10^{31}$ ergs. We computed the count-to-energy conversion factor of 2.78×10^{29} erg ct^{-1} for the *EUVE* DS, to 4.76×10^{29} erg ct^{-1} for the *BeppoSAX* LECS, and to 2.55×10^{30} erg ct^{-1} for the MECS, based on a 3-temperature model (reported in Table 5.2) determined from the LECS and MECS data by spectral fitting of the quiescent emission. From this, we obtain the minimum energy of flares used for the simulation, as shown in column 5 of Table 5.3. In other words, extrapolating the power-law distribution of flares down to the reported energies is necessary and sufficient to explain the complete observed quiescent flux. The LECS provides a lower limit of 3.8×10^{29} ergs. For the derived flare time profile, this energy corresponds to a peak flux of approximately 1.0×10^{27} erg s^{-1} in the combined X-ray and EUV ranges. Such flares correspond to small solar flares. Similar values hold for the MECS and DS data (Table 5.3, columns 5 and 6).

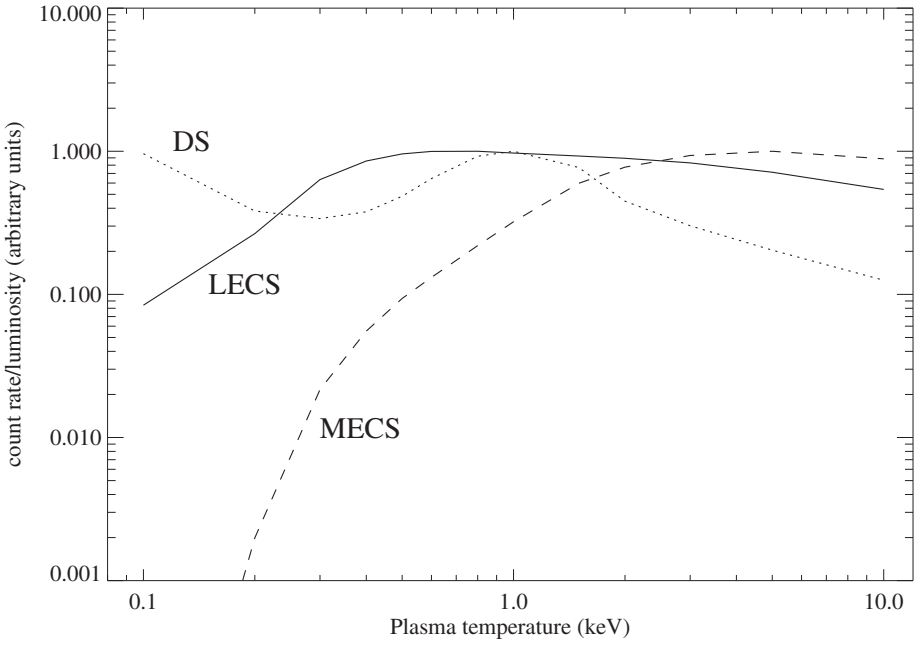

Figure 5.5: *Efficiency (count rate/luminosity) as a function of (isothermal) plasma temperature for the EUVE DS, and the BeppoSAX LECS and MECS detectors (arbitrarily normalized).*

We note that the actually *detected* flares typically exceed these levels by ≈2 orders of magnitude. A small flare reaching a peak count rate 3σ above its pre-flare level corresponds to 3×10^{31} ergs in the DS, 1.4×10^{31} ergs in the LECS, and 3.6×10^{31} ergs in the MECS (Table 5.3, column 7). The apparently quiescent level is thus composed of flares between the cut-off limit and the above 3σ count rate detection limits. In terms of peak luminosity, this interval covers the $\sim 5 \times 10^{25} - 10^{29}$ erg s^{-1} range (see Table 5.3, columns 6 and 8, for details). Assuming an average radiative loss function (radiative energy loss per unit EM) of 2×10^{-23} erg cm^3 s^{-1} (appropriate for $T = 5 - 40$ MK) we find that the peak EMs of these flares are approximately $2.4 \times 10^{48} - 5 \times 10^{50}$ cm^{-3} for the DS quiescent level, $5 \times 10^{49} - 2 \times 10^{51}$ cm^{-3} for the LECS quiescent level, and $1.5 \times 10^{50} - 5 \times 10^{51}$ cm^{-3} for the MECS quiescent level. From Figure 2 of Feldman et al. (1995) we estimate that the peak temperatures of these flares are 15–30 MK for the DS, 25–33 MK for the LECS, and 27–37 MK for the MECS (after Aschwanden 1999, these temperatures are smaller by a factor of ~ 1.5). If we consider that most of the flares in the power-law distribution are close to the lower end of the temperature intervals, we see that most of the LECS quiescent level is primarily composed of flares that reach no more than about 20 MK at peak but mostly reside at lower temperatures. The MECS effective area shows a steep gradient below 25−30 MK, thus most of the LECS quiescent emission is suppressed in the MECS, explaining the large contrast between flares and quiescent emission in the *BeppoSAX* MECS detector. This leads to an apparent small systematic shift of the MECS results relative to those from LECS, by approximately $\Delta\alpha = 0.1 - 0.2$ to lower α, i.e., the MECS distribution is somewhat harder. We thus recognize the MECS result as biased by detector

properties. As far as the DS results are concerned, they agree well with the LECS results which is consistent with the relatively flat efficiency curve (ratio between observed count rate and incident flux) of the DS (Fig. 5.5).

One may extend this analysis to solar HXR data that have traditionally been used as a diagnostic of the total flare energy release (Lin et al. 1984). If the production of hard X-rays is more efficient in strong flares (the "Big Flare Syndrome", Kahler 1982), then hard X-ray flare energy distributions are shallower than those constructed from soft X-ray or EUV data.

5.5 Conclusions

We have investigated the role of statistical flares in coronal heating of magnetically active stars. Long observations of AD Leo were obtained in order to maximize flare statistics. Flares have been suspected to play an important role in coronal energy release and subsequent impulsive heating of chromospheric material to high temperatures. Chromospheric evaporation induced by chromospheric overpressure lifts the hot plasma into the corona where it fills closed magnetic loops. Since (solar) flares are always related not only to an increase in emission measure but to a significant increase in the average plasma temperature, they are natural candidates to heat perhaps all of the detected coronal plasma. Recent progress in solar physics (Krucker & Benz 1998; Aschwanden et al. 2000; Parnell & Jupp 2000) has added new momentum to this hypothesis.

We have studied the distribution of EUV and X-ray flares in energy, seeking power laws of the form $dN/dE = kE^{-\alpha}$ where k is the normalization of the distribution and α determines the steepness of the distribution. We have applied two methods, one based on the flux distribution of binned data, and the second related to the arrival-time difference distribution of the original photon lists (only for *EUVE*). Despite the fundamentally different approaches, the results of both methods are in excellent agreement for the *EUVE* data and indicate $\alpha = 2.1-2.5$. Simultaneous X-ray observations obtained with *BeppoSAX* LECS and MECS were treated with the first method and again agree with the *EUVE* results, namely $\alpha = 2.1 - 2.6$. These values are compatible with the findings of Audard et al. (2000, Chapter 4) who applied a flare-identification algorithm to explicitly record flares and to measure their energies. At first sight, our α values support a model in which the complete coronae are heated by a statistical distribution of flares, involving flares with energies down to a few times 10^{29} ergs (of radiated energy).

We conclude this chapter by emphasizing two observational circumstances: i) It may be pivotal in which energy range relevant for coronal losses the observations are made. Observations that exclusively record the harder part of soft X-rays selectively favor detections of large flares and suppress the relevance of low-energy flares. ii) The power-law distribution may depend on the flare energy range considered. There are indications in solar observations to this effect, and we can safely state that the power laws found here cannot be extrapolated to arbitrary energies: There must be a low-energy break (possibly changing to a harder distribution) in order to confine the total radiated power, and there must be a high-energy limit, corresponding to the largest physically possible flares.

Part II

High-Resolution X-Ray Spectroscopy

X-ray astronomy has received new momentum with the advent of the new X-ray observatories *XMM-Newton* and *Chandra* at the eve of the second millennium. The combination of the large effective areas and the high-resolution spectroscopic capabilities of the new devices has provided high-quality spectra from many astronomical objects. In the field of stellar coronae, these spectra have given access to direct measurements of the temperature structure, the densities, and the elemental abundances of the coronal plasma.

This part of the thesis concentrates on the investigation of stellar coronae by means of high-resolution X-ray spectra obtained in the early phases of the *XMM-Newton* satellite. In Chapter 6, results from the spectroscopic investigation of a flare in the RS CVn binary HR 1099 are presented. In Chapter 7, the analysis of the bright X-ray spectrum of Capella is discussed. Apart from the derivation of the emission measure distribution, of coronal abundances and plasma densities, we show that numerous L-shell lines from minor species are missing in the atomic codes. The investigation of the quiescent and flaring spectra of the rapidly rotating AB Doradus is presented in Chapter 8. The coronal structure of the Castor sextuplet has been investigated (Chapter 9); Castor AB has for the first time been clearly resolved, and a coronal map of the Castor C (YY Gem) binary system has been derived by means of eclipse modeling. Chapter 10 presents results from an investigation of the elemental composition of the coronae of solar analogs and RS CVn binary systems.

Chapter 6

Flare Heating in the Coronae of HR 1099

Summary

The RS CVn system HR 1099 was observed by *XMM-Newton* for a time span of 25 days during the commissioning phase. Rotational modulation in the RGS light curve has been detected with maximum flux when the active K1 IV star is in front. Following a quiescent phase of emission, the rise and peak of a large flare were observed. Time-dependent spectroscopy has been performed to derive elemental abundances and their variations during the various stages of the flare. Emission measure distributions have been reconstructed. Two different components are detected: a very hot plasma (up to 100 MK) that evolves rapidly, and a stable quiescent plasma. Low first-ionization-potential elemental (such as Fe and Si) abundances increase significantly during the flare, while the abundance of the high-FIP element Ne stays constant at the quiescent value. We report direct detection of a flux increase in the Fe XXIV X-ray lines during a stellar flare.

6.1 Introduction

Flares are frequently observed on magnetically active stars from the radio to the X-ray regime. Sudden reconfiguration of the magnetic field through reconnection is believed to release magnetic energy. In a standard model, coronal electrons are accelerated; part of these electrons collide in the dense chromospheric layer of the stellar atmosphere, producing non-thermal hard X-ray emission (e.g., Dennis 1985). Energy dissipation in the dense layers produces heating of chromospheric material: neutral or already partially ionized material is further ionized. The pressure increases and coronal loops become filled with hot material (chromospheric evaporation; see Antonucci, Gabriel, & Dennis 1984). Radiative cooling occurs mainly through various bound-bound electronic transitions of elements such as Fe, Si, S, Ne, C, N, O, Mg, etc, and continuum emission composed of a superposition of two-photon processes, free-bound emission and thermal bremsstrahlung (free-free emission). The emission lines allow us to derive

The work presented in this chapter has been published in Audard et al. (2001a).

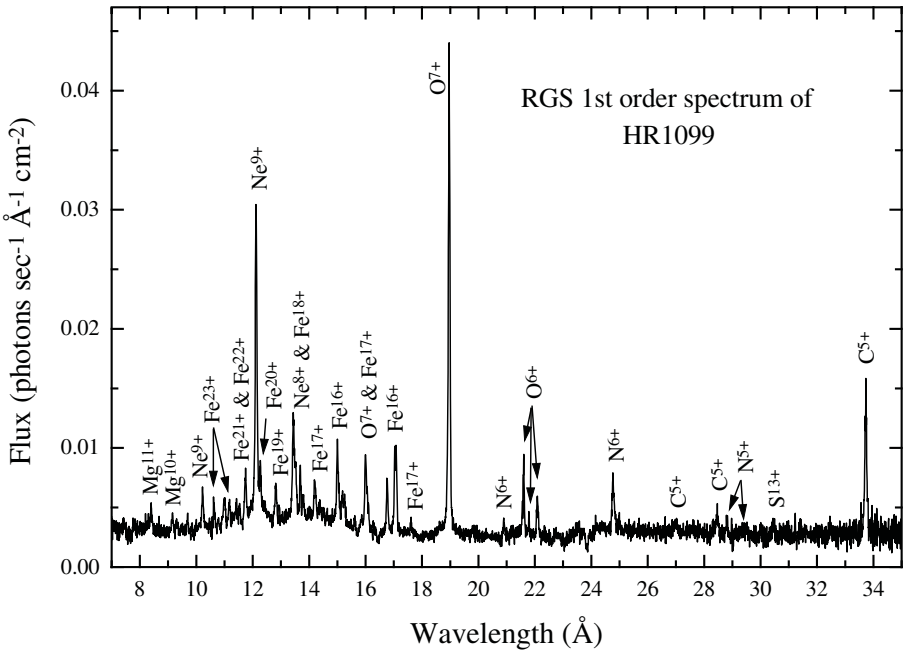

Figure 6.1: *First order spectrum of HR 1099 as measured by the RGS instruments on board XMM-Newton. The most prominent spectral features are indicated just above the spectrum by the corresponding emitting ion. From Brinkman et al. (2001).*

several plasma properties, such as the distribution of emission measure (EM) as a function of plasma temperature, elemental abundances, or average electron densities (see Mewe 1999).

Flares are of central importance to coronal heating. Large flares can display very high temperatures (e.g., Pallavicini & Tagliaferri 1998). Tsuboi et al. (1998) report temperatures of at least 100 MK in a flare on the weak-lined T Tau star V773 Tau. Güdel et al. (1999) showed that the flare EM distribution of the RS CVn binary UX Ari evolved to temperatures of 50 to 100 MK and was accompanied by individual elemental abundance variations. Such variations were already suggested in previous observations, although elemental abundances were often linked together to provide best fits with an "average" metal abundance (e.g., Ottmann & Schmitt 1996; Favata et al. 2000). Data with low spectral resolution could not disentangle the emission lines from the underlying continuum, which led to some uncertainties about metal-deficient coronal abundances in stars compared to their photospheric values (Schmitt et al. 1996). Furthermore, on some stars, elements with low first ionization potentials (FIP) are found to be enhanced with respect to their photospheric abundances (the FIP effect), while on others they are not (e.g., Drake, Laming, & Widing 1995, 1997).

HR 1099 (V711 Tauri; HD 22468) is a binary system of the RS CVn class. The system consists of K1 IV + G5 IV stars that are tidally locked with a period of 2.84 days and an inclination

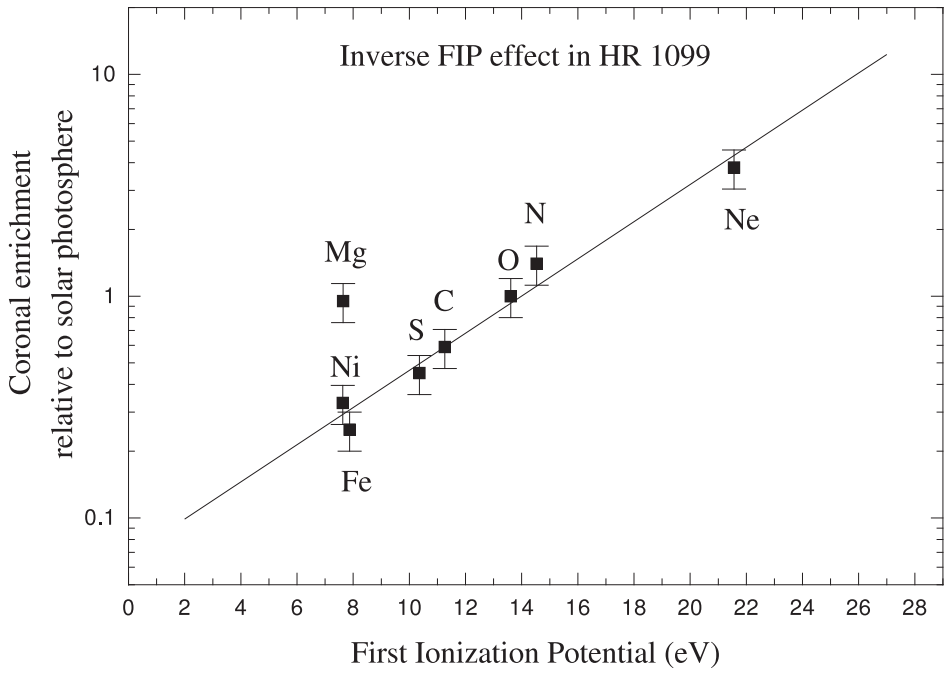

Figure 6.2: *Enrichment of elemental abundances in the HR 1099 coronae relative to (solar) photospheric values, plotted as a function of the first ionization potential (FIP). All values are given with error bars of 20%. Note the increase of the relative abundances with increasing FIP, opposite to the trend observed in the average solar corona. From Brinkman et al. (2001).*

of i=33° (Bopp & Fekel 1976; Fekel 1983). At a distance of 28.97 pc (Perryman et al. 1997), it is one of the brightest members of its class. HR 1099 has been extensively studied in the optical, the ultra-violet and the radio, while its extreme ultra-violet (EUV) and X-ray emission was analyzed in the context of surveys of coronal emission from RS CVn systems (Majer et al. 1986; Pasquini, Schmitt, & Pallavicini 1989; Schmitt et al. 1990; Griffiths & Jordan 1998). Possible detection of rotational modulation in the EUV light curve of HR 1099 was reported by Drake et al. (1994), with a minimum flux occurring near the phase when the G5 star is in front ($\phi = 0.5$), consistent with a previously reported correlation between binary phase and X-ray intensity by Agrawal & Vaidya (1988). Recently, Ayres et al. (2001) found in *Chandra* HETG data of HR 1099 that wavelength shifts in the Ne X Lyα line are consistent with the orbital motion of the active K1 IV star. In the context of spectroscopy, Drake & Kashyap (1998) studied the coronal metallicity of HR 1099. They reported a coronal iron abundance of $[\mathrm{Fe/H}] \approx -0.4$, consistent with photospheric iron abundance of the K1 star ($[\mathrm{Fe/H}] \approx -0.6$, Randich et al. 1994). However, noting the difference in photospheric abundances between the primary and the secondary, they argued that the measurements of photospheric abundances of RS CVn systems may be incorrect. Brinkman et al. (2001) analyzed *XMM-Newton* RGS data, discussing coronal elemental abundances in HR 1099. They compare coronal elemental enrichment with solar abundance ratios and find and *inverse FIP effect* for the time-averaged

Table 6.1: *Observation log on 2000 February 18/19.*

α [hh:mm:ss]	δ [dd:mm:ss]	PA [dd:mm:ss]
03:37:14.7[a]	+00:36:40.3[a]	257:41:00.9[a]
Detector	Start [UT]	Stop [UT]
RGS1	13:25:10	05:25:15
RGS2	13:25:10	05:25:18
MOS1[b]	14:26:33	05:26:00
MOS2	14:26:35	05:26:00
pn[b]	14:14:56	03:48:27

[a] Off-axis pointing by -7′ in dispersion direction.
[b] Source fell on CCD gaps, therefore no useful data.

X-ray emission (see Fig. 6.1 and Fig. 6.2). The present chapter complements the Brinkman et al. paper by investigating the variability of the X-ray emission of HR 1099, the variation of the elemental abundances and of the temperature structure during a large flare (Table 6.1).

6.2 Data Reduction and Analysis

HR 1099 was observed during the early commissioning phase of *XMM-Newton* (Jansen et al. 2001). The satellite carries 5 X-ray detectors and an optical telescope: two MOS European Photon Imaging Cameras (EPIC; Turner et al. 2001), one EPIC pn (Strüder et al. 2001), two Reflection Grating Spectrometers (RGS; den Herder et al. 2001) and an Optical Monitor (Mason et al. 2001). HR 1099 was, as the first-light target of the RGS, monitored over a time span of about 25 days (see Fig. 6.3).

The data were analyzed with the official ESA XMM Science Analysis System (SAS) software, version 4.1, together with the latest calibration files available at the time of the analysis. The metatask RGSPROC 0.73.3 was used to process the RGS data. Normally, the dispersion angles can be corrected for attitude drifts during the exposure. However, since the full attitude information was not available for these early observations, no correction was applied. Nevertheless, preliminary attitude data showed that the observation was stable during the data acquisition. Spectra were extracted along the dispersion direction using a spatial mask together with a cut in the plane of dispersion angle vs. CCD energy. The RGS response matrix was created with RGSRMFGEN 0.29. The metatask EMPROC 1.8 was used to process the EPIC MOS2 data (the source was placed in the middle of a CCD gap for both EPIC MOS1 and pn). The EPIC MOS2 data were taken in the PRI FULL WIN mode and with the MEDIUM filter, hence they suffered from severe pile-up and optical contamination. Lumb et al. (2000) showed that removing the center of the Point Spread Function, which is heavily piled-up, and extracting source counts

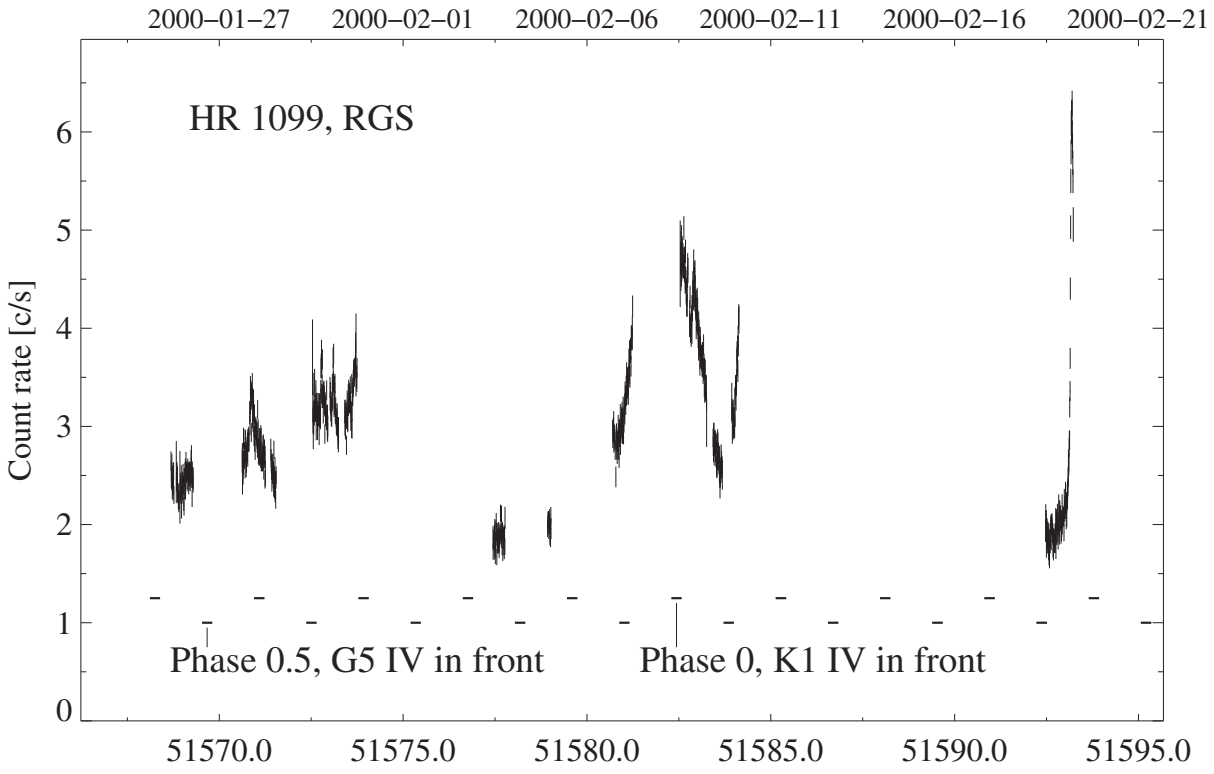

Figure 6.3: *Total 1st and 2nd order RGS2 light curve of HR 1099. Between MJD 51580.702 – 51581.244, RGS1 data were added, because RGS2 was not observing. The ephemeris of Vogt et al. (1999) has been used for the orbital phases.*

from an annulus permits a compromised use of the data, naturally with a reduced count rate. The MOS2 response and ancillary response matrices were created by RMFGEN 1.37.2 and ARFGEN 1.35, respectively.

Time-dependent spectroscopy was performed for EPIC MOS2 and both RGS instruments. To study the large flare which occurred after MJD 51593.1, we have selected four time intervals, designated “quiescent”, “rise part 1”, “rise part 2”, and “peak” (Table 6.2). Figure 6.4 shows the chosen time slices together with the light curves in the analyzed instruments.

6.3 Results

6.3.1 Rotational Modulation

The long light curve of HR 1099 (Fig. 6.3) displays evident variability on short and long timescales. Additional to the large flare at MJD 51593.1, several other possible smaller flares can be seen (e.g., at 51571 d, and around 51573 d). An additional feature of the light curve that we interpret as rotational modulation is seen around MJD 51582. The X-ray flux appears to peak

Table 6.2: *Time intervals for the phase-dependent analysis.*

Interval	Start [UT]	Stop [UT]	MJD [51592.0 +]
Quiescent.....	13:25:10[a]	01:38:30	0.55914 - 1.06840
Rise part 1.....	01:38:30	03:01:50	1.06840 - 1.12627
Rise part 2.....	03:01:50	03:51:50	1.12627 - 1.16100
Peak	03:51:50	05:26:00	1.16100 - 1.22639

[a] MOS2 observation begins 1 hour later.

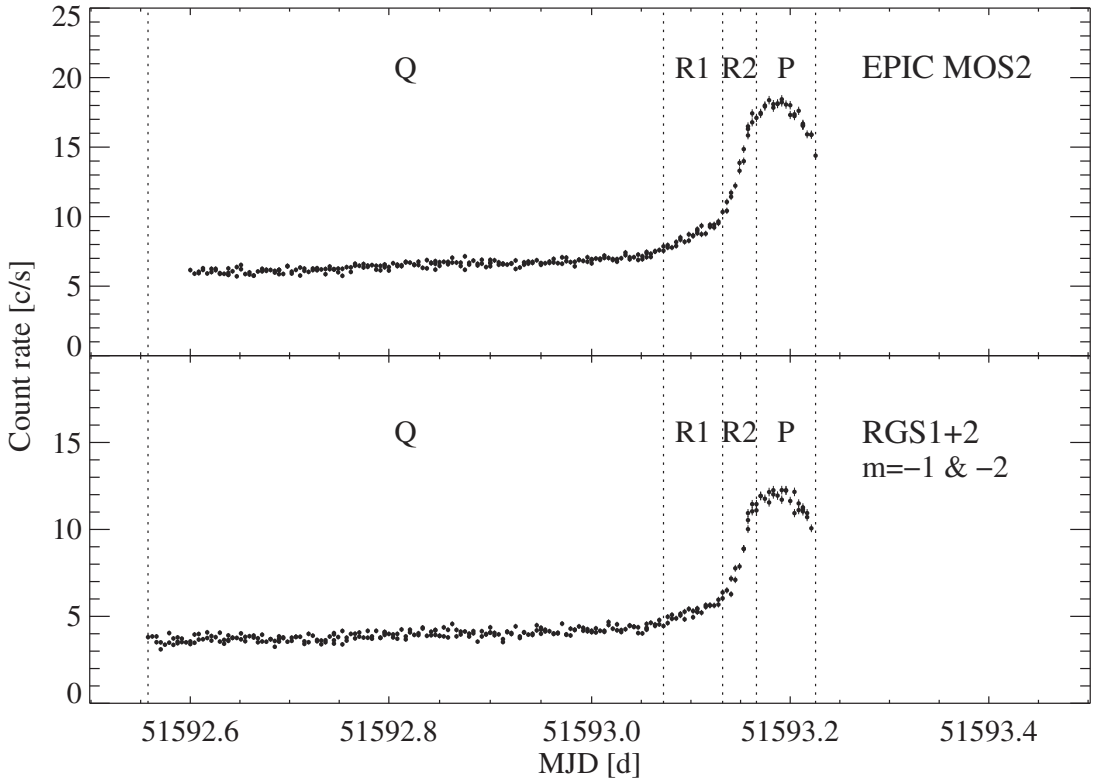

Figure 6.4: *EPIC MOS2 and coadded RGS1+2 1st and 2nd order light curves with chosen time intervals (Tab. 6.2).*

when the active K1 star is in front (phase $\phi = 0$), while the flux diminishes until it reaches a minimum value when the companion G5 star is in front. On a smaller scale of flux variations, this behavior is also suggested during earlier phases (MJD 51571.3, 51573.8). The strong variability from one rotation period to the other may suggest that long-term flaring is involved, and that the MJD 51582 emission is rotationally modulated flare emission. Spectral hardness analysis, however, does not show clear signatures of heating and cooling, in contrast to the later flare discussed below. The episode around MJD 51582 may represent general enhanced

Table 6.3: *Best fit to the time-dependent RGS2 spectra with 90% confidence ranges for a single parameter. "..." entries mean that the value was kept fixed to its quiescent value (see text for details). Abundances are relative to solar photospheric values (Anders & Grevesse 1989).*

Parameter	Q	R1[a]	R2[a]	P[a]
kT_1 [keV]	$0.29^{+0.17}_{-0.06}$	...	...	...
kT_2 [keV]	$0.65^{+0.04}_{-1.1}$	...	...	...
kT_3 [keV]	$1.24^{+0.16}_{-0.20}$	...	...	...
kT_4 [keV]	$2.58^{+2.7}_{-0.77}$	...	...	...
kT_5 [keV]	–	$1.20^{+0.60}_{-0.25}$	$2.50^{+0.88}_{-0.51}$	$3.12^{+0.96}_{-0.57}$
$\log \mathrm{EM}_1$ [cm^{-3}]	$52.32^{+0.38}_{-0.32}$	...	...	...
$\log \mathrm{EM}_2$ [cm^{-3}]	$53.38^{+0.06}_{-0.07}$	...	...	...
$\log \mathrm{EM}_3$ [cm^{-3}]	$53.42^{+0.16}_{-0.30}$	...	...	...
$\log \mathrm{EM}_4$ [cm^{-3}]	$53.41^{+0.19}_{-0.31}$	...	...	...
$\log \mathrm{EM}_5$ [cm^{-3}]	–	$53.51^{+0.07}_{-0.08}$	$54.00^{+0.03}_{-0.03}$	$54.22^{+0.02}_{-0.02}$
C	$0.38^{+0.08}_{-0.08}$	...	...	...
N	$0.60^{+0.55}_{-0.54}$	...	...	...
O	$0.35^{+0.03}_{-0.03}$	$0.03^{+0.15}_{-0.03}$	...	$0.46^{+0.19}_{-0.13}$
Ne	$0.93^{+0.10}_{-0.09}$	$0.46^{+0.69}_{-0.45}$	...	$1.32^{+0.62}_{-0.44}$
Mg	$0.10^{+0.07}_{-0.07}$	...	...	$0.44^{+0.66}_{-0.44}$
Si	$0.18^{+0.12}_{-0.12}$	$1.02^{+1.28}_{-1.02}$	$1.56^{+1.45}_{-1.30}$	$1.94^{+0.97}_{-0.78}$
S	$0.07^{+0.05}_{-0.07}$	...	...	...
Ar	$1.23^{+0.63}_{-0.56}$	...	...	...
Ca	$0.10^{+0.19}_{-0.10}$	...	...	...
Fe	$0.15^{+0.02}_{-0.02}$	$0.09^{+0.12}_{-0.06}$	$0.32^{+0.20}_{-0.13}$	$0.40^{+0.19}_{-0.11}$
Ni	$0.06^{+0.10}_{-0.06}$	...	...	...

[a] Entries related to the free CIE model (see text).

activity on the more active hemisphere.

6.3.2 Time-Dependent Spectroscopy

Table 6.3 gives best-fit results for the time-dependent spectral analysis of RGS2 data. Although the detailed description of the response of both spectrometers is expected to evolve over time, we have used RGS2 for the present analysis as this description was more advanced than for RGS1 at the time of the analysis. Similar elemental abundance variations and a similar temperature structure are, however, also observed in RGS1.

We have fitted the quiescent RGS2 spectrum with collisional ionization equilibrium (CIE) models in the Utrecht software SPEX 2.0 (Kaastra et al. 1996a). In order to obtain an optimum description of the thermal structure and to determine, at the same time, the elemental abun-

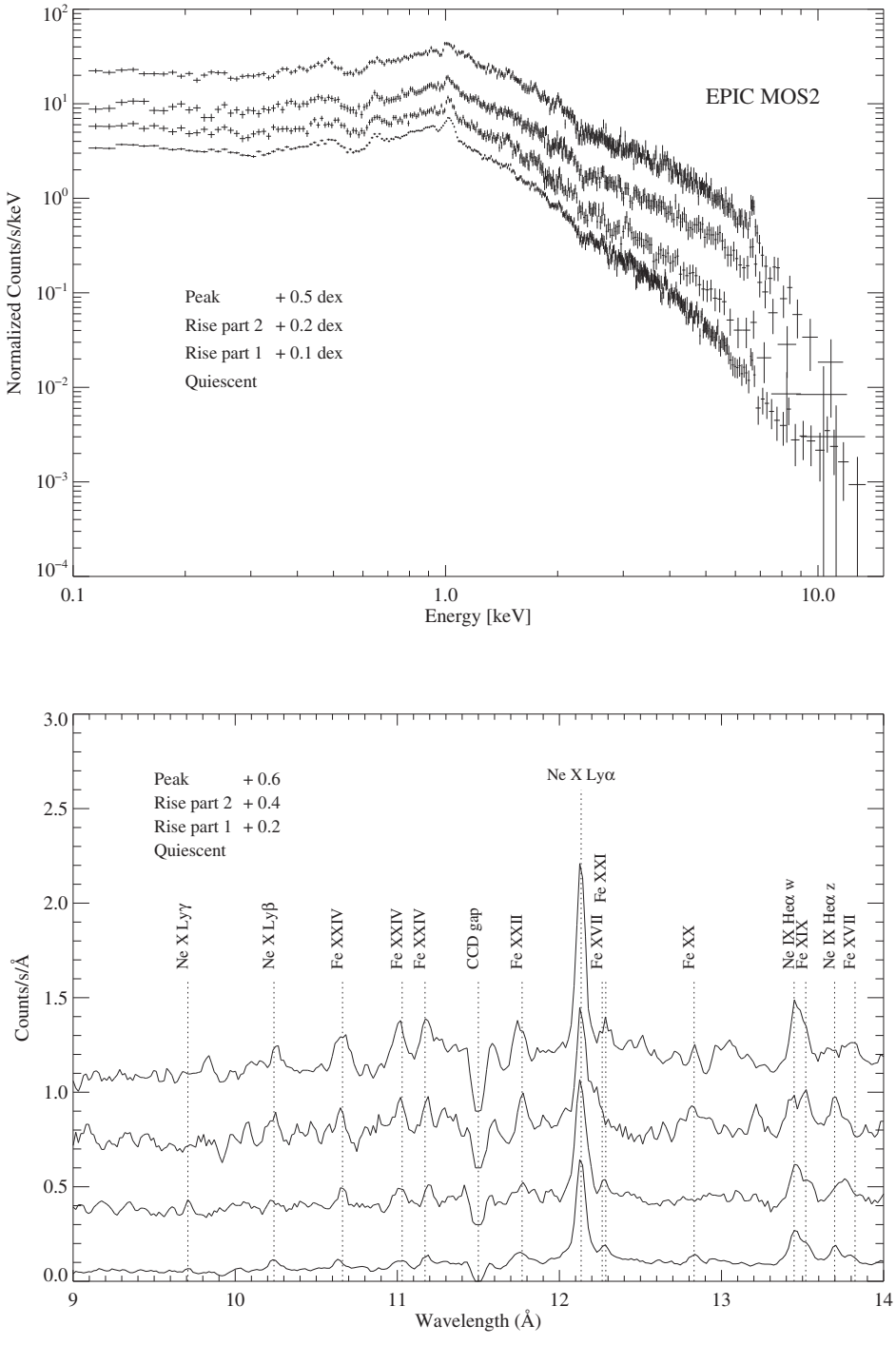

Figure 6.5: *Top: MOS2 spectra of the four time segments, from quiescent (lowest spectrum) to flare peak (uppermost spectrum). Spectra are shifted in flux as indicated, for illustration. Bottom: Extract from smoothed RGS spectra of the four time segments (lowest: quiescent; uppermost: flare peak). Note relative shifts of the spectra in count rate.*

dances, we used as many components as possible and necessary to obtain a good fit to the data. We found that four components lead to good results. The χ^2 procedure did not require a fifth temperature component, and three or fewer CIE components were insufficient. For the flare parts, the quiescent best-fit model was frozen and an additional CIE component was added to describe the flare plasma. We refrain from fitting the MOS data in terms of a full coronal model with variable abundances at this time, since the combination of its still improving calibration with considerable optical contamination and residual X-ray pile-up due to the brightness of HR 1099 (both optically and in X-rays) may bias the results. We obtained, however, rough fitting estimates for the emission measures and temperatures of the hotter components - see below. Figure 6.5 shows an extract of the RGS2 and the EPIC MOS2 spectra for the four time intervals. Signatures of heating are evident: the high-T tail of the CCD spectra flattens significantly during the flare, a direct sign of a temperature increase. Furthermore, the RGS spectra show that the Fe XXIV lines increase in intensity, relative to the underlying continuum.

Several elements that show lines in the RGS band had their abundances (relative to the solar photospheric values given by Anders & Grevesse 1989) left free to vary in the fitting process. In the quiescent model, the abundance of each element is kept at the same value in all three CIE components. For the flare parts, the abundances of the free CIE model were independent of the quiescent abundances. Several free elements did not improve the fit, and therefore their abundances were kept fixed at their quiescent values. During the flare, the elemental abundances were difficult to derive due to the low signal-to-noise (S/N) ratio. Nevertheless, Fe and Si abundances appear to increase significantly (although with large 90% confidence ranges). The RGS2 data determine an increase of temperature from 1.2 keV to 3.1 keV. From the MOS2 data, we tentatively derive a high-temperature component of 2.8, 4.4, 8.0, 7.2 keV in the quiescent, flare rise (part 1 & 2), and flare peak intervals, respectively. These temperatures do not contradict the apparently lower T determined by the RGS2. At such temperatures, there are too few spectroscopic features in the RGS band to discriminate between different temperatures, and small residual calibration uncertainties become important. For flare studies, combining the RGS (for elemental abundance studies and $T \leq 2$ keV) with the EPICs (to constrain high-T tails) is ideal. We also note that the MOS2 data support the view that the Fe and Si abundances increase, with values consistent with RGS2 results. But note also that the high-FIP element Ne appears to have an abundance that does not vary beyond the significance limits.

Using abundances from the multi-CIE fits, EM distributions have been derived from RGS spectra. Fig. 6.6 shows realizations of the EM distribution for the quiescent and flare peak spectra. Consistent with the multi-CIE approach, the quiescent EM distribution spans over a decade in temperature, with significant emission measure from 5 MK to 30 MK. Note that the presence of EM around 3–5 MK is also significant and mainly necessary to fit the bright O VII He-like triplet around 22 Å and the C VI Lyα line at 33.7 Å. The flare EM distribution displays a gradual increase in the upper temperature. Fits for the flare peak (Fig. 6.6) show that a very hot EM (> 30 MK) dominates the emission. During the flare, the cooler EM ($T < 20$ MK) is consistent with the quiescent distribution. The quiescent density derived from the O VII triplet is low, with $n_{\rm e} < 10^{10}$ cm^{-3} for the cooler material. During the flare, despite the poor S/N, the data suggest that the density of this relatively cool material does not increase. This behavior is

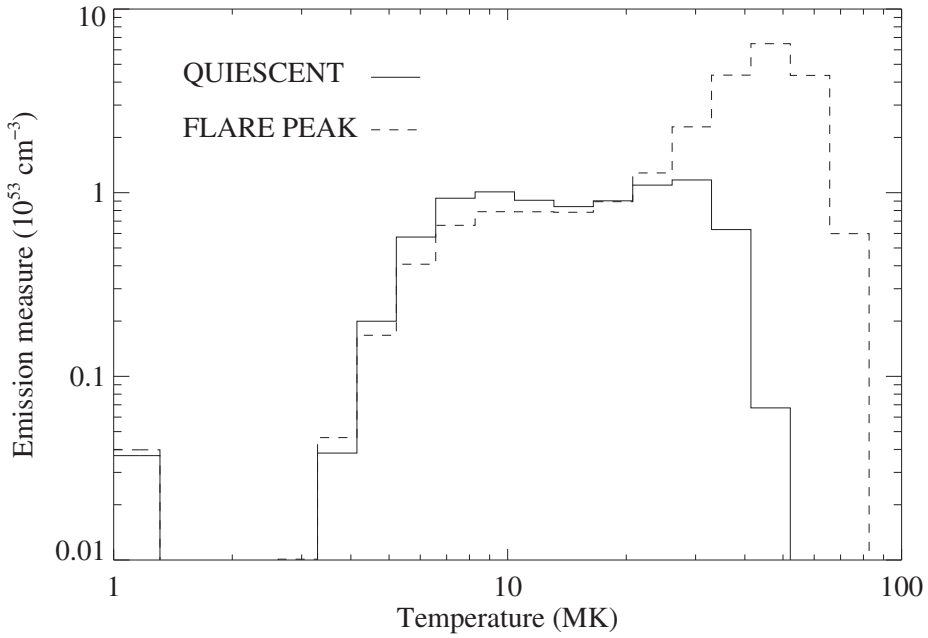

Figure 6.6: *Realizations of the quiescent (solid) and flare peak (dash) EM distributions using Chebychev polynomials of order 6.*

consistent with the absence of detection of a density increase in the cool plasma during flares found on AB Dor (Chapter 8).

6.4 Discussion and Conclusions

A part of the "first light" observations of *XMM-Newton* has been analyzed, concentrating on overall light-curve variability and on the large flare at the end of the observation.

We found considerable variability over the 25 d observing time span. The X-ray flux varies with the binary phase, with the X-ray minimum at $\phi = 0.5$, and maximum flux at $\phi = 0$. A similar result was previously described by Agrawal & Vaidya (1988) and Drake et al. (1994). In *Chandra* HETG data, Ayres et al. (2001) reported the detection of Ne X line shifts consistent with the orbital motion of the active K1 IV star. Additionally, optical light curves showed, via Doppler imagery, the presence of a long-lived (≈ 11 yr) polar spot on HR 1099, together with transient (< 1 yr) low-latitude spots on the surface of the active K star (Vogt et al. 1999). Taken together, these observations suggest that one or several active regions are present on the hemisphere of the K1 star that is facing away from the G5 star. Since HR 1099 shows this effect consistently over years, it must be related to a fundamental pattern in its magnetic activity. It appears that the tidally locked rotation of the K star alters the internal dynamo in such a way that strong activity on the hemisphere facing the G star is suppressed. This, in turn, does not

support the hypothesis that much of the X-ray emission in RS CVn binaries originates from the interbinary space (Siarkowski et al. 1996).

The maximum flux is not identical at every conjunction of the K star, consistent with a variable quiescent flux level coming from active regions. Note that it is difficult to distinguish between flares and rotationally modulated strong active regions in cases such as the wave at MJD 51582. Indeed, the maximum flux there is similar to the flare peak flux. Hardness analysis, however, clearly sets the flare at MJD 51593 apart from any other event during all other observations. On the other hand, EUV light curves from HR 1099 showed that large flares can have durations of one to two days (Osten & Brown 1999), perhaps suggesting that the event at MJD 51582 is a slowly evolving but rotationally modulated flare. Conversely, it can be argued that the large flare at MJD 51593 is rotationally modulated as well, but given its restricted coverage, there is no clear evidence for geometric modulation.

Time-dependent spectroscopy of the large flare allowed us to derive time-dependent EM distributions and abundances. The EM reconstructions show a broad distribution in temperature, consistent with previous reports of broad hot EM distributions for RS CVn systems (e.g., Griffiths & Jordan 1998; Güdel et al. 1999). The flare EM peaks around 50–60 MK; the quiescent EM seems to remain present during the flares, at least below 30 MK, indicating that the flare does not affect a very large fraction of the plasma in the visible active regions (see also Güdel et al. 1999). Audard et al. (2001b) discuss the influence of potential inaccuracies in the atomic data utilized in the current version of SPEX on spectral fitting of RGS data (Chapter 7). Especially, caution is in order for the S abundance. During the flare, Fe and Si (low-FIP; possibly S from MOS2 data) abundances appear to increase significantly, while the Ne (high-FIP) abundance stays at a value consistent with its quiescent value, within the error limits. The increase of low-FIP elemental abundances during the flare when high-FIP elemental abundances stay at quiescent values can be interpreted as a direct signature of a FIP effect during flares. The quiescent abundances, however, are not compatible with a FIP effect. First, we find that all quiescent abundances are lower than solar photospheric abundances, in contrast to solar coronal behavior (Feldman 1992). Second, the low-FIP elements generally show lower abundances than the high-FIP elements. This "inverse FIP" effect (Fig. 6.2) was noted by Brinkman et al. (2001) and studied in detail for the higher-S/N *time-averaged* RGS spectrum of HR 1099 (Fig. 6.1) that comprises all observations shown in Fig. 6.3.

Taken together, these observations seem to contradict the model that "quiescent" coronae are heated by a multitude of unresolved flares, since the FIP effect during the large flare counteracts trends in quiescent abundances. However, the solar case has shown a much larger complexity. There are several types of flares that show deviations from the standard picture. Schmelz (1993) reported on a class of flares that are selectively Ne rich. Brinkman et al. (2001) show that Ne is strongly overabundant with respect to O, and they suggest that there are flare-like mechanisms different from very large flares that bring material into the corona, with a composition compatible with observations during quiescence. In any case, additional systematic studies using high-resolution spectroscopy will address this problem further.

Chapter 7

High-Resolution X-Ray Spectroscopy of Capella

Summary

We present the high-resolution RGS X-ray spectrum of the stellar binary Capella observed by the *XMM-Newton* satellite. A multi-thermal approach has first been applied to fit the data and derive elemental abundances. Using the latter, the emission measure distribution has been reconstructed using a Chebychev polynomial fit. Its shape is found to display a sharp peak around 7 MK, consistent with previous *EUVE* and *ASCA* results. A smaller but significant amount of emission measure is required around 1.8 MK in order to explain the O VII He-like triplet and the C VI Lyα line. We have applied the temperature diagnostics of dielectronic recombination satellite lines to the He-like O VII triplet to constrain the cool plasma temperature, and have obtained a lower limit consistent with the global reconstruction of the emission measure distribution. We have used line ratios from the forbidden, intercombination, and resonance lines of the O VII triplet to derive an average density for the cool coronal plasma ($n_{\rm e} < 1 \times 10^{10}$ cm^{-3}). Implications for the coronal structure of Capella are discussed.

7.1 Introduction

Since the discovery a quarter of a century ago of weak X-ray emission from the first coronal object other than the Sun, Capella (Catura, Acton, & Johnson 1975), the solar-stellar connection has been in the focus of the efforts to interpret stellar coronae. Despite the overall similarity of solar and stellar coronae, a number of features set active stellar coronae apart from the solar example. Are stellar coronae scaled-up versions of the solar corona? Is the coronal heating mechanism identical, given the very different average coronal temperatures?

The high X-ray flux of the binary star Capella makes it one of the best candidates to study the

The work presented in this chapter has been published in Audard et al. (2001b).

X-ray emission from stellar coronae and to identify its role in the larger solar-stellar connection picture. One of the most powerful tools to derive physical properties of stellar coronae is X-ray spectroscopy, providing access to emission measure distributions in temperature, elemental abundances, densities, and mass motions. Previous X-ray satellites carried low-resolution devices, or if high-resolution was available, then the effective area was small. The advent of a new generation of X-ray satellites, including *Chandra* and *XMM-Newton*, allows us to obtain high-resolution spectroscopy with moderately high effective areas. We use the Capella spectrum to derive fundamental parameters of its coronae that we compare with previous measurements. The large signal-to-noise ratio of Capella's spectrum allows us to also discuss limitations in the presently available spectral codes.

7.2 Previous Knowledge on Capella

Capella (α Aurigae; 13 Aurigae; HD 34029; HR 1708) is, at a distance of 12.93 pc (Perryman et al. 1997), one of the brightest X-ray objects visible in the sky. It is composed of G1 III + G8 III star (Strassmeier & Fekel 1990; Hummel et al. 1994) separated by 56.47 mas (Hummel et al. 1994). The orbital period ($P = 104$ d) is not linked to the rotation period of each component, the G1 giant completing about 12 revolutions in one orbital period (Hummel et al. 1994). Catura et al. (1975) first detected weak X-ray emission from Capella, quickly confirmed by Mewe et al. (1975). Subsequent extreme ultraviolet (EUV) and X-ray observations have been prolific with most satellites (e.g., Cash et al. 1978; Holt et al. 1979; Mewe et al. 1982; Vedder & Canizares 1983; Lemen et al. 1989; Dupree et al. 1993; Schrijver et al. 1995; Favata et al. 1997; Brickhouse et al. 2000; Brinkman et al. 2000; Canizares et al. 2000; Behar et al. 2001), however still leaving unresolved problems in the interpretation of Capella's coronal spectrum.

Linsky et al. (1998) found that the contribution of both stars to the total flux of the coronal Fe XXI line in the ultraviolet regime was similar. Dupree et al. (1993) showed that iron (Fe XV-XXIV) was dominating the *EUVE* spectrum. Their emission measure (EM) distribution ranged from 0.1 to 63 MK, with minimum EM around 1 MK and a sharp peak around 6 MK. Based on lines of highly ionized Fe XXI, they derived an electron density of $4 \times 10^{11} - 10^{13}$ cm^{-3}. However, their EM distribution was not in agreement with later *BeppoSAX* results (Favata et al. 1997). Brickhouse et al. (2000) studied simultaneous *EUVE* and *ASCA* observations of Capella. They found that the low first-ionization-potential (FIP) elements Mg, Si, S, and Fe have coronal abundances consistent with solar photospheric values, while the high-FIP element Ne appears to be underabundant by a factor of 3 to 4. However, they were not able to constrain the O abundance, while Brickhouse (1996) derived a subsolar O abundance from the *EUVE* data. Dupree & Brickhouse (1996) found a long-term variability in the EUV intensities of Fe XXI to Fe XXIV by up to a factor of 4.

Early high-resolution spectroscopic results on Capella were obtained from *Chandra* HETG/LETG (Brinkman et al. 2000; Canizares et al. 2000; Behar et al. 2001; Mewe et al. 2001; Ness et al. 2001), confirming the dominance of highly ionized Fe lines in the X-ray spectrum of Capella. Density diagnostics applied to the C V, N VI and O VII triplets for LETG data

implied a low density regime (2.8 ± 1.3, 6 ± 3, and < 5 times 10^9 cm^{-3}, respectively). In HETG data, the O VII triplet, formed at low T, gave a slightly higher density ($0.8 - 2 \times 10^{10}$ cm^{-3}), while the Mg XI and Si XIII triplets, formed at higher T, gave upper limits near 7×10^{11} and 1×10^{12} cm^{-3}. Little (or no) evidence for opacity effects in the 15.014 Å Fe XVII line has been seen. Behar et al. (2001) reproduced fairly well the HETG Fe L-shell spectrum by assuming a single electron temperature of 0.6 keV. The present chapter presents first results from the observation of Capella with *XMM-Newton*.

7.3 Data Reduction and Analysis

Capella was observed several times by *XMM-Newton* (Jansen et al. 2001) for calibration purposes. In this chapter, we present the Reflection Grating Spectrometer (RGS; den Herder et al. 2001) data of the on-axis observation (2000-03-25, 11:36:59 UT until 2000-03-26, 02:53:49 UT) which had a low instrumental background. The effective exposure times were 52.3 and 52.4 ksec for RGS1 and RGS2, respectively. The data from the other X-ray instruments onboard *XMM-Newton* could not be used, because they were severely piled-up and optically contaminated by the brightness of Capella.

The data were analyzed with the official ESA XMM Science Analysis System (SAS) software, version 4.1, and an update of several RGS tasks together with the latest calibration files available at the time of the analysis. The metatask RGSPROC 0.77 was used to process the RGS data. Spectra were extracted along the dispersion direction using a spatial mask together with a cut in the plane of dispersion angle vs. CCD energy. The satellite pointing was stable, except for a short (600 sec) deviation of the attitude pointing that had no significant influence on the RGS spectra of Capella. The RGS response matrices were generated by RGSRMFGEN 0.29. Although the detailed description of the response of both spectrometers is expected to evolve over time, we should note that the description of the RGS2 response is more advanced than for RGS1 at the time of this analysis. Some systematic errors may be introduced for RGS1 results. However, any future RGS analysis with a more advanced response is not expected to give results that deviate more than $\approx 10 - 25$ % from the current results.

7.3.1 Line Fluxes

A number of individual line fluxes have been measured in the RGS spectra (Tab. 7.1). First, a constant "background" level was adjusted in order to account for the real continuum or for the pseudo-continuum created by the overlap of several weak or neglected lines. Especially in the 9–18 Å region, the overlap of the line wings (originating from the instrumental line spread function, LSF) created an important pseudo-continuum. We used the instrumental LSF in order to derive the integrated line fluxes. For comparison, we also give line fluxes as measured by *Chandra* HETG (Canizares et al. 2000) and LETG (Mewe et al. 2001). Within the instrumental and calibration uncertainties, the RGS fluxes are similar to the non-simultaneously measured *Chandra* fluxes. There may be some indications for higher flux values in *Chandra* for lower stages of ionization. This could also suggest that the low temperature plasma has lower EM

Table 7.1: *Line fluxes in* 10^{-4} s^{-1} cm^{-2}. *RGS2 fluxes (except for* O VII *only available in RGS1) are compared to Chandra HETG (Canizares et al. 2000) and LETG (Mewe et al. 2001) measurements.*

Ion	λ (Å)	RGS	HETG	LETG
Mg XII	8.421	2.2 ± 0.4	1.5	2.0 ± 0.2
Mg XI	9.169	3.9 ± 0.6	3.5	3.2 ± 0.3
Mg XI	9.231	0.9 ± 0.3	0.6	0.7 ± 0.2
Mg XI	9.314	1.5 ± 0.3	1.9	1.6 ± 0.2
Fe XVII	15.014	37.9 ± 1.7	30.4	34.1 ± 1.1
Fe XVII	16.775	23.1 ± 1.3	20.0	20.4 ± 0.8
Fe XVII	17.051	26.4 ± 1.5	26.4	30.9 ± 1.9
Fe XVII	17.100	31.1 ± 1.6	24.4	24.4 ± 3.0
O VIII	18.969	26.8 ± 1.5	26.3	26.4 ± 1.0
O VII	21.602	7.6 ± 0.8	9.7	9.9 ± 0.7
O VII	21.804	1.1 ± 0.3	2.6	1.9 ± 0.3
O VII	22.101	4.8 ± 0.6	7.4	6.9 ± 0.6
N VII	24.781	6.3 ± 0.7	5.5	6.9 ± 0.8
C VI	33.734	7.9 ± 0.8	$\cdots$	8.7 ± 0.9

during the *XMM-Newton* observation. This is however opposite to the suggestion of Dupree & Brickhouse (1996) who found flux variations in the *hot* plasma component.

7.3.2 Working Procedure

In this chapter, we have used a "global fitting" approach. This approach allows us to obtain a self-consistent solution that best fits the data and that takes into account *simultaneously* the contributions of the continuum components and of all emission lines. Line blends and the overlap of line wings are therefore fully accounted for, and the line fluxes are correctly reproduced within the accuracy of the code. However, as will be discussed in the following sections, the fit depends on the completeness of the atomic database used by the spectral fitting code. We have used the publicly available Utrecht software SPEX 2.0 (Kaastra et al. 1996a). It contains a collisional ionization equilibrium (CIE) model that is equivalent to the MEKAL (Mewe, Kaastra, & Liedahl 1995) code available in the XSPEC software (Arnaud 1996), except that the former includes a significant update of the wavelengths of Fe L-shell lines between 10–18 Å, based on the solar data by Phillips et al. (1999).

A spectral model using three CIE components with a column density $N_{\mathrm{H}} = 1.8 \times 10^{18}$ cm^{-2} (Linsky et al. 1993) allowed us to obtain an initial representation of the temperature structure in Capella. This model was used to derive coronal elemental abundances from a variety of bright and weak lines. We added further components (up to ten) in the multi-T approach

Table 7.2: *Best fits for a 3-T CIE model with 90% confidence ranges for a single parameter. The elemental abundances are given relative to the solar photospheric value (Anders & Grevesse 1989). See text for a discussion on the significance of the elemental abundances.*

Parameter	RGS1	RGS2
$\log N_{\rm H}$ [cm^{-2}].....	$= 18.255$	$= 18.255$
kT_1 [keV].....	$0.159^{+0.006}_{-0.006}$	$0.13^{+0.01}_{-0.01}$
kT_2 [keV].....	$0.593^{+0.002}_{-0.002}$	$0.58^{+0.003}_{-0.004}$
kT_3 [keV].....	$1.14^{+0.07}_{-0.07}$	$0.93^{+0.07}_{-0.07}$
$\log {\rm EM}_1$ [cm^{-3}].....	$51.90^{+0.03}_{-0.02}$	$51.65^{+0.08}_{-0.09}$
$\log {\rm EM}_2$ [cm^{-3}].....	$52.86^{+0.009}_{-0.01}$	$52.98^{+0.01}_{-0.01}$
$\log {\rm EM}_3$ [cm^{-3}].....	$51.81^{+0.05}_{-0.05}$	$51.85^{+0.08}_{-0.09}$
C.....	$0.50^{+0.04}_{-0.04}$	$0.52^{+0.04}_{-0.04}$
N.....	$0.82^{+0.07}_{-0.07}$	$1.01^{+0.08}_{-0.08}$
O.....	$0.44^{+0.02}_{-0.01}$	$0.39^{+0.01}_{-0.01}$
Ne.....	$0.51^{+0.03}_{-0.03}$	$0.34^{+0.02}_{-0.02}$
Mg.....	$1.13^{+0.06}_{-0.05}$	$0.74^{+0.04}_{-0.04}$
Si.....	$0.41^{+0.06}_{-0.06}$	$0.48^{+0.06}_{-0.06}$
S.....	$0.14^{+0.02}_{-0.02}$	$0.09^{+0.02}_{-0.02}$
Ar.....	$0.23^{+0.1}_{-0.1}$	$0.17^{+0.14}_{-0.14}$
Ca.....	$0.27^{+0.08}_{-0.08}$	$0.27^{+0.11}_{-0.11}$
Fe.....	$0.62^{+0.02}_{-0.01}$	$0.51^{+0.01}_{-0.01}$
Ni.....	$0.88^{+0.07}_{-0.07}$	$0.54^{+0.05}_{-0.05}$

to investigate whether they are required for a better description of the fit parameters. This was not the case. We therefore interpret our abundances as sufficiently accurate within the limitations of the spectral code. The best-fit results are given in Table 7.2 for RGS2 data, and for completeness also for RGS1. The uncertainties do not include systematic uncertainties that may be introduced by calibration uncertainties (especially for RGS1, see § 7.3). A continuous emission measure distribution has then been reconstructed using the Chebychev polynomial fit approach, using the best-fit coronal elemental abundances obtained from the 3-T CIE model.

The very high signal-to-noise ratio of the RGS spectra of Capella makes visible several places where the spectral code systematically over- or underestimates the data. Since these deviations are systematic and localized, we do not give χ^2 values. A *formally* (based on χ^2) unacceptable fit does not imply, in this case, that the global fit is overall incorrect, but rather that there are well-identified local problems with separate lines (see Fig. 7.1 for a model fit).

7.3.3 Elemental Abundances

We estimate, in the following, the influence of the fitting discrepancies on our results. The most important discrepancies occur for the Si XIII lines at 6.6 Å, for the Fe XVII–XX lines at

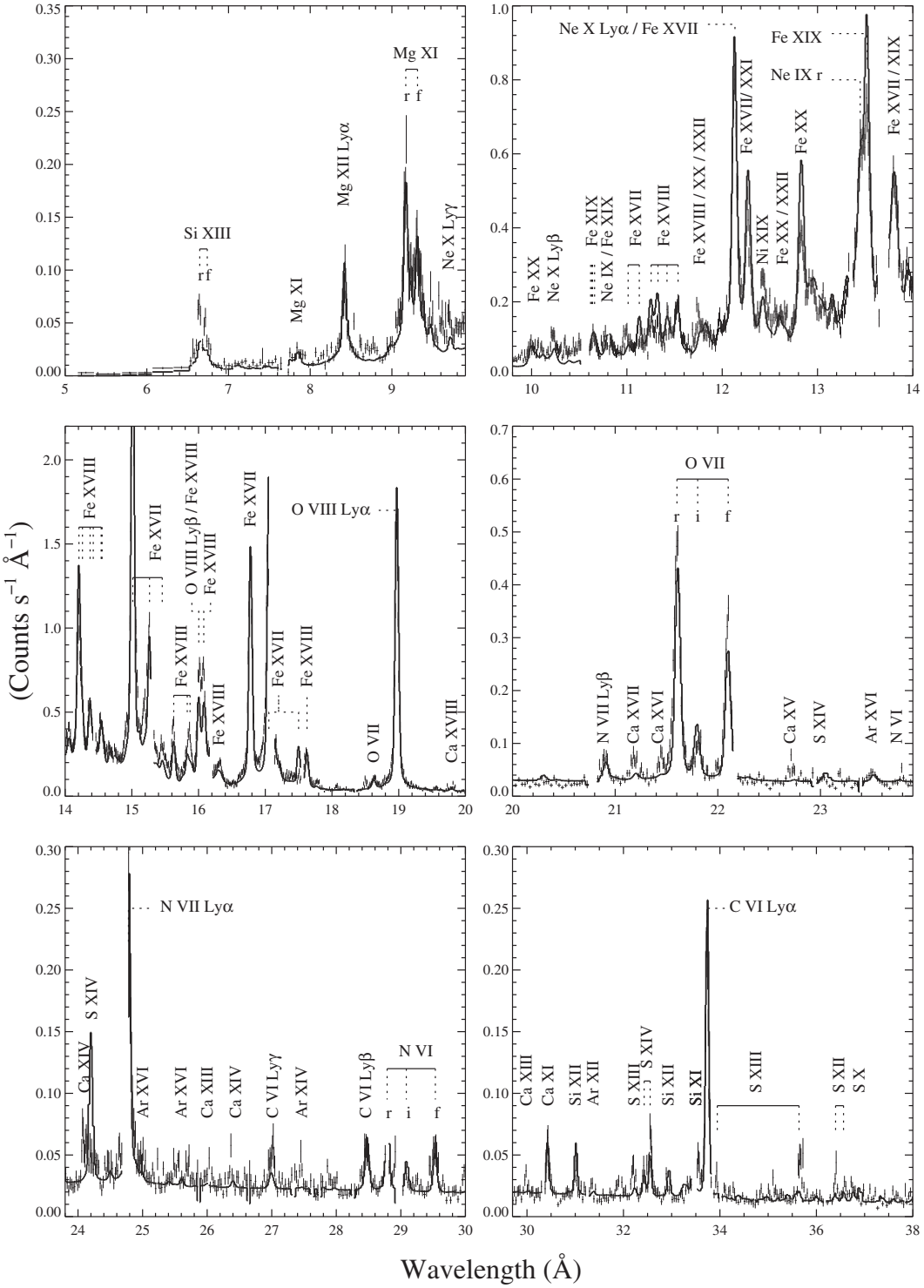

Figure 7.1: *RGS1 data with the overlaid best-fit model (thick line) derived from a reconstructed emission measure distribution (Fig. 7.2). The labels identify major lines. Note the different scales in each panel.*

$11.0 - 11.4$ Å, at 12.8 Å, at 13.5 Å, and for the Fe XVIII lines around 16 Å. The spectral code underestimates the flux around $9.6 - 10.6$ Å, which has been interpreted by Brickhouse et al. (2000) as being due to missing high excitation ($n > 5$) lines of Fe XVII–XIX. Furthermore, the energy dependency of the collision strengths of Fe L-shell lines needs to be updated in SPEX/MEKAL. Additionally, we note that the spectral code fails to pick up some of the weak lines observed in the long-wavelength part of the spectrum. HULLAC (Bar-Shalom et al. 1998) calculations indicate that these should mostly be attributed to L-shell emission from Si, S, Ar, and Ca. The mentioned discrepancies are related to the incompleteness of the atomic database of the CIE model in SPEX, and similarly of the MEKAL model in XSPEC. We conclude that L-shell lines from several elements (e.g., S, Si, Ca, Ar, Ni) and high excitation Fe L-shell lines are insufficiently described in these codes.

To test the robustness of the derived elemental abundances, we have iteratively eliminated emission lines and parts of the continuum that showed poor fit results, thus moving from global fitting towards a "single line analysis" approach. As an aside, we note here that the overlapping line wings as well as several line blends in the present RGS spectrum introduce considerable uncertainty if single line fluxes in the Fe L-shell region are measured without modeling; we therefore kept the "global" approach for this test, even when eventually only a few bright lines contributed to the results. Despite the large reduction of the spectral information, the abundances turned out to be quite robust. In all test runs, the Fe abundance was confined to within $0.50 - 0.68$ (times the solar photospheric value), O within $0.24 - 0.39$, and Ne within $0.75 - 1.05$. The S abundance is basically derived from weak L-shell lines in the RGS band. The determination of its abundance is mostly influenced by the S XIV line at 24.2 Å in the model that is not as strong in the data. When the data around this line are removed, the abundance increases to 0.35 ± 0.04, and the model better fits the remaining weak S lines. Similarly, by removing L-shell Si ions (in the long wavelength band), the bright Si He-like triplet is correctly fitted, with an abundance of $0.7 - 1.0$ times the solar photospheric value.

7.3.4 Emission Measure Distribution

Using coronal elemental abundances derived from the 3-T model, the EM distribution has been self-consistently reconstructed. Figure 7.2 shows one realization of the EM distribution using a Chebychev polynomial of order 5. No EM above 10 MK is needed for this realization. A sharp peak around 7 MK dominates the spectral emission lines, similar to previous results (Dupree et al. 1993; Schrijver et al. 1995; Brickhouse et al. 2000) and recent results from *Chandra* (Behar et al. 2001). However, the approximate upper envelope to the EM distribution found by Canizares et al. (2000) does not reproduce the sharp peak, but indicates a broad distribution of temperature. It is likely that their assumption of solar abundances explains the discrepancy. On the other hand, Mewe et al. (2001) obtained a similar EM distribution from *Chandra* LETG.

7.3.5 He-like Ions

Using the line ratios R=f/i and G=$(i + f)/r$ (see, e.g., Gabriel & Jordan 1969; Pradhan et al. 1982) from the fluxes of the resonance line (r), the intercombination line (i) and the forbidden

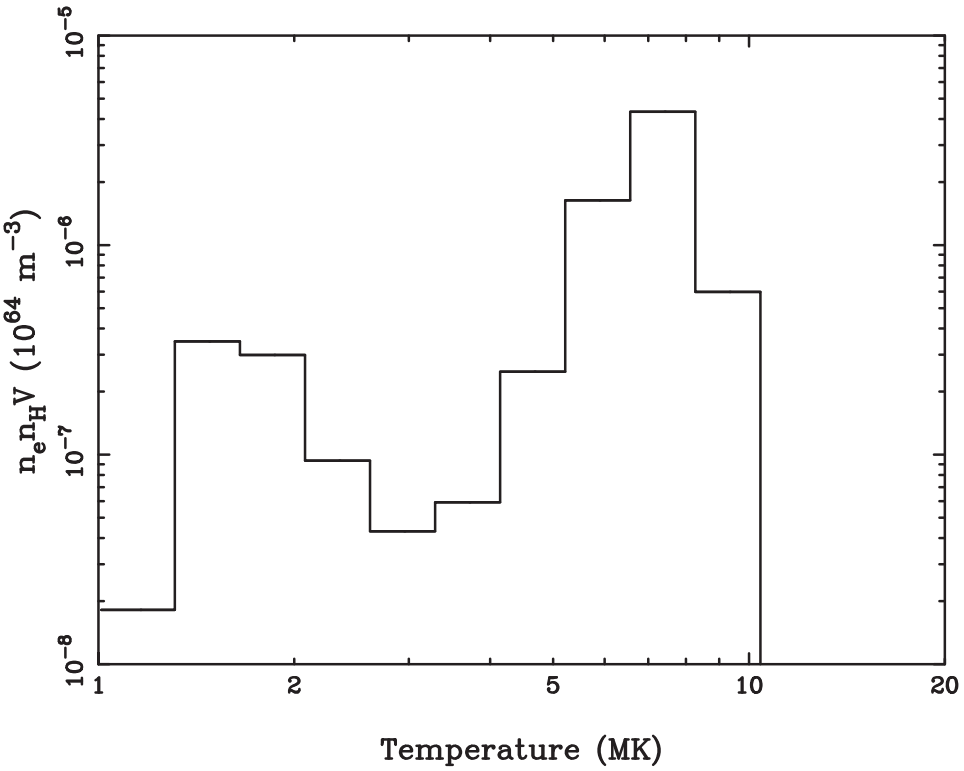

Figure 7.2: *Realization of the EM distribution using Chebychev polynomials of order 5. The distribution does not show any significant EM above 10 MK.*

line (f) of the O VII and, tentatively, Mg XI triplets, we have derived average coronal densities. The Si triplet is strongly blended because of the decreasing spectral resolution of the RGS at short wavelengths, while the Ne triplet is heavily blended by Fe and Ni lines. For the weak N VI triplet, the line intensities were not unambiguously determined. Due to the spatially unresolved nature of stellar coronal X-ray emission, any derived value of a density should be considered as a weighted average of the densities in the various regions of both coronae of Capella.

We used theoretical calculations (Porquet et al. 2001) that take into account the radiative and dielectronic recombinations, and the electronic collisional excitations (see Porquet & Dubau 2000 for the atomic data); they also take into account the influence of the radiation field (photo-excitation) which is important for low-Z ions. We refer to Ness et al. (2001) for additional details. From the measured RGS line fluxes (Tab. 7.1), the ratios for O VII are $R_{\rm obs} = 4.36 \pm 1.3$ and $G_{\rm obs} = 0.78 \pm 0.12$, implying an average electron temperature of $T \approx 2.7$ MK and an upper limit for the average density of $< 1 \times 10^{10}$ cm^{-3}. For the Mg triplet, we tentatively get $R_{\rm obs} = 1.67 \pm 0.65$ and $G_{\rm obs} = 0.62 \pm 0.14$, leading to $T \approx 7$ MK and $n_{\rm e} = 7^{+18}_{-3} \times 10^{12}$ cm^{-3}. However, due to the low spectral resolution at short wavelengths in the RGS (e.g., compared to HETG), the Mg triplet line fluxes are difficult to measure, therefore the derived density should be taken with caution.

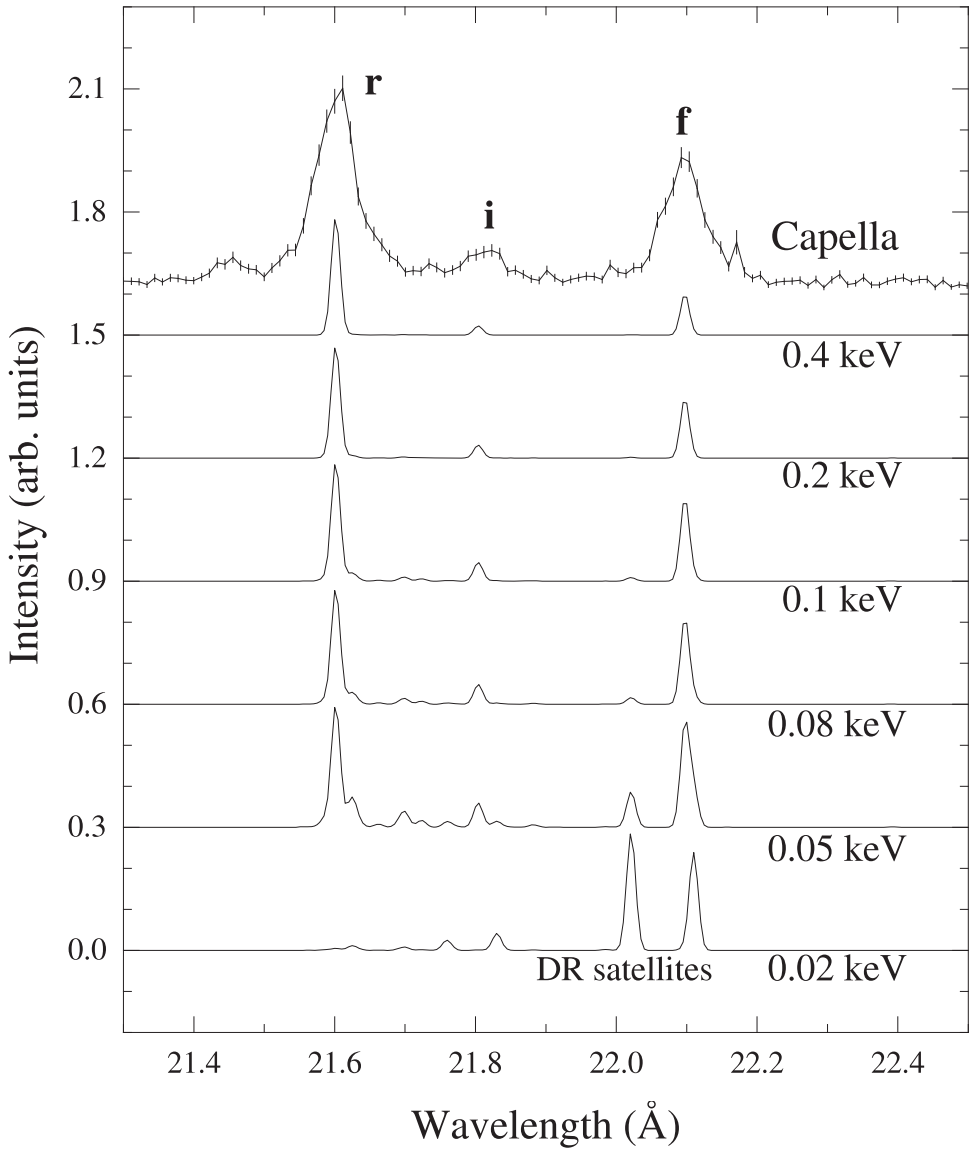

Figure 7.3: *Observed* O VII *triplet with calculated spectra of the* O VII *and* O VI *DR satellite lines for six different electron temperatures. The plots are normalized to the strongest line in each spectrum. Note the steep temperature sensitivity of the DR satellites (see text).*

7.3.6 Dielectronic Recombination Satellite Lines

The O VII spectral region has been separately investigated for the presence or absence of dielectronic recombination (DR) satellite lines. DR satellite lines of He-like spectral lines in hot collisional plasmas are excellent additional tracers of the cool (< 1 MK) plasma otherwise not sufficiently constrained by the available lines. It is, to our knowledge, the first time that such diagnostics is applied to the X-ray spectrum of a stellar corona. The SPEX (and MEKAL) spectral code does presently not include a sufficient description of the DR satellite lines for

low-Z ions such O. Therefore, the lower temperature component of the EM distribution is not well constrained below 1 MK. Using the HULLAC code, we have calculated the emitted spectrum of the He-like lines of O VII including the O VI DR satellite lines in the low-density limit. All of the 1snl and 1s2$ln'l'$ (n' = 2 to 4) levels are included in the computations. The resulting theoretical O spectra, as a function of electron temperature, are depicted in Figure 7.3 together with the data. The strongest DR satellites are at 22.02 Å and at 22.11 Å (Gabriel 1972). The bottom plot (0.02 keV) in the figure clearly demonstrates how the DR satellites dominate the spectrum at low temperature. At slightly higher temperature (0.05 keV), the higher lying satellites, in particular 1s2l3l', produce relatively strong lines at 21.70 Å and at 21.63 Å, but eventually, as the temperature increases, the DR lines become weak and the He-like triplet lines prevail. The RGS data do not allow the identification of DR satellite lines, setting a lower limit of ≈ 1.2 MK to the temperature of the cooler plasma component that forms the O VI–VII lines.

7.4 Discussion and Conclusions

The high-resolution, high signal-to-noise X-ray spectrum of Capella measured by the RGS instruments on board the *XMM-Newton* satellite offers unprecedented spectroscopic power for the study of stellar coronal plasma. It also gives insight into some deficiencies in the present spectral codes.

The derived elemental abundances from the Capella RGS spectrum are found to be generally below their solar photospheric values, or close to them. The abundances are generally similar to the abundances derived from a continuous-temperature model applied simultaneously on *ASCA* and *EUVE* data (Brickhouse et al. 2000; their Table 4). For the O and Ar abundances, we refer to Brickhouse (1996, also reported in Col. 2 of Tab. 4 in Brickhouse et al. 2000).

Recent analysis of the RGS spectrum of the active RS CVn binary star HR 1099 (Brinkman et al. 2001) suggested the presence of an *inverse* FIP effect, i.e., elements with a *high* FIP are overabundant with respect to their photospheric abundances. In Capella, we do not find a clear distinction between the coronal abundances of low-FIP and high-FIP elements. The high-FIP elements Ne, O, and C have abundances below the solar photospheric values; N, another high-FIP element, is consistent with its solar abundance. Low-FIP elements such as Fe, Si, and Mg have coronal abundances also slightly below solar, or consistent with solar. The high Fe abundance ($\approx$0.5) sets Capella apart from other active stars that typically have Fe abundances well below $(0.1 - 0.3)$ the solar photospheric value (e.g., Audard et al. 2001a; Güdel et al. 2001a,b, Chapters 6, 8, 9). It is important to note that McWilliam (1990) derived a photospheric Fe abundance for Capella of 0.43 times solar photospheric, with large errors, however. This may indicate that the coronal Fe abundance is indeed comparable with Capella's photospheric abundance.

The S abundance ($\approx$ 0.1, but $\approx$ 0.35 when the data around the S XIV line at 24.2 Å is removed) is much lower than the abundance derived by Brickhouse (1996) and Brickhouse et al. (2000) who found consistency with the solar photospheric abundance. Note that the RGS spectrum only contains weak L-shell lines of S. We believe that the incompleteness of the atomic

database for these lines largely influences the determination of the coronal abundance of S. Similarly, the Ar, Ca and Ni abundances should be taken with caution.

A realization of the EM distribution (Fig. 7.2) shows that it is continuous but a sharp peak is found between $5 - 8$ MK. Such a peak was suggested from previous *EUVE* data (Dupree et al. 1993; Schrijver et al. 1995; Brickhouse et al. 2000) and recent *Chandra* LETG (Mewe et al. 2001), and HETG data (Behar et al. 2001). Another peak is found at lower temperatures ($1.2 - 2.5$ MK), albeit with a lower EM. This bump is mainly required in order to account for the bright emission lines from the relatively cool O VII triplet and C VI Lyα.

For the first time, to our knowledge we have used the information from the dielectronic satellite lines of the He-like O VII triplet in a stellar spectrum to constrain the plasma EM. Such DR lines are very sensitive to the lowest temperature (< 1 MK) coronal components of the plasma. We did not detect these lines, setting a lower limit of ≈ 1.2 MK for the plasma forming O VI–VII lines, consistent with the lowest temperature with "significant" EM in the globally derived EM distribution.

Best-fit densities from the "cool" O VII and "hot" Mg XI triplets appear to differ considerably, the former indicating an upper limit of 10^{10} cm^{-3}, consistent with both LETG (Brinkman et al. 2000; Ness et al. 2001) and HETG results (Canizares et al. 2000), and the latter tentatively indicating $10^{12} - 10^{13}$ cm^{-3}. This is higher than a recent estimate of the density derived for Mg by Canizares et al. (2000). However, Dupree et al. (1993) derived from highly ionized Fe XXI an electron density similar to ours.

If the above density values are confirmed, it then appears that the coronae of Capella may be bi-modal: On the one hand, we find a low-density cool plasma, and on the other hand, we measure high densities for the hot plasma. Because it is likely that there is a broad distribution of electron densities in the coronae of Capella, we cannot exclude the presence of cool high-density and hot low-density material. It is likely that the two detected plasma portions belong to distinct and different features in the stellar coronae, given the magnitude of their density and temperature differences. This would suggest the simultaneous presence of low-lying, compact hot loops and of larger, cooler loops in the stellar coronal atmospheres of Capella (Mewe et al. 2001).

Our observations suggest clear limitations for the applicability of solar coronal concepts to more active stars. Although Capella is intermediate in its activity between the Sun and extremely active stars such as HR 1099 or dMe stars, its abundance pattern is neither reminiscent of the latter nor in any way similar to the average solar corona (FIP effect). To uncover systematic trends, it will be important to survey the complete range of activity between inactive, solar-like stars and stars like Capella with further high-resolution spectroscopic observations.

Chapter 8

X-Ray Spectroscopy of AB Doradus

Summary

We report results of deep X-ray observations of AB Doradus obtained with the *XMM-Newton* observatory during its Performance Verification phase. The main objective of the analysis is a study of the spectral variability of coronal plasma in a very active star, including investigations of the variable thermal structure, abundance variations, and possible density changes during flares. AB Dor revealed both quiescent and flaring emission. The RGS spectra show flux changes in lines of highly ionized Fe during the flares, and an increase of the continuum. Elemental abundances increase in the early flare phases, by a factor of three. The quiescent abundances are lower than corresponding solar photospheric values, and tend to *increase* with increasing first ionization potential, contrary to the behavior in the solar corona. High-resolution spectra show an average density of the cool plasma of $\approx 3 \times 10^{10}$ cm^{-3}; this value does not change during the flares. We analyze and model the temporal behavior of heating and cooling, and present model results for one of the flares. We find that magnetic loops with a semilength of the order of 2.5×10^{10} cm $\approx$0.3 $R_\star$ are involved.

8.1 Introduction

Late-type stars that have newly arrived on the Zero-Age Main-Sequence (ZAMS) are ideal objects for coronal studies since they are supposed to lack strong circumstellar disks while showing an enhanced level of activity, due to their high rotation rates. AB Doradus, first detected in X-rays by Pakull (1981), is a particularly interesting nearby example. Initially identified as a pre-main sequence weak-lined T Tau star, it is now believed to be located precisely on the ZAMS, based on accurate distance information from Hipparcos (Perryman et al. 1997; 14.9$\pm$0.1 pc) and VLBI (Guirado et al. 1997; 15.0$\pm$0.1 pc). Its age has been estimated to be 20$-$30 Myr (Collier Cameron & Foing 1997). Its short rotation period of 0.514 d (Pakull 1981) is thought to be responsible for the very high ("saturated") X-ray luminosity of $\approx 10^{30}$ ergs s^{-1},

The work presented in this chapter has been published in Güdel et al. (2001a).

Table 8.1: *Observing log*

	First observation: 2000 April 30/May 1	
Instrument	UT range	JD range 2451665.0 +
RGS	19:19:12 - 00:29:24	0.30500 - 0.52042
	02:30:21 - 19:46:29	0.60441 - 1.32395
pn	19:49:42 - 23:27:54	0.32618 - 0.47771
	02:30:21 - 19:32:29	0.60441 - 1.31422
MOS1 . . .	22:02:17 - 00:07:09	0.41825 - 0.50497
MOS2 . . .	20:42:04 - 00:07:11	0.36255 - 0.50499
	Second observation: 2000 June 7	
Instrument	UT range	JD range 2451702.0 +
RGS	05:29:46 - 21:53:16	0.72900 - 1.41199
pn	09:44:12 - 21:22:32	0.90569 - 1.39065

with $L_{\rm X}/L_{\rm bol} \approx 10^{-3}$ (Vilhu & Linsky 1987). AB Dor has been a favorite object for the study of stellar flares, showing an X-ray flare rate of ≈two per day (Vilhu et al. 1993). For further overall properties of AB Dor, we refer to Maggio et al. (2000).

Being the nearest K-type ZAMS star, AB Dor has been the subject of extensive investigations across all wavelength bands. X-ray observations were discussed by Vilhu & Linsky (1987), Collier Cameron et al. (1988), Vilhu et al. (1993), Rucinski et al. (1995), Mewe et al. (1996), White et al. (1996), Kürster et al. (1997), Ortolani et al. (1998), and Maggio et al. (2000). High activity levels were consistently reported, with extremely powerful flares reaching temperatures (T) of 100 MK (Maggio et al. 2000); unusually low coronal abundances were reported from *ASCA*, *Beppo*SAX, and *EUVE*, the typical metallicity level being at $Z \approx 0.3\ Z_{\odot}$ (Mewe et al. 1996; Ortolani et al. 1998; Maggio et al. 2000) despite the measured solar-like photospheric abundances of this star (Vilhu et al. 1987).

AB Dor is an ideal object to study spectral variability in active stellar coronae. X-ray spectroscopy is well suited to investigate the thermal structure, the abundance stratification, and densities of its corona. For this purpose, we have obtained long observations of AB Dor with the *XMM-Newton* X-ray observatory. The telescope's unrivaled sensitivity combined with AB Dor's high X-ray flux allow us to study time variability of the above diagnostics. The present chapter discusses first results from this campaign.

8.2 Observations and Data Analysis

The observations reported here were obtained by *XMM-Newton* (Jansen et al. 2001) in two closely spaced intervals on 2000 April 30/May 1, and on 2000 June 7 (Table 8.1). We refer

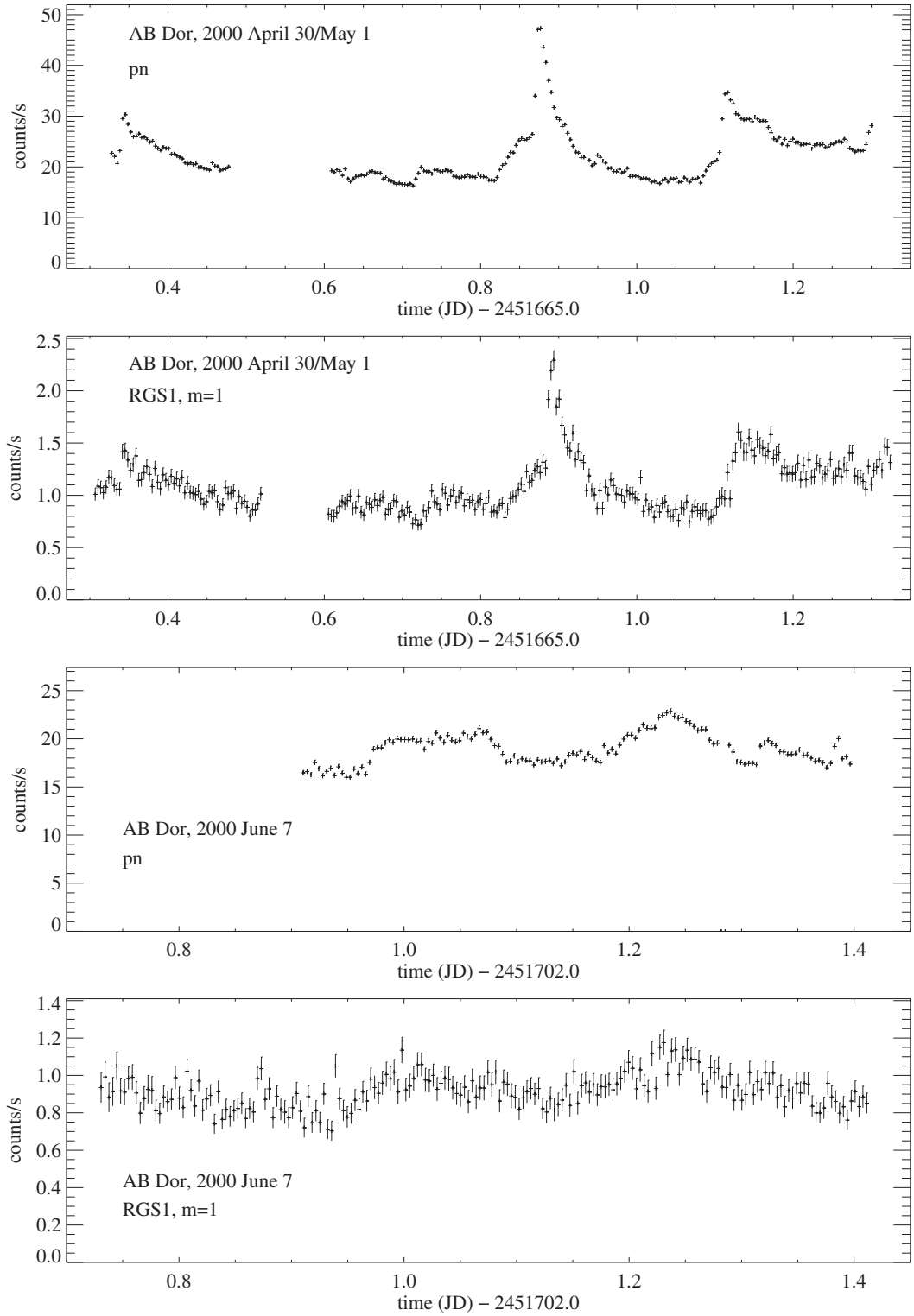

Figure 8.1: *Light curve of AB Dor derived from EPIC pn and RGS1, for the April 30/May 1 observations (upper two panels), and for the June 7 observation (lower two panels). Bin size is 300 s.*

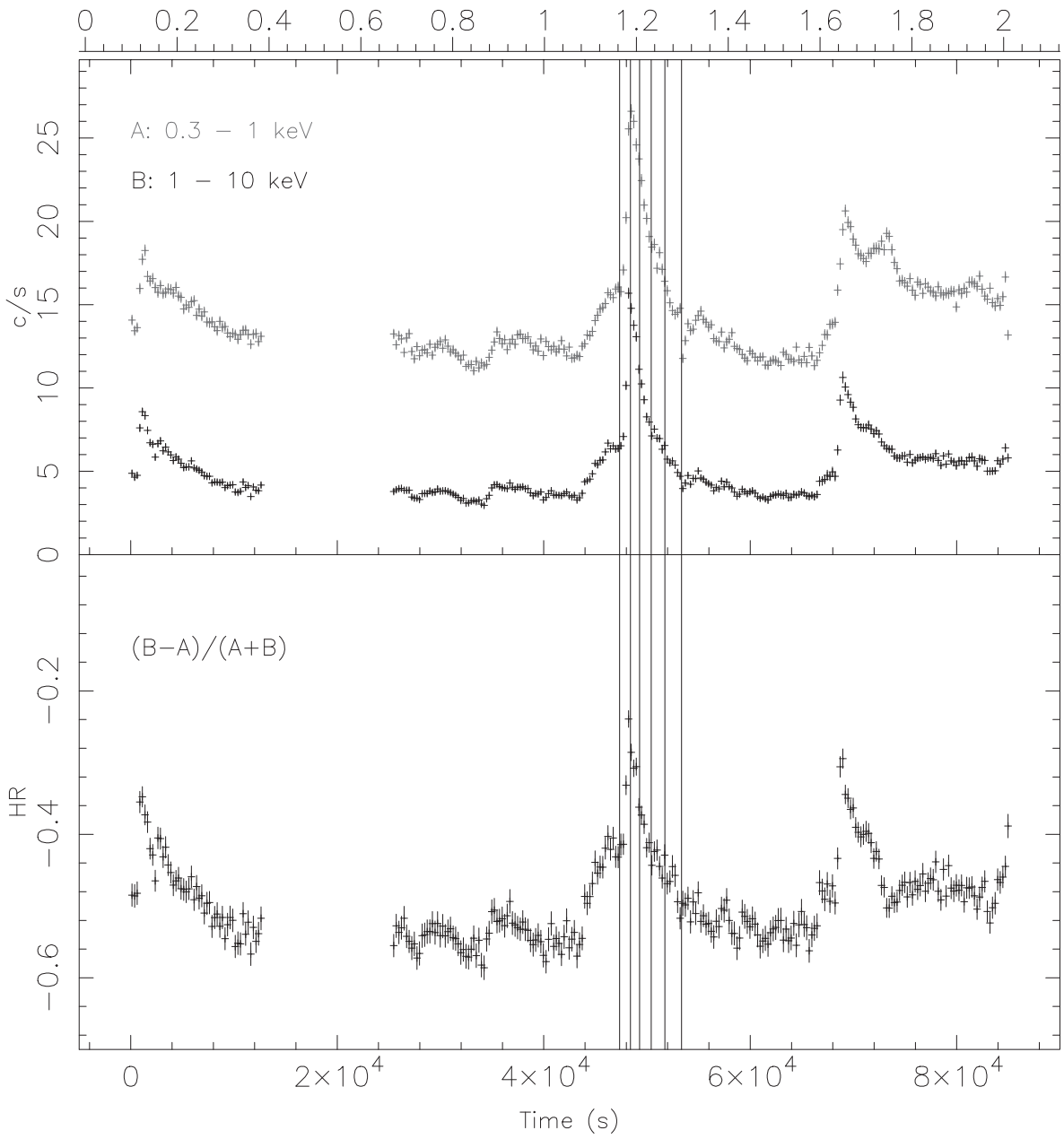

Figure 8.2: *EPIC pn light curves of AB Dor in the 0.3-1.0 (A, upper curve) and 1.0-10 keV (B, lower curve) bands and hardness ratio* $(B - A)/(A + B)$*. Only the first observation is shown. The topmost scale shows the rotational phase calculated from the ephemeris of Innis et al. (1988). The vertical lines define the time segments discussed in Sect. 8.4.*

to den Herder et al. (2001), Strüder et al. (2001), and Turner et al. (2001) for details on the X-ray instruments. In short, three telescopes focus X-rays onto three EPIC cameras (two MOS and one pn camera, sensitivity range 0.1–15 keV). About half of the photons in the converging beams of the telescopes that feed the MOS instruments are diffracted by sets of reflection

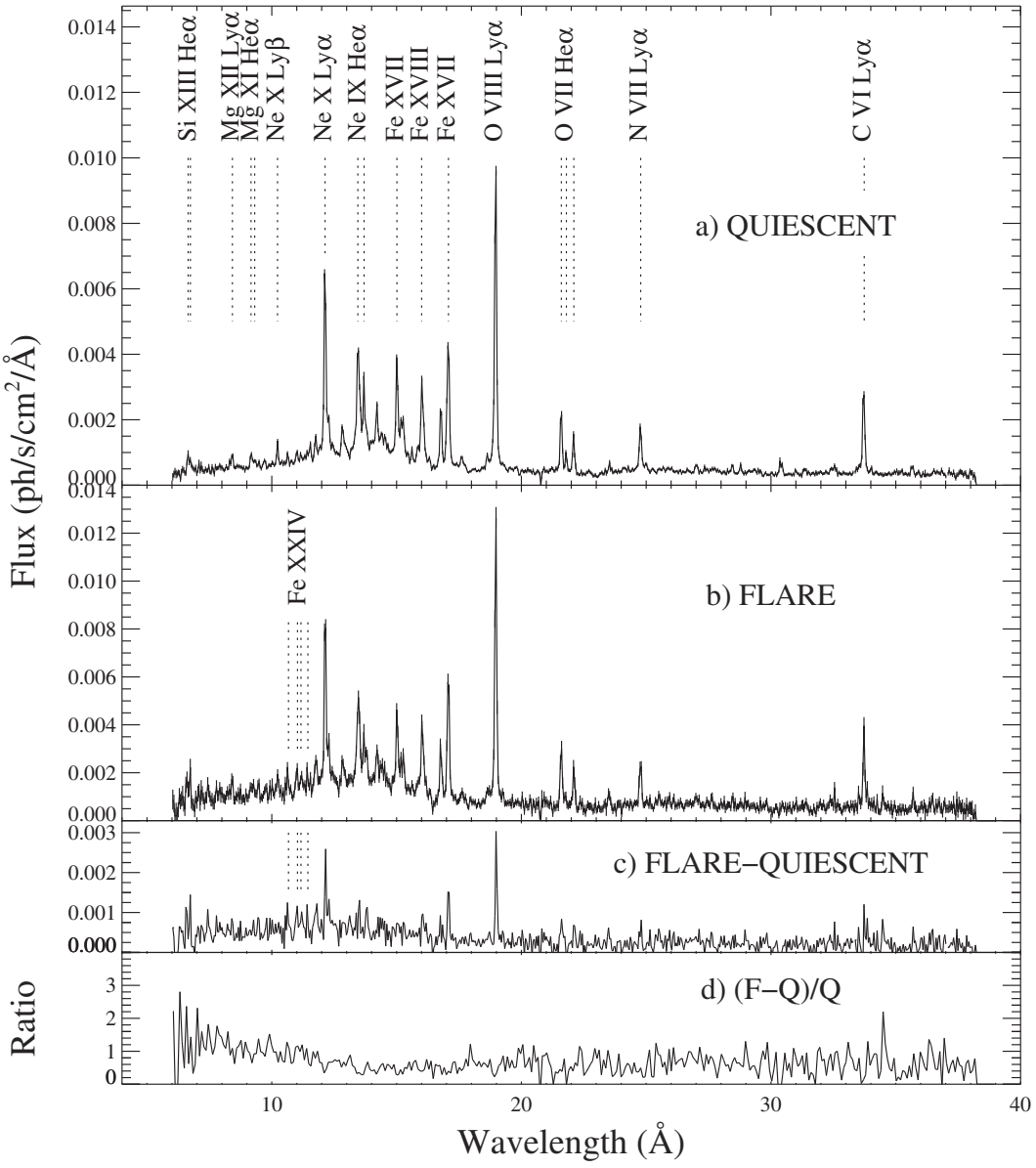

Figure 8.3: *RGS fluxed spectrum of the (a) quiescent and (b) flaring AB Dor, (c) the difference spectrum, and (d) the ratio "(flare−quiescent)/quiescent". Data are binned to a resolution of 0.04375 Å for (a-c) and to 0.0875 Å for (d). Note different flux scales. The* Fe XXIV *lines and an excess continuum shortward of 10 Å are evident in (c) and (d).*

gratings, and are then focused onto the RGS detectors. The RGS spectrometers provide spectral resolution of $\approx$70−500 from 5–35 Å (0.35–2.5 keV). The EPIC pn observed in the small window mode, while the EPIC MOS's used the full window mode in the first observation but were closed during the later observations. MOS1&2 saw only a few hours of exposure time in total, and will not be further discussed. With regard to EPIC pn, we concentrate on the first

observation as this was the only observation that had been processed with the small window calibration at the time of the analysis. It is also the most interesting observation to study spectral variability.

All data were reduced with the *XMM-Newton* Science Analysis System (SAS) software v4.1, using several updates of individual tasks. For the RGS data, standard processing was performed using the RGSPROC task, followed by the spectral extraction and response generation. Analogously, we reduced the pn data with the EPPROC task. The spectral products were analyzed in the Utrecht spectral software SPEX v.2.0 using the MEKAL Collisional Ionization Equilibrium model (Kaastra et al. 1996a), and in XSPEC v11.0 (Arnaud 1996) using the corresponding VMEKAL model. Although the calibration of the response of both RGS is expected to evolve over time, we have used RGS2 for the spectral fit analysis as its calibration was more advanced than for RGS1, except for the analysis of the O VII triplet that is not available from RGS2 (due to the loss of one CCD, see den Herder et al. 2001).

The two observations show a very different behavior (Fig. 8.1). While the first observation reveals repeated flaring, the June observation is dominated by quiescent and slowly varying emission. No evidence for rotational modulation is seen. To identify heating events for further modeling, we defined a hardness ratio (HR) for pn spectra as $(B - A)/(A + B)$, where A is the number of counts in the 0.3−1.0 keV band and B the number of counts in the 1.0−10 keV band. This ratio was found to be sensitive to T variations in a single-T MEKAL plasma, while A and B contain a comparable number of counts to minimize the uncertainty in HR. Background-subtracted light curves in A and B were constructed from counts in the source region ($27''$ radius) and a distant background region (Fig. 8.2, top). The light curves again show the three flares and some additional modulation. A plot of the HR with time (Fig. 8.2, bottom) clearly indicates a correlation between count-rate and hardness (and hence plasma T).

Fig. 8.3ab show the coadded AB Dor high-resolution RGS spectra, calibrated in flux, during quiescence and during the two larger flares (at 0.9 d and 1.1 d, total of ≈8 ks). A series of highly ionized Fe lines and several lines of the Ly and He-like series are visible, most notably from C, N, O, Ne, Mg, and Si. During the flares, strong additional lines appear around 10-12 Å which are partly attributed to Fe XXIV (see difference spectrum in Fig. 8.3c). There is also a significant change in the continuum during the flare (excess continuum suggested by the "ratio" plot in Fig. 8.3d). Both changes suggest a significantly increasing emission measure (EM) at very high temperatures during the flares. Details on the time-variable thermal structure elemental abundances will be discussed in Sect. 8.4.

8.3 Densities From the RGS

The RGS range contains the density-sensitive line triplets of N VI, O VII, Ne IX, Mg XI, and Si XIII. Of these, only the O VII triplet at 22 Å, formed at 1−3 MK, is strong enough in AB Dor for further analysis. We derived an electron density of $n_{\rm e} = (3 \pm 1.5) \times 10^{10}$ cm^{-3} from a global fit in SPEX (90% confidence intervals for a single parameter of interest, $\Delta\chi^2 = 2.71$) - see Fig. 8.4. Combining data from the two larger flare peaks (3000 s around flare peak at 0.9 d,

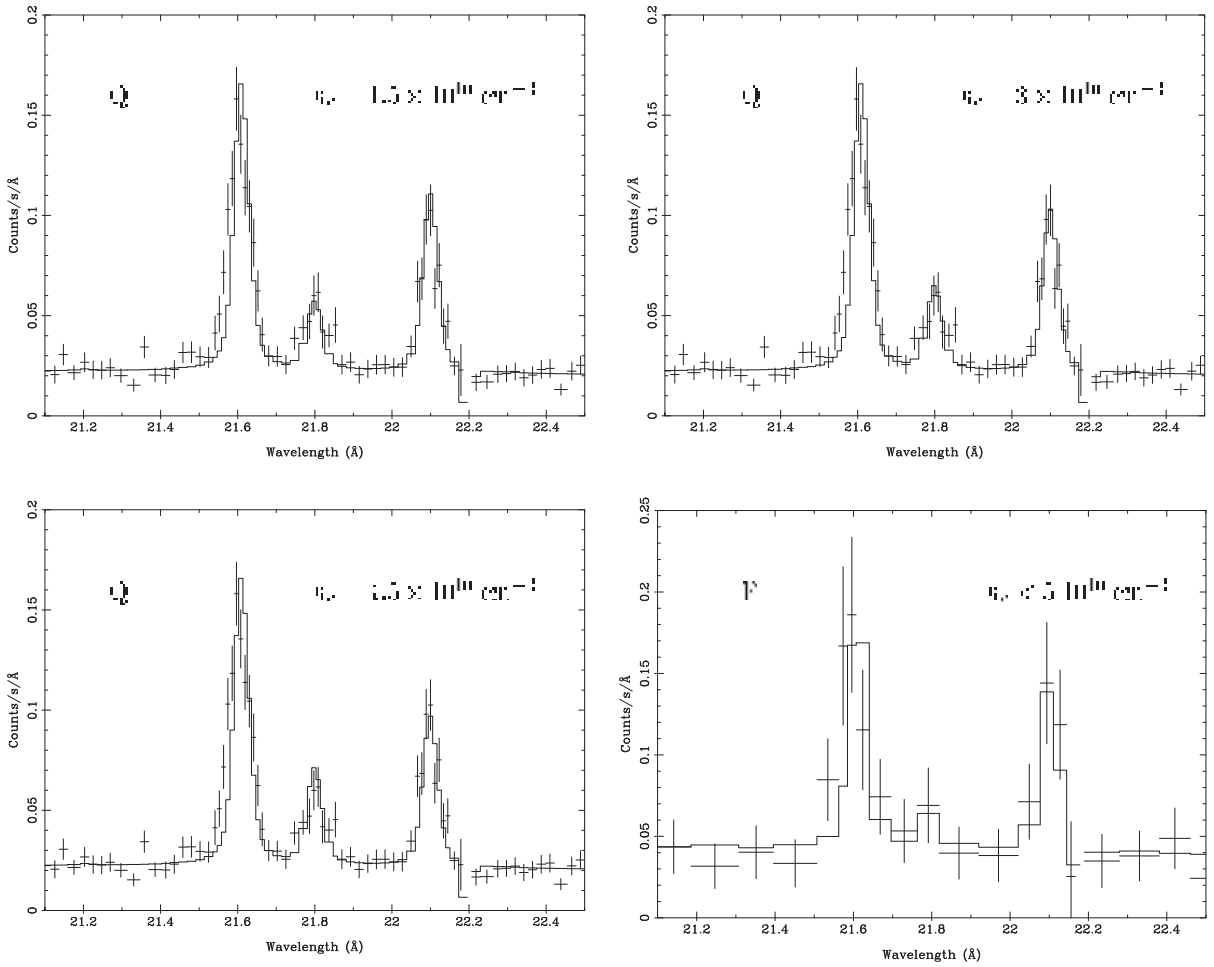

Figure 8.4: *Density-sensitive line triplet of He-like* O VII *(resonance, intercombination, and forbidden lines for increasing wavelength). Upper right panel shows best-fit (histogram) to RGS1 data (error bars) during quiescence, while upper left and lower left plots illustrate deviations for densities of* 1.5×10^{10} *cm*$^{-3}$ *and for* 4.5×10^{10} *cm*$^{-3}$*, corresponding to the 90% confidence limits of* $n_{\rm e}$*. The lower right panel shows the triplet during the two large flares.*

and 5000 s around peak at 1.1 d) we found $n_{\rm e} < 5 \times 10^{10}$ cm^{-3}, comparable with the quiescent value, i.e., there is no appreciable change in the *average* density of the emitting *cooler* material.

To confirm these results, we used an alternative approach by fitting the calibrated line spread function to the individual forbidden (f) and intercombination (i) lines. A flux ratio $f/i = 2.34 \pm 0.69$ was found. Given that the emission is most probably originating from plasma with $T \approx 2 - 3$ MK (Sect. 8.4.1), the new calculations by Porquet et al. (2001) for the O VII triplet indicate $n_{\rm e} = (2.1^{+2.3}_{-1.3}) \times 10^{10}$ cm^{-3} for $T = 3$ MK, and $n_{\rm e} = (2.5^{+2.7}_{-1.4}) \times 10^{10}$ cm^{-3} for $T = 2$ MK. Both values are in very good agreement with the SPEX global fit result.

Table 8.2: *Time ranges of extracted pn spectra (in s from beginning of second part, after the gap, of first observation). Live exposure times are about 66% of the observation time.*

Interval	Start time	End time	Expos. time	Source counts
Quiescent.....	0	18050	11913	247790
I1.....	22050	23111	700	25270
I2.....	23111	23984	576	27780
I3.....	23984	25111	744	27751
I4.....	25111	26436	875	27685
I5.....	26436	28050	1065	27946
Background.....	0	35000	23100	≈9000

8.4 Time-Resolved Spectroscopy

We examined the temperature variation and possible changes in the elemental abundances by performing time-resolved spectral fitting of different sections of the largest flare (0.9 d), and of the quiescent emission. For the EPIC pn, a quiescent spectrum was extracted from the first (pre-flare) 18 ks after the observing gap of the first observation, and fitted in the 0.15–10 keV range with multi-T VMEKAL components. We further chose five intervals across the flare, defined as I1-I5 henceforth (Fig. 8.2). They contain a roughly equal number of counts per spectrum (Table 8.2). All background-subtracted pn spectra were binned to a minimum of 20 counts per bin and fitted using XSPEC with the latest pn medium filter response matrix.

RGS2 spectra of both observations were fitted in SPEX. For quiescence, superior statistics was available from the second observation, although the best-fit results are very similar to the results from the shorter quiescent pieces in the first observation. Spectral analysis of the flare required stronger rebinning than for the pn in order to achieve a sufficient signal-to-noise ratio. We therefore fitted data from sections I2 and I3 together.

8.4.1 The Quiescent Spectrum

The spectral fits of the EPIC pn spectrum used a common global abundance Z and a fixed absorbing column of 2×10^{18} cm^{-2} (e.g., Rucinski et al. 1995). A 4-T MEKAL fit using solar photospheric abundances was found to be significantly better than a 3-T fit (χ^2/ν = 820/550 versus χ^2/ν = 1077/552), but neither was formally acceptable and inspection of the residuals showed evidence for line emission suggesting abundance differences among metals (relative to solar values). The single-parameter 90% confidence interval for the global abundance was (0.22-0.25) solar. The spectrum was therefore fitted with a 3-T VMEKAL model that allowed abundance variations between elements. The abundances of C, N, and Ca were set to their RGS values since these elements show only very weak or unresolved features in the pn spectrum. This produced a much better fit ($\chi^2/\nu = 696/543$; see Tab. 8.3 and Fig. 8.5).

Table 8.3: *3-temperature fit to the quiescent spectrum allowing individual elemental abundances*[a] *to vary. The best-fitting values are given together with their 90% confidence intervals for a single parameter of interest ($\Delta\chi^2 = 2.71$).*

	pn (April 30/May 1):		RGS2 (June 7):	
Parameter	Value	90%	Value	90%
kT_1 [keV]	0.11	(0.106-0.114)	0.32	(0.296-0.337)
kT_2 [keV]	0.62	(0.609-0.627)	0.68	(0.671-0.687)
kT_3 [keV]	1.90	(1.762-2.002)	1.93	(1.79-2.14)
EM_1 [10^{51} cm^{-3}]	16.1	(14.7-17.4)	8.30	(7.10-9.54)
EM_2 [10^{51} cm^{-3}]	57.3	(54.1-60.3)	36.5	(34.0-39.2)
EM_3 [10^{51} cm^{-3}]	19.6	(18.2-21.7)	33.4	(31.5-35.2)
C	=0.46	...	0.46	(0.26-0.69)
N	=0.53	...	0.53	(0.46-0.61)
O	0.49	(0.46-0.52)	0.40	(0.37-0.43)
Ne	0.70	(0.61-0.79)	0.99	(0.92-1.06)
Mg	0.31	(0.28-0.36)	0.27	(0.21-0.33)
Si	0.29	(0.26-0.33)	0.14	(0.05-0.23)
S	0.38	(0.29-0.48)	0.04	(0.01-0.07)
Ar	1.13	(0.79-1.46)	0.86	(0.60-1.16)
Ca	=0.18	...	0.18	(0.00-0.43)
Fe	0.19	(0.17-0.20)	0.22	(0.21-0.23)
Ni	1.33	(1.13-1.55)	0.47	(0.36-0.57)

[a]Abundances relative to solar photospheric (Anders & Grevesse 1989)

Table 8.3 also reports the RGS2 best-fit results of the second observation. There is acceptable agreement between pn and RGS, with a few exceptions. We note, however, that the instruments are complementary: The pn provides good results for high temperatures and the elements Si, S, Ar, and Fe, while the RGS is sensitive to intermediate temperatures and provides good access to strong, individual lines in particular of C, N, O, Ne, Mg, Si, and Fe. The discrepancies for S and Si are most likely due to some poor atomic data used in the code, related to L-shell transitions of these elements (Chapter 7). Overall, the results show underabundances of all elements relative to solar photospheric values (Anders & Grevesse 1989). Note that elements with a high First Ionization Potential (FIP), such as C, N, O, and Ne, tend to show higher abundances than some low-FIP elements (Fe, Mg, Si). This "inverse FIP effect" was also noted by Brinkman et al. (2001) for HR 1099. Abundances from RGS and pn (only RGS for C, N, and Ca) are illustrated in Fig. 8.6, normalized to the oxygen abundance. The abundances of Ne and Ar (the two highest-FIP elements) and Ni are particularly high (disagreement between pn and RGS results for Ne and Ni, however). We note that the results are overall remarkably consistent with findings from *ASCA* and *EUVE* spectroscopy (Mewe et al. 1996).

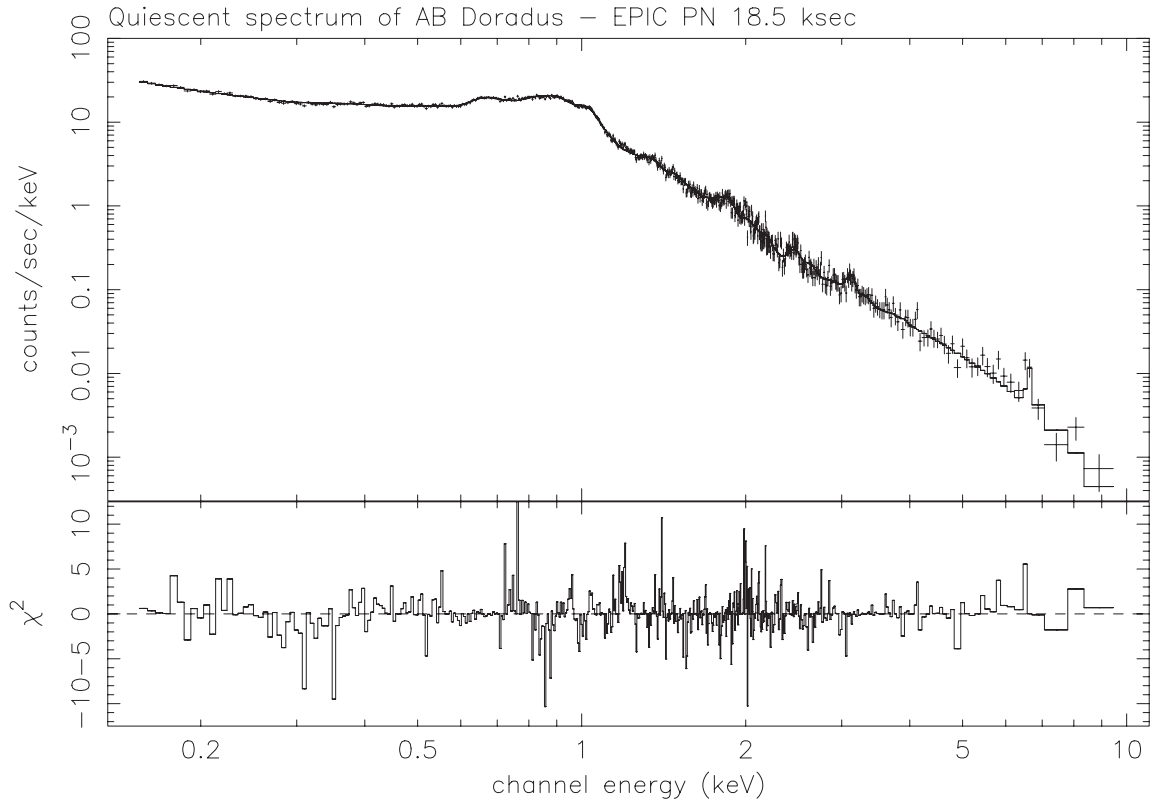

Figure 8.5: *3-temperature fit to the EPIC pn quiescent spectrum. The χ^2 residuals are shown.*

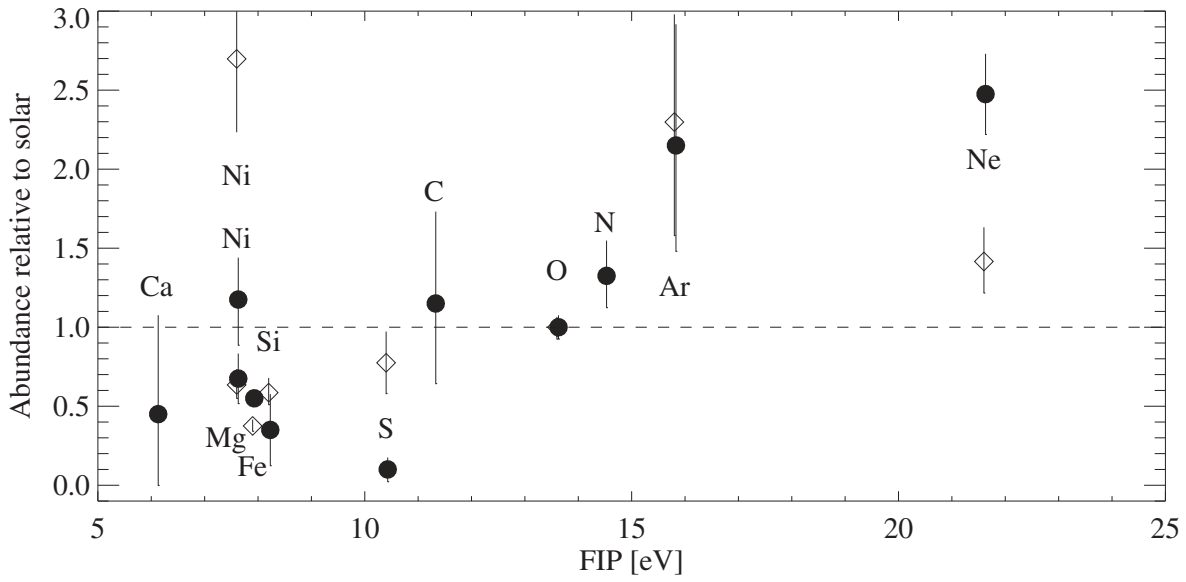

Figure 8.6: *Elemental abundances relative to solar photospheric values (Anders & Grevesse 1989), normalized to the oxygen abundance. Filled circles: from RGS; diamonds: from pn.*

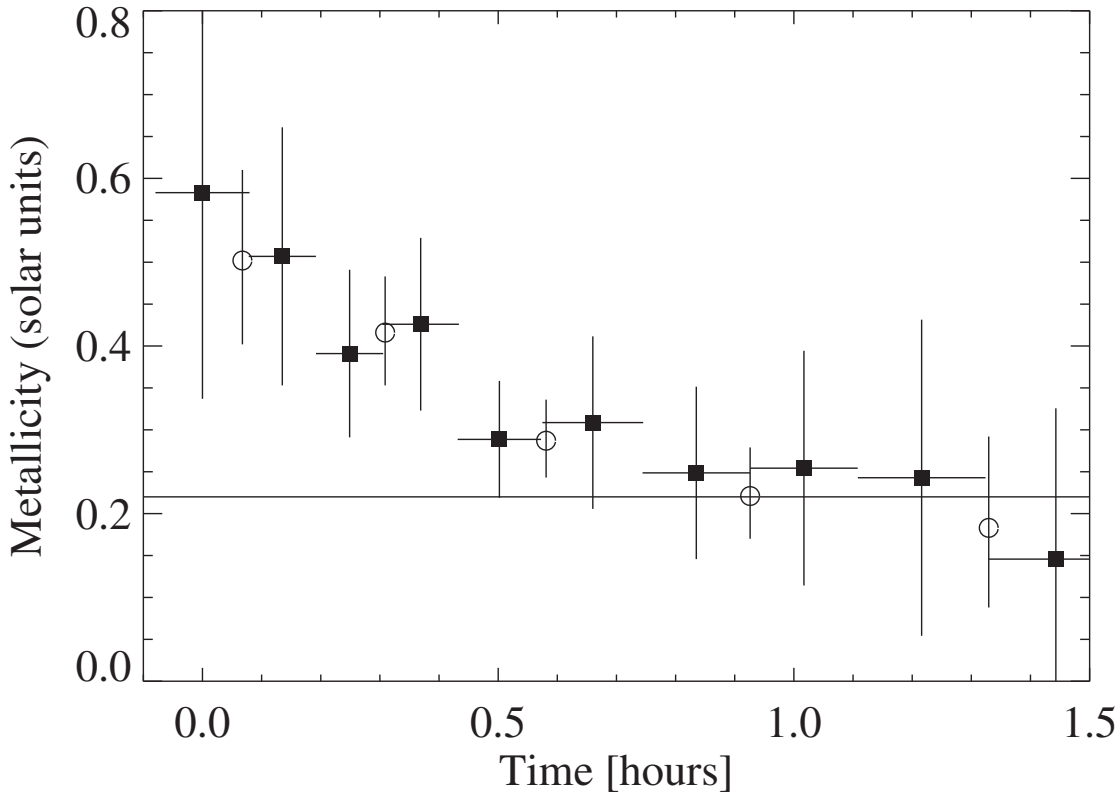

Figure 8.7: *Time variation of the best-fit plasma metallicity Z during the flare. The open symbols refer to the results reported in Tab. 8.4; the filled circles show Z at double resolution. Only the time intervals (horizontal error bars) related to the latter results are shown, for clarity.*

8.4.2 The Flare Spectra

The pn spectra of the flare at 0.9 d were modeled with the fixed 3-T quiescent model (Sect. 8.4.1) plus a single VMEKAL plasma component. Given the short timescales of the flare and the limited statistics, we fitted a "global metallicity" Z instead of individual abundances. Note, however, that Z is largely dominated by the element Fe. The results for each flare section can be seen in Table 8.4.

The emission measure of the flare component follows the overall flux level. The temperature and the global metallicity Z appear to be highest during the rise phase of the flare (I1) and decrease thereafter, although the temperature seems to stall as it falls to the temperature of the hottest quiescent component. Only in the final two sections is the metallicity statistically consistent with the quiescent Z value (Sect. 8.4.1). We have repeated the metallicity analysis at higher time resolution, and all results are summarized in Fig. 8.7. This plot confirms that an abundance enhancement by a factor $\approx$3 occurred at the very beginning of the flare. The results for RGS2 (combined intervals I2 and I3) are also reported in Table 8.4. The best-fit Z abundance is similar to the pn value, although with large confidence error ranges.

Table 8.4: *4-temperature fits to the flare section spectra. Three components are fixed to the quiescent model while the temperature, normalization and global abundance Z of the fourth component are allowed to vary. The final column shows the improvement in χ^2 over a similar fit with the elemental abundances constrained to their individual quiescent levels. For RGS2, kT_4 was constrained to ≤ 2.5 keV.*

Instrument	Interval	kT_4	90%	EM_4^a	90%	Z_4	90%	χ^2/ν	χ^2_ν	$\Delta\chi^2$
pn	I1	2.85	(2.71-3.06)	31.7	(30.3-33.0)	0.502	(0.402-0.610)	454/390	1.17	32
	I2	2.40	(2.19-2.51)	51.4	(59.7-53.1)	0.416	(0.353-0.483)	524/396	1.32	42
	I3	1.72	(1.65-1.79)	32.1	(30.8-33.4)	0.287	(0.243-0.336)	482/369	1.31	17
	I4	1.73	(1.64-1.82)	21.6	(20.5-22.7)	0.221	(0.170-0.279)	438/354	1.24	1
	I5	1.96	(1.75-2.14)	11.0	(10.1-11.9)	0.183	(0.088-0.292)	351/340	1.03	0
RGS2	I2&I3	2.5	(1.12-2.5)	106	(85.1-126.3)	0.349	(0.127-0.642)	60/242	0.25	-1.8

[a] EM in units of 10^{51} cm^{-3}

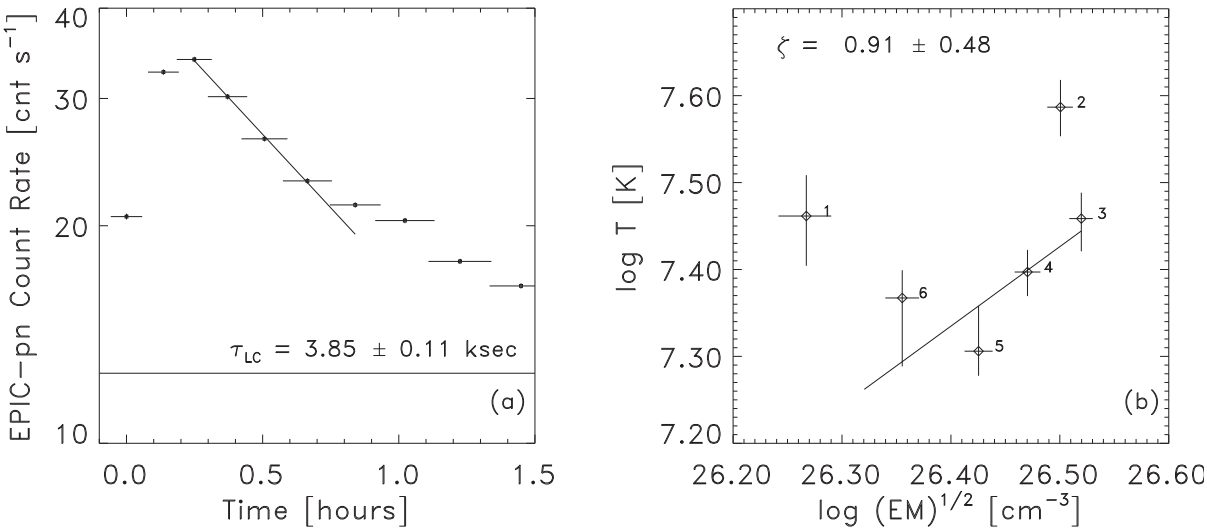

Figure 8.8: *(a) EPIC pn light curve with best-fit exponential law. The horizontal line indicates the quiescent emission level. (b) Flare evolution in the* $\log T$ *vs.* $\log \sqrt{EM}$ *diagram with best-fit linear regression curve (for points 3−6). The numbers indicate the first 6 time intervals in (a).*

8.5 Flare Decay Analysis

We have analyzed the decay phase of the flare at 0.9 d with the approach developed by Reale et al. (1997) and Reale & Micela (1998) in order to derive the dimension of the flaring stellar loops. We refer to these references for further information. The method is based on detailed hydrodynamic models, and it is sensitive to the presence of sustained heating during the flare decay. For the present study, the technique has been calibrated (courtesy of F. Reale) for the EPIC pn response, in the energy band 0.15-10 keV.

We divided the whole flare into 10 time bins, by splitting in two each interval reported in Table 8.2 in order to get an adequate sampling of the flare decay. Spectral analysis was performed as in Sect. 8.4.2. The flare decay shows a double-exponential behavior (Fig. 8.8a) with an initial e-folding decay time, $\tau_{\rm LC}$, of about one hour. We first determine the slope ζ of the decay in the $\log T$ vs. $\log \sqrt{EM}$ diagram (Fig. 8.8b). The method is applicable in the range $0.4 < \zeta \leq 1.9$, where the lower bound corresponds to the case of a flare decay entirely driven by sustained heating, and the upper bound to the case of no heating during the decay. We find a best-fit slope $0.8 < \zeta < 1.1$. This result thus implies continuous loop heating, corresponding to a heating decay time of ≈ 2 ks. The resulting loop semilength is $L = (2.5 \pm 1.5) \times 10^{10}$ cm, which implies – for a loop in hydrostatic equilibrium – a plasma pressure of $\approx 5 \times 10^3$ dyne cm^{-2}, at the time of the T peak (loop apex $T_{\rm max} = 7 \times 10^7$ K), and a maximum heating rate of ≈ 4 erg cm^{-3} s^{-1} (Rosner et al. 1978).

8.6 Conclusions

Our observations present AB Dor in many facets: Quiescent, slowly varying, and moderately flaring intervals have been investigated spectroscopically, using both CCD and grating spectra from *XMM-Newton*. Spectroscopy of the He-like O VII lines allows us to measure an average coronal density of 3×10^{10} cm^{-3} for plasma of $\approx$1–3 MK. No change is seen during the flares. We attribute this result to the fact that flare plasma is predominantly hot and does not significantly contribute to the O VII line flux.

All data sets show low elemental abundances (below solar photospheric) although the photospheric abundances of AB Dor are near-solar (Vilhu et al. 1987). This result confirms previous measurements with low-resolution devices, e.g., onboard *ASCA* and *EUVE* (Mewe et al. 1996; Ortolani et al. 1998) and *Beppo*SAX (Maggio et al. 2000). Interestingly, the high-FIP elements, in particular Ne, show very high relative (to oxygen) abundances. There is, in fact, evidence for an "inverse FIP effect", i.e., abundances increase with increasing FIP, contrary to solar coronal behavior (Meyer 1985; Feldman 1992). A detailed study of the inverse FIP effect is presented by Brinkman et al. (2001), who used the *XMM-Newton* RGS instruments for a deep exposure of the X-ray emission of HR 1099. During the larger flare at 0.9 d, we detect an increase of the metal abundance (dominated by Fe), which however rapidly decays back (within $\approx$30 minutes) to the quiescent level. At the same time, the temperature of the flare component decreases, but only to a value corresponding to the hotter component in the quiescent emission. It appears that the plasma in these flaring loops is maintained at high temperatures long after the flare peak.

This flare has been modeled with the same approach used recently in the interpretation of a number of X-ray flares seen from AB Dor with *ASCA* and *Beppo*SAX (Ortolani et al. 1998; Maggio et al. 2000). Our analysis suggests continuous heating during the decay on a time scale of $\approx$2 ks and a loop semilength of $\approx 2.5 \times 10^{10}$ cm. Assuming for AB Dor a radius of ≈ 1 R$_\odot$ (Maggio et al. 2000), the loop semilength is ≈ 0.3 R$_\star$. This is similar to or somewhat smaller than the sizes derived with the same method for two large flares on AB Dor observed by *Beppo*SAX (which gave loop semilengths of 3.5×10^{10} and 4.9×10^{10} cm, respectively; Maggio et al. 2000) and for a moderate-size flare seen by *ASCA* (which resulted in a loop semilength of 3.2×10^{10} cm; Ortolani et al. 1998). Note that the flare seen by *XMM-Newton*, with an estimated total energy of $\approx 10^{34}$ erg, is much smaller than the flares seen by *Beppo*SAX which had a total energy in X-rays two orders of magnitude larger and reached a much higher coronal temperature ($\approx 10^8$ K). This indicates the extreme variability of the magnetically active corona of AB Dor, ranging from relatively quiescent phases (as observed during the *XMM-Newton* observation on 2000 June 7) to moderate-sized flares, and to episodes of extremely powerful flares. Yet, the typical dimensions of all these flares derived with the same method do not differ by more than a factor of 2 and represent a significant fraction of the stellar radius.

Chapter 9

Coronal Structure in the Castor X-Ray Triplet

Summary

We present results of a comprehensive X-ray investigation of the multiple stellar system Castor AB + YY Gem. The observations were obtained with the *XMM-Newton* observatory. We report the first *spatially separated* detection and identification of both Castor A and B as frequently flaring X-ray sources. Spectral modeling of the YY Gem and Castor coronal sources indicates a broad plasma distribution between $2-15$ MK. Elemental abundances are found to be below solar photospheric values, with the abundance of Ne being highest (≈ 0.7 times solar photospheric). The abundances increase during a large flare, most notably for Fe. The O VII He-like line triplet indicates average coronal densities of the cooler plasma of a few times 10^{10} cm^{-3} for YY Gem and Castor. The YY Gem light curve shows three deep eclipses, indicating that the coronae of both binary components are similarly active and are relatively compact. A 3-D light curve inversion shows that coronal active regions follow density scale heights compatible with spectroscopically measured temperatures. The dominant densities also agree with spectroscopic values. Most active regions are located between ± 50 degrees latitude, in agreement with findings from previous Doppler imaging. We also report the tentative detection of line broadening due to orbital motion.

9.1 Introduction

Close binary systems are of great value for the study of atmospheric structuring. Although short-period binaries are often tidally locked, the mutual influence of the components on the internal structure and dynamo is poorly understood; it appears that the principal effect of binarity is the enforced rapid rotation of the components, which generates strong magnetic fields through a dynamo (Guinan & Giménez 1993).

The work presented in this chapter has been published in Güdel et al. (2001b).

Comparison between coronal properties of binary components and single, active field stars potentially provides information on the generation of the dynamo. The ubiquitous magnetic activity in close binary stars suggests the presence of a strong magnetic dynamo in the stellar interiors which, according to current theory, is generated by convection and differential rotation. Given their strong tidal effects, however, close binary stars are expected to show little or no differential rotation. It thus seems that differential rotation plays a minor role in the generation of the dynamo, or that the stellar interiors rotate differentially despite the observed tidal locking of the photospheres (Guinan & Giménez 1993). *Eclipsing* binaries further offer a unique advantage for the study of the spatial extent, the distribution, and the location of emitting material. Such systems may provide information on the location of the underlying dynamo.

Some stars or binaries indicate the presence of solar-like coronal structures that are comparable with solar active regions (Schmitt & Kürster 1993), while observations of other systems suggest extended structures in particular between the components, perhaps related to intrabinary magnetic fields (Uchida & Sakurai 1983; Siarkowski et al. 1996). Giant magnetic structures have been identified on RS CVn binaries through eclipse mapping (White et al. 1990). Spectral differences at different phases of the eclipse may indicate radial structuring, but reported results are ambiguous and contradictory (Walter et al. 1983; White et al. 1990; Ottmann, Schmitt, & Kürster 1993).

Strong polar magnetic fields have been proposed for magnetically active stars (Schüssler & Solanki 1992) based on arguments involving Coriolis forces in the stellar interior. Doppler imaging of active stars indeed suggests active regions concentrated at high latitudes (e.g., Strassmeier & Rice 1998b). Corresponding *coronal* geometries have also been reported from radio observations (Benz, Conway, & Güdel 1998; Mutel et al. 1998) and from X-ray observations of a flaring region that was occulted during an eclipse of Algol (Schmitt & Favata 1999). Radio Very Long Baseline Interferometry (VLBI) observations provide clues for very extended magnetospheres, including structures of the size of the intrabinary distance in binary systems (Mutel et al. 1985, 1998; Alef, Benz, & Güdel 1997; Benz, Conway, & Güdel 1998). The question then is whether such features are generally found on active stars, whether they contain hot plasma, whether they are preferred on single stars or on binaries, and whether there is additional strong activity at low latitudes. To address these questions, we have obtained a long observation of the Castor triplet of stellar binaries with the *XMM-Newton* observatory.

9.2 The Castor System: Previous Knowledge

Castor is a hierarchical sextuplet system at a distance of 15.81 ± 0.31 pc (Perryman et al. 1997). The principal optical components are Castor A (A1 V) and Castor B (A5Vm) in an orbit with a period of $\approx$467 yrs and a separation of presently $3\farcs9$. Each component is accompanied by an invisible late-type star in a close orbit. Castor A's companion is most likely to be a late K star (Güdel & Schmitt 1996) in a 9.21 d eccentric orbit, while Castor B's companion appears to be an early M dwarf (Güdel & Schmitt 1996) in a 2.93 d circular orbit (orbit information from

Table 9.1: *Observing log on 2000 April 24/25*

Instrument	UT range	JD range 2451659.0 +
RGS	18:20:42 - 00:49:19	0.26438 - 0.53425
	02:54:14 - 21:15:19	0.62100 - 1.38564
MOS	19:22:12 - 00:45:25	0.30708 - 0.53154
	03:55:40 - 20:52:16	0.66366 - 1.36963
pn	18:42:50 - 00:47:50	0.27975 - 0.53322
	03:16:26 - 20:54:41	0.63641 - 1.37131

Batten, Fletcher, & Mann 1978; Heintz 1988; Haisch et al. 1990).

YY Gem (= Castor C) is a short-period spectroscopic binary and flare star (e.g., Haisch et al. 1990) located $71''$ south of the Castor system. It is gravitationally bound to Castor but only marginally so (Anosova & Orlov 1991). It consists of two almost identical dMe stars in a circular 0.814 d orbit. Due to the fortunate orbit inclination angle of $86\overset{\circ}{.}2$ (Pettersen 1976), the system produces nearly total primary and secondary eclipses, where the primary has a slightly larger radius (0.66 vs 0.58 $R_\odot$) and mass (0.62 vs 0.57 $M_\odot$) than the secondary (Haisch et al. 1990). Doppler imaging shows magnetic photospheric spot concentrations in mid-latitude bands (around $\pm 45^\circ$), with a weaker spot at the equator (Hatzes 1995).

YY Gem has been extensively observed in X-rays. Pallavicini et al. (1990b) report quiescent and flaring emission not only from YY Gem itself, but they detect the (unresolved) Castor AB system as a somewhat weaker X-ray source as well. This led to some speculation about possible X-ray emission from A stars. Later observations obtained by *ROSAT* (PSPC & HRI) and by *ASCA* addressed this problem further (Schmitt et al. 1994; Gotthelf et al. 1994). Castor AB was identified again, revealing a surprisingly high rate of flares. Positional analysis indicated that the emission is most probably coming from Castor A. The observed X-ray luminosity requires a mass $> 0.4 M_\odot$ if a single star is responsible (Schmitt et al. 1994).

Schmitt et al. (1994) present the first high-resolution radio observations of the Castor system, revealing radio emission not only from YY Gem as reported earlier (Linsky & Gary 1983), but also from Castor A, where the flux ratio $f_{\rm Castor}/f_{\rm YYGem}$ is similar to the X-ray flux ratio. The discovery of the third radio source, coincident with Castor B, showed that all three binary systems are "magnetically active" (Güdel & Schmitt 1996). VLBI studies revealed a coronal size of $2\ 10^{11}$ cm for YY Gem, corresponding to the intrabinary distance (Alef et al. 1997). The absence of a detected radio eclipse supports the large size. However, indications of deep eclipses were reported from X-ray observations (Haisch et al. 1990), clearly suggesting different structures for radio and X-ray emitting plasma.

9.3 Observations and Data Analysis

The observations reported here were obtained by *XMM-Newton* (Jansen et al. 2001) in two closely separated intervals (Table 9.1). Two EPIC MOS cameras (Turner et al. 2001) provide an angular resolution of $\approx 4''$, just comparable with the separation between Castor A and B. Both MOS were operated in the "partial window mode 2", thus including both Castor and YY Gem. The EPIC pn camera (Strüder et al. 2001) was operated in the small window mode, with Castor AB outside the field of view. The two RGS detectors (den Herder et al. 2001) were in spectroscopy mode. The optical monitor (Mason et al. 2001) was in a closed position, due to the strong optical light of Castor AB.

All data were reduced with the XMM-Newton Science Analysis System (SAS) software version 4.1, using several updates of individual tasks. For the RGS data, standard processing was performed using the RGSPROC task, followed by spectral extraction and response generation. The RGS fully separates Castor from YY Gem. The RGS spectral products were analyzed in the Utrecht spectral software SPEX using the Collisional Ionization Equilibrium model CIE (Kaastra et al. 1996a).

The EPIC MOS data were processed using EMPROC. For the spectral analysis, we used a response matrix provided by Turner et al. (2001). The EPIC pn data were reduced with EPPROC. A preliminary calibration was applied to the small window data. We used EVSELECT for source extraction. Spectral analysis was performed in XSPEC (Arnaud 1996) using multi-T models for optically thin plasma (VMEKAL) that are compatible with the CIE model.

9.4 Results

9.4.1 X-Ray Images and Light Curves of YY Gem and Castor AB

The EPIC MOS show for the first time spatially separated images of Castor A and B and thus prove that *both* Castor binaries (i.e., most probably their low-mass companions) are X-ray sources (Fig. 9.1), compatible with their radio detections (Güdel & Schmitt 1996). Their separation and position angle coincide with the optically determined values (Heintz 1988). Overall, Castor A is X-ray brighter. Both stars flare frequently (Fig. 9.2b), in fact at a surprisingly high rate, so that no part of the light curve is constant, with Castor B's flare rate being somewhat higher. A closer look at Fig. 9.2b shows that flares on Castor B reveal rapid decays, while on Castor A they decay less rapidly. The light curve of YY Gem will be discussed further below.

9.4.2 The RGS Spectra, and Density Analysis

Fig. 9.3 shows the coadded and fluxed spectra of YY Gem and Castor AB from all RGS observations. A series of lines of highly ionized Fe and several lines of the Ly and He series are visible, most notably from C, N, O, and Ne. The significant continuum indicates the presence of hot plasma in both sources. The flux ratio between the forbidden (f) and the intercombination (i) lines of the He-like O VII triplet at 22Å is density-sensitive in the range $10^9 - 10^{13}$ cm^{-3}

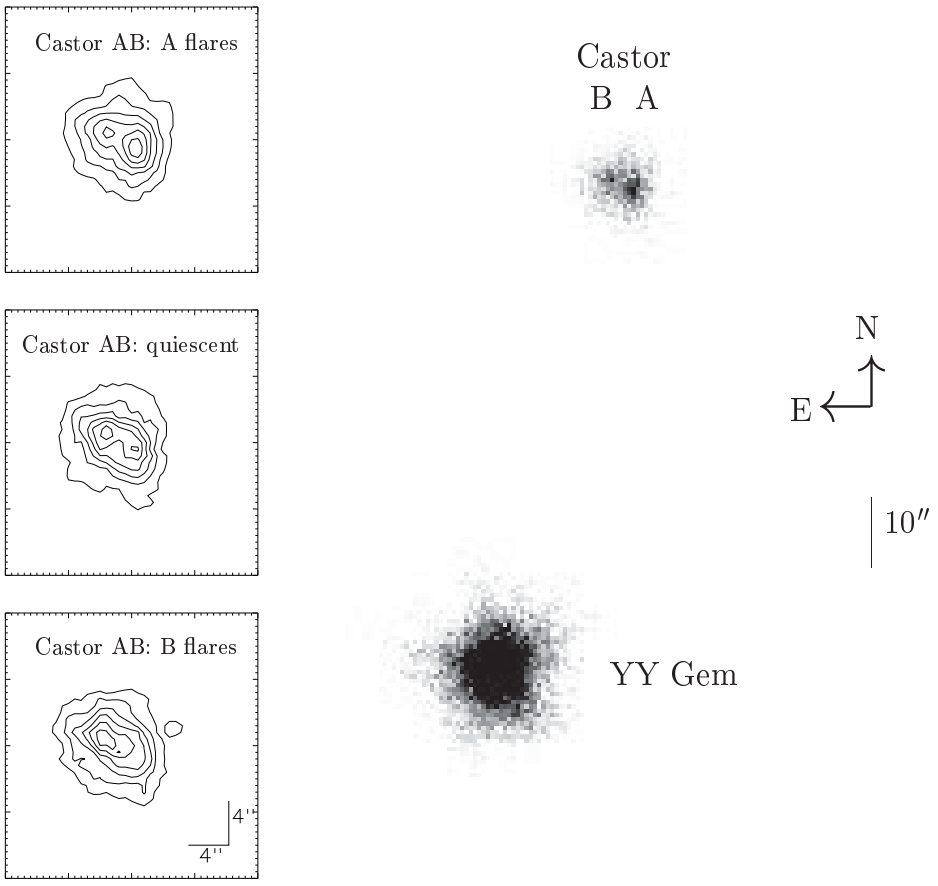

Figure 9.1: *EPIC MOS1 image of the Castor system. The components are labeled. Insets: Contour plots (normalized relative to peak) of Castor AB data subsets. Top: Only flares on Castor A. Middle: Low-level emission. Bottom: Only flares on Castor B (see Fig. 9.2b).*

(Mewe et al. 1985). We have fitted (Fig. 9.4a) the triplet for the quiescent RGS1 spectrum of YY Gem in SPEX and found $n_{\rm e} = (2.9^{+3.4}_{-2.5}) \times 10^{10}$ cm^{-3}, where the errors signify 90% confidence limits. To confirm this value, we derived the individual f and i fluxes by fitting the line spread function to the lines, to obtain a flux ratio f/i = 2.75$\pm$0.92. Given that the emission is most probably originating from plasma with $T \approx 3$ MK (Sect. 9.4.3), the new calculations by Porquet et al. (2001) for the O VII triplet indicate $n_{\rm e} = (1.6^{+2.6}_{-1.4}) \times 10^{10}$ cm^{-3}, in agreement with SPEX. For Castor, we find a similar value from SPEX, $n_{\rm e} = (1.6^{+2.3}_{-1.6}) \times 10^{10}$ cm^{-3}, although it is not constrained toward low densities.

9.4.3 Thermal Structure and Abundances

We fitted separately RGS2, MOS and pn data for the quiescent YY Gem before the large flare at 1.35 d with 3-T coronal models (Table 9.2). For the MOS, the time interval was $t =$

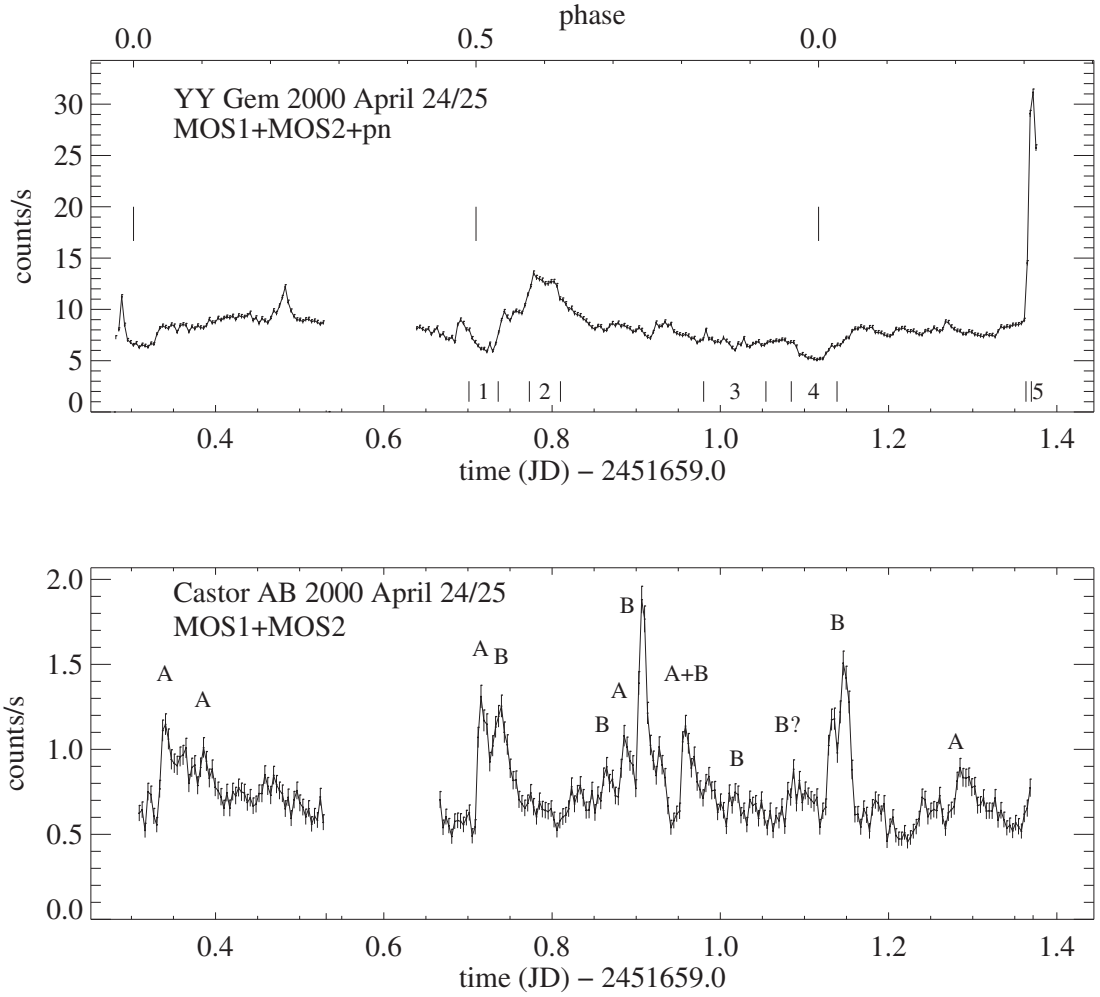

Figure 9.2: *Top: Co-added light curve of YY Gem from MOS1&2 and pn binned to 300 s (the first ≈40 minutes of each segment were observed only by the pn camera; its count rate was adjusted by a factor of ∼1.7 determined from later time intervals). The upper vertical bars indicate the eclipse times (primary-secondary-primary), the lower bars give the intervals used for MOS fits (Sect. 9.4.3 and Fig. 9.6). Bottom: Light curve of Castor AB, derived from MOS1&2. Labels (A or B) identify flaring star. Note the different vertical scales in the two figures.*

$1.157 - 1.351$ d (Fig. 9.2a). For the RGS we included data between $t = 0.85 - 1.19$ d after which time a new RGS observing segment started. Both intervals show very similar hardness characteristics. We modeled the flare at $t > 1.35$ d for MOS and pn by keeping the quiescent model found before fixed, and adding one or two further thermal models, for which we fitted abundances, T, and EMs. Multi-T fit results are reported in Table 9.2.

All three fits to the quiescent spectra agree quite well. The most notable trends are *low* abundances for elements with a *low* First Ionization Potential (FIP), most clearly for Fe, while

Table 9.2: *Model fits for RGS2, MOS1, and pn*[a]

	————YY Gem QUIESCENT————			Castor AB
Parameter	RGS2	MOS1	pn	MOS1
kT_1	$0.29^{+0.05}_{-0.04}$	$0.37^{+0.03}_{-0.05}$	$0.25^{+0.02}_{-0.02}$	$0.17^{+0.8}_{-0.07}$
kT_2	$0.66^{+0.04}_{-0.03}$	$0.74^{+0.05}_{-0.06}$	$0.60^{+0.03}_{-0.02}$	$0.67^{+0.02}_{-0.02}$
kT_3	$1.33^{+\cdots}_{-0.43}$	$1.82^{+0.42}_{-0.30}$	$1.12^{+0.21}_{-0.10}$	$2.05^{+\cdots}_{-0.58}$
$\log EM_1^{\rm b}$	$51.98^{+0.12}_{-0.18}$	$52.07^{+0.06}_{-0.16}$	$51.80^{+0.10}_{-0.08}$	$50.79^{+0.4}_{-\cdots}$
$\log EM_2^{\rm b}$	$52.26^{+0.11}_{-0.13}$	$52.21^{+0.07}_{-0.08}$	$51.98^{+0.13}_{-0.09}$	$51.75^{+0.13}_{-0.14}$
$\log EM_3^{\rm b}$	$51.67^{+0.36}_{-0.70}$	$51.65^{+0.17}_{-0.13}$	$51.85^{+0.10}_{-0.11}$	$51.02^{+0.19}_{-0.41}$
C	$0.48^{+0.30}_{-0.16}$	$= 1$	$= 1$	$= 1$
N	$0.60^{+0.35}_{-0.19}$	$= 1$	$= 1$	$= 1$
O	$0.29^{+0.13}_{-0.06}$	$0.35^{+0.04}_{-0.04}$	$0.38^{+0.04}_{-0.04}$	$0.22^{+0.17}_{-0.11}$
Ne	$0.75^{+0.38}_{-0.15}$	$0.63^{+0.09}_{-0.10}$	$0.74^{+0.34}_{-0.29}$	$0.46^{+0.19}_{-0.14}$
Mg	$0.17^{+0.27}_{-0.17}$	$0.17^{+0.07}_{-0.07}$	$0.30^{+0.10}_{-0.09}$	$0.26^{+0.15}_{-0.10}$
Si	$0.44^{+0.73}_{-0.44}$	$0.29^{+0.09}_{-0.08}$	$0.42^{+0.09}_{-0.08}$	$0.25^{+0.11}_{-0.09}$
S	$0.14^{+0.23}_{-0.14}$	$0.27^{+0.17}_{-0.16}$	$0.36^{+0.15}_{-0.15}$	$0.47^{+0.32}_{-0.28}$
Ca	$= 1$	$= 1$	$= 1$	$= 1$
Fe	$0.14^{+0.05}_{-0.03}$	$0.15^{+0.03}_{-0.02}$	$0.24^{+0.05}_{-0.04}$	$0.12^{+0.06}_{-0.04}$
Ni	$0.21^{+0.23}_{-0.21}$	$0.00^{+0.16}_{-0.00}$	$= 0.21$	$0.13^{+0.35}_{-0.13}$
χ^2/dof	$183/321$	$186/140$	$372/360$	$160/130$
	———YY Gem FLARE ($t > 1.35$ d)[c]———			
Parameter	MOS1	MOS2	pn	
kT_1	...	...	$0.77^{+0.07}_{-0.06}$	
kT_2	$3.22^{+0.32}_{-0.32}$	$3.47^{+0.39}_{-0.35}$	$3.21^{+0.27}_{-0.22}$	
$\log EM_1^{\rm b}$	...	...	$51.59^{+0.11}_{-0.08}$	
$\log EM_2^{\rm b}$	$52.58^{+0.03}_{-0.04}$	$52.54^{+0.04}_{-0.05}$	$52.49^{+0.03}_{-0.03}$	
O	$0.15^{+1.04}_{-0.15}$	$1.80^{+1.54}_{-1.24}$	$1.53^{+0.61}_{-0.52}$	
Ca	$3.50^{+3.24}_{-3.26}$	$0.00^{+2.24}_{-0.00}$	$4.83^{+2.69}_{-2.71}$	
Fe	$0.74^{+0.25}_{-0.22}$	$0.85^{+0.36}_{-0.29}$	$0.74^{+0.16}_{-0.15}$	
χ^2/dof	$84/124$	$123/123$	$369/354$	

[a] Errors give 90% confidence intervals based on $\chi^2_{\rm min}$+2.706. Some parameters were held fixed ("$= x$"). "$\cdots$" indicate unconstrained parameters. Abundances are relative to solar photospheric abundances (Anders & Grevesse 1989).

[b] Due to the lack of Good Time Intervals for pn data, we normalized the count rates with the length of the time interval; this implies a lower limit for the EM values for pn.

[c] These flare components are additional to the fixed quiescent 3-T model. EMs are averages over rise and flare peak.

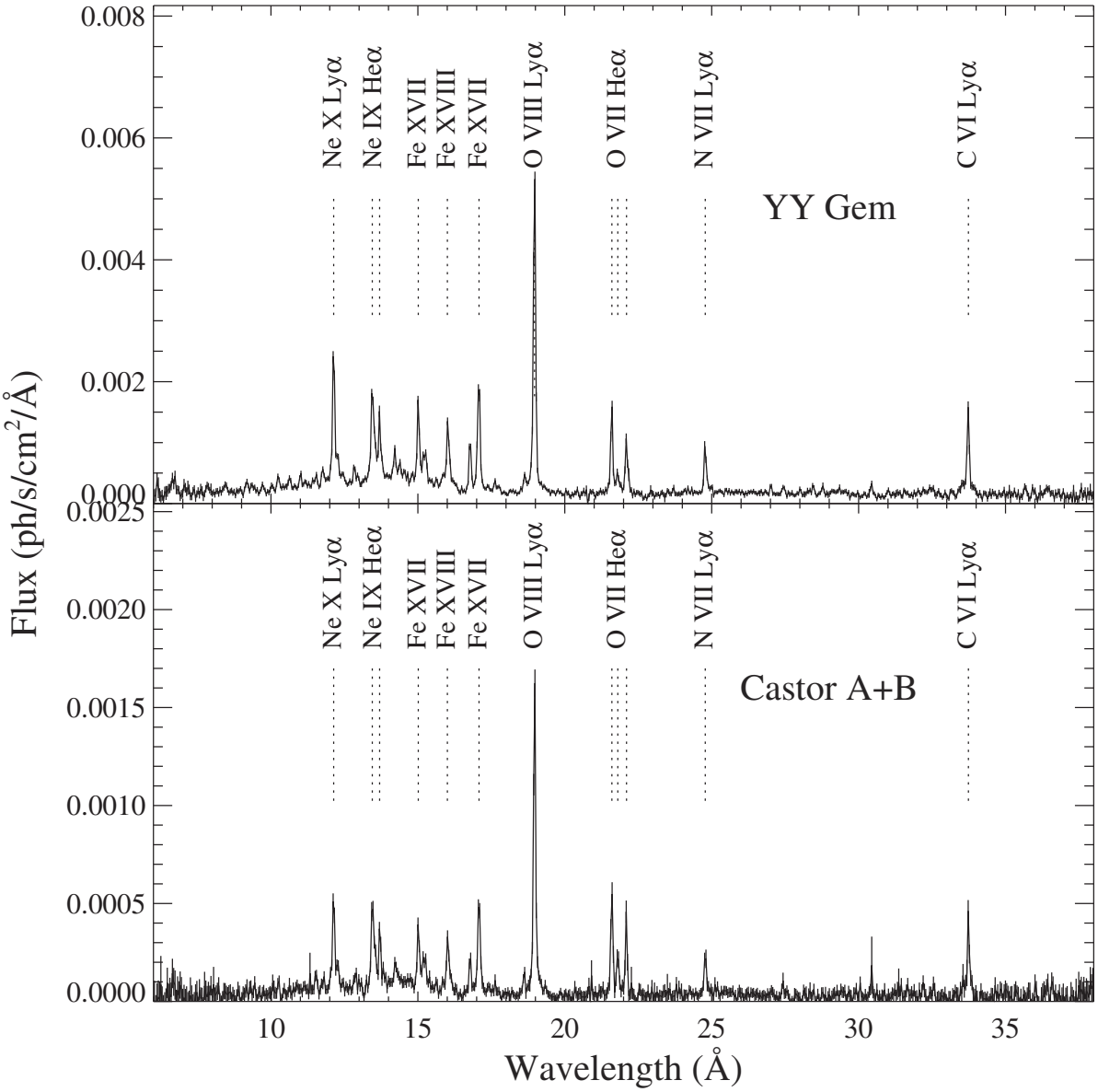

Figure 9.3: *RGS1&2 fluxed spectra of YY Gem and Castor AB (bin resolution: 0.04375Å). Note the different vertical scales in the two panels.*

high-FIP elements, in particular Ne, show *higher* abundances. The poor result for S from the RGS is due to weak lines with poor atomic data (Audard et al. 2001b). Fig. 9.4b shows an EM distribution recovered from the RGS2 spectrum, using Chebychev polynomials of degree 5. A broad distribution from 2–15 MK compatible with the $3-T$ fit results is evident. There is little plasma with $T < 2$ MK: A number of lines of C VI, N VI, N VII, and O VII with formation temperatures in this range constrain this regime. During the flare, some elemental abundances increase, in particular Fe which increases by a factor of 3–5. Note, however, that

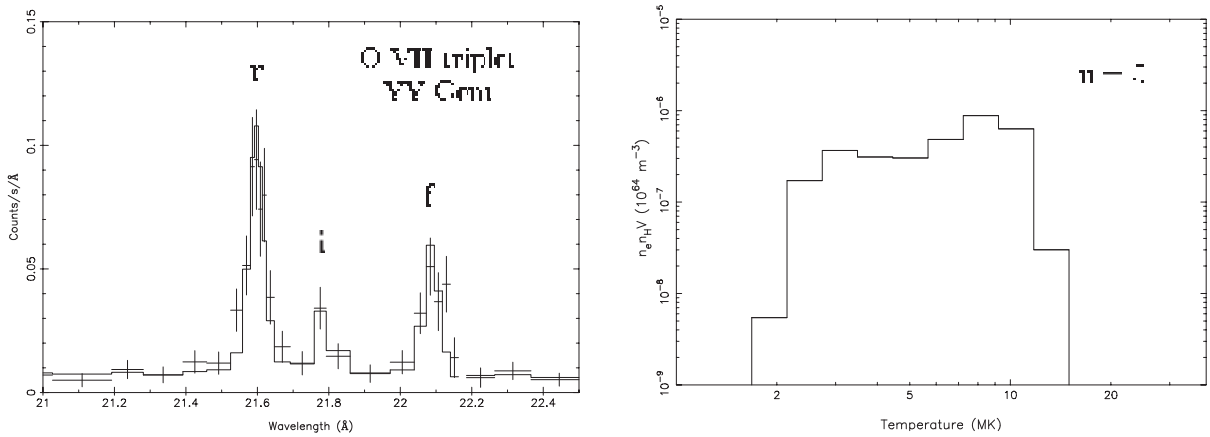

Figure 9.4: *(Left): Density-sensitive He-like* O VII *triplet of quiescent YY Gem. (Right): EM distribution for the quiescent YY Gem, derived from RGS2. A polynomial degree of 5 was used.*

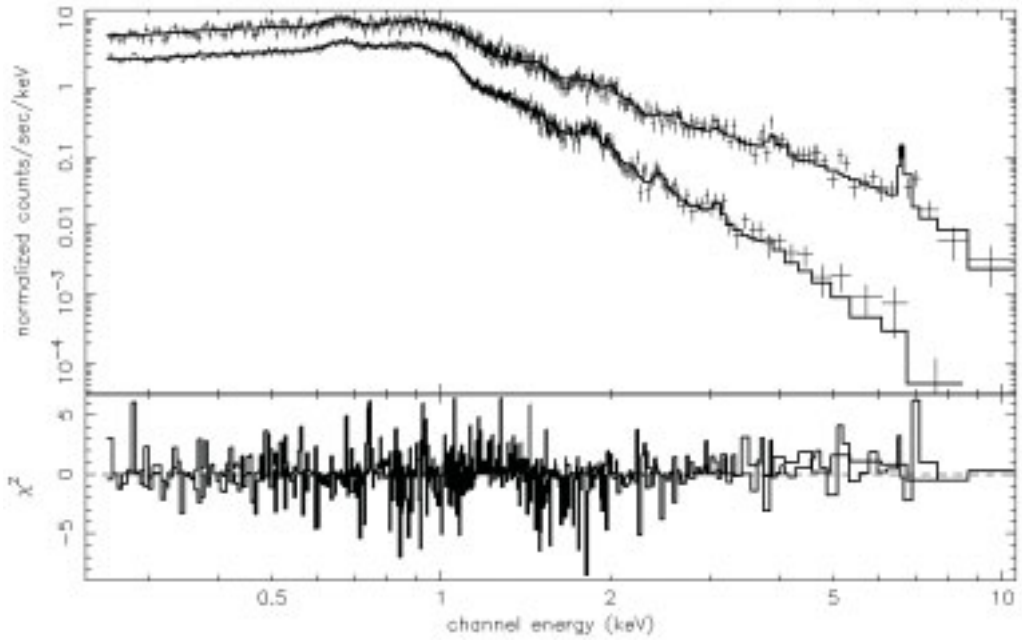

Figure 9.5: *YY Gem EPIC pn spectra (top: flaring; bottom: quiescent).*

the significance of the flare abundance values for the other elements are clearly at the limit of the present calibration and the S/N available.

Fig. 9.5 illustrates spectral fits to the YY Gem pn data for quiescence and for the large flare. More detailed time-resolved spectroscopy was performed with MOS, with five segments selected as follows (Fig. 9.2a): (1) secondary eclipse – (2) flare peak at ≈0.8 d – (3) quiescent emission (around 1 d) – (4) primary eclipse – (5) flare (including rise) at 1.37 d. Two T components were sufficient for the given S/N ratio. The results are shown graphically in Fig. 9.6. The

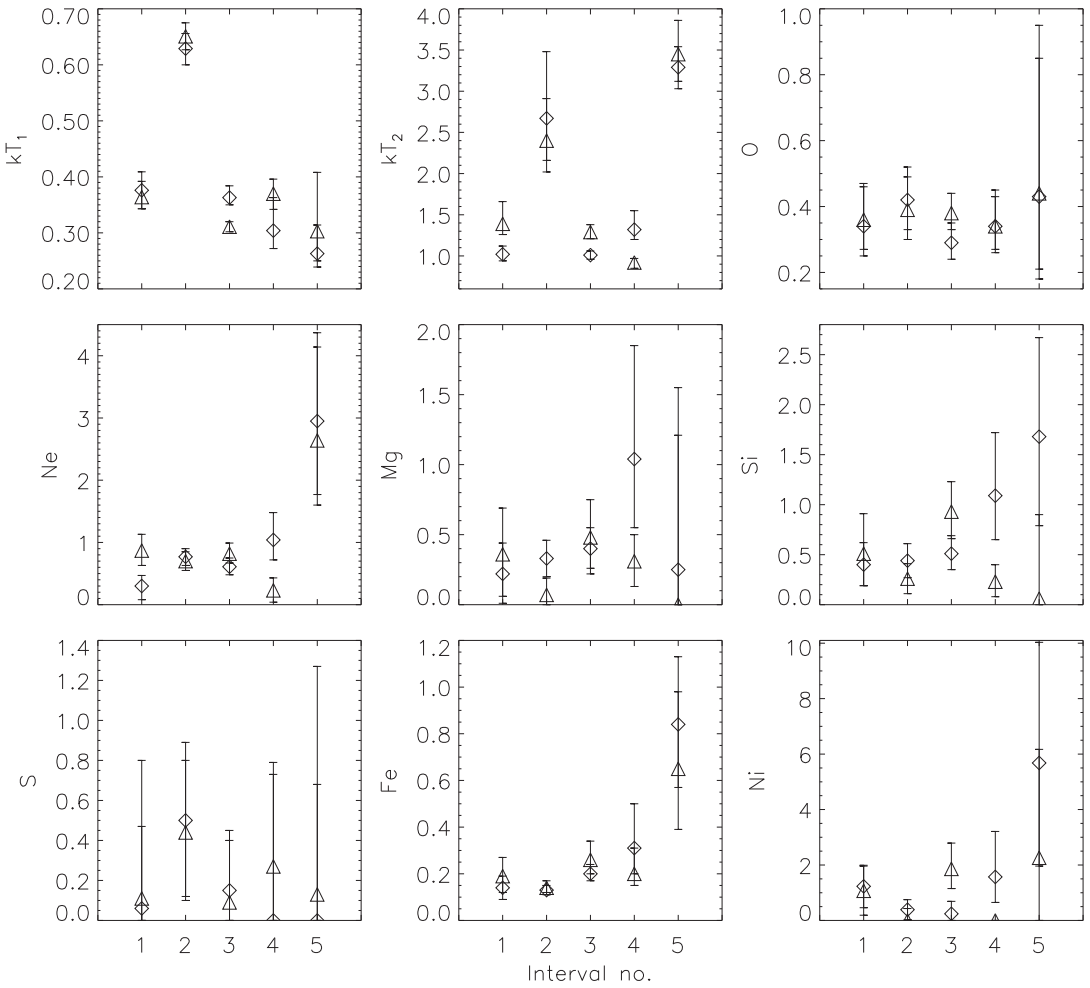

Figure 9.6: *Time resolved MOS1 (diamonds) and MOS2 (triangles) spectroscopy of YY Gem based on $2-T$ spectral fits, showing the parameters kT_1, kT_2, abundances of O, Ne, Mg, Si, S, Fe, and Ni. The numbers on the x-axis identify time intervals (see text and Fig. 9.2a). Error bars indicate 90% confidence ranges based on $\chi^2_{\rm min} + 2.706$.*

heating effects during the flares are evident. Note also the trend for higher metal abundances (in particular of Fe and Ne) during the large flare, while no significant changes are seen during the eclipses.

How different is Castor AB from YY Gem? Close inspection of the RGS spectra in Fig. 9.3 reveal higher flux ratios of O VIII/O VII and Ne X/Ne IX for YY Gem than for Castor, indicating that YY Gem's corona is on average hotter *despite the ongoing flaring on Castor*. Some support for this result comes from multi-T fits reported in Table 9.2 (from the integrated MOS1 observation). The ratio between the EMs of the hottest to the intermediate component is larger for YY Gem. The abundance pattern is, within the errors, rather similar.

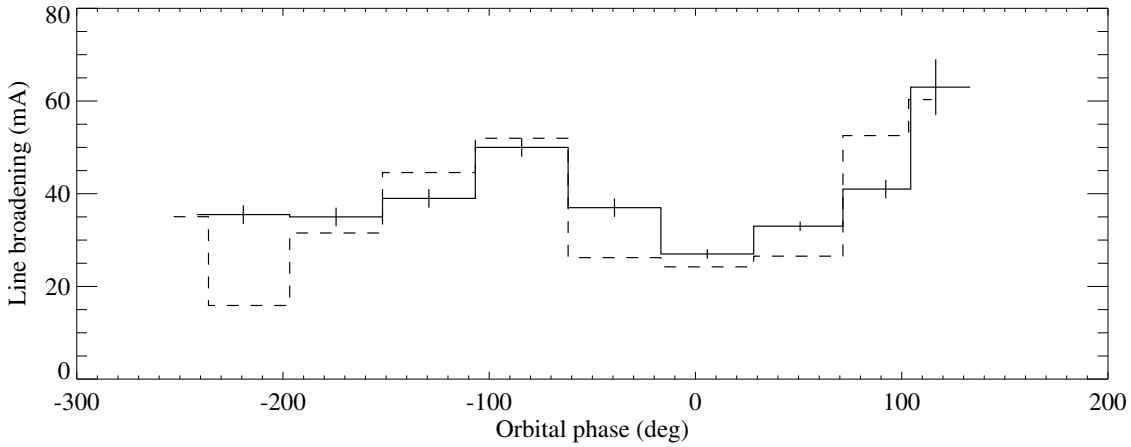

Figure 9.7: *Line broadening of the* O VIII *Lyα line as a function of orbital phase, for RGS2. Two methods were applied: fit with the line spread function (dashed) and with a double-Gaussian profile (solid).*

9.4.4 Orbital Motion of YY Gem

Radial velocity variations due to the orbital motion of the two stars in YY Gem may be evident as broadening of the spectral lines during the orbital period. Eclipse times and orbital phases were taken from Haisch et al. (1990) who predict a primary eclipse at JD = 2451660.11676, consistent with the three eclipses seen in the *XMM-Newton* observations (Fig. 9.2a).

The RGS spectra for the second observation were subdivided into time segments for which maximum or minimum line broadening would be expected (i.e., around quadrature -90° or 90° and conjunction 0° and -180°). Two segmentations were used, firstly the observation was divided into 8 segments with segment 6 centered on the primary eclipse. Each segment, with the exception of segment 1, was approximately 8800 s in duration. A second set of time segments, shifted by about 2200 s relative to the first, was also constructed which optimized the counts in the first segment. Line broadening and centroids for the strongest emission line in the spectrum, that of O VIII at 18.969 Å, were determined firstly with SPEX using the calibrated line spread function in the response matrix for the RGS and secondly within the software package DIPSO (Howarth, Murray, & Mills 1998) by correcting for the effective area variation and fitting a combination of two Gaussian functions, which was found to give an acceptable representation of the line spread function.

The variation of line broadening for RGS2 (average for the two segmentations) for each of the methods used is shown in Fig 9.7. It shows the expected sinusoidal variation with orbital phase, with minimum broadening occurring near conjunction (phases of 0° and -180°). It should be noted that the value for the 8th segment was determined without including the flare. The amplitude of the variation is approximately 12 mÅ, corresponding to a velocity of 190 km s^{-1} which is in reasonable agreement with the expected value of up to 160 km s^{-1}, determined

from the orbital motion (including the stellar sizes). No anomalous broadening, resulting from the inhomogeneity seen in the light curve modeling (Sect. 9.5), was detected.

The sinusoidal variation is not clearly evident in the results obtained from the RGS1 spectra. Although there is some variation during the observation it is not clearly correlated with the orbital period. We note, however, that although the detailed description of the response of both spectrometers is expected to evolve over time, we have preferred RGS2 for the present analysis as this description is more advanced than for RGS1.

9.4.5 An Eclipsed Flare?

A closer look at Fig. 9.2a may suggest that the small flare at 0.7 d is merely the beginning of a larger flare that is subsequently eclipsed and that "reappears" at 0.78 d. Note that after the eclipse, a plateau (at 0.75 d) first appears, which we interpret as being the end of the eclipse of the bulk "quiescent" material, while the flare, then required to be located about 80° away in longitude from the substellar point, reappears later. Proving this scenario is difficult. We have nevertheless tentatively estimated location and extent of such a structure, both from the "ingress" and "egress" durations and the duration of the occultation. The optimum latitude is approximately -10°. An appreciable height is required to explain the long occultation (up to $\approx 0.8 R_*$ above the photosphere). The longitudinal extent is of the same order (i.e., $[2-3] \times 10^{10}$ cm).

9.5 Eclipse Modeling

The long light curve available for YY Gem includes three eclipses (two primary and one secondary eclipse). We have applied a method first presented by Siarkowski (1992) and Siarkowski et al. (1996) for a 3-D deconvolution of X-ray light curves. In short, the stellar environment is divided into regular volume bins that are occupied by variable amounts of EM. After each iteration step, the model and the observed light curves are compared. For each phase, the EMs of all visible volume elements are increased by a factor equal to the ratio of observed flux to modeled flux. We have slightly modified the original procedure by applying volume bins defined in *spherical* coordinates. Bins are located at positions (r_i, θ_i, ϕ_i). In the radial direction, we subdivide the interval from R_* to $1.99 R_*$ for the primary ($2.15 R_*$ for the secondary) into 16 regular bins. In θ (co-latitude) direction, we define 36 equidistant bins from 0 (north pole) to π (south pole). Finally, the width of the volume bins in ϕ (longitude) direction is such that all volumes at a given radius are equal, i.e., $\Delta\phi \propto \sin\theta$, with 72 equidistant bins at the equator. To prevent ambiguities at the pole, we keep at least four ϕ bins at each co-latitude.

Several words of caution are in order. i) The light curve clearly shows flares which must not enter into the modeling process. We therefore removed obvious flares at 0.48 d, 0.7 d, 0.8 d, and 1.37 d (Fig. 9.2a), and linearly interpolated from the pre-flare to the post-flare count rate. The gap around 0.6 d was also linearly interpolated. This is a serious limitation of the present modeling also in the light of the possible presence of further small flares. We selected the interval $0.55-1.36$ d for modeling, corresponding to one orbit period. ii) Light curve inversion

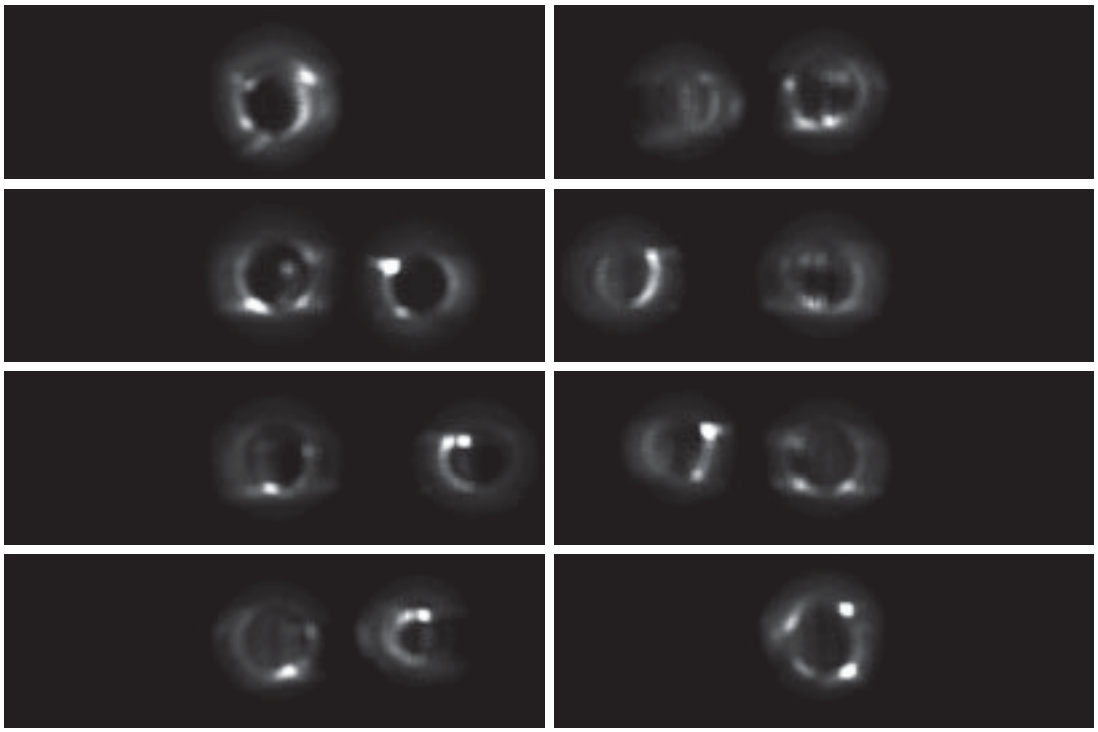

Figure 9.8: *Model for the coronal structure in the dMe binary YY Gem derived from light curve inversion. The primary star is in the center and is eclipsed by the secondary at phase 0. The panels show the aspect in phase steps of 45°, starting with phase $\phi = 0$ (top left; primary eclipsed) and continuing counter-clockwise ($\phi = 0.25$ is in the third panel from top on the left side, $\phi = 0.5$ is in the lower right corner, and $\phi = 0.75$ is the second panel from top on the right column).*

is an ill-posed problem and generally satisfies multiple solutions (Siarkowski 1992; Siarkowski et al. 1996). Physically reasonable spatial restrictions should be introduced to confine the problem to sensible solutions. We have done so by restricting the radial extent of the coronae to $\approx 1R_*$ above the photosphere but, as we will see, this constraint will automatically be fulfilled for most of the EM. iii) There is much correlation between neighboring bins, depending on the time resolution and the signal-to-noise ratio of the measurements. The finest structures in the solutions are ambiguous or not significant. iv) Since the observer is located close to the orbital plane, some north-south ambiguity could be introduced, i.e., features are mirrored at the equator. Some features may also be found on both stars at similar coordinates relative to the star centers.

With these caveats in mind, our goal is *not* to reconstruct a real coronal image but to investigate *statistical properties* of physically reasonable solutions that are compatible with the light curve. While the most stringent restrictions are due to the eclipses, the most difficult part of the modeling is the underlying quasi-steady emission. Any axisymmetric distribution with matching total luminosity can reproduce this emission if it is sufficiently extended *or* lies close to

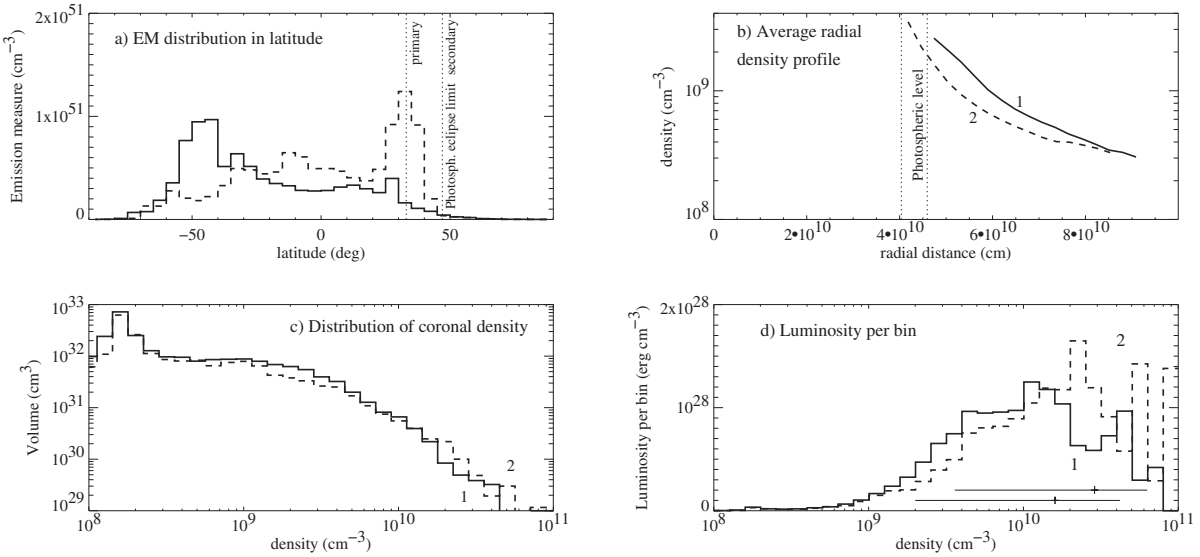

Figure 9.9: *Light curve modeling results for YY Gem. Primary and secondary components are designated with "1" and "2" and shown by solid and dashed lines, respectively. (a): Distribution of EM in stellar latitude. (b): Average radial density profiles; vertical lines indicate photospheric levels. (c): Distribution of density values in all bins around each star. (d): Relative luminosity contributions from plasma of given density (assuming volume filling factor = 1 in each volume bin). The spectroscopically measured density ranges (two methods, see Sect. 9.4.2) are indicated at the bottom.*

the uneclipsed north poles of the stars. We have studied three special but suggestive cases that are specified as starting conditions: i) a diffuse underlying corona with $n_{\rm e} \propto r^{-1}$; ii) a diffuse underlying corona with $n_{\rm e} = $ const. iii) Addition of a strong, uneclipsed active region at each of the two north poles.

Case (iii) suppresses diffuse axisymmetric components during the iteration, essentially leaving the inhomogeneous structure for modeling. The latter was found identically from all three starting conditions. Fig. 9.8 illustrates a possible model for one orbital revolution of the two stars as seen from the Earth (solution for case [i]; the primary star is held in the center). Note that

- the coronal plasma is inhomogeneous. This accounts for the *asymmetric, deep,* and *short* eclipses, and also for the eclipse profile.
- Most bright areas are found at mid-latitudes (see also Fig. 9.9a), in agreement with findings from surface Doppler imaging (Hatzes 1995).

After the modeling process, we removed the undetermined north polar active region and investigated the statistical and geometric properties of the solution (Fig. 9.9). The average density

profile of the inhomogeneous part was computed (Fig. 9.9b) for each star. Evidently, most of the emitting material is closely concentrated near the stellar surfaces, and the density rapidly decreases outwards. The scale height is $\sim (1-4) \times 10^{10}$ cm. The density scale height of an isothermal plasma is

$$\Lambda = \frac{kT}{\mu m_{\rm H} g} = \frac{kT}{\mu m_{\rm H}} \frac{R_*^2}{GM_*} \tag{9.1}$$

where k is the Boltzmann constant, $m_{\rm H}$ is the mass of the hydrogen atom, $\mu \approx 0.67$ the mean molecular weight, and G the gravitational constant. With the stellar parameters R_* and M_*, we find a mean temperature of $\log T = 6.5 - 7.1$ [K], in good agreement with the spectroscopic measurements (Fig. 9.4b).

Fig. 9.9c shows the statistical distribution of densities in all bins considered. While most bins are of low density (i.e., the high-density plasma has a *small filling factor*), the emissivity of a plasma scales with $n_{\rm e}^2$ so that most of the observed emission stems from plasma with densities of $\log n_{\rm e} \approx 9.7 - 10.5$ (Fig. 9.9d). This is again in gratifying agreement with the explicit density measurements in the RGS spectra. Finally, the total luminosities of the two stars are very similar: the non-axisymmetric portions modeled above contribute 1.3×10^{29} erg s^{-1} and 1.5×10^{29} erg s^{-1} from the primary and the secondary, respectively. The total system luminosity is 3.7×10^{29} erg s^{-1} (as determined from the MOS data).

9.6 Summary and Conclusions

We have addressed a number of issues relevant for stellar coronal structure by making use of a high-quality *XMM-Newton* observation of the Castor/YY Gem system. The eclipse observations allow us to assess the statistical properties of the coronal plasma, such as its density scale height and the location of strongly emitting features. Our 3-D light curve inversion shows excellent agreement with spectroscopic results: i) the average density scale height implies a temperature that is in good agreement with the range measured from the available spectroscopy; ii) densities that dominate the X-ray emissivity agree well with spectroscopically determined average densities of a few times 10^{10} cm^{-3}; iii) the active regions are mainly distributed between $\pm 50^\circ$ in latitude, in agreement with previous findings from Doppler imaging (Hatzes 1995). The preference of mid-latitude regions is at variance with reports on polar magnetic spots on active stars. We may only speculate here whether the tidal interaction in this close system of almost fully convective M stars plays a role for this scenario. On the other hand, eclipse modeling does not exclude the presence of active regions near the north polar regions of the system.

At any rate, there is clear evidence that the coronae are *highly structured* and that *both* components are similarly active: i) Deep eclipses require similar amounts of EM on both stars, and relatively compact active regions. We find no indications for very extended magnetospheres as inferred from radio observations (Alef et al. 1997). This is, in retrospect, not surprising: Radio emission is due to high-energy electrons trapped in magnetic fields; they radiate more

efficiently in a low-density environment where they suffer fewer collisions. On the other hand, efficient X-ray emission originates preferentially in high-density environments since the emissivity scales with $n_{\rm e}^2$. Such places are naturally found closer to the stellar surfaces. ii) The asymmetries seen in the eclipse light curves clearly require structured coronae. And iii) we see indications for periodic line broadening, compatible in phase and amplitude with two orbiting stars of similar brightness.

We have investigated the thermal and elemental abundance structure both during quiescence and during flares. We find a broad distribution of EM above 2 MK, with little material below. The EM distribution peaks at about 8 MK, with a tail that may reach 15–20 MK as derived from EPIC data. There is no appreciable change during the eclipses, but we do see significant increases of some abundances during the larger flare that reaches temperatures around 40 MK.

Finally, we report the definitive detection and identification of *both* Castor A and B as flaring X-ray sources. Although the Castor AB source was detected in X-rays before (Pallavicini et al. 1990b; Schmitt et al. 1994; Gotthelf et al. 1994), the individual coronal components have hitherto been detected only as radio sources (Güdel & Schmitt 1996). The new detections support the view that both Castor A and B have low-mass companions that are magnetically very active, as judged from the high flare rate.

Chapter 10

Elemental Abundances in Stellar Coronae with XMM-Newton

Summary

We have used high-resolution X-ray spectra from *XMM-Newton* to determine coronal abundances of the elements C, N, O, Ne, Mg, Si, and Fe in four solar-type stars and four RS CVn binary systems. Bias from unknown stellar photospheric abundances is avoided for solar-type stars by selecting stars that by all arguments are of solar photospheric composition. The solar analogs cover a wide range of coronal activity, including the empirical X-ray saturation regime, commensurate with their range of rotation periods, ages, and X-ray luminosities. The RS CVn binary systems however only span the high end of coronal activity, with the exception of the intermediately active Capella. Elements with a low First Ionization Potential (FIP) are underabundant relative to high-FIP elements in the most active stars, signifying an *Inverse FIP Effect*, whereas less active stars show low-FIP abundance enhancements by factors of about $5-7$ (*normal FIP effect*). We suggest that stellar coronae switch from the inverse to the normal FIP effect as a consequence of decreasing activity. We speculate that the depletion of low-FIP elements in very active stars is related to an enhanced flux of coronal high-energy electrons that induce a downward drift of weakly ionized low-FIP elements in the chromosphere.

10.1 Introduction

X-ray observations of magnetically active stars with low-spectral resolution devices, in particular with the CCD detectors onboard the *ASCA* satellite, provided compelling evidence for anomalous elemental compositions of active stellar coronae when compared to the solar photosphere (White 1996; Drake 1996). While the average *solar* corona shows enhancements of elements with a First Ionization Potential (FIP) below 10 eV, typically by factors of about 4 relative to high-FIP elements and hydrogen (Feldman 1992), spectra from many active stars

The work presented in this chapter has been published in Audard & Güdel (2002) and Güdel et al. (2002b).

reveal significant underabundances of most accessible elements such as N, O, Ne, Mg, Si, S, and Fe (White 1996). Evidence for depleted metal abundances in active stellar coronae was found in higher-resolution grating spectra from the *EUVE* satellite as well (e.g., Schmitt et al. 1996; Mewe et al. 1996, 1997). On the other hand, spectra from inactive stars revealed either no abundance anomalies relative to the photospheric composition, or evidence for a solar-like FIP effect (Drake, Laming, & Widing 1995, 1997), suggesting systematic abundance differences in the two classes of stars (Drake 1996). We note, however, that the photospheric composition of most stars is poorly determined or unknown, although abundance anomalies should strictly refer to the underlying *stellar* photospheric abundances (rather than to solar values).

Some uncertainties in coronal abundance measurements remained due to the insufficient spectral resolution of previous X-ray detectors. Abundances of the crucial elements Ne and O, for example, are difficult to measure with CCD spectral resolution (Drake 1996). High-resolution spectroscopy now available with *XMM-Newton* and *Chandra* offers for the first time access to individual X-ray atomic transitions of a series of important elements. Analyzing *XMM-Newton* observations of the HR 1099 system, Brinkman et al. (2001) found most of the abundances to fulfill a nearly exponential dependence on their FIP, such that higher-FIP elements are more abundant. The Ne/Fe ratio was an order of magnitude larger than the solar photospheric ratio. This "Inverse FIP Effect" (IFIP effect henceforth) was found in *XMM-Newton* observations of other active stars as well (Güdel et al. 2001a,b, Chapters 8 and 9). Large ratios of Ne/Fe and Ar/Fe were also derived from *Chandra* grating observations (Drake et al. 2001).

To study the coronal conditions (e.g., the overall activity, temperatures, or the flare rate) that control coronal abundances apart from the photospheric composition, we have observed several solar-type stars with known photospheric metallicity. This chapter discusses first results on the abundances. A more comprehensive presentation will be given in a future paper.

10.2 Targets and Observations

10.2.1 Solar Analogs

Our solar-type targets (Table 10.1) are near-solar analogs, their main difference being their rotation periods $P_{\rm rot}$ and hence their (dynamo-induced) magnetic activity level. The two least X-ray luminous stars, π^1 UMa (HD 72905; G1 V) and χ^1 Ori (HD 39587; G0 V), are both members of the Ursa Major Stream, with an estimated age of ≈300 Myr, compatible with their $P_{\rm rot}$ of 4.7 and 5.08 d, respectively (Dorren & Guinan 1993). Stars in the Ursa Major Stream are known to be of near-solar composition (Soderblom & Mayor 1993), supported by the measured [Fe/H] values of our targets (the logarithm of the photospheric Fe abundance relative to the solar photospheric value) between –0.08 and –0.01 (π^1 UMa), and between –0.18 and +0.11 (χ^1 Ori; see Cayrel de Strobel et al. 2001 and references therein), indistinguishable from the solar photospheric composition. Their $\log(L_{\rm X}/L_{\rm bol}) \approx -4.6$, intermediate between very active stars and inactive stars like the Sun. EK Dra (HD 129333; dG0e), a Zero-Age Main-Sequence (ZAMS) star with an age of ≈100 Myr and $P_{\rm rot} \approx 2.7$ d, is the most active solar analog

Table 10.1: *Stellar Parameters and Abundance Ratios*

Object	Spec. type[a]	$(\log L_{\rm X}/L_{\rm bol})$[b]	Fe/O[c]	Ne/O[c]
AB Dor	K0 V	-3.08	0.58 ± 0.02	2.4 ± 0.1
EK Dra	dG0e	-3.47	2.0 ± 0.2	3.0 ± 0.5
π^1 UMa	G1 V	-4.56	6.6 ± 0.9	2.8 ± 0.5
χ^1 Ori	G0 V	-4.64	7.1 ± 0.9	2.4 ± 0.4
HR 1099	K1 IV+G5 IV-V	-3.12	0.35 ± 0.08	2.3 ± 0.4
UX Ari	K0 IV+G5 V	-3.14	0.23 ± 0.05	3.2 ± 0.6
VY Ari	G8 IV-III	-3.35	0.5 ± 0.2	2.9 ± 0.9
λ And	K3-4 IV-V	-4.28	0.5 ± 0.1	2.6 ± 0.7
Capella	G0 III+G8 III	-5.48	2.7 ± 0.3	1.7 ± 0.2

[a] From Gliese & Jahreiss (1991) for the solar analogs; for AB Dor: Collier Cameron et al. (1999). From Strassmeier et al. (1993) for the RS CVn binaries
[b] Calculated from $L_{\rm X}$ between 0.1–10 keV, bolometric magnitudes, and distances; see Perryman et al. (1997)
[c] Using solar photospheric abundances of Anders & Grevesse (1989) (update for Fe from Grevesse & Sauval 1999); errors refer to 90% confidence limits

accessible to high-resolution spectroscopy (Dorren & Guinan 1993), with $\log(L_{\rm X}/L_{\rm bol}) \approx -3.5$. It is a kinematic member of the Local Association (the Pleiades Moving Group), a stellar group with solar photospheric metallicity (Eggen 1983). To study activity at its extreme, we added the active ZAMS star AB Dor (HD 36705; $P_{\rm rot} = 0.51$ d, Pakull 1981) to our sample, despite its somewhat later spectral type of K0 V. This star represents saturated activity, with $\log(L_{\rm X}/L_{\rm bol}) \approx -3.1$ (Vilhu & Linsky 1987). It is also a member of the Local Association, with a measured photospheric metallicity [M/H] $\approx 0.1 \pm 0.2$ for the metals Al, Ca, Fe, and Ni (Vilhu et al. 1987).

10.2.2 RS CVn Binary Systems

The data presented here are part of the Guaranteed Time of *XMM-Newton*'s Reflection Grating Spectrometer Team. We study here only the "quiescent" (non-flaring) X-ray spectra of our four targets, HR 1099, UX Ari, VY Ari, λ And, and Capella. Note that the HR 1099 and Capella data, published previously (Audard et al. 2001a,b, Chapters 6 and 7), have been reanalyzed with more recent and accurate calibrations. A number of their properties are also given in Table 10.1. These non-eclipsing binaries are X-ray bright (Dempsey et al. 1993b), with enhanced activity levels relatively to single main-sequence solar-type stars. Despite binarity, X-ray emission is believed to generally originate from the evolved star (e.g., Ayres et al. 2001; except for Capella, where both giants emit significantly in X-rays, Linsky et al. 1998).

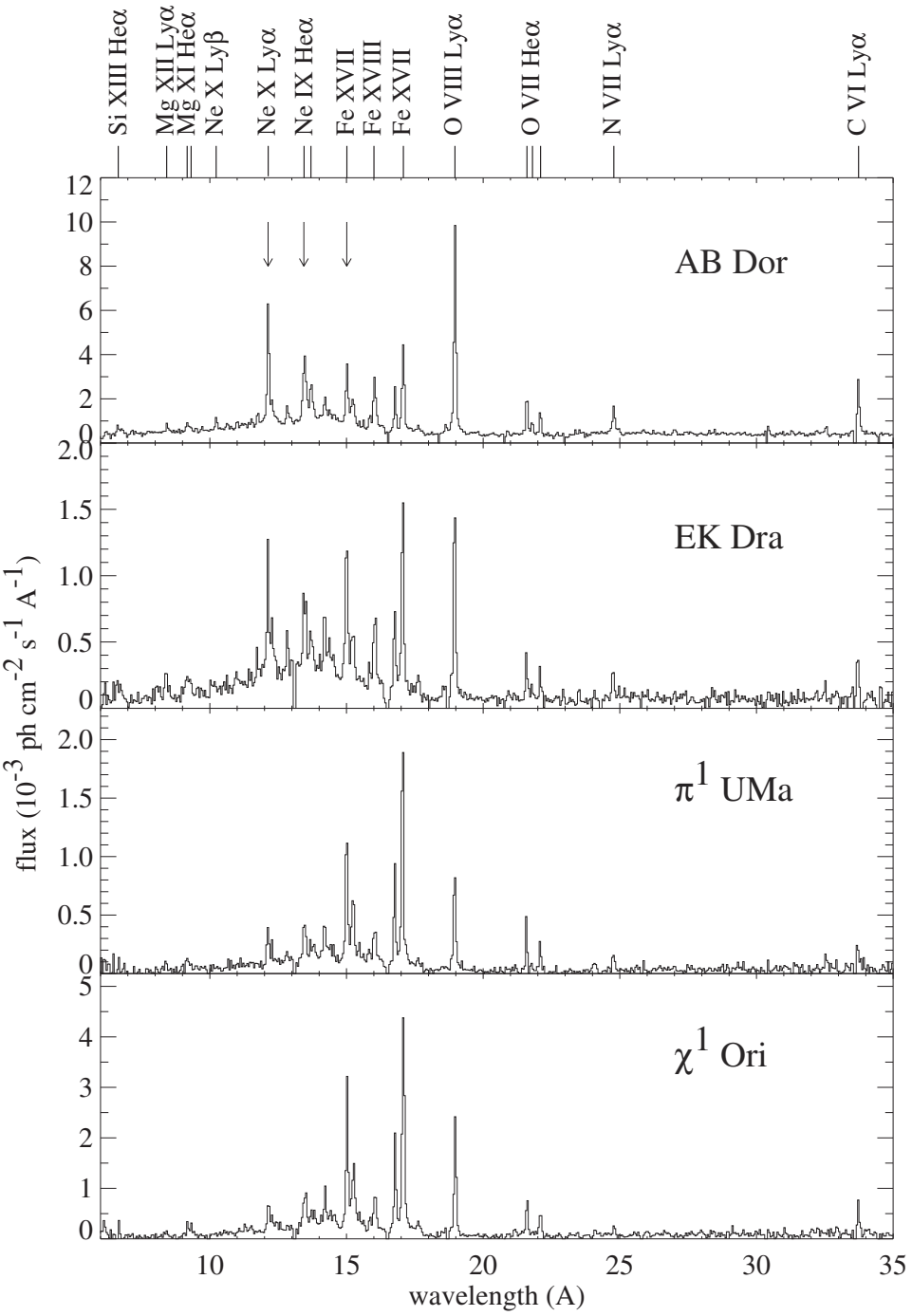

Figure 10.1: *Fluxed RGS spectra of the four solar-type targets, binned to 0.047 Å. The three arrows point at lines (of* Ne X*,* Ne IX*, and* Fe XVII *from left to right) with similar maximum line formation temperatures, while the* Ne/Fe *flux ratios differ strongly from star to star.*

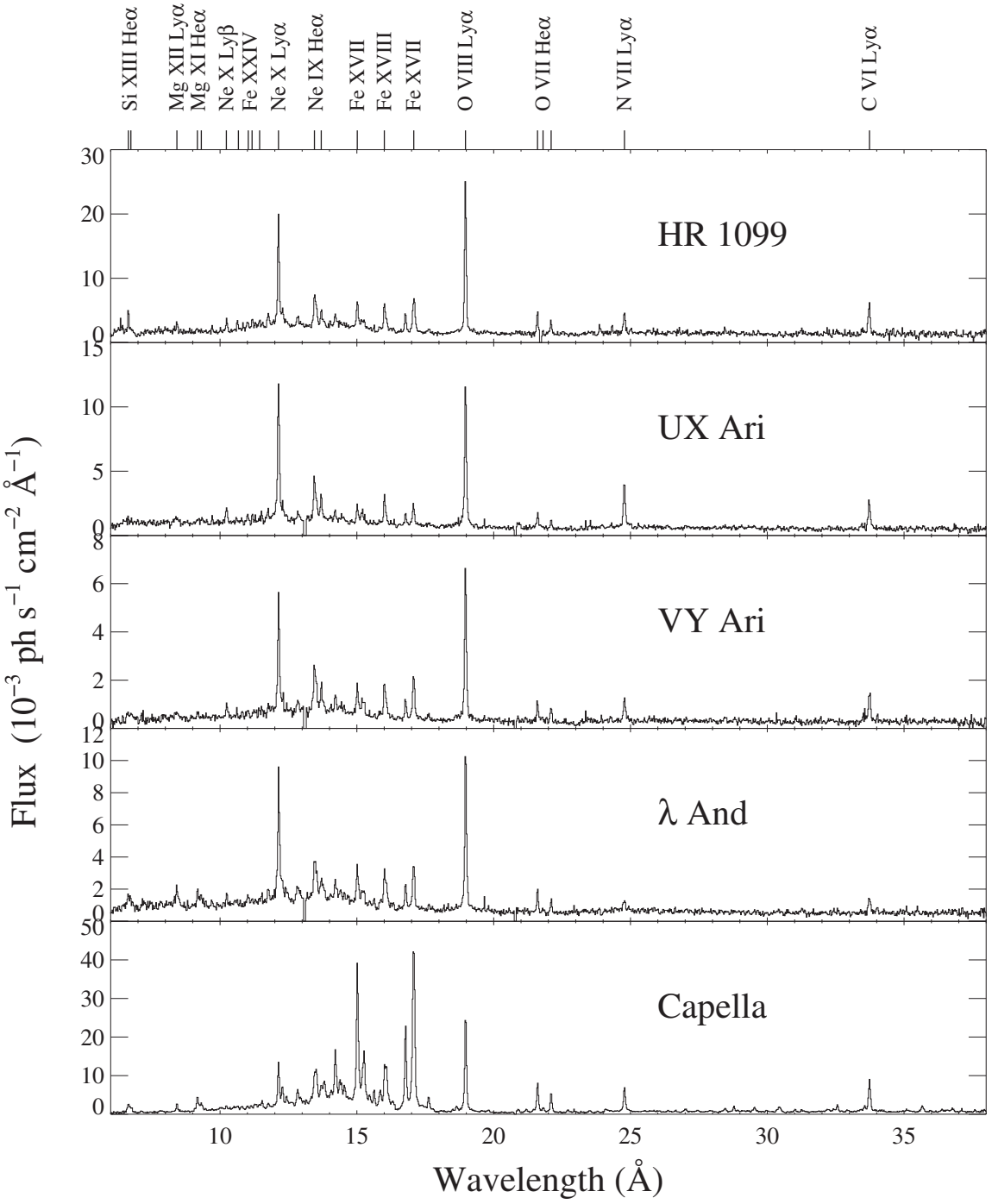

Figure 10.2: *Fluxed RGS spectra of the RS CVn binary systems, binned to 0.025 Å. The activity of these binaries decreases from top to bottom.*

10.3 Analysis

Our targets were observed with *XMM-Newton* (Jansen et al. 2001) for $\approx 30 - 59$ ksec each. All data were analyzed following standard procedures within the SAS software. We principally used the high-resolution RGS data (den Herder et al. 2001), with a spectral resolution of 100−500 in the bandpass from 5−38 Å. The combined and fluxed RGS1+2 spectra of the solar analogs and the RS CVn binary systems are shown in Figures 10.1 and 10.2, respectively. To constrain high-temperature plasma components and to measure resolved He-like and H-like lines of Mg, Si, S, and Ar, we included in our analysis one of the MOS CCD spectra (Turner et al. 2001), but only above ≈1.4 keV (with the exception of Capella for which no useful EPIC data are available). Since MOS was closed during the AB Dor observation, we used the corresponding EPIC PN data instead (Strüder et al. 2001). The restricted use of the low-resolution EPIC data was adopted to prevent their dominance in the spectral fits, given their much larger count rates.

We ignored several spectral ranges that contain transitions with poor atomic data in the present codes (see also Audard et al. 2001b): In particular, the region between 23−33.5 Å (poorly calculated L-shell transitions from Si, S, Ar, and Ca) except for the N VII λ24.8 Lyα line and the N VI He-like triplet at 28.8−29.5 Å. The RGS range shortward of 8 Å showed very low S/N ratios and was flagged in favor of the EPIC spectra.

The three spectra were simultaneously fitted using either of two different model sets: i) A model of 4 (respectively 5 for the RS CVn binaries) collisional ionization equilibrium plasmas at different temperatures T, with identical (linked) elemental abundances. We used the VAPEC model in XSPEC v.11.0.1aj (Arnaud 1996) and the CIE model in SPEX90 (containing the MEKAL code; Mewe, Kaastra, & Liedahl 1995; Kaastra, Mewe, & Nieuwenhuijzen 1996a). The former uses the ionization balance from Mazzotta et al. (1998) while the latter refers to Arnaud & Rothenflug (1985) and, for Fe only, to Arnaud & Raymond (1992). Fit parameters were the temperatures, the emission measures (EM), the abundances of C, N, O, Ne, Mg, Si, S, Ar, Ca, Fe, and Ni, and an interstellar absorption column density. All elemental abundances refer to the solar photospheric abundances given by Anders & Grevesse (1989) except for Fe for which we adopted the revision by Grevesse & Sauval (1999). ii) Since the formation temperatures of the detected lines occupy a range that may be too sparsely covered by 4 (5) components (with possible consequent bias in the abundance determination), we constructed a 10-component model at a temperature grid distributed equidistantly in log(T), between 1 and 100 MK. The fit parameters are the same as for case 1, except that the temperatures remain fixed.

While systematic variations are to be expected from different, incomplete spectroscopic databases and ionization balances, the results from SPEX90 and XSPEC are in qualitative agreement (the former giving somewhat less extreme low-FIP/high-FIP abundance ratios, e.g., Fe/O = 4.0 instead of 7.1 for χ^1 Ori, and Fe/O = 0.69 instead of 0.58 for AB Dor; see below). Results from models 1 and 2 were similar for a given code, with reduced χ^2 values between $\approx 1.3 - 2.2$. In this chapter, we restrict our discussion to the XSPEC results, deferring more

comprehensive presentations and comparisons to a later paper.

10.4 Results

The spectra in Figures 10.1 and 10.2 show obvious differences in their relative line fluxes. The most active stars, HR 1099, UX Ari, VY Ari, λ And and AB Dor, reveal strong lines of O VIII, Fe XVII, Fe XVIII, Ne IX, and Ne X. A well-developed continuum, large flux ratios of O VIII $\lambda 18.97$/O VII $\lambda 21.6$ and of Fe XVIII $\lambda 16.1$/Fe XVII $\lambda 17.05$ are indicators of a predominantly hot ($\approx 10-20$ MK) corona. The spectrum of the intermediately active Capella shows however a dominance for bright Fe XVII and Fe XVIII lines, suggesting a cooler plasma around $6-8$ MK. The spectra of π^1 UMa and χ^1 Ori are reminiscent of somewhat cooler plasma. However, the flux ratios between Ne or O lines and the Fe XVII lines in the latter solar analogs are strikingly smaller than in AB Dor or EK Dra (Figure 10.1). This trend is difficult to explain with a broad EM distribution given that the maximum formation temperatures $T_{\rm m}$ of Ne IX ($\log T_{\rm m} \approx 6.6$) and of Ne X ($\log T_{\rm m} \approx 6.76$) bracket $T_{\rm m}$ of Fe XVII ($\log T_{\rm m} \approx 6.73$), *unless* the coronae differ in their elemental composition: the Fe/O and Fe/Ne ratios must increase toward lower-activity stars.

Our spectral analysis corroborates this suggestion. We plot in Figures 10.3 and 10.4 the abundances relative to O, normalized with the solar (and hence, stellar in the case of the solar analogs) photospheric abundance ratios (abundances that could not reasonably be constrained are omitted; for Fe/O and Ne/O, see also Table 10.1). In the case of solar analogs, the values are averages from models 1 and 2. For RS CVn binary systems, the values come model 2 (but are similar to model 1). The error bars represent either 90% confidence limits (solid lines) from model 1 or one half of the difference between the two best-fit ratios (dotted lines), whichever is larger (except for RS CVn binaries, where only 90% confidence limits from model 2 are shown). AB Dor shows a clear trend toward an IFIP effect, with a Ne/Fe ratio of ≈ 4. EK Dra indicates a relatively flat abundance distribution, with a slight increase both toward low and high FIP. In contrast, both π^1 UMa and χ^1 Ori reveal large ratios for Fe/O, Mg/O, and Si/O, and a ratio of Ne/Fe $\approx 0.3-0.45$. The RS CVn binaries, with their activity level close to that of AB Dor, tend to show an IFIP effect. The intermediately active Capella, however, shows no clear trend. λ And reveals a trend toward an IFIP effect with somewhat high low-FIP/O ratios.

Figure 10.5 shows the abundance ratio Fe/O for all four solar analogs, as a function of the activity indicator $\log(L_{\rm X}/L_{\rm bol})$. Also indicated are the EM-weighted logarithmic averages of the coronal temperature (bottom of figure). The Fe/O ratio clearly decreases with decreasing activity, by about one order of magnitude. However, no trend is evident for Ne/O (triangles in Figure 10.5). Similarly, the Fe/O and Ne/O ratios as a function of the average coronal temperature are shown in Figure 10.6ab, for solar analogs and RS CVn binary systems. Again the Fe/O ratio clearly decreases with decreasing activity, whereas there is no trend visible for Ne/O. Surprisingly, the ratios from the RS CVn binaries fit well into the same trend as the solar analogs, although we note that their stellar photospheric abundances are essentially unknown. Previous high-resolution X-ray measurements of the Ne/O ratio in other stellar targets agree

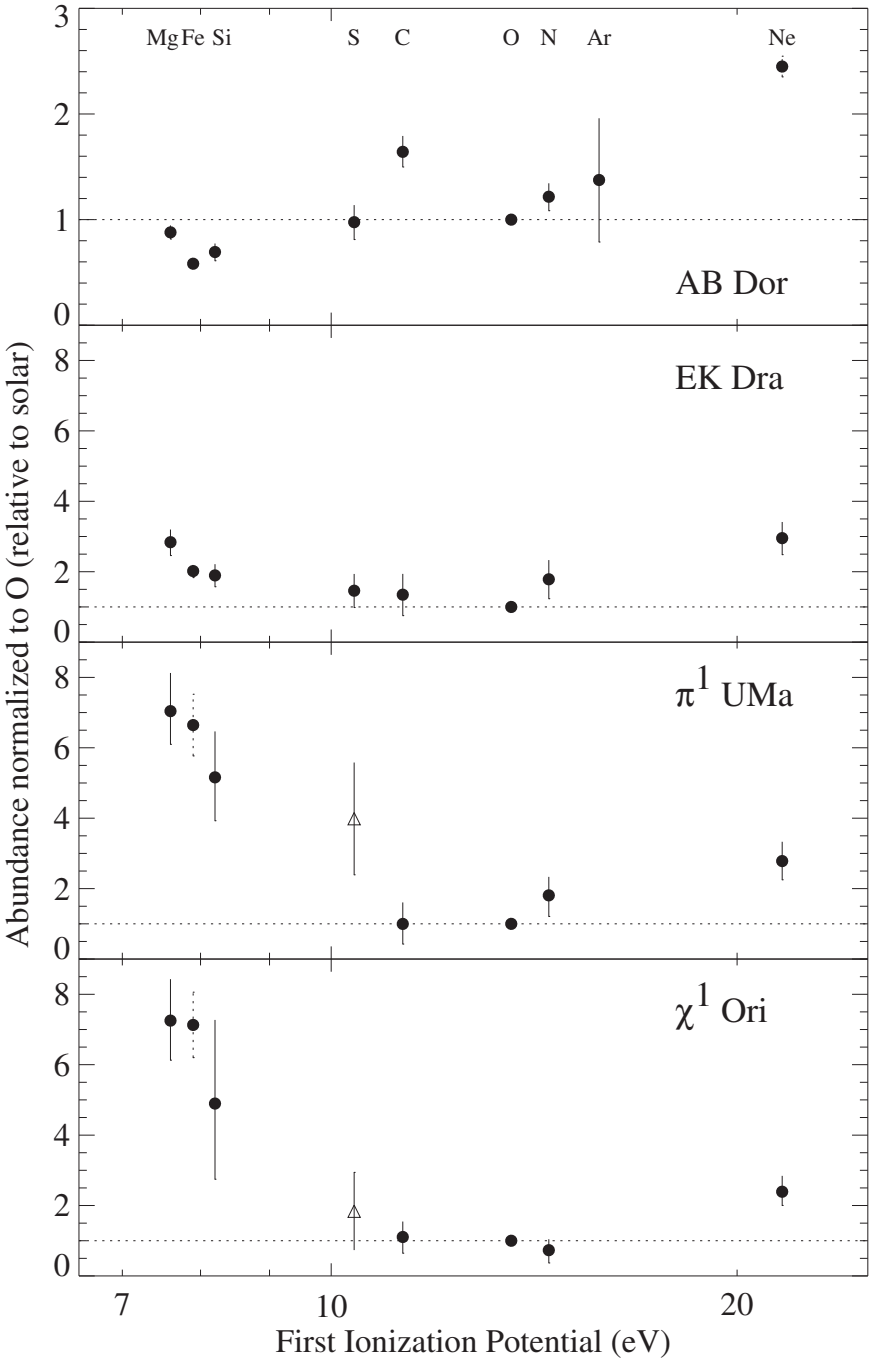

Figure 10.3: *Abundance ratios with oxygen, relative to the respective solar photospheric ratios, as a function of FIP, showing enhanced low-FIP element abundances in low-activity stars (bottom). Note different y axis scale for AB Dor. The values shown by triangles were estimated from selected L-shell lines but are of low quality:* S XIV $\lambda 30.423, 32.554$ *for* π^1 *UMa, and* S XIII $\lambda 32.236$ *&* S XIV $\lambda 32.430$ *for* χ^1 *Ori. See text for explanation of error bars.*

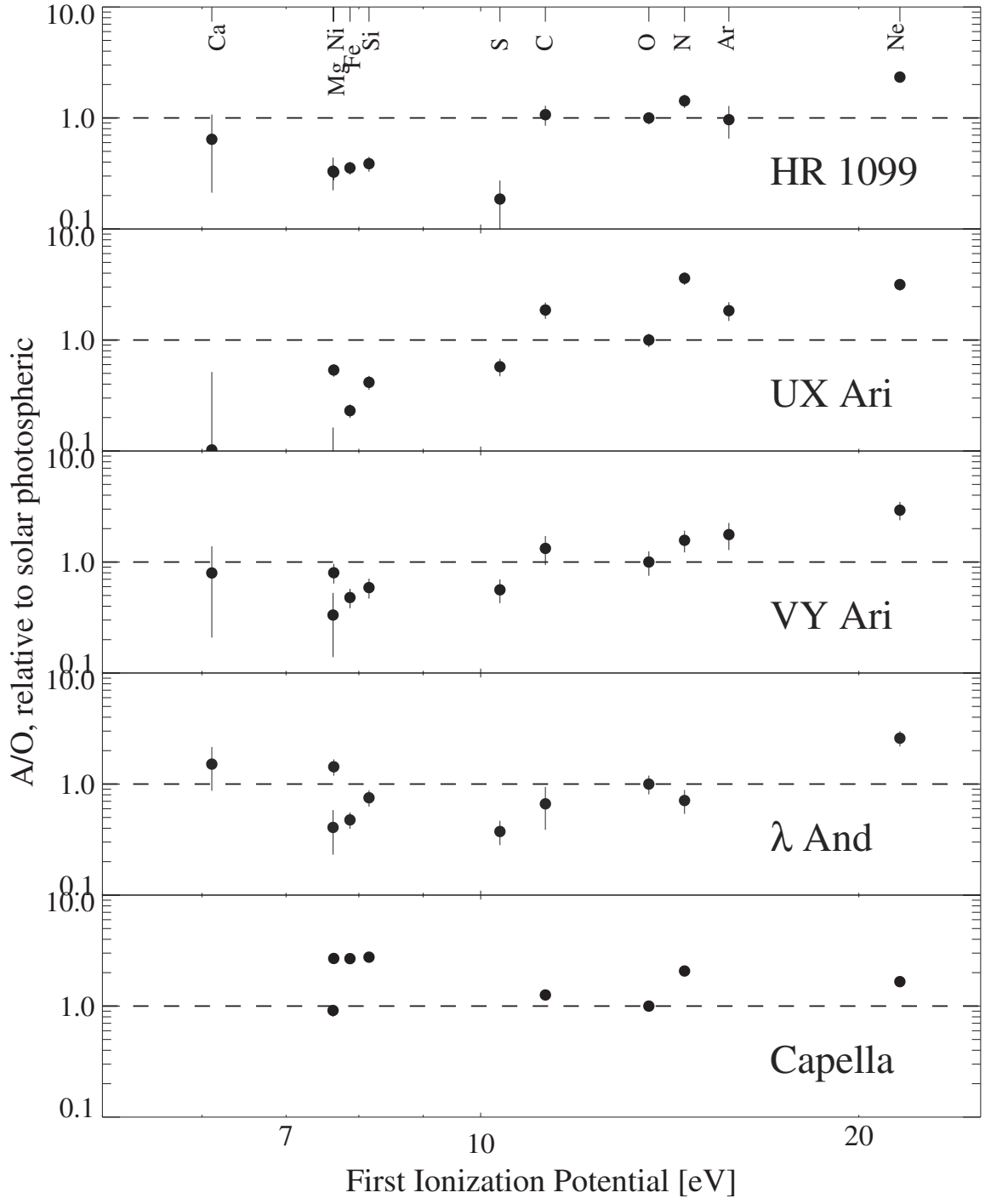

Figure 10.4: *Abundance ratios with oxygen, relative to the respective solar photospheric ratios, as a function of FIP for the RS CVn binary systems.*

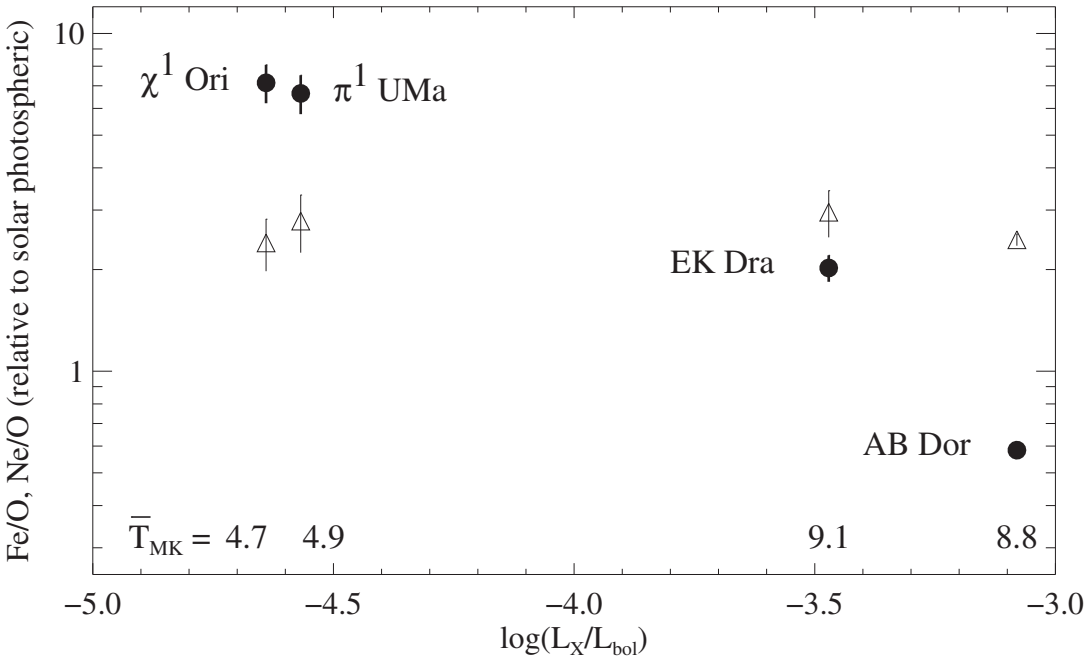

Figure 10.5: *Ratios of* Fe/O *(filled circles) and* Ne/O *(open triangles) relative to solar photospheric values, as a function of* $L_{\rm X}/L_{\rm bol}$*. Numbers at the bottom give EM weighted logarithmic averages of the coronal temperatures for the four targets in MK.*

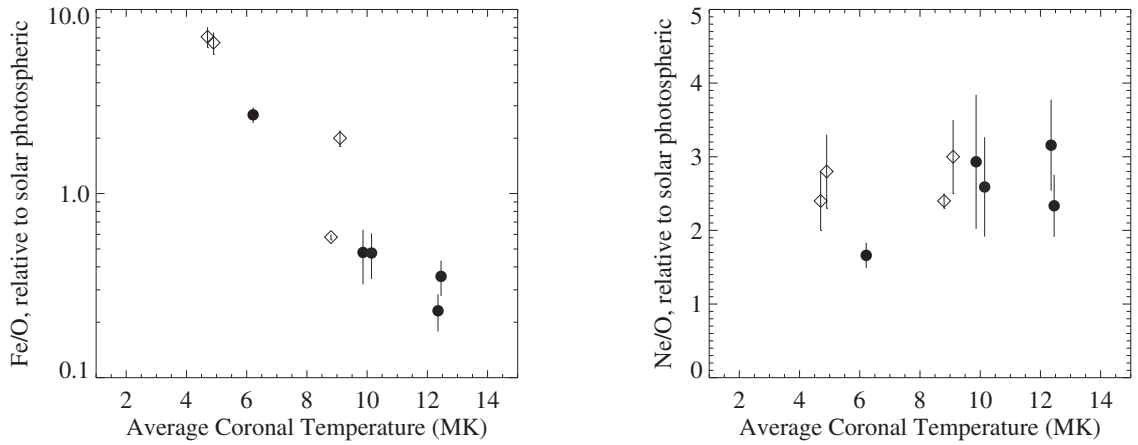

Figure 10.6: *Ratios of* Fe/O *(left) and* Ne/O *(right) relative to solar photospheric values, as a function of the average coronal temperature* T*. Note the different vertical scales (logarithmic for* Fe/O *and linear for* Ne/O*). Data from solar analogs (with stellar photospheric abundances close to solar) are shown with open diamonds, while data from RS CVn binaries (with essentially unknown stellar photospheric abundances) are shown as filled circles.*

with ours, Ne/O $\approx 2-3$ (Audard et al. 2001a,b; Brinkman et al. 2001; Drake et al. 2001; Güdel et al. 2001a,b)). This may indicate that the tabulated solar abundance of Ne is in error, unless the solar Ne abundance is exceptional among all stars considered.

10.5 Discussion and Conclusions

There is compelling evidence that the photospheres of all four solar analogs are of near-solar composition. We are thus, in the case of these stars, not subject to uncertainty related to stellar composition and are led to the conclusion that the overall magnetic activity level alone governs the amount of FIP or IFIP bias. We find that a solar-like star switches its average coronal abundance behavior from an IFIP to a FIP bias with decreasing activity, i.e., decreasing $L_{\rm X}/L_{\rm bol}$ or decreasing average T. This result appears to imply that the average coronal abundance pattern systematically changes during the long-term evolution of a solar-type star. While their photospheric abundances are essentially not available, all five bright RS CVn binary systems tend to follow the same correlation between the activity level and the FIP bias. There is no broad consensus as to what causes the coronal FIP effect (e.g., Hénoux 1995), and the situation is no better in the case of the inverse FIP bias found in some stars. Our stellar sample, however, indicates trends worthy of some speculation:

1) The average coronal temperature T of a star increases with increasing overall magnetic activity (e.g., Schrijver, Mewe, & Walter 1984), a trend that has been particularly well measured for solar analogs (Güdel, Guinan, & Skinner 1997b). It has been attributed to a higher rate of (micro-)flares that heat more active stellar coronae (Güdel 1997). Flares may influence the coronal abundances at least twofold: i) The Sun develops a class of Ne and S-rich flares (Reames, Ramaty, & Rosenvinge 1988; Murphy et al. 1991; Schmelz 1993) interpreted by Shemi (1991) as being due to the large photoionization cross section of Ne which consequently behaves like a low-FIP element. Brinkman et al. (2001) hypothesized that the high coronal abundance of Ne and other high-FIP elements in the active HR 1099 system is related to this class of flares. ii) However, many solar flares either show little FIP bias or none at all, which is possibly due to the transport of "fresh" and unfractionated photospheric material into the corona, while a FIP effect typically evolves in older coronal structures over days (Feldman & Widing 1990; Feldman 1992; McKenzie & Feldman 1992). This would be compatible with our observation that a FIP effect is seen only in the less active stars while it appears to be suppressed in AB Dor and EK Dra. Strong stellar flares show a preferential enrichment of low-FIP elements, i.e., the coronal composition moves from an IFIP composition closer to the putative photospheric composition (Güdel et al. 1999; Osten et al. 2000; Audard et al. 2001a).

2) Many magnetically active stellar coronae contain a large number of high-energy electrons detected by their gyrosynchrotron emission. It drops very rapidly with decreasing activity in solar analogs (Güdel et al. 1997b; Gaidos, Güdel, & Blake 2000). While the active RS CVn binary systems and AB Dor are prolific radio source (Lim et al. 1992), EK Dra's radio luminosity is weaker by almost an order of magnitude (Güdel et al. 1997b), while in the less active stars, it must be less than 1/300th of AB Dor's luminosity, if present at all (Gaidos et al. 2000). If

the electrons do not loose all their kinetic energy by radiation in coronal regions, there will be a net downward electron current into the chromosphere. The penetration depth $\ell \propto \epsilon^2/n_c$ for electrons of energy ϵ and a chromospheric layer of constant density n_c (Nagai & Emslie 1984). For $n_c = 10^{13}$ cm^{-3}, we obtain $\ell \approx 10^{17}\epsilon^2_{\rm keV}/n_c[{\rm cm}] \approx 10 - 1000$ km for $\epsilon = 10 - 100$ keV, i.e., a significant fraction of the chromospheric thickness (after equation 13 in Nagai & Emslie 1984). We require a sufficiently small electron flux in order to balance the energy influx in particles by radiation before heating exceeds 10^5 K, i.e., to prevent explosive chromospheric evaporation that transports all of the affected material into the corona (a corresponding criterion is given by Fisher, Canfield, & McClymont 1985). A charge separation is thus built up in the chromosphere that requires a return current. The electric field therefore drives protons and ions downward. Consequently, the upper layers of the chromosphere from where the coronal material is ultimately supplied with material, becomes depleted of (typically singly ionized) low-FIP elements while (mostly neutral) high-FIP elements remain unaffected. This effect operates on a smaller level also due to the transition-region temperature gradient that induces a thermoelectric field, dragging positive charge downward. We note that even if coronal proton beams accompany the energetic electrons, downward drag of heavy ions will result due to the large collisional coupling coefficient between protons and ions, compared to neutrals (Wang 1996). Transport of the upper chromospheric layers into the corona by whatever means, e.g., microflares, will thus produce an IFIP biased coronal plasma. Only when the electron flux is large enough to produce explosive evaporation of a larger part of the chromosphere will the IFIP enrichment be quenched, i.e., the composition returns back to near-photospheric (or FIP-biased in the model of Wang 1996), in agreement with observations of large stellar flares (see above).

Chapter 11

Outlook

This doctoral thesis has shown that flares probably play an important role in magnetically active stars. They may be active agents of coronal heating, and they may also be relevant to explain the First Ionization Potential bias observed in the Sun and stars. A better understanding of the flare physics in stars is thus needed. Thanks to high-resolution X-ray spectroscopy, plasma diagnostics in quiescent and flaring states can provide useful information about the physical processes taking place in stellar coronae. Past experience has shown that crucial information can be obtained from simultaneous multi-wavelength observations as well. Early results with *XMM-Newton* and *Chandra* are promising, however they have raised new questions that need to be addressed. For example,

- How are coronal abundances related to the physics of stellar coronae? Are they generally and physically related to the activity level, to age?
- Is a FIP bias (inverse or normal) ubiquitous in stars? Are stars without FIP bias the rule or the exception? What can we learn from these stars?
- What is the effect of mass transport in flares? Is the FIP bias related to it?
- Do we measure different electron densities from lines formed at low temperature ($1 - 3$ MK) than from lines formed at higher temperature? How does this relate to coronal structures?
- What are the implications of flares for very young stars and for their environment?

The answers will modify our understanding of high-energy processes in stellar coronae, and will have far-reaching consequences from ionization of stellar environments and planetary atmospheres to indirect influences on the origin of life.

Bibliography

Agrawal, P. C., & Vaidya, J. 1988, MNRAS, 235, 239
Alef, W., Benz, A. O., & Güdel M. 1997, A&A, 317, 707
Anders, E., & Grevesse, N. 1989, Geochim. Cosmochim. Acta, 53, 197
Anosova, J. P., & Orlov, V. V. 1991, A&A, 252, 123
Antiochos, S. K. 1994, Adv. Space. Res., 14, 139
Antonucci, E., Gabriel, A. H., & Dennis, B. R. 1984, ApJ, 287, 917
Arnaud, K. A. 1996, in ASP Conf. Ser. 101, Astronomical Data Analysis Software and Systems V, ed. G. Jacoby & J. Barnes (San Francisco: ASP), 17
Arnaud, M., & Rothenflug, R. 1985, A&AS, 60, 425
Arnaud, M., & Raymond, J. 1992, ApJ, 398, 394
Aschwanden, M. J. 1999, Sol. Phys., 190, 233
Aschwanden, M. J., Tarbell, T. D., Nightingale, R. W., Schrijver, C. J., Title, A., Kankelborg, C. C., Martens, P. C. H., & Warren, H. P. 2000, ApJ, 535, 1047
Audard, M. & Güdel, M. 2002, A&A, in preparation
Audard, M., Güdel, M., & Guinan, E. F. 1998, in Proceedings of the First XMM Workshop on "Science with XMM", Noordwijk, The Netherlands, M. Dahlem (ed.), URL `http://astro.estec.esa.nl/XMM/news/ws1/ws1_papers.html`
Audard, M., Güdel, M., & Guinan, E. F. 1999, ApJ, 513, L53
Audard, M., Güdel, M., Drake, J. J., & Kashyap, V. L. 2000, ApJ, 541, 396
Audard, M., Behar, E., Güdel, M. et al. 2001b, A&A, 365, L329
Audard, M., Güdel, M., & Mewe, R. 2001a, A&A, 365, L318
Ayres, T. R., Linsky, J. L., Vaiana, G. S., Golub, L., & Rosner, R. 1981, ApJ, 250, 293
Ayres, T. R., Brown, A., Osten, R. A. et al. 2001, ApJ, 549, 554
Bai, T. 1993, ApJ, 404, 805
Baliunas, S. L., Vaughan, A. H., Hartmann, L. W., Middelkoop, F., Mihalas, D., Noyes, R. W., Preston, G. W., Frazer, J., & Lanning, H. 1983, ApJ, 275, 752
Bar-Shalom, A., Klapisch, M., Goldstein, W. H., & Oreg, J. 1998, *The HULLAC code for atomic physics*, (unpublished)
Batten, A. H., Fletcher, J. M., & Mann, P. J. 1978, Publ. Dominion Astrophys. Obs., 15, 121
Behar, E., Cottam, J., & Kahn, S. M. 2000, ApJ, 548, 966
Benz, A. O., & Güdel, M. 1994, A&A, 285, 621
Benz, A. O., Conway, J., & Güdel M. 1998, A&A, 331, 596
Boella, G., Butler, R. C., Perola, G. C., Piro, L., Scarsi, L., & Bleeker, J. A. M. 1997a, A&AS,

122, 299
Boella, G., Chiappetti, L., Conti, G., et al. 1997b, A&AS, 122, 327
Bopp, W., & Fekel, F. C. 1976, AJ, 81, 771
Brickhouse, N. S. 1996, in IAU Colloq. 152, Astrophysics in the Extreme Ultraviolet, ed. S. Bowyer & R. F. Malina (Dordrecht: Kluwer), 105
Brickhouse, N. S., Dupree, A. K., Edgar, R. J. et al. 2000, ApJ, 530, 387
Brinkman, A. C., Behar, E., Güdel, M. et al. 2001, A&A, 365, L324
Brinkman, A. C., Gunsing, C. J. T., Kaastra, J. S. et al. 2000, ApJ, 530, L111
Bromund, K. R., McTiernan, J. M., & Kane, S. R. 1995, ApJ, 455, 733
Burnight, T. R. 1949, Phys. Rev. A, 76, 165
Caillault, J.-P., & Helfand, D. J. 1985, ApJ, 289, 279
Canizares, C. R., Huenemoerder, D. P., Davis, D. S. et al. 2000, ApJ, 539, L41
Cash, W., Bowyer, S., Charles, P. A., Lampton, M., Garmire, G., & Riegler, G. 1978, ApJ, 223, L21
Catura, R. C., Acton, L. W., & Johnson, H. M. 1975, ApJ, 196, L47
Cayrel de Strobel, G., Soubiran, C., & Ralite, N. 2001, A&A, 373, 159
Christensen-Dalsgaard, J., Gough, D. O., & Thompson, M. J. 1991, ApJ, 378, 413
Collier Cameron, A., & Foing, B. H. 1997, Observatory, 117, 218
Collier Cameron, A., Bedford, D. K., Rucinski, S. M., Vilhu, O., & White, N. E. 1988, MNRAS, 231, 131
Collier Cameron, A., Walter, F. M., Vilhu, O., et al. 1999, MNRAS, 308, 493
Collura, A., Pasquini, L., & Schmitt, J. H. M. M. 1988, A&A, 205, 197
Crawford, D. F., Jauncey, D. L., & Murdoch, H. S. 1970, ApJ, 162, 405
Crosby, N. B., Aschwanden, M. J., & Dennis, B. R. 1993, Sol. Phys., 143, 275
Datlowe, D. W., Elcan, M. J., & Hudson, H. S. 1974, Sol. Phys., 39, 155
Daw, A., DeLuca, E. E., & Golub, L. 1995, ApJ, 453, 929
Delfosse, X., Forveille, T., Perrier, C., & Mayor, M. 1998, A&A, 331, 581
Dempsey, R. C., Linsky, J. L., Fleming, T. A., & Schmitt, J. H. M. M. 1993a, ApJS, 86, 599
Dempsey, R. C., Linsky, J. L., Fleming, T. A., & Schmitt, J. H. M. M. 1997, ApJ, 478, 358
Dempsey, R. C., Linsky, J. L., Schmitt, J. H. M. M., & Fleming, T. A. 1993b, ApJ, 413, 333
Dennis, B. R. 1985, Sol. Phys., 100, 465
Dere, K. P., Bartoe, J.-D. F., & Brueckner, G. E. 1989, Sol. Phys., 123, 41
Dorren, J. D., & Guinan, E. F. 1993, ApJ, 428, 805
Doyle, J. G., & Butler, C. J. 1985, Nature, 313, 378
Drake, J. F. 1971, Sol. Phys., 16, 152
Drake, J. J., & Kashyap, V. L. 1998, in ASP Conf. Ser. 154, Tenth Cambridge Workshop on Cool Stars, Stellar Systems, and the Sun, ed. R. A. Donahue & J. A. Bookbinder (San Francisco: ASP), 1014
Drake, J. J., Brickhouse, N. S., Kashyap, V., Laming, J. M., Huenemoerder, D. P., Smith, R., & Wargelin, B. J. 2001, ApJ, 548, L81
Drake, J. J., Brown, A., Patterer, R. J., Vedder, P. W., Bowyer, S., & Guinan, E. F. 1994, ApJ, 421, L43
Drake, J. J., Laming, J. M., & Widing, K. G. 1995, ApJ, 443, 393

Drake, J. J., Laming, J. M., & Widing, K. G. 1997, ApJ, 478, 403
Drake, S. A. 1996, in 6th Annual Astrophysics Conference, Maryland, ed. S. S. Holt & G. Sonneborn (San Francisco: ASP), 215
Drake, S. A., Simon, T., Linsky, J. L. 1989, ApJS, 71, 905
Drake, S. A., Simon, T., Linsky, J. L. 1992, ApJS, 82, 311
Dupree, A. K., & Brickhouse, N. S. 1996, in Poster Proc., IAU Symp. 176: Stellar Surface Structure (Wien: Institut für Astronomie), 184
Dupree, A. K., Brickhouse, N. S., Doschek, G. A., Green, J. C., & Raymond, J. C. 1993, ApJ, 418, L41
Eggen, O. J. 1983, MNRAS, 204, 405
Ehle, M., Breitfellner, M., Dahlem, M., Guainazzi, M., Rodriguez, P., Santos-Lleo, M., Schartel, N., & Tomas, L. 2001, XMM-Newton Users' Handbook, issue 2.0, 15.08.2001
Favata, F., Mewe, R., Brickhouse, N. S., Pallavicini, R., Micela, G., & Dupree, A. K. 1997, A&A, 324, L37
Favata, F., Reale, F., Micela, G., Sciortino, S., Maggio, A., & Matsumoto, H. 2000, A&A, 353, 987
Fekel, F. C 1983, ApJ, 268, 274
Fekel, F. C. 1997, PASP, 109, 514
Feldman, U., Laming, J. M., & Doschek, G. A. 1995, ApJ, 451, L79
Feldman, U. 1992, Phys. Scripta, 46, 202
Feldman, U., & Widing, K. G. 1990, ApJ, 363, 292
Feldman, U., Doschek, G. A., & Klimchuk, J. A. 1997, ApJ, 474, 511
Feldman, U., Schühle, U., Widing, K. G., Laming, J. M. 1998, ApJ, 505, 999
Fiore, F., Guainazzi, M., & Grandi, P. 1999, Cookbook for BeppoSAX NFI Spectral Analysis, version 1.2: 7 January 1999
Fisher, G. H., Canfield, R. C., & McClymont, A. N. 1985, ApJ, 289, 425
Fontenla, J. M., & Avrett, E. H. 1992, in Proceedings of the first SOHO workshop, ESA SP-348, 335
Frontera, F., Costa, E., & dal Fiume, D. 1997, A&AS, 122, 357
Franciosini, E., Pallavicini, R., Tagliaferri, G. 2001, A&A, 375, 196
Gabriel, A. H. 1972, MNRAS, 160, 99
Gabriel, A. H, & Jordan, C. 1969, MNRAS, 145, 241
Gaidos, E. J., Güdel, M., & Blake, G. A. 2000, Geophys. Res. Lett., 27, 501
Gehrels, N. 1986, ApJ, 303, 336
Geiss, A. 1982, Space. Sci. Rev, 33, 201
Gliese, W., & Jahreiss, H. 1991, Preliminary version of the Third Catalogue of Nearby Stars, on: The Astronomical Data Center CD-ROM: Selected Astronomical Catalogues, Vol. 1; ed. L. E. Brotzmann & S. E. Gesser, NASA/Astronomical Data Center, Goddard Space Flight Center, Greenbelt, MD
Golub, L. & Pasaschoff, J. M. 1997, The Solar Corona, (Cambridge: CUP)
Gotthelf, E. V., Jalota, L., Mukai, K., & White N. E. 1994, ApJ, 436, L91
Grevesse, N., & Sauval, A. J. 1999, A&A, 347, 348
Griffiths, N. W., & Jordan, C. 1998, ApJ, 497, 883

Groot, P. J., Piters, A. J. M., & van Paradijs, J. 1996, A&AS, 118, 545
Grotrian, W. 1939, Naturwissen., 27, 214
Güdel, M. 1994, ApJS, 90, 743
Güdel, M. 1997, ApJ, 480, L121
Güdel, M. 2002, Adv. Space Res., submitted
Güdel, M., & Benz, A. O. 1993, ApJ, 405, L63
Güdel, M., & Schmitt, J. H. M. M. 1996, in: Radio Emission from the Stars and the Sun, eds. A. R. Taylor and J. M. Paredes (San Francsisco: ASP) 315
Güdel, M., Audard, M., Briggs, K. et al. 2001a, A&A, 365, L336
Güdel, M., Audard, M., Kashyap, V. L., & Drake, J. J. 2002a, ApJ, in preparation
Güdel, M., Audard, M., Magee, H. et al. 2001b, A&A, 365, L344
Güdel, M., Audard, M., Smith, K. W, et al. 2002c, ApJ, submitted
Güdel, M., Audard, M., Sres, A., Wehrli, R., & Mewe, R. 2002b, ApJ, submitted
Güdel, M., Benz, A. O., Schmitt, J. H. M. M., & Skinner, S. L. 1996, ApJ, 471, 1002
Güdel, M., Guinan, E. F., Mewe, R., Kaastra, J. S., & Skinner, S. L. 1997a, ApJ, 479, 416
Güdel, M., Guinan, E. F., & Skinner, S. L. 1997b, ApJ, 483, 947
Güdel, M., Guinan, E. F., Etzel, P. B., et al. 1998, in The Tenth Cambridge Workshop on Cool Stars, Stellar Systems and the Sun, eds. R. A. Donahue & J. A. Bookbinder (San Francisco: ASP), 1247
Güdel, M., Linsky, J. L., Brown, A., & Nagase, F. 1999, ApJ, 511, 405
Güdel, M., Schmitt, J. H. M. M., & Benz, A. O. 1995, A&A, 293, L49
Guinan, E. F., & Giménez, A. 1993, in: The Realm of Interacting Binary Stars, eds. J. Sahade et al. (Dordrecht: Kluwer), 51
Guirado, J. C., Reynolds, J. E., Lestrade, J.-F. et al. 1997, ApJ, 490, 835
Haisch, B., & Schmitt, J. H. M. M. 1996, PASP, 108, 113
Haisch, B. M., Schmitt, J. H. M. M., Rodonò, M., & Gibson D. M. 1990, A&A, 230, 419
Hatzes, A. P. 1995, in: Stellar Surface Structure - Poster Proceedings, ed. K. G. Strassmeier, Vienna, p. 90
Hawley, S. L., Fisher, G. H., Simon, T., et al. 1995, ApJ, 453, 464
Hearn, A. G. 1975, A&A, 40, 355
Heintz, W. D. 1988, PASP, 100, 834
Hénoux, J.-C. 1995, Adv. Space Res., 15, 23
Hénoux, J.-C. 1998, Space Sci. Rev., 85, 215
Hénoux, J.-C., & Somov, B. V. 1997, A&A, 241, 613
Hénoux, J.-C., & Somov, B. V. 1997, A&A, 318, 947
den Herder, J. W., Brinkman, A. C., Kahn, S. M. et al. 2001, A&A, 365, L7
Holt, S. S., White, N. E., Becker, R. H. et al. 1979, ApJ, 234, L65
Howarth, I. D., Murray, M. J., & Mills D. 1998, SERC Starlink User Note No. 50
Hudson, H. S. 1991, Sol. Phys., 133, 357
Hudson, H. S., Peterson, L. E. & Schwartz, D. A. 1969, ApJ, 157, 389
Hummel, C. A., Armstrong, J. T., Quirrenbach, A., Buscher, D. F., Mozurkewich, D., & Elias II, N. M. 1994, AJ, 107, 1859
Hünsch, M., Schmitt, J. H. M. M., Sterzik, M. F., & Voges, W. 1999, A&AS, 135, 319

Hünsch, M., Schmitt, J. H. M. M., & Voges, W. 1998, A&AS, 132, 155
Innis, J. L., Thompson, K., Coates, D. W., & Lloyd Evans, T. 1988, MNRAS, 235, 1411
Ionson, J. A. 1985, Sol. Phys., 100, 289
Jakimiec, J., Sylwester, B., Sylwester, J., Serio, S., Peres, G., & Reale, G. 1992, A&A, 253, 269
Jansen, F., Lumb, D. H., Altieri, B. et al. 2001, A&A, 365, L1
Jordan, C., & Montesinos, B. 1991, MNRAS, 252, 21
Jordan, C., Ayres, T. R., Brown, A., Linsky, J. L., & Simon, T. 1987, MNRAS, 225, 903
Kaastra, J. S., Mewe, R., Liedahl, D. A., Singh, K. P., White, N. E., & Drake, S. A. 1996b, A&A, 314, 547
Kaastra, J. S., Mewe, R., & Nieuwenhuijzen, H. 1996a, in UV and X-ray Spectroscopy of Astrophysical and Laboratory Plasmas, eds. K. Yamashita & T. Watanabe (Tokyo: Univ. Acad. Press), 411
Kahler, S. W. 1982, JGR, 87, 3439
Kashyap, V. L., Drake, J. J., Audard, M., & Güdel, M. 2000, BAAS, 196, 13.05
Kashyap, V. L., Drake, J. J., Güdel, M. & Audard, M., 2002, ApJ, in preparation
Kopp, R. A., & Poletto, G. 1993, ApJ, 418, 496
Kraft, R. P. 1967, ApJ, 150, 551
Krucker, S., & Benz, A. O. 1998, ApJ, 501, L213
Kürster, M., Schmitt, J. H. M. M., & Cutispoto, G. 1994, A&A, 289, 899
Kürster, M., Schmitt, J. H. M. M., Cutispoto, G., & Dennerl, K. 1997, A&A, 320, 831
Laming, J. M., & Drake, J. J. 1999, ApJ, 516, 324
Laming, J. M., Drake, J. J., & Widing, K. G. 1995, ApJ, 443, 416
Laming, J. M., Drake, J. J., & Widing, K. G. 1996, ApJ, 462, 948
Lemen, J. R., Mewe, R., Schrijver, C. J., & Fludra, A. 1989, ApJ, 341, 474
Lim, J., Nelson, G. J., Castro, C., Kilkenny, D., & van Wyk, F. 1992, ApJ, 388, L27
Lin, R. P., Schwartz, R. A., Kane, S. R., Pelling, R. M., & Hurley, K. 1984, ApJ, 283, 421
Linsky, J. L. 1985, Sol. Phys., 100, 333
Linsky, J. L., & Gary, D. E. 1983, ApJ, 274, 776
Linsky, J. L., & Wood, B. E. 1994, ApJ, 430, 342
Linsky, J. L., Ayres, T. R., Basri, G. S., et al. 1978, Nature, 275, 389
Linsky, J. L, Brown, A., Gayley, K., et al. 1993, ApJ, 402, 694
Linsky, J. L., Wood, B. E., Brown, A., Osten, R. A. 1998, ApJ, 492, 767
Lumb, D. H., Gondoin, Ph., Turner, M. J. L. et al. 2000, in SPIE Proceedings vol. 4140, 22
Maggio, A., Pallavicini, R., Reale, F., & Tagliaferri, G. 2000, A&A, 356, 627
Majer, P., Schmitt, J. H. M. M., Golub, L., Harnden, F. R., & Rosner, R. 1986, ApJ, 300, 360
Malina, R. F., & Bowyer, S. 1991, in Extreme Ultraviolet Astronomy, eds. R. F. Malina & S. Bowyer (New York: Pergamon), 397
Marsch, E., von Steiger, R., & Bochsler, P. 1995, A&A, 301, 261
Mason, K. O., Breeveld, A., Much, R. et al. 2001, A&A, 365, L36
Mazzotta, P., Mazzitelli, G., Colafrancesco, S., & Vittorio, N. 1998, A&A, 133, 403
McKenzie, D. L., & Feldman, U. 1992, ApJ, 389, 764
McWilliam, A. 1990, ApJS, 74, 1075

Mewe, R. 1999, in X-ray Spectroscopy in Astrophysics, EADN School X., ed. J. van Paradijs & J. A. M. Bleeker (Berlin: Springer), 109
Mewe, R., Gronenschild, E. H. B. M., Westergaard, N. J. et al. 1982, ApJ, 260, 233
Mewe, R., Gronenschild, E. H. B. M., & van den Oord G. H. J. 1985, A&AS, 62, 197
Mewe, R., Heise, J., Gronenschild, E. H. B. M., Brinkman, A. C., Schrijver, J., & den Boggende, A. J. F. 1975, ApJ, 202, L67
Mewe, R., Kaastra, J. S., & Liedahl, D. A. 1995, Legacy, 6, 16
Mewe, R., Kaastra, J. S., van den Oord, G. H. J., Vink, J., & Tawara, Y. 1997, A&A, 320, 147
Mewe, R., Kaastra, J. S., White, S. M., & Pallavicini, R. 1996, A&A, 315, 170
Mewe, R., Raassen, A. J. J., Drake, J. J., Kaastra, J. S., van der Meer, R. L. J., & Porquet, D. 2001, A&A, 368, 888
Meyer, J.-P. 1985, ApJS, 57, 173
Miller, A. 1997, Extreme Ultraviolet Guest Observer Program Handbook
Monsignori Fossi, B. C., Landini, M., Del Zanna, G., & Bowyer, S. 1996, ApJ, 466, 427
Murphy, R. J., Ramaty, R., Kozlovsky, B., & Reames, D. V. 1991, ApJ, 371, 793
Mutel, R. L., Lestrade, J. F., Preston, R. A., & Phillips R. B. 1985, ApJ, 289, 262
Mutel, R. L., Molnar, L. A., Waltman, E. B., & Ghigo F. D. 1998, ApJ, 507, 371
Nagai, F., & Emslie, A. G. 1984, ApJ, 279, 896
Narain, U., & Ulmschneider, P. 1990, Space Sci. Rev., 54, 377
Narain, U., & Ulmschneider, P. 1996, Space Sci. Rev., 75, 453
Ness, J. U., Mewe, R., Schmitt, J. H. M. M., Raassen, A. J. J., Porquet, D. et al. 2001, A&A, 367, 282
Neupert, W. M. 1968, ApJ, 153, L59
Noyes, R. W., Hartmann, L. W., Baliunas, S. L., Duncan, D. K., & Vaughan, A. H. 1984, ApJ, 279, 763
Ortolani, A., Pallavicini, R., Maggio, A., Reale, F., & White, S. M. 1998, in: 10th Cambridge Workshop on Cool Stars, Stellar Systems, and the Sun, ed. R. A. Donahue & J. A. Bookbinder (San Francisco: ASP), 1532
Osten, R. A., & Brown, A. 1999, ApJ, 515, 746
Osten, R. A., Brown, A., Ayres, T. R., Linsky, J. L., Drake, S. A., Gagné, M., & Stern, R. A. 2000, ApJ, 544, 953
Ottmann, R., & Schmitt, J. H. M. M. 1996, A&A, 307, 813
Ottmann, R., Schmitt, J. H. M. M., & Kürster M. 1993, ApJ, 413, 710
Pakull, M. W. 1981, A&A, 104, 33
Pallavicini, R., & Tagliaferri, G. 1998, Nucl. Phys. B (Proc. Suppl.), 69, 29
Pallavicini, R., Golub, L., Rosner, R., Vaiana, G. S., Ayres, T., & Linsky, J. L. 1981, ApJ, 248, 279
Pallavicini, R., Monsignori-Fossi, B. C., Landini, M., & Schmitt, J. H. M. M. 1988, A&A, 191, 109
Pallavicini, R., Tagliaferri, G., Pollock, A. M. T., Schmitt, J. H. M. M., & Rosso, C. 1990b, A&A, 227, 483
Pallavicini, R., Tagliaferri, G., & Stella, L. 1990a, A&A, 228, 403
Parker, E. N. 1955, ApJ, 122, 293

Parker, E. N. 1988, ApJ, 330, 474
Parker, E. N. 1993, ApJ, 408, 707
Parmar, A. N., Guainazzi, M., & Oosterbroek, T. 1999, A&A, 345, 611
Parmar, A. N., Martin, D. D. E., & Bavdaz, M. 1997, A&AS, 122, 309
Parnell, C. E., & Jupp, P. E. 2000, ApJ, 529, 554
Pasquini, L., Schmitt, J. H. M. M., & Pallavicini, R. 1989, A&A, 226, 225
Perryman, M. A. C., Lindegren, L., Kovalevsky, J., et al. 1997, A&A, 323, L49
Peter, H. 1996, A&A, 312, L37
Peter, H. 1998, A&A, 335, 691
Pettersen, B. R. 1976, in: Catalogue of Flare Star Data, Rept. No. 46 (Oslo: Inst. of Theoretical Astrophysics)
Pettersen, B. R., Olah, K., & Sandmann, W. H. 1992, A&AS, 96, 497
Phillips K. J. H., Mewe R., Harra-Murnion L. K., Kaastra J. S., Beiersdorfer P., Brown G. V., Liedahl D. A., 1999, A&AS138, 381
Porquet, D., & Dubau, J. 2000, A&AS, 143, 495
Porquet, D., Mewe, R., Raassen, A. J. J., Kaastra, J. S., & Dubau, J. 2001, 376, 1113
Porter, J. G., Fontenla, J. M., & Simnett, G. M. 1995, ApJ, 438, 472
Pradhan, A. K. 1982, ApJ, 263, 477
Press, W. H., Teukolsky, S. A., Vetterling, W. T., & Flannery, B. P. 1992, Numerical Recipes in Fortran 77: the art of scientific computing – 2nd ed., (Cambridge: CUP), 637
Randich, S., Giampapa, M. S., & Pallavicini, R. 1994, A&A, 283, 893
Randich, S., Schmitt, J. H. M. M., Prosser, C. F., & Stauffer, J. R. 1996, A&A, 305, 785
Reale, F., & Micela, G. 1998, A&A, 334, 1028
Reale, F., Betta, R., Peres, G., Serio, S., & McTiernan, J. 1997, A&A, 325, 782
Reames, D. V., Ramaty, R., & von Rosenvinge, T. T. 1988, ApJ, 332, L87
Robinson, R. D., Carpenter, K. G., & Percival, J. W. 1999, ApJ, 516, 916
Robinson, R. D., Carpenter, K. G., Percival, J. W., & Bookbinder, J. A. 1995, ApJ, 451, 795
Rosner, R., Tucker, W. H., & Vaiana, G. S. 1978, ApJ, 220, 643
Rucinski, S. M., Mewe, R., Kaastra, J. S., Vilhu, O., & White, S. M. 1995, ApJ, 449, 900
Schmelz, J. T. 1993, ApJ, 408, 373
Schmidt-Kaler, T. H. 1982, In Landolt-Börnstein New Series, Vol. 2B, Astronomy & Astrophysics – stars and star clusters, ed. K. Schaifers & H. H. Voigt, (Berlin: Springer), 15 & 453
Schmitt, J. H. M. M., & Favata F. 1999, Nature, 401, 44
Schmitt, J. H. M. M., & Kürster M. 1993, Science, 262, 215
Schmitt, J. H. M. M., Collura, A., Sciortino, S., Vaiana, G. S., Harnden, F. R., & Rosner, R. 1990, ApJ, 365, 704
Schmitt, J. H. M. M, Fleming, T. A., & Giampapa, M. S. 1995, ApJ, 450, 392
Schmitt, J. H. M. M., Güdel, M., & Predehl, P. 1994, A&A, 287, 843
Schmitt, J. H. M. M., Stern, R. A., Drake, J. J., & Kürster, M. 1996, ApJ, 464, 898
Schrijver, C. J. & Zwaan, C. 2000, Solar and Stellar Magnetic Activity, Cambridge Astrophysics Series 34, (Cambridge: CUP)
Schrijver, C. J., Aschwanden, M. J., & Title, A. M 2002, Sol. Phys., in press

Schrijver, C. J., Mewe, R., & Walter, F. M. 1984, A&A, 138, 258
Schrijver, C. J., Mewe, R., van den Oord, G. H. J., & Kaastra, J. S. 1995, A&A, 302, 438
Schüssler, M., & Solanki, S. K. 1992, A&A, 264, L13
Sciortino, S., Maggio, A., Favata, F., & Orlando, S. 1999, A&A, 342, 502
Shemi, A. 1991, MNRAS, 251, 221
Shimizu, T. 1995, PASJ, 47, 251
Siarkowski, M. 1992, MNRAS, 259, 453
Siarkowski, M., Preś, P., Drake, S. A., White, N. E., & Singh, K. P. 1996, ApJ, 473, 470
Simon, T. 2001, In Eleventh Cambridge Workshop on Cool stars, Stellar Systems, and the Sun, ed. R. J. García López, R. Rebolo, & M. R. Zapatero Osorio (San Francisco:ASP), 235
Simon, T., Boesgaard, A. M., Herbig, G. 1985, ApJ, 293, 551
Singh, K. P., White, N. E., & Drake, S. A. 1996, ApJ, 456, 766
Skumanich, A. 1972, ApJ, 171, 565
Skumanich, A. 1985, Aust. J. Phys., 38, 971
Soderblom, D. R., & Mayor, M. 1993, AJ, 105, 226
Spiesman, W. J., & Hawley, S. L. 1986, AJ, 92, 664
Stauffer, J. R. & Hartmann, L. W., PASP, 98, 1233
Stauffer, J. R., Caillault, J.-P., Gagné, M., Prosser, C. F., & Hartmann, L. W. 1994, ApJS, 91, 625
Stauffer, J. R., Hartmann, L. W., Prosser, C. F., Randich, S., Balachandran, S., Patten, B. M., Simon, T., & Giampapa, M. 1997, ApJ, 479, 776
Strassmeier, K. G., & Fekel F. C. 1990, A&A, 230, 389
Strassmeier, K. G., & Rice, J. B. 1998a, A&A, 330, 685
Strassmeier, K. G., & Rice J. B. 1998b, A&A, 339, 497
Strassmeier, K. G., Bartus, J., Cutispoto, G., & Rodonò, M. 1997, A&AS, 125, 11
Streissmeier, K. G., Hall, D. S., Fekel, F. C., & Scheck, M. 1993, A&AS, 100, 173
Stępień, K. 1993, in The Cosmic Dynamo, ed. F. Krause, K.-H. Rädler, & G. Rüdiger, (Dordrecht: Kluwer), 141
Strüder, L., Briel, U. G., Dennerl, K. et al. 2001, A&A, 365, L18
Sylwester, J., Lemen, J. R., & Mewe, R. 1984, Nature, 310, 665
Tagliaferri, G., Covino, S., Fleming, T. A., Gagné, M., Pallavicini, R., Haardt, F., & Uchida, Y. 1997, A&A, 321, 850
Tsuboi, Y., Koyama, K., Murakami, H., Hayashi, M., Skinner, S., & Ueno, S. 1998, ApJ, 503, 894
Turner, M. J. L., Abbey, A., Arnaud, M. et al. 2001, A&A, 365, L26
Uchida, Y., & Sakurai, T. 1983, in: Activity in Red Dwarf Stars. ed. M. Rodonó & P. Byrne (Dordrecht: Reidel) 629
Vaiana, G. S., Fabbiano, G., Giacconi, R., et al. 1981, ApJ, 245, 163
van den Oord, G. H. J., Mewe, R., & Brinkman, A. C. 1988, A&A, 205, 181
Vauclair, S. 1996, A&A, 308, 228
Vauclair, S., & Meyer, J.-P. 1985, Proc. 19th Int. Cosmic Ray Conf., 4, 233
Vedder, P. W., & Canizares, C. R. 1983, ApJ, 270, 666
Vilhu, O. 1984, A&A, 133, 117

Vilhu, O., & Linsky, J. L. 1987, PASP, 99, 1071
Vilhu, O., & Walter, F. M. 1987, ApJ, 321, 958
Vilhu, O., Gustafsson, B., Edvardsson, B. et al. 1987, ApJ, 320, 850
Vilhu, O., Tsuru, T., Collier Cameron, A. et al. 1993, A&A, 278, 467
Voges, W., Aschenbach, B., Boller, T., et al. 2000, IAU Circ. 7432
Vogt, S. S., Hatzes, A. P., Misch, A. A., & Kürster, M. 1999, ApJS, 121, 547
von Steiger, R., & Geiss, J. 1989, A&A, 225, 222
von Steiger, R., Schweingruber, R. F. Wimmer, Geiss, J., Gloeckler, G. 1995, Adv. Space. Res., 15, 3
Walter, F. M. 1981, ApJ, 245, 677
Walter, F. M. 1982, ApJ, 253, 745
Walter, F. M., & Bowyer, S. 1981, ApJ, 245, 671
Walter, F. M., Cash, W., Charles, P. A., & Bowyer, C. S. 1980, ApJ, 236, 212
Walter, F. M., Neff, J. E., Gibson, D. M., Linsky, J. L., Rodonò, M., Gary, D. E., & Butler, C. J. 1983, A&A, 186, 241
Wang, Y. M. 1996, ApJ, 464, L91
Watanabe, T., Hara, H., Shimizu, T., et al. 1995, Sol. Phys., 157, 169
Weber, E. J., & Davis, L. Jr. 1967, ApJ, 148, 217
White, N. E. 1996, in 9th Workshop on Cool Stars, Stellar Systems, and the Sun, ed. R. Pallavicini and A. K. Dupree (San Francisco: ASP), 193
White, S. M., Pallavicini, R., & Lim, J. 1996, in: 9th Cambridge Workshop on Cool Stars, Stellar Systems, and the Sun, ed. R. Pallavicini & A. K. Dupree (San Francisco:ASP), 299
White, N. E., Shafer, R. A., Parmar, A. N., Horne, K., & Culhane, J. L., 1990, ApJ, 350, 776
Wood, B. E., Harper, G. M., Linsky, J. L., & Dempsey, R. C. 1996, ApJ, 458, 761
Zirker, J. B. 1993, Sol. Phys., 148, 43

Curriculum Vitae

Name	Marc Audard
Date of birth	May 1, 1974
Place of birth	Lausanne (Vaud), Switzerland
Nationality	Swiss, citizen of Lausanne (VD)

1980 - 1984	Elementary school in Le Mont (VD)
1984 - 1990	Secondary schools in Lausanne and Pully (VD)
1990 - 1993	Gymnase de la Cité in Lausanne, type XB
1993	*Baccalauréat ès lettres, mention Latin-Mathématiques* & *Maturité fédérale type B*
1993 - 1998	Studies in physics at the University of Lausanne
1995 - 1998	Teaching assistant at the Institute of Experimental Physics, Univ. of Lausanne
1996 - 1997	Research assistant at the Institute of Astronomy, University of Lausanne
1998	*Diplôme de physicien*, University of Lausanne
	Diploma thesis in astrophysics:
	"X-ray Variability of Active Galactic Nuclei"
	Thesis supervision: Prof. T. Courvoisier and Prof. B. Hauck
1998	Teaching assistant at the Institute of Astronomy, University of Lausanne
1998 - 2002	Research assistant at the Laboratory for Astrophysics, Paul Scherrer Institut and PhD student at ETH Zürich
2002	Doctoral thesis in astrophysics:
	"Extreme Ultraviolet and X-Ray Studies of Flare Heating and Elemental Composition of Stellar Coronae"
	Thesis supervision: PD Dr. M. Güdel and Prof. A. O. Benz

List of Publications

A full list of publications is given below, differentiating between papers published in refereed journals and papers published in non-refereed conference proceedings. At the end, papers in preparation or submitted to refereed journals are also given. The entries are ordered in a reverse chronological order.

Refereed

1. THE XMM-NEWTON VIEW OF STELLAR CORONAE: FLARE HEATING IN THE CORONAE OF HR 1099.
   Audard, M., Güdel, M., & Mewe, R. 2001, A&A, 365, L318

2. FIRST LIGHT MEASUREMENTS WITH THE XMM-NEWTON REFLECTION GRATING SPECTROMETERS: EVIDENCE FOR AN INVERSE FIRST IONISATION POTENTIAL EFFECT AND ANOMALOUS NE ABUNDANCE IN THE CORONAE OF HR 1099.
   Brinkman, A. C., Behar, E., Güdel, M., **Audard, M.**, den Boggende, A. J. F., Branduardi-Raymont, G., Cottam, J., Erd, C., den Herder, J. W., Jansen, F., Kaastra, J. S., Kahn, S. M., Mewe, R., Paerels, F. B. S., Peterson, J. R., Rasmussen, A. P., Sakelliou, I., & de Vries, C. 2001, A&A, 365, L324

3. THE XMM-NEWTON VIEW OF STELLAR CORONAE: HIGH-RESOLUTION X-RAY SPECTROSCOPY OF CAPELLA.
   Audard, M., Behar, E., Güdel, M., Raassen, A. J. J., Porquet, D., Mewe, R., Foley, C. R., & Bromage, G. E. 2001, A&A, 365, L329

4. THE XMM-NEWTON VIEW OF STELLAR CORONAE: X-RAY SPECTROSCOPY OF THE CORONA OF AB DORADUS.
   Güdel, M., **Audard, M.**, Briggs, K., Magee, H., Maggio, A., Mewe, R., Pallavicini, R., & Pye, J. 2001, A&A, 365, L336

5. THE XMM-NEWTON VIEW OF STELLAR CORONAE: CORONAL STRUCTURE IN THE CASTOR X-RAY TRIPLET.
   Güdel, M., **Audard, M.**, Magee, H., Franciosini, E., Grosso, N., Cordova, F., Pallavicini, R., & Mewe, R. 2001, A&A, 365, L344

6. THE REFLECTION GRATING SPECTROMETER ON BOARD XMM-NEWTON.
   den Herder, J. W., Brinkman, A. C., Kahn, S. M., Branduardi-Raymont, G., Thomsen,

K., Aarts, H., **Audard, M.**, Bixler, J. V., den Boggende, A. J. F., Cottam, J., Decker, T., Dubbeldam, L., Erd, C., Goulooze, H., Güdel, M., Guttridge, P., Hailey, C. J., al Janabi, K., Kaastra, J. S., de Korte, P. A. J., van Leeuwen, B. J., Mauche, C., McCalden, A. J., Mewe, R., Naber, A., Paerels, F. B. S., Peterson, J. R., Rasmussen, A. P., Rees, K., Sakelliou, I., Sako, M., Spodek, J., Stern, M., Tamura, T., Tandy, J., de Vries, C. P., Welch, S., & Zehnder, A. 2001, A&A, 365, L7

7. XMM-Newton Observation of the Tycho Supernova Remnant.
Decourchelle, A., Sauvageot, J. L, **Audard, M.**, Aschenbach, B., Sembay, S., Rothenflug, R., Ballet, J., Stadlbauer, T., & West, R. G. 2001, A&A, 365, L218

8. High-Resolution X-Ray Spectroscopy and Imaging of Supernova Remnant N132D.
Behar, E., Rasmussen, A. P., Griffiths, R. G., Dennerl, K., **Audard, M.**, Aschenbach, B., & Brinkman, A. C. 2001, A&A, 365, L242

9. Extreme-Ultraviolet Flare Activity in Late-Type Stars.
Audard, M., Güdel, M., Drake, J. J., & Kashyap, V. L. 2000, ApJ, 541, 396

10. Implications from Extreme-Ultraviolet Observations for Coronal Heating of Active Stars.
Audard, M., Güdel, M., & Guinan, E. F. 1999, ApJ, 513, L53

Non-refereed

1. Elemental Abundances in Stellar Coronae with XMM-Newton.
Audard, M., & Güdel, M. 2002, in "New Visions of the X-ray Universe in the XMM-Newton and Chandra Era", ed. F. Jansen, in press

2. The Chandra LETG and XMM-Newton Spectra of HR 1099.
Audard, M., Güdel, M., & van der Meer, R. L. J. 2002, in "New Visions of the X-ray Universe in the XMM-Newton and Chandra Era", ed. F. Jansen, in press

3. Reducing Reflection Grating Spectrometer Data for Point-like Sources.
Audard, M. 2002, in "New Visions of the X-ray Universe in the XMM-Newton and Chandra Era", ed. F. Jansen, in press

4. XMM Observations of the WR+O System Gamma Velorum.
Dumm, T., Güdel, M., Schmutz, W., **Audard, M.**, Schild, H.-R., Leutenegger, M., van der Hucht, K. 2002, in "New Visions of the X-ray Universe in the XMM-Newton and Chandra Era", ed. F. Jansen, in press

5. An XMM-Newton Study of Proxima Centauri.
Güdel, M., **Audard, M.**, Horvath, M., Smith, K. W., Skinner, S. L., Linsky, J. L., & Drake, J. J. 2002, in "New Visions of the X-ray Universe in the XMM-Newton and Chandra Era", ed. F. Jansen, in press

6. XMM-Newton Observation of Θ^1 Tau, The Brightest Hyades Giant.
Pallavicini, R., Franciosini, E., Maggio, A., Micela, G., **Audard, M.**, & Güdel, M. 2002, in "New Visions of the X-ray Universe in the XMM-Newton and Chandra Era", ed. F. Jansen, in press

7. Calibration of the Reflection Grating Spectrometers onboard XMM-Newton.
den Herder, J. W., Brinkman, A. C., Kahn, S. M., Branduardi-Raymont, G., **Audard, M.**, den Boggende, . J., Cottam, C., Erd, C., Güdel, M., Kaastra, J. S., Paerels, F. B., Peterson, J. R., Rasmussen, A. P., Reynolds, J. D., Tamura, T., & de Vries, C. P. 2002, in "New Visions of the X-ray Universe in the XMM-Newton and Chandra Era", ed. F. Jansen, in press

8. Temperature Determination and Emission Measure Modeling of the Corona of AT Mic.
Raassen, A. J. J., **Audard, M.**, Mewe, R., Güdel, M., & Kaastra, J. S. 2002, in "New Visions of the X-ray Universe in the XMM-Newton and Chandra Era", ed. F. Jansen, in press

9. Pre-main Sequence Dwarfs near Gamma Velorum.
Smith, K. W., Güdel, M., **Audard, M.**, & Jeffries, R. 2002, in "New Visions of the X-ray Universe in the XMM-Newton and Chandra Era", ed. F. Jansen, in press

10. The Neupert Effect in Sigma Geminorum.
Smith, K. W., Güdel, M., **Audard, M.**, Behar, E., & Mewe, R. 2002, in "New Visions of the X-ray Universe in the XMM-Newton and Chandra Era", ed. F. Jansen, in press

11. A Menagerie of Stellar Flares.
Smith, K. W., Güdel, M., & **Audard, M.** 2002, in "New Visions of the X-ray Universe in the XMM-Newton and Chandra Era", ed. F. Jansen, in press

12. A Study of the Coronal Plasma in RS CVn Binary Systems: HR 1099 and co.
Audard, M., Güdel, M., Sres, A., Mewe, R., Raassen, A. J. J., Behar, E., Foley, C. R., & van der Meer, R. L. J. 2002, in The Twelfth Cool Stars, Stellar Systems and the Sun, eds. A. Brown, T. R. Ayres, G. M. Harper, (Boulder: Univ. of Colorado), in press

13. The Quiescent Corona of UX Ari as seen by Chandra.
Drake, S. A., Brenneman, L., White, N. E., Simon, T., Singh, K. P., Güdel, M., & **Audard, M.** 2002, in The Twelfth Cool Stars, Stellar Systems and the Sun, eds. A. Brown, T. R. Ayres, G. M. Harper, (Boulder: Univ. of Colorado), in press

14. A Systematic Spectroscopic X-Ray Study of Stellar Coronae with XMM-Newton
Güdel, M., **Audard, M.**, Smith, K. W., Sres, A., Escoda, C., Wehrli, R., Guinan, E. F.,

Ribas, I., Beasley, A. J., Mewe, R., Raassen, A. J. J., Behar, E., & Magee, H. 2002, in The Twelfth Cool Stars, Stellar Systems and the Sun, eds. A. Brown, T. R. Ayres, G. M. Harper, (Boulder: Univ. of Colorado), in press

15. TEMPERATURE DETERMINATION AND EMISSION MEASURE MODELING OF THE CORONAE OF α CENTAURI AND PROCYON.
Raassen, A. J. J., Kaastra, J. S., van der Meer, R. L. J., Mewe, R., **Audard, M.**, Güdel, M., Ness, J.-U., & Behar, E. 2002, in The Twelfth Cool Stars, Stellar Systems and the Sun, eds. A. Brown, T. R. Ayres, G. M. Harper, (Boulder: Univ. of Colorado), in press

16. MODELING STELLAR MICROFLARES.
Kashyap, V., Drake, J. J., Güdel, M., & **Audard, M.** 2002, in Statistical Challenges in Modern Astronomy III, eds. G. J. Babu & E. D. Feigelson (New York: Springer), in press

17. A STUDY OF THE CORONAL PLASMA IN RS CVN BINARY SYSTEMS: HR 1099 AND CO.
Audard, M., Güdel, M., Sres, A., Mewe, R., Raassen, A. J. J., Behar, E., Foley, C. R., & van der Meer, R. L. J. 2002, in 35$^{\rm th}$ ESLAB Symposium, eds. F. Favata & J. J. Drake (San Francisco: ASP), in press

18. XMM-NEWTON PROBES THE SOLAR PAST: OBSERVATIONS OF SOLAR ANALOGS AT DIFFERENT AGES.
Güdel, M., **Audard, M.**, Sres, A., Wehrli, R., Behar, E., Mewe, R., Raassen, A. J. J., & Magee, H. R. M. 2002, in 35$^{\rm th}$ ESLAB Symposium, eds. F. Favata & J. J. Drake (San Francisco: ASP), in press

19. FLARES AND CORONAL HEATING IN ACTIVE STARS - A STATISTICAL INVESTIGATION.
Güdel, M., **Audard, M.**, Kashyap, V. L., Drake, J. J., & Guinan, E. F. 2002, in 35$^{\rm th}$ ESLAB Symposium, eds. F. Favata & J. J. Drake (San Francisco: ASP), in press

20. FLARES HEATING OF STELLAR CORONAE.
Kashyap, V. L., Drake, J. J., Güdel, M., & **Audard, M.** 2002, in 35$^{\rm th}$ ESLAB Symposium, eds. F. Favata & J. J. Drake (San Francisco: ASP), in press

21. EMISSION MEASURE MODELING AND ABUNDANCE DETERMINATION OF PROCYON BY MEANS OF A VARIETY OF INSTRUMENTS ON BOARD CHANDRA AND XMM-NEWTON.
Raassen, A. J. J., **Audard, M.**, Mewe, R., Güdel, M., van der Meer, R. L. J., & Behar, E. 2002, in 35$^{\rm th}$ ESLAB Symposium, eds. F. Favata & J. J. Drake (San Francisco: ASP), in press

22. THE JOINT XMM-NEWTON AND CHANDRA VIEW OF YY GEM.
Stelzer, B., Burwitz, V., Neuhäuser, R., **Audard, M.**, Schmitt, J. H. M. M. 2002, in 35$^{\rm th}$ ESLAB Symposium, eds. F. Favata & J. J. Drake (San Francisco: ASP), in press

23. VIABILITY OF FLARE HEATING OF STELLAR CORONAE.
Kashyap, V. L., Drake, J. J., Güdel, M., & **Audard, M.** 2001, AGU 2001 Spring Meeting, Solar-Planetary Space Physics and Aeronomy, Session SP51C (Nanoflare Statistics, Self-Organized Criticality, and Coronal Heating II), SP51C-09, *oral*

24. STELLAR CORONAE WITH XMM-NEWTON RGS. II. X-RAY VARIABILITY.
Audard, M., Güdel, M., den Boggende, A. J., Brinkman, A. C, den Herder, J. W., Kaastra, J. S., Mewe, R., Raassen, A. J. J., de Vries, C., Behar, E., Cottam, J., Kahn, S. M., Paerels, F. B. S., Peterson, J. M., Rasmussen, A. P., Sako, M., Branduardi-Raymont, G., Sakelliou, I., & Erd, C. 2001, in ASP Conf. Ser. 234, X-Ray Astronomy 2000, ed. R. Giacconi, S. Serio & L. Stella, (San Francisco: ASP), 79

25. STELLAR CORONAE WITH XMM-NEWTON RGS. I. CORONAL STRUCTURE.
Güdel, M., **Audard, M.**, den Boggende, A. J., Brinkman, A. C, den Herder, J. W., Kaastra, J. S., Mewe, R., Raassen, A. J. J., de Vries, C., Behar, E., Cottam, J., Kahn, S. M., Paerels, F. B. S., Peterson, J. M., Rasmussen, A. P., Sako, M., Branduardi-Raymont, G., Sakelliou, I., & Erd, C. 2001, in ASP Conf. Ser. 234, X-Ray Astronomy 2000, ed. R. Giacconi, S. Serio & L. Stella, (San Francisco: ASP), 73

26. AD LEO FROM X-RAYS TO RADIO: ARE FLARES RESPONSIBLE FOR THE HEATING OF STELLAR CORONAE?
Güdel, M., **Audard, M.**, Guinan, E. F., Drake, J. J., Kashyap, V. L., Mewe, R., & Alekseev, I.Y. 2001, in ASP Conf. Ser. 234, X-Ray Astronomy 2000, ed. R. Giacconi, S. Serio & L. Stella, (San Francisco: ASP), on CD-ROM

27. BEPPOSAX OBSERVATIONS OF THE RAPIDLY-ROTATING YOUNG STAR AB DORADUS.
Franciosini, E., Maggio, A., Pallavicini, R., Reale, F., Tagliaferri, G., Cutispoto, G., Güdel, M., & **Audard, M.** 2001, in ASP Conf. Ser. 234, X-Ray Astronomy 2000, ed. R. Giacconi, S. Serio & L. Stella, (San Francisco: ASP), on CD-ROM

28. XMM-NEWTON RGS OBSERVATIONS OF MCG-6-30-15 AND MRK 766: EVIDENCE FOR EMISSION LINES FROM A RELATIVISTIC ACCRETION DISK.
Branduardi-Raymont, G., Page, M. J., Sakelliou, I., Zane, S., den Boggende, A. J., Brinkman, A. C, den Herder, J. W., Kaastra, J. S., Mewe, R., de Vries, C., Behar, E., Cottam, J., Kahn, S. M., Paerels, F. B. S., Peterson, J. M., Rasmussen, A. P., Sako, M., **Audard, M.**, Güdel, M., Kuster, M., Wilms, J., & Erd, C. 2001, in ASP Conf. Ser. 234, X-Ray Astronomy 2000, ed. R. Giacconi, S. Serio & L. Stella, (San Francisco: ASP), 477

29. X-RAY SPECTROSCOPY OF CLUSTERS OF GALAXIES WITH XMM.
Kaastra, J. S., den Boggende, A. J., Brinkman, A. C, Ferrigno, C., den Herder, J. W., Mewe, R., Tamura, T., de Vries, C., Cottam, J., Kahn, S. M., Paerels, F. B. S., Peterson, J. M., Rasmussen, A. P., Branduardi-Raymont, G., Sakelliou, I., **Audard, M.**, Güdel, M.,

& Erd, C. 2001, in ASP Conf. Ser. 234, X-Ray Astronomy 2000, ed. R. Giacconi, S. Serio & L. Stella, (San Francisco: ASP), 351

30. STELLAR CORONAE WITH XMM-NEWTON RGS.
Audard, M., Güdel, M., Mewe, R., Raassen, A. J. J., Behar, E. 2001, in proceedings of the X-Ray Astronomy Workshop, (Toulouse), 19

31. FLARES AS HEATING AGENTS OF ACTIVE LATE-TYPE STELLAR CORONAE?
Audard, M., Güdel, M., Drake, J. J., Kashyap, V., & Guinan, E. F. 2001, in ASP Conf. Ser. 223, Eleventh Workshop on Cool Stars, Stellar Systems, and the Sun, "Challenges for the New Millenium", ed. R. J. García López, R. Rebolo, & M. R. Zapatero Osorio (San Francisco: ASP), 1121

32. THE UPS AND DOWNS OF AD LEO.
Güdel, M., **Audard, M.**, Guinan, E. F., Mewe, R., Drake, J. J., & Alekseev, I. Y. 2001, in ASP Conf. Ser. 223, Eleventh Workshop on Cool Stars, Stellar Systems, and the Sun, "Challenges for the New Millenium", ed. R. J. García López, R. Rebolo, & M. R. Zapatero Osorio (San Francisco: ASP), 1085

33. RADIO CHARACTERISTICS OF COOL STARS AND THE HRD.
Güdel, M., & **Audard, M.** 2001, in ASP Conf. Ser. 223, Eleventh Workshop on Cool Stars, Stellar Systems, and the Sun, "Challenges for the New Millenium", ed. R. J. García López, R. Rebolo, & M. R. Zapatero Osorio (San Francisco: ASP), 961

34. HIGH RESOLUTION SPECTROSCOPY OF THE NUCLEAR REGION OF NGC1068 WITH XMM-NEWTON/RGS.
Paerels, F. B. S., **Audard, M.**, Behar, E., Branduardi-Raymont, G., Brinkman, A. C., Cottam, J., den Boggende, A. J., den Herder, J. W., de Vries, C., Ferrigno, C., Güdel, M., Kaastra, J., Kahn, S. M., Mewe, R., Peterson, J. M., Rasmussen, A. P., Sakelliou, I., Sako, M., Tamura, T., van der Heyden, K. 2000, HEAD 2000 (Hawaii), Session 1 (Active Galaxies: Seyferts), 1.05 *oral*

35. XMM-NEWTON OBSERVATION OF THE COMPLEX ABSORBING MEDIUM IN IRAS 13349+2438.
Sako, M., **Audard, M.**, Behar, E., den Boggende, A. J., Boller, Th., Branduardi-Raymont, G., Brinkman, A. C., Cottam, J., Erd, C., Ferrigno, C., Güdel, M., den Herder, J. W., Kaastra, J., Kahn, S. M., Lagostina, A., Mewe, R., Paerels, F. B. S., Peterson, J. R., Pierre, M., Puchnarewicz, E. M., Rasmussen, A. P., Tamura, T., Sakelliou, I., Thomsen, K., de Vries, C., 2000, HEAD 2000 (Hawaii), Session 2 (Active Galaxies), 2.03 *poster*

36. X-RAY SPECTROSCOPY OF CLUSTERS OF GALAXIES WITH XMM-NEWTON.
Peterson, J. R., **Audard, M.**, Behar, E., den Boggende, A. J., Branduardi-Raymont, G., Brinkman, A. C., Cottam, J., Erd, C., Ferrigno, C., Güdel, M., den Herder, J. W., Jernigan, J. G., Kaastra, J., Kahn, S. M., Mewe, R., Paerels, F. B. S., Rasmussen, A. P., Sako, M., Tamura, T., Sakelliou, I., Thomsen, K., de Vries, C. 2000, HEAD 2000 (Hawaii), Session 13 (Clusters of Galaxies), 13.22 *poster*

37. THE MAGELLANIC CLOUD SUPERNOVA REMNANT SAMPLE AS OBSERVED BY XMM-NEWTON RGS.
Rasmussen, A. P., Behar, E., Cottam, J., Kahn, S. M., Paerels, F. B. S., Peterson, J. M., Sako, M., Bleeker, J. A. M., den Boggende, A. J., Brinkman, A. C., den Herder, J. W., van der Heyden, K. J., Kaastra, J., Mewe, R., Tamura, T., de Vries, C., Branduardi-Raymont, G., Sakelliou, I., **Audard, M.**, Güdel, M., Erd, C. 2000, HEAD 2000 (Hawaii), Session 40 (Supernova Remnants/Interstellar Medium), 40.03 *oral*

38. MODELING OF NON EQUILIBRIUM IONIZING PLASMAS: APPLICATIONS AND COMPARISON WITH SUPERNOVA REMNANT OBSERVATIONS BY THE RGS SPECTROMETER.
Behar, E., Rasmussen, A. P., Cottam, J., Kahn, S. M., Paerels, F. B. S., Peterson, J. M., Sako, M., Brinkman, A. C., den Boggende, A. J., den Herder, J. W., de Vries, C. P., Ferrigno, C., Kaastra, J., Mewe, R., Tamura, T., van der Heyden, K. J., Branduardi-Raymont, G., Sakelliou, I., **Audard, M.**, Güdel, M., Erd, C. 2000, HEAD 2000 (Hawaii), Session 40 (Supernova Remnants/Interstellar Medium), 40.04 *oral*

39. HIGH-RESOLUTION X-RAY SPECTROSCOPY OF ZETA PUPPIS AND ETA CARINAE WITH THE RGS ON XMM.
Leutenegger, M. A., **Audard, M.**, Behar, E., den Boggende, A. J., Brinkman, A. C., Branduardi-Raymont, G., Cottam, J., Erd, C., Ferrigno, C., Güdel, M., den Herder, J. W., Kaastra, J., Kahn, S. M., Magee, H., Mewe, R., Paerels, F. B. S., Pallavicini, R., Peterson, J. M., Rasmussen, A. P., Rauw, G., Sako, M., Tamura, T., Sakelliou, I., Thomsen, K., de Vries, C., 2000, HEAD 2000 (Hawaii), Session 42 (Stars and Stellar Coronae), 42.01 *poster*

40. STELLAR CORONAL SPECTROSCOPY WITH THE XMM-NEWTON RGS.
Güdel, M., **Audard, M.**, Behar, E., Cottam, J., Kahn, S. M., Paerels, F. B. S., Peterson, J. M., Rasmussen, A. P., Branduardi-Raymont, G., Sakelliou, I., den Boggende, A. J., Brinkman, A. C., den Herder, J. W., Kaastra, J., Mewe, R., Tamura, T., de Vries, C., Erd, C., XMM Collaboration 2000, HEAD 2000 (Hawaii), Session 45 (Stellar Coronae/Cataclismic Variables), 45.03 *oral*

41. IN-FLIGHT CALIBRATION OF THE XMM-NEWTON REFLECTION GRATING SPECTROMETERS.
Erd, C., **Audard, M.**, den Boggende, A. J., Branduardi-Raymont, G., Brinkman, A. C., Cottam, J., Dubbeldam, L., Güdel, M., den Herder, J. W., Kaastra, J. S., Kahn, S. M., Mewe, R., Paerels, F. B., Peterson, J. R., Rasmussen, A. P., Sakelliou, I., Spodek, J., Thomsen, K., de Vries, C., Zehnder, A. 2000, Proc. SPIE 4140, 13

42. FLARE DISTRIBUTIONS AND CORONAL HEATING ON FK AQR.
Kashyap, V. L., Drake, J. J., **Audard, M.**, Güdel, M. 2000, 196th AAS Meeting (Rochester), Session 13 (EUVE), 13.05 *oral*

43. ACTIVE STELLAR CORONAE: LOTS OF LITTLE FLARES?
Drake, J. J., Kashyap, V. L., **Audard, M.**, Güdel, M. 2000, 196th AAS Meeting (Rochester), Session 54 (Applications of Statistics), 54.07 *poster*

44. ACTIVE LATE-TYPE STELLAR CORONAE: HINTS FOR FLARE HEATING?
Audard, M., Güdel, M., Drake, J. J., Kashyap, V., & Guinan, E. F. 2000, in IAU Symp. 195, "Highly Energetic Physical Processes and Mechanisms for Emissions from Astrophysical Plasmas", ed. P. C. H. Martens, S. Tsuruta, & M. A. Weber (San Francisco: ASP), 377

45. THE EUV CORONAE OF THE YOUNG SOLAR ANALOGS 47 CAS & EK DRA: AN EUVE SPECTROSCOPIC AND TIMING STUDY OF CORONAL HEATING.
Audard, M., Güdel, M., & Guinan, E. F. 1998, in Proceedings of the First XMM Workshop on "Science with XMM", ed. M. Dahlem

Submitted/In preparation at the time of thesis submission

1. FIRST IONIZATION POTENTIAL BIAS IN RS CVN BINARY SYSTEMS OBSERVED BY XMM-NEWTON.
Audard, M., & Güdel, M. 2002, in preparation

2. THE CHANDRA LOW-ENERGY TRANSMISSION GRATING SPECTROMETER SPECTRUM OF THE RS CVN BINARY SYSTEM HR 1099.
Audard, M.. Güdel, M., et al. 2002, in preparation

3. FIRST DETECTION OF THE NEUPERT EFFECT IN THE CORONA OF AN RS CVN BINARY SYSTEM BY XMM-NEWTON AND THE VLA.
Güdel, M., **Audard, M.**, Smith, K. W., Behar, E., & Mewe, R. 2002, ApJ, submitted

4. ELEMENTAL ABUNDANCES IN STELLAR CORONAE: LONG-TERM EVOLUTION FROM THE INVERSE TO THE NORMAL FIRST IONIZATION POTENTIAL EFFECT.
Güdel, M, **Audard, M.**, Sres, A., Wehrli, R., & Mewe, R. 2002, ApJ, submitted

5. HIGH-RESOLUTION X-RAY SPECTROSCOPY OF PROCYON BY CHANDRA AND XMM-NEWTON.
Raassen, A. J. J., Mewe, R., **Audard, M.**, Güdel, M., Behar, E., Kaastra, J. S., van der Meer, R. L. J., Foley, C. R., & Ness, J.-U. 2002, A&A, submitted

6. XMM-NEWTON OBSERVATIONS OF γ^2 VELORUM.
Schmutz, W., Dumm, T., **Audard, M.**, Güdel, M., Leutenegger, M. A., Schild, H.-R., van der Hucht, K. A., & 2002, in preparation

7. SIMULTANEOUS X-RAY SPECTROSCOPY WITH CHANDRA AND XMM-NEWTON.
Stelzer, B., Burwitz, V., **Audard, M.**, Güdel, M., Ness, J.-U., Grosso, N., Neuhäuser, R., Schmitt, J. H. M. M., Predehl, P., & Aschenbach, B. 2002, A&A, submitted